ABSTRACT

Title of Document: PLASMA INTERACTIONS WITH MASKING MATERIALS FOR NANOFABRICATION

Florian Georg Chrysostomus Weilnboeck,

Doctor of Philosophy, 2011

Directed By: Prof. G.S. Oehrlein,

Department of Materials Science and Engineering

Plasma-based transfer of patterns into other materials is a key process for production of nano-scale devices used in micro-electronic technology. With the continuously decreasing feature-size of integrated circuits, manufacturing tolerances are becoming increasingly smaller and complex interactions of plasmas and patterned mask materials require an atomistic understanding to meet future processing tolerances. In this work, we investigated how plasma-material interactions in typical low-k pattern transfer processes depend on individual plasma components and properties of polymeric and metallic

masks. First, we studied modifications of 193nm and 248nm photoresist (PR) by plasma ultraviolet/vacuum ultraviolet (UV) radiation, quantifying contributions of plasma radiation to the overall material modifications for direct interaction with plasma. Energetic ions (~125 eV) led to rapid (~3-5 s) formation of a graphitic ion-crust (~1.8 nm) and introduced together with simultaneous UV modifications of the material bulk significantly higher roughness for 193nm PR (~6 nm) than for 248nm PR (~1 nm). During ion-crust formation, 193nm PR softened by chain-scissioning and pendant group detachment in a depth of ~60 nm by UV radiation, while 248nm PR was radiation stable showing surface-close cross-linking (~4 nm). Pretreating 193nm PR with a radiation-dominated He plasma and introducing UV modifications before ion-crust formation in the subsequent plasma etch reduces synergistic roughness formation as explained by wrinkling theory. Second, we studied interactions of fluorocarbon (FC) plasmas with Ti and TiN and compared these with organosilicate glass (OSG). Metal hardmasks are expected to provide improved etching selectivity (ES) and low-k damage compared to PR during pattern transfer. Erosion stages and dependencies of etch rates (ER) on FC layer thickness and energy deposition by ions were identified. ES were low (~4-8) in the diffusion-limited regime (thick FC layers) where OSG experienced strong reduction in ER, but high (up to 15) in the chemical sputtering regime (thin FC layers) at low ion energies where removal of Ti etch products was limited. TiN exhibited higher ER and lower ES than Ti due to increased surface reactivity after rapid removal of N. Overall, findings give directions for rational design of masking materials and plasma discharges for future nanofabrication pattern transfer processes.

PLASMA INTERACTIONS WITH MASKING MATERIALS FOR NANOFABRICATION

by

Florian Georg Chrysostomus Weilnboeck

Dissertation submitted to the Faculty of the Graduate School of the
University of Maryland, College Park in partial fulfillment
of the requirements for the degree of
Doctor of Philosophy
2011

Advisory Committee:

- Prof. G. S. Oehrlein, Department of Materials Science and Engineering, Chair
- Prof. R. M. Briber, Department of Materials Science and Engineering
- Dr. N. Fuller, Thomas J. Watson Research Center, IBM
- Prof. J. Melngailis, Department of Electrical and Computer Engineering
- Prof. J. Seog, Department of Materials Science and Engineering

Acknowledgements

First of all, I would like to thank my advisor, Prof. G.S. Oehrlein, for guiding me throughout the five years at UMD. You helped me to mature as a scientist and engineer by encouraging me, showing me how to attack scientific problems and conduct research, and develop a fundamental understanding that will pass the test of time.

I would like to thank my dissertation committee for their interest in my work: Prof. R. M. Briber, Dr. N. Fuller, Prof. J. Melngailis, and Prof. J. Seog.

For financial support, I would like to thank the National Science Foundation (Award Numbers DMR-0406120 and DMR-0705953), the Semiconductor Research Corporation (Task ID 1292.050), and Texas Instruments. For support of the projects from industry, I want to thank Dow Electronic Materials, IBM, and Lam Research.

I would like to thank Dr. D. Nest, T.-Y. Chung, Prof. D. Graves (University of California, Berkeley), D. Farber, T. Lii, and C. Lenox (Texas Instruments) for collaborating with me. Without all your contributions, ideas and comments I would have never been able to gain the insights presented here. I am especially grateful to Dr. E. Hudson who supervised me during my internship at Lam Research and influenced my way of effectively performing research and presenting findings.

To my former colleagues at UMD, Dr. R. L. Bruce, Dr. S. Engelmann, and Dr. M.-S. Kuo - thank you for introducing me to plasma science and guiding me through the first years of my research. I will never forget the time we worked together.

To my colleagues in the plasma processing group, N. Fox-Lyon, E. Bartis, and D. Metzler – I enjoyed working with you and training you in plasma science. I want to thank you for all the support with experiments and paper revisions and don't know how I could have finished up the work without your help.

I am also very grateful to all of the undergraduate students that I worked with over the years: T. Godo, M. Graves, P. Lambert, I. Liu, T. Muanankese, and M. Sweat. N. Kumar and S. Shachar, it was a pleasure working with you and I am proud of you being a coauthor of my publications.

To my parents, Georg and Elisabeth Weilnboeck, and my Uncle Benno - thank you for all your support in this adventure and keeping my spirits up during the time far away from home.

Table of Contents

List of Figures

Chapter 3:

List of Tables

Chapter 1

Introduction

1.1 Progress in Semiconductor Device Fabrication

In the semiconductor industry, reduction of feature sizes and increased control over critical dimensions (CD) have closely followed Moore's law in the past decades.[1.1] Plasma-based transfer of photoresist (PR) patterns into other materials is a key process for production of nano-scale devices used in micro-electronic technology (see Fig. 1.1). The PR, a sacrificial polymer layer functionalized with photosensitive additives, is patterned in a lithographic step using high energy radiation (ultraviolet (UV), vacuum ultraviolet (VUV), or extreme ultraviolet (EUV) light) making the exposed areas soluble (positive resist).[1.2] Removing the soluble material in the development step generates a mask which can be transferred into the underlying substrate using a plasma etching process.[1.3] The remaining PR mask material is removed after patterning by a plasma-based stripping process also called plasma ashing. This multistep process is the basis for the fabrication of ultra-large scale integrated circuits at high throughput and fidelity.[1.4]

During this process of creating a nano-scale pattern and transferring it into a substrate, the plasma etch is one of the most critical processing steps because the final device performance is determined by the quality of the transferred feature. With the continuously decreasing feature size of devices in integrated circuits, manufacturing tolerances are becoming increasingly narrower.[1.1] The sacrificial resist layers are known to experience extreme material modifications during the plasma etch step leading to a reduction of the feature CD, increased surface roughness, line edge (LER), and line width roughness (LWR), distortion and even collapse of the resist features (flop-over). [1.5-1.12]

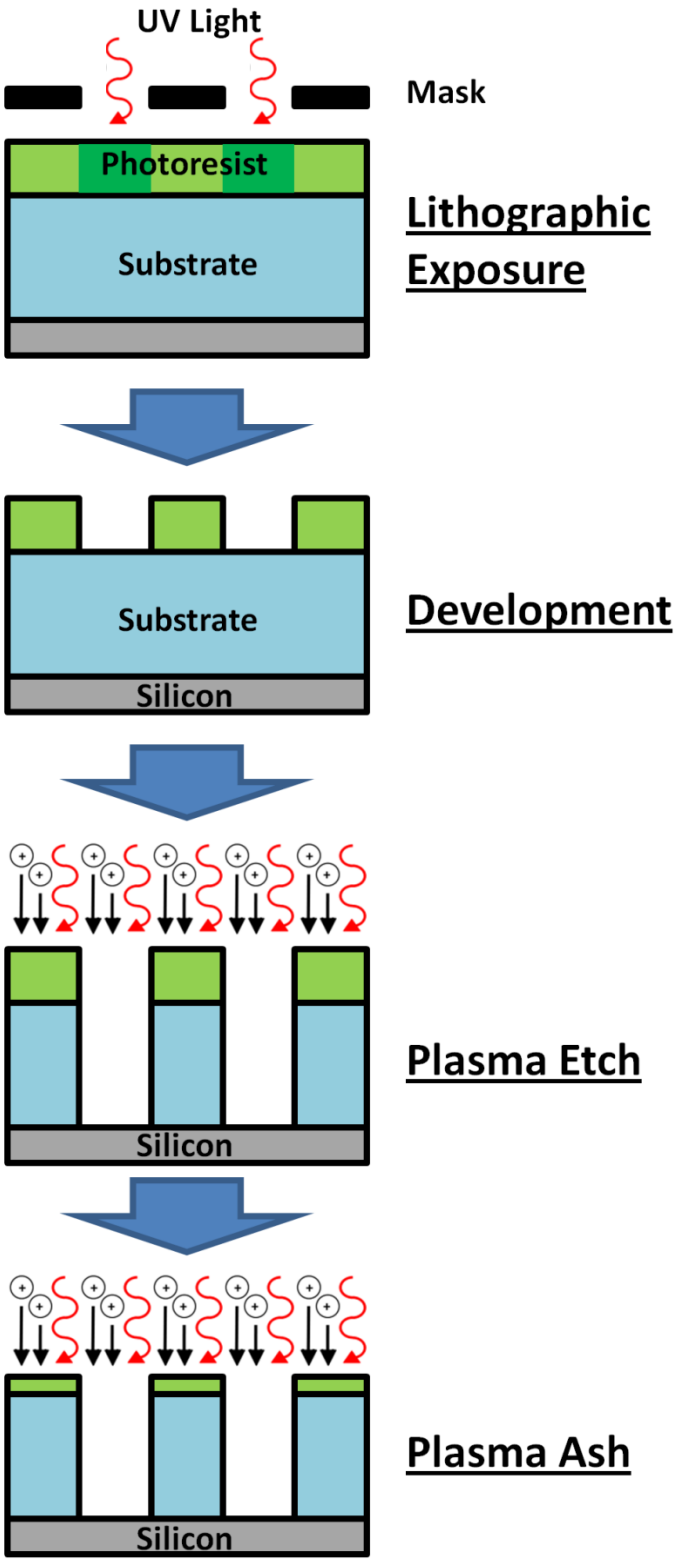

Figure 1.1: *Schematic of pattern transfer processing steps.*

The challenge of plasma-based pattern transfer originates from the complex nature of plasma-polymer interactions where many different plasma species, such as ions, excited neutrals, radicals, electrons, and UV/VUV radiation can modify the resist at the film surface and in the material bulk.[1.6, 1.13] In order to understand plasma-polymer interactions, plasma conditions and effects of specific plasma components on a particular polymer structure must be considered.

The continuous reduction of feature size recently required reduction in exposure wavelength during the lithographic exposure from 248 nm to 193 nm, requiring a dramatic change in the resist polymer structure.[1.7, 1.10] 248nm PR are based on styrene-type polymers. Due to the high absorbance at smaller wavelength, 248nm PR were replaced by more UV transparent methacrylate-based 193nm PR. These PR polymers are typically used for transferring patterns into SiO_2 or other low-k materials using highly selective plasma chemistries consisting of Ar and fluorocarbon (FC) gases. It was found, that 193nm PR, when exposed to this plasma environment, exhibited significantly reduced etch resistance and increased roughness development when compared to 248nm PR. However, it is not clear which plasma species and polymer components lead to those material specific differences.

In order to compensate for the poor etch resistance of 193nm PR, multilayer resist structures have been introduced. The multilayer resist structures typically consist of three layers: a layer of 193nm PR with a bottom anti-reflection coating (BARC) at the top, a thin Si-containing resist in the middle, and a thick carbon-rich organic polymer layer (OPL) at the bottom (see Fig. 1.2, left).[1.14] The 193nm PR layer is patterned by photolithography, serving as a mask for patterning the Si-containing layer with an Ar/FC

plasma. Subsequently, the pattern in the Si-containing layer is transferred into the carbon-rich hard mask with an O_2-based plasma process followed by a pattern transfer of the OPL hard mask into the low-k material by an Ar/FC plasma process. Each processing step has a high selectivity of the mask over the unpatterned material, enabling the fabrication of small features with high aspect ratios.[1.14] However, loss in pattern fidelity can occur in each individual step and is subsequently transferred into the underlying layers. This emphasizes the importance of preventing or at least reducing PR distortions and roughness formation in the top masking layer.

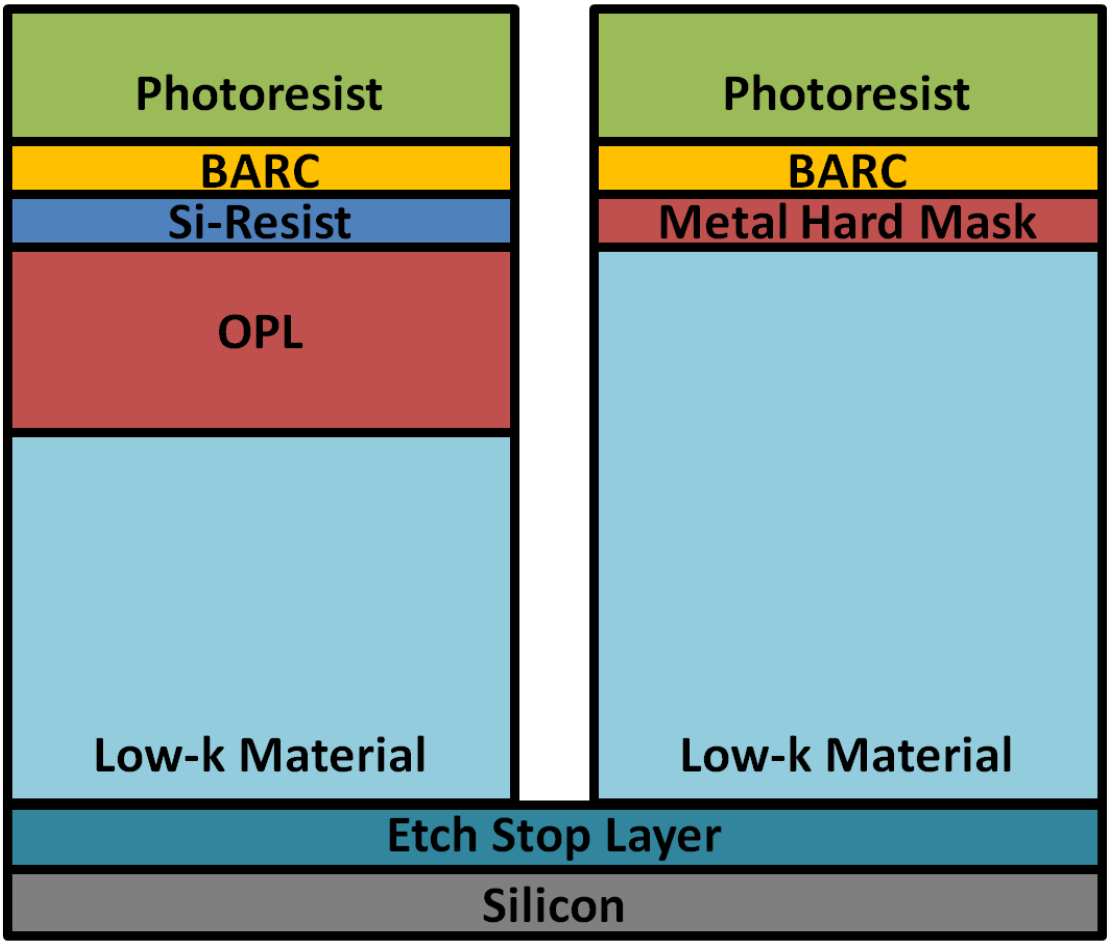

Figure 1.2: *Schematic of multilayer resist based on Si-resist and a carbon hard mask (left) and based on a metallic hard mask (right).*

One promising approach to improve the PR performance during pattern transfer is a pretreatment with a 'mild' plasma discharge, also referred to as plasma curing. This pretreatment step is expected to significantly increase stability and pattern fidelity of PR during the plasma etch step.[1.15-1.19] Alternatively, metallic hard mask may replace the OPL in future generation patterning approaches in order to achieve higher aspect ratios (see Fig. 1.2, right). The most promising materials are Ti and TiN, but plasma-material interactions during pattern transfer into low-k materials and differences between individual hardmask materials are poorly understood.[1.20-1.22] However, to improve the plasma-based pattern transfer processes in current applications and for future technologies a fundamental understanding of the plasma material interactions for different masking materials is required.

1.2 Collaborative Research

This research project was based on world-class interdisciplinary collaborations with leading experts from academia and industry on two topics. A chart of the participating organizations in both topics and their competencies is shown Tab. 1.1.

Project Member	Members	Collaboration	Task	Project
UMD	Oehrlein	ICP reactor, ellipsometry, XPS, OES, AFM,	plasma processing etch and modification rates plasma properties surface composition surface morphology	
UCB	Graves Nest Chung	beam system, AFM, FTIR	beam processing surface morphology bulk composition	Topic 1 Stage 1
Lam Research	Hudson	CCP reactor, SEM	state of the art materials processing	
Dow Electronic Materials	Li Wang Andes	PR spin coating, lithography, SEM	state of the art resist synthesis pattern morphology	
IBM	Fuller Engelmann Bruce	ICP reactor, curing reactor, AFM, FTIR, SEM	future technology plasma processing of resist materials	Topic 1 Stage 2
NIST	Benck	UV/VUV OES	state of the art plasma spectroscopy	
Texas Instruments	Farber Lii Lenox	metallic hardmask materials and processing	future technology plasma processing of hard mask materials	Topic 2 TI

Table 1.1: *Organization chart of collaborators and competencies.*

Topic 1 focused on the plasma interactions with polymeric masking materials. In Stage 1 we studied material modifications by plasma radiation and determined the contribution of radiation modification to the overall PR degradation and roughness formation. Special attention was paid to the dependencies on PR structure and composition, as well as plasma chemistry. In Stage 2 we investigated how plasma radiation can be facilitated to pretreat PR materials before pattern transfer processes in order to enhance plasma stability and fidelity during pattern transfer.

Topic 2 focused on the plasma interactions with metallic masking materials and investigated the performance of Ti and TiN films in FC-based pattern transfer plasmas. As stated above, metal hardmasks are being considered for future high aspect ratio feature fabrication as they are expected to be superior to polymeric masking materials in terms of selectivity. Special attention was paid to material specific differences in the erosion behavior and the underlying mechanism leading to selective pattern transfer into low-k materials.

1.3 Experimental Approach

1.3.1 Plasma Processing of Advanced Electronic Materials

Plasma processing and material characterization were mostly performed in the Laboratory for Plasma Processing of Materials at the University of Maryland. The plasma exposures were performed in two inductively coupled plasma (ICP) reactors connected to a surface analysis chamber.

The two ICP systems (see Fig. 1.3) used in this study have been previously described in detail.[1.23, 1.24] Briefly, a planar coil is placed on top of a quartz window and powered through an L-type matching network with a 13.56 MHz power supply (0-2000 W). The ion bombardment energies on the 125 mm and 300 mm diameter substrates can be independently controlled using a bias power supply (0-1000 W) at 3.7 MHz and 13.56 MHz, respectively. The temperature of the bottom electrode is kept at 10 °C and samples are thermally bonded to the bottom electrode using thermal grease. The base pressure achieved in the chambers before processing of each sample was as low as $2x10^{-6}$ Torr. Processing conditions cover a wide range, with operating pressure between 10 mTorr and 100 mTorr achieved by an exhaust throttle valve, a flow rate between 40 sccm and 200 sccm (cubic centimeter per minute at standard conditions) and an inductive power between 200 W and 800 W. Ion energies were determined by the substrate potential which was selected between the plasma potential (~20 V) and a self-bias voltage of -150 V.[25] Typical plasma conditions used in semiconductor fabrication and in this work are low temperature discharges with electron temperatures, T_e, of a few eV ($T_e \approx 1$-10 eV) and plasma densities, n, in the range of $n \approx 10^8$-10^{13} cm^{-3}.[1.26]

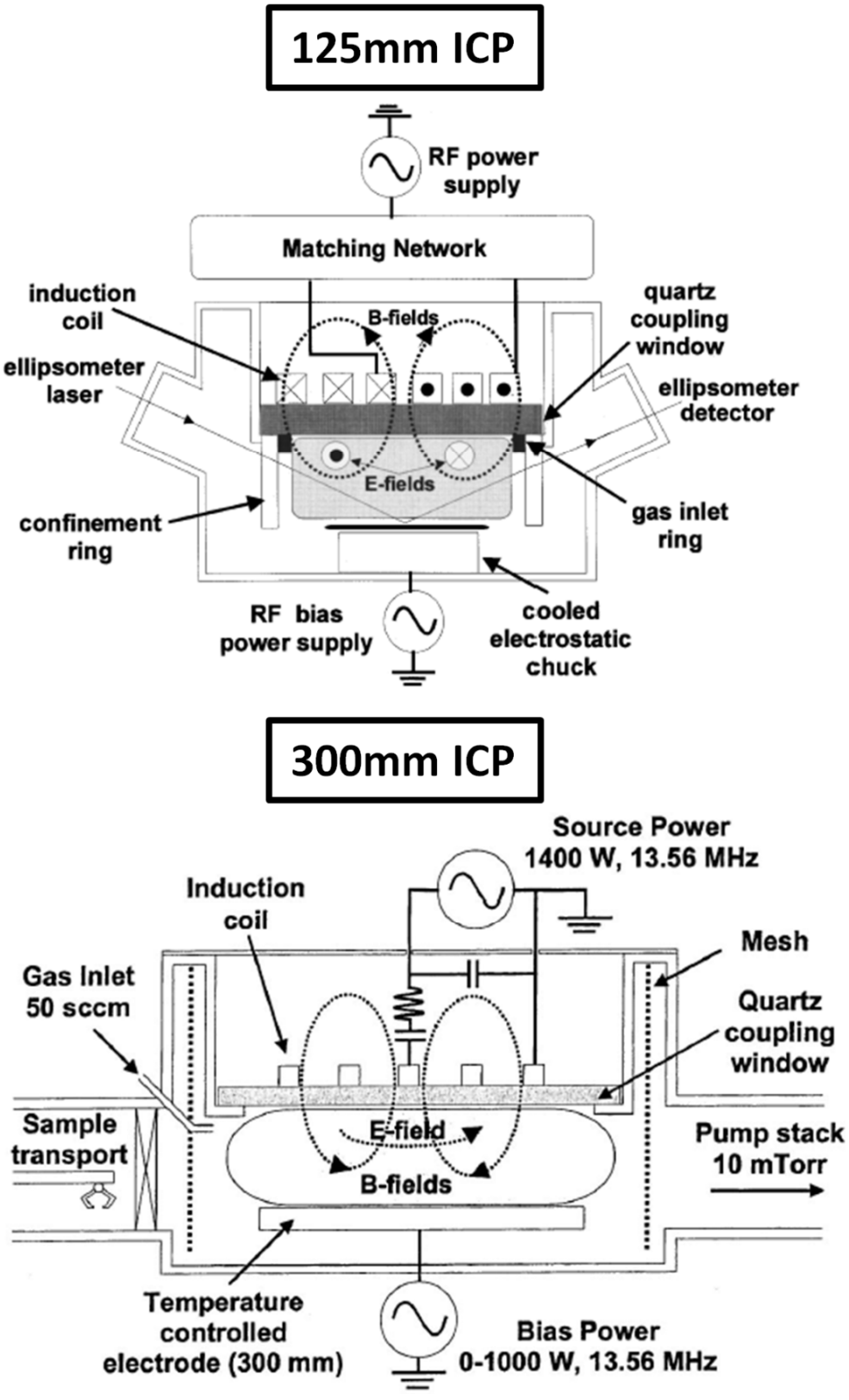

Figure 1.3: *Schematic of the inductively coupled plasma reactors used in this study.*

1.3.2 Description of Materials

1.3.2.1 Polymeric Masking Materials

In this study we investigated plasma-material interactions with methacrylate-based 193nm PR and styrene-based 248nm PR (see Fig. 1.4). 193nm PR consists of methyl-2-adamantyl-methacrylate (MAMA) in the leaving group, α-gamma-butyrolactone-methacrylate (α-GBLMA) in the lactone group, and R-functionalized–adamantyl-methacrylate (RAMA) in the polar group. 248nm PR consists of hydroxystyrene (HOSt), styrene (St), and t-butylacrylate (TBA). Both materials were spin coated on Si together with photoacid generator and a base.

The two PR materials are representative for polymers used in traditional photolithography, immersion lithography, electron-beam lithography, EUV lithography, and as BARC. Material selection for various applications is based on their transparency in a particular wavelength range which is required for the photolithographic patterning of the resist (see Fig. 1.5).[1.27]

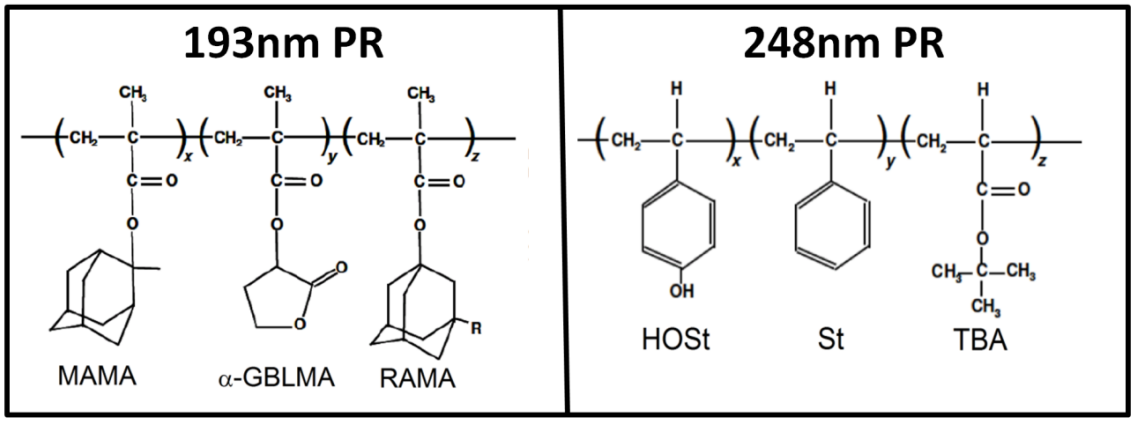

Figure 1.4: *Polymer structures of 193nm and 248nm PR used in this work.*

Methacrylate-based materials have carbon-rich aliphatic pendant groups (e.g. adamantane) attached to the ester group, are oxygen-rich (~10-20 at.% O), and can contain small amounts of F or N. High transmission for wavelengths below ~280 nm makes these materials ideal for 193 nm lithography and BARC for 248 nm lithography. In addition to dry 193 nm lithography, methacrylates are also used for immersion lithography when functionalized with an additional surface coating and are expected to be relevant for electron beam and EUV lithography.[1.28, 1.29] Due to the lower lithographic exposure wavelength methacrylate-based materials can be patterned with significantly smaller features but also exhibit significantly reduced etch resistance due to their high oxygen content. Furthermore, these materials have shown poor plasma stability leading to roughness development (surface roughness, LER and LWR) and pattern distortion (wiggling and flop over).[1.5, 1.7, 1.12]

Aromatic materials contain ring structures in the polymer, are relatively oxygen-poor (~5-10 at.% O), and exhibit high absorption at wavelengths below ~280 nm. This high absorption below ~280 nm makes styrene-based materials suitable for 248 nm lithography PR and 193 nm lithography BARC. In addition to 248 nm lithography, other aromatic and carbon rich materials are considered for future masking materials. Naphthalene-based resist are being tested for EUV lithography due to their high absorption of energetic radiation leading to the formation of an insoluble pattern (negative resist).[1.30] Furthermore carbon-rich OPL are being discussed as organic hard mask materials and expected to replace conventional inorganic hard masks such as SiO_2 and SiC.[1.22]

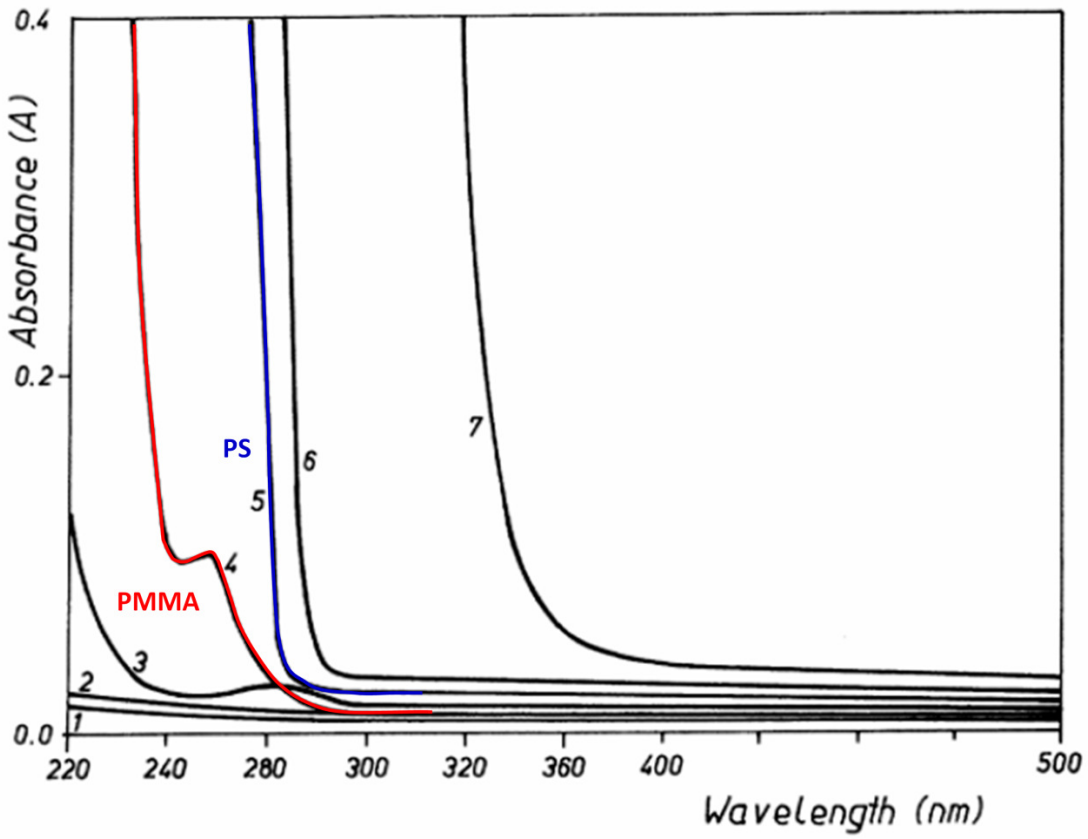

Figure 1.5: *Absorption spectra of various polymers: (4) poly(methyl-methacrylate) and (5) polystyrene.*

1.3.2.2 Metallic Masking Materials

For future integrated chip generations, metallic materials are being considered as replacements for organic masks. The materials used in this work, Ti and TiN, are promising candidates due to their outstanding etch performance (higher selectivity of hard mask over low-k material) and pattern transfer fidelity (less faceting).[1.21, 1.22]

1.3.3 Material Characterization

Plasma processes were monitored in real-time by *in-situ* ellipsometry and optical emission spectroscopy. After processing materials were either transferred through the vacuum-transfer system to a surface analysis system for x-ray photoelectron spectroscopy characterization or exposed to atmosphere for *ex-situ* post plasma characterization by ellipsometry, Fourier transform infrared spectroscopy, atomic force microscopy, and scanning electron microcopy.

1.3.3.1 Ellipsometry

Film thicknesses and optical properties (refractive index and extinction coefficient) were measured *in-situ* during plasma processing and *ex-situ* after plasma processing using a SOFIE STE70 ellipsometer at 632.8 nm wavelength (HeNe laser). The ellipsometer is an automated rotating compensator ellipsometer in the polarizer-compensator-sample analyzer (PCSA) configuration. The angle of incidence off surface normal was ~72 $^{\circ}$ and the refractive index for the Si substrates was fixed at $\tilde{N}$=3.866-0.028*i*.[1.31] The measured parameters, Ψ and Δ, are related to amplitude ratio and phase shift of the polarized laser light components, respectively. Fundamental physical properties of the film such as thickness, refractive index, and extinction coefficient can be extracted by using optical multilayer models and solving the Fresnel reflection coefficients for the physical property values.[1.31, 1.32]

1.3.3.2 Emission Spectroscopy

Emission spectra of the plasma discharges were measure in the visible, UV, and VUV spectral region with wavelengths as low as 114 nm.

1.3.3.3 X-ray Photoelectron Spectroscopy (XPS)

XPS analysis provided information on changes in chemical composition at the film surface. Analysis was performed in a Vacuum Generators ESCA Mk II surface analysis chamber using a non-monochromatic Al Kα source (1486.5 eV) or Mg Kα source (1253.6 eV). The pass energy of the hemispherical analyzer was set to 20 eV and electrons were detected at a takeoff angle of 90 $^{\circ}$. Reducing the takeoff angle to lower values (20 $^{\circ}$) enabled to get a more surface sensitive signal and provided information on the film thickness and compositional depth distributions of thin surface layers. Sample charging was compensated for polymeric masking materials by adjusting the binding energy position of the C─C/C─H peak in the C 1*s* spectra to 285 eV.[1.33] Vacuum transfer of samples from the plasma reactor to the analysis chamber directly following plasma processing prevented contamination and surface oxidation.

1.3.3.4 Fourier-Transform Infrared Spectroscopy (FTIR)

FTIR characterized changes in chemical composition of the material bulk. The analysis was performed *ex-situ* with a Digilab FTS-3000 at a spectral resolution of 2 cm^{-1}. The background and Si substrate signal were subtracted before spectral analysis. The polymeric masking materials were monitored for changes in the C─O─C group (1050─1350 cm^{-1}), ─CH_x group (2800─3100 cm^{-1}) and C═O group (1650─1900 cm^{-1}).

1.3.3.5 Atomic Force Microscopy (AFM)

Surface topography evolution of processed materials was measured with a Veeco Instruments AFM in tapping mode at a fixed scan size of 1x1 μm^2 and compared with unprocessed materials. The surface roughness values were calculated from the root mean

square (RMS) of the surface profile after the measurement. The characteristic roughness wavelength was extracted from two-dimensional power spectral densities of the AFM images.

1.3.3.6 Scanning Electron Microscopy (SEM)

Pattern morphology of masks was characterized with an AMRAY SEM at a magnification of 75,000x. SEM images are evaluated using SUMMIT (SEM Metrology Interactive Toolbox) for changes in pattern feature height, CD, LER, and LWR.

1.4 Thesis Outline

This dissertation summarizes an investigation of plasma-material interactions relevant to current and future technology pattern transfer processes for cutting edge large-scale nanofabrication. The continuous shrinkage of feature size to few nanometers requires a fundamental understanding of plasma-material interactions is required on the atomic level. This research contributes to this goal by: 1) identifying the contribution of individual plasma components to the overall modifications of masking materials during plasma-based pattern transfer, 2) determining the influence of material structure and composition on the plasma-induced material modifications, and 3) establishing criteria for plasma conditions, material structure and composition to improve pattern transfer processes.

In Chapter 2, we present on PR modifications by plasma UV/VUV radiation and discuss dependencies on polymer structure and emission spectrum of the plasma discharge. In Chapter 3, we describe real-time measurements of PR modifications in direct plasmas and indentify the individual contributions of UV/VUV radiation and ions. Differences in roughness development during processing are compared to material dependent differences in modification dynamics. In Chapter 4, we show that plasma-based pretreatments of PR with strong UV/VUV emission can reduce roughness formation in the subsequent plasma process and explain the underlying mechanism.

In Chapter 5, we present on erosion stages and plasma parametric erosion dependencies of Ti, a potential candidate for future hardmasks. The underlying mechanism leading to selective etching of Ti and a reference low-k material in FC plasmas is discussed. In Chapter 6, we compare etching of TiN with Ti and discuss

material dependent differences in the erosion mechanism which lead to varying etch rates and low-k etch selectivities.

In Chapter 7, we summarize the main conclusions of the dissertation and outline directions for future work in the topics of plasma interactions with polymer and metal hardmasks.

Chapter 2

Photoresist modifications by plasma vacuum ultraviolet radiation: The role of polymer structure and plasma chemistry

F. Weilnboeck, R. L. Bruce, S. Engelmann, and G. S. Oehrlein

Department of Materials Science and Engineering and Institute for Research in Electronics and Applied Physics, University of Maryland

D. Nest, T.-Y. Chung, and D. Graves

Department of Chemical Engineering, University of California, Berkeley

M. Li, D. Wang, and C. Andes

Dow Electronic Materials

E. A. Hudson

Lam Research Corporation

Journal of Vacuum Science and Technology B, 28 (5), 993, 2010

Abstract

While vacuum ultraviolet (VUV) photon irradiation has been shown to significantly contribute to material modifications of polymers during plasma exposures, the impact of radiation-induced material alterations on roughness development during plasma processing has remained unclear. The authors have studied the interaction of the radiation of Ar and C_4F_8/Ar plasma discharges with 193nm and 248nm advanced photoresists (PR). Optical filters were used to vary the radiation exposure wavelength range in the ultraviolet (UV) and VUV emission spectra. This enables clarification of the respective roles of plasma photon radiation wavelength and PR polymer structure on the chemical and structural changes produced in the materials. Chemical changes in polymer composition at the film surface and in the material bulk were determined by vacuum transfer x-ray photoelectron spectroscopy and Fourier-transform infrared spectroscopy. Morphological changes, film thickness reduction, and changes in surface and pattern morphology were characterized by ellipsometry, scanning electron microscopy, and atomic force microscopy. The exposure of methacrylate based 193nm PR to photon radiation in the UV/VUV spectral range (λ=112-143 nm) leads to detachment and removal of oxygen containing polymer pendant groups to a depth of about 200 nm. This causes changes in the polymer structure by chain-scission, significant film thickness reduction, and reduced pattern critical dimensions and line edge roughness. Chain-scission reactions and residual detached polymer pendant groups are expected to effectively soften layers of 193nm PR. In contrast to 193nm PR, styrene based 248nm PR was found to be significantly more stable under plasma-produced irradiation due to the low oxygen content, low ester linkage concentration, and absence of lactone. Small

thickness reduction, reduced oxygen loss, and cross-linking were observed in the surface region of 248nm PR. Radiation-induced material modifications of both PR materials decreased with increasing photon wavelength in Ar discharges. Increasing modification of 193nm PR was observed for increasing photon flux at higher wavelengths (λ=143-300 nm) by the emission characteristic of fluorocarbon containing plasmas. In C_4F_8/Ar plasma, the authors observed strongly increased loss of oxygen at the film surface and in the C–O–C and C=O lactone bonds in the material bulk along with film thickness reduction compared to pure Ar discharges. These modifications are directly relevant to plasma processes used for pattern transfer, which often contain fluorocarbon species.

2.1 Introduction

The continued shrinking of semiconductor feature size led to the transition from 248 to 193 nm photolithography requiring a fundamental change in photoresist (PR) structure. The challenges of this transition in terms of plasma processing, including decreased etch resistance and the increased surface and line edge roughness (LER), have been discussed in detail, but the underlying mechanism of roughness development during plasma etch is not well understood.[2.1-2.5] Furthermore, it is not clear how PR roughening depends on resist formulations and/or the generally complex gas chemistries and processing conditions of plasma discharges.[2.5]

We have recently reproduced the surface roughness development of 193nm PR and 248nm PR during Ar plasma processing with a beam system approach. It was shown that the more severe surface roughness of 193nm PR compared to 248nm PR only develops if the material is simultaneously exposed to vacuum ultraviolet (VUV) radiation, ion bombardment, and elevated temperatures. During separate exposures to the individual components (photon radiation, ion bombardment, or heat), the film surfaces remained smooth.[2.6, 2.7]

A proposed mechanism of surface roughness development under direct plasma exposure is based on the formation of compressive stress between a thin stiff ion-modified overlayer (~2 nm) constrained to a relatively softer VUV-modified underlayer (~100 nm), leading to stress relaxation by surface buckling.[2.8-2.11] This synergistic effect has highlighted the importance of plasma photon radiation and leads to the hypothesis that material dependent differences in modification by plasma photon radiation are a key factor for roughness development.

The present study is an effort to understand the fundamental differences in plasma photon radiation modification between 193nm PR and 248nm PR based on their polymer structures and radiation wavelengths. The PR materials were exposed to selected wavelength ranges of an Ar plasma discharge in the visible, UV, and VUV wavelength ranges in a plasma system relevant to industrial processing. Observations are explained based on the differences in the polymer structure in Sec. 2.4.1. Furthermore, this study investigates in Sec. 2.4.2 the dependence of radiation modifications of 193nm PR on the optical emission spectrum for an C_4F_8/Ar plasma discharge relevant to plasma pattern transfer.

2.2 Experiment

2.2.1 Description of materials

In this study, two fully formulated advanced PR systems, both provided by Dow Electronic Materials, were selected to gain insight into the interactions of plasma photon radiation and the PR polymer structure. The PR used were 193nm PR and 248nm PR based on fundamentally different polymer structures.

The 193nm PR is a terpolymer structure consisting of three methacrylate based components functionalized with methyl adamantyl, lactone, and R-functionalized adamantyl. 248nm PR is a mainly styrene based terpolymer structure consisting of hydroxyl styrene, styrene, and t-butylacrylate.[2.4, 2.12] Detailed descriptions of the PR chemical structures are presented in our previous work.[2.4] The significantly higher ester linkage concentration of 193nm PR than 248nm PR leads to higher atomic oxygen content for 193nm PR (~9%) compared to 248nm PR (~5%).[2.5, 2.12]

Both PR systems were spin coated with photoacid generator and base on silicon wafers as 400 nm thick blanket films. For comparison, patterned samples were also produced by lithographic exposure and consisted of 150 nm wide trenches with a 450 nm pitch. Further discussion of the PR materials and the functionality of each individual component can be found elsewhere.[2.4, 2.13]

2.2.2 Plasma processing

The inductively coupled high-density plasma reactor used in this study has been described in a previous publication.[2.14] Briefly, a planar coil is placed on top of a quartz window and powered through an L-type matching network at 13.56 MHz with a power supply (0-2000 W). The plasma induced by the electromagnetic field is confined to a

narrow region of 2-3 cm below the window. The ion bombardment energy can be independently controlled using another 13.56 MHz bias power supply (0-1000 W). The temperature of the 300 mm bottom electrode is kept at 10 °C by the circulation of a cooling liquid. During plasma processing, the PR samples are bonded to the bottom electrode using thermal grease between sample and electrode. Stabilizing the temperature by substrate cooling and thermal bonding of the samples is essential to rule out contributions of temperature effects on our observations.

In this study, optical filters were directly placed onto the PR surfaces (25x25 mm^2 samples) allowing only the plasma photon radiation component to interact with the PR and preventing gaseous plasma species, i.e., ions, neutrals, and radicals, to reach the PR surface. The filters used were MgF_2, Al_2O_3, and borosilicate glass with optical cutoff wavelengths (at 20% transmittance) at the low wavelength side of 112, 143, and 293 nm, respectively.[2.15, 2.16] The borosilicate glass filter and the Al_2O_3 filter will be referred to as the glass filter and the sapphire filter, respectively. This approach enables an investigation of the role of the characteristic plasma photon radiation and wavelength ranges on the material modification during plasma processing. The cutoff wavelengths of the filter materials used and the characteristic emission wavelengths of Ar and fluorocarbon (FC) species in the VUV spectral range are summarized in Tab. 2.1.

PR materials were exposed to Ar and C_4F_8/90% Ar discharges to correlate material modification effects with the characteristic emission of the FC and Ar components of the plasma discharge. FC containing discharges, such as C_4F_8/90% Ar, are typically used for a high aspect ratio or a contact hole etch of dielectrics.[2.17-2.19] While the VUV photon fluxes in our reactor have not been characterized, they are expected to be

similar to those found in comparable systems.[2.20] It is known that Ar plasmas mainly emit radiation in the VUV range at two Ar I (neutral atom) resonance lines at 104.8 and 106.7 nm and a continuum emission spectrum of the Ar molecules (Ar_2^*) with the most intense emission between 100.0 and 140.0 nm.[2.21, 2.22] In FC containing plasma discharges, additional emission lines are observed in the VUV range for F at ~79-98 nm, C at ~126-193 nm, and FC at ~198-214 nm.[2.20]

Filter material	Cutoff wavelength (nm)	Argon emission	Wavelengths (nm)	FC emission	Wavelengths (nm)
MgF_2	112nm	Ar I	104.8 106.7	F	79-98
Sapphire	143nm			C	126-193
Glass	293nm	Ar_2^*	100-140	CF	198-214

Table 2.1: *Summary of experimental approach: cutoff wavelengths of used filter materials and characteristic emission wavelengths of Ar and FC species in the VUV spectral range.*

The chamber base pressure before the processing of each sample was $2x10^{-5}$ Torr for Ar and $5x10^{-5}$ Torr for C_4F_8/90% Ar discharges. Plasma processing conditions used were a total gas flow rate of 50 SCCM (SCCM denotes cubic centimeters per minute at standard temperature and pressure) and 10 mTorr operating pressure achieved through an exhaust throttle valve. The inductive power was set to 400 W. A self-bias voltage of -125 V was applied for C_4F_8/90% Ar discharges using the bias power supply in order to reduce the deposition of a FC film on the optical filters. Before each experiment with C_4F_8/90% Ar, the chamber was cleaned using O_2 plasma followed by a 1 min C_4F_8/90% Ar plasma chamber conditioning step. For Ar discharges, no bias voltage was applied, and the ion energy was determined by the plasma potential (~20 V).[2.23]

2.2.3 Characterization

After radiation exposure, materials were characterized by vacuum transfer x-ray photoelectron spectroscopy (XPS), Fourier-transform infrared spectroscopy (FTIR), ellipsometry, scanning electron microscopy (SEM), and atomic force microscopy (AFM).

The thickness reduction of the PR films was estimated by measuring the polymer film thicknesses before and after plasma processing using a He-Ne ellipsometer in the polarizer-rotating compensator-sample-analyzer configuration at a wavelength of 632.8 nm. For evaluating the measurements, the refractive index of the Si substrate was fixed to $\tilde{N}$=3.866-0.028*i*.[2.24] Changes in the refractive index of the PR film upon radiation exposure were minute and have no impact on thickness reduction measurements.

XPS analysis provided information on chemical composition changes of the material at the film surface. Vacuum transfer of PR samples from the plasma reactor to the analysis chamber right after processing prevented contamination and surface oxidation. The analysis was performed with a vacuum generator ESCA Mk II surface analysis chamber at an electron takeoff angle of 90 deg relative to the surface. Electrons were excited using a non-monochromatic Mg *K*α source (1253.6 eV). The pass energy of the hemispherical analyzer was set to 20 eV, and sample charging was compensated by adjusting the binding energy position of the C─C/C─H peak to 285 eV.[2.25]

Elemental spectra were decomposed using a least squares fit with Gaussian peaks after correction with a Shirley background. The individual C 1*s* spectra were decomposed with three peaks accounting for the chemical shifts: C^*─C/C^*─H (285.0 eV), C^*─O─C (286.5 eV), and O─C^*═O (289.0 eV).[2.25, 2.26] The O 1*s* spectra were peak-fitted with 532.3 eV for the carbonyl group (C═O^*), 532.7 eV for the C─O^*H group, and 533.8 eV

for the ether group (C─O*═C) after applying the sample charging found for the corresponding C 1*s* spectrum.[2.25, 2.26] The structural component experiencing a shift in binding energy is indicated with *. Elemental ratios were calculated using the method described by Standaert *et al.*[2.27].

FTIR was used to obtain information on changes in the chemical composition of the material bulk. The analysis was performed *ex-situ* with a Digilab FTS-3000 with a spectral resolution of 2 cm^{-1}. The spectra show the signal of the polymer film after subtraction of the background and the Si substrate signal. The PR materials were monitored for changes in the C─O─C group (1050-1350 cm^{-1}), the ─CH_2─ and ─CH_3 group (2800-3100 cm^{-1}), and the C═O ester group (1650-1900 cm^{-1}). The peak at ~1796 cm^{-1} corresponds to lactone (cyclic ester) pendant group in 193nm PR.[2.28]

PR pattern morphology was characterized with an AMRAY critical dimension (CD) SEM at a magnification of 75 000x. SEM images were evaluated using SEM metrology interactive toolbox (SUMMIT) for changes in pattern height, critical dimension, and line edge roughness.

The surface morphology evolution of processed materials was measured by a tapping mode AFM (Veeco Multimode) with a fixed scan size of 1x1 μm^2 and compared with unexposed materials. The surface roughness values reported were calculated from the root mean square (rms) of the surface profile after the measurement.

2.3 Photodegradation of polymers

Photon radiation-PR material interaction can be classified into two regimes: interaction with lower wavelength VUV photons ($\lambda<160$ nm) and higher wavelength VUV/UV photons ($160<\lambda<380$ nm). All incident photons in the lower wavelength regime are absorbed by hydrocarbons mainly due to dipole transitions and electronic excitations of C─H and C─C σ bonds in the polymer backbone and/or photoionization.[2.29-2.32] For photons in the higher wavelength regime, photoabsorption by chromophores and defects, i.e., C═C and oxygen containing groups, in the polymer structure play the dominant role.[2.33]

In principle, radiation in the low wavelength UV and VUV spectral ranges ($\lambda<250$ nm) is energetic enough to break most of the chemical bonds typically found in PR materials (dissociation wavelengths: λ_D(C─C)═336 nm, λ_D(C─O)═286-357 nm, λ_D(C─H)═286-301 nm, and λ_D(O─H)═249-336 nm).[2.33, 2.34] However, photon energies higher than the dissociation energy are not sufficient to break bonds. The crucial factor that determines if chemical bond breakage by radiation takes place is that the energy of the incident photon must be equal to the difference between two energy levels of a particular bond in the polymer structure in order to transfer the energy.[2.33]

For styrene based 248nm PR, absorption for $\lambda>160$ nm is due to π electrons in a benzene ring,[2.30, 2.31] whereas methacrylate based 193nm PR absorbs at $\lambda\approx210$ nm due to $n \rightarrow \pi$ transitions of the carbonyl chromophore and at $\lambda\approx180$ nm due to $\pi \rightarrow \pi^*$ transitions in the repeating unit.[2.15, 2.33] The broken bonds lead to the formation of free radicals. These radicals can recombine with the polymer cage or other radicals, migrate along the polymer chain, participate in termination reactions, remove hydrogen from a neighboring

C atom, or form new chemical functionalities, such as C=C bonds and/or a cross-linked network. Radicals not participating in the secondary reactions, however, can diffuse through the polymer free volume into the vacuum leading to material loss.[2.35-2.39]

Differences in the wavelength dependent absorption of the PR materials as a function of polymer composition and the spectral intensity distribution of the plasma photon radiation also lead to material characteristic penetration depths of photons. Since UV radiation (λ=200-380 nm) penetrates several micrometers into hydrocarbon polymers, modification of the entire polymer films can be assumed.[2.33, 2.40] For lower wavelength photons, the PR materials show a significant difference in penetration depth. For 248nm PR, VUV photons can be expected to penetrate ~15-40 nm into the polymer film for λ=110-172 nm, as estimated for polystyrene.[2.15] For methacrylate based 193nm PR, VUV photons with a wavelength below 200 nm penetrate 100-200 nm into the PR film.[2.15, 2.41] This wavelength dependence of photon penetration leads to a gradient or layered behavior of material modification for both materials.

In addition to cleavage of pendant groups, radiation exposure can lead to either main chain-scission reactions or chain cross-linking of the polymer. A key factor in the polymer structure is the size and electronegativity of the chemical group at the α-position, i.e., the bond opposing the polymer pendant group.[2.42, 2.43] Polymers with bulky groups and high electronegativity in the α-position tend to chain-scission, whereas polymers with smaller or electropositive groups tend to cross-link upon radiation exposure.[2.42, 2.43]

A classic example for this behavior is the cross-linking poly(methyl acrylate), with an α-H on the backbone, and the chain-scissioning poly(methyl methacrylate), which is saturated at the α-site of the backbone with a methyl group instead (α-

methyl).[2.42, 2.44] Similar observations were made for styrene-type polymers, which show cross-linking for α-H saturation in the case of polystyrene and chain-scission reactions for α-methyl in the case of poly(α-methyl styrene).[2.42] Thus, in our case, the polymer prone to scission reactions is 193nm PR, and the polymer prone to cross-linking is 248nm PR.

2.4 Results and discussion

2.4.1 Polymer structure dependent material modification

The dependencies of material degradation by plasma photon radiation on the polymer structure were tested for 193nm PR and 248nm PR. Materials were exposed to plasma photon radiation of Ar discharges for 30-300 s. Wavelengths in the VUV/UV and visible ranges were selected by applying MgF_2 and glass filters, respectively.

2.4.1.1 Results of surface characterization by XPS

The evolution of the chemical composition of the PR surfaces was analyzed by XPS. Figures 2.1(a) and 2.1(b) show the C 1*s* and O 1*s* spectra, respectively, of 193nm PR before and after 300 s exposure along with corresponding difference spectra. In the C 1*s* spectra, little material modification is observed for the glass filter, while exposure using the MgF_2 filter leads to a drastic loss of oxygen from the PR. This is shown by an increase in the C─C and C─H peaks and by a decrease in the C─O and C═O bond related signals. The O 1*s* spectra reveal that the oxygen spectrum is shifted toward lower binding energies for exposures using the MgF_2 filter. This suggests a change in the chemical environment of the oxygen contained in the surface regions. The data are consistent with preferential loss of C─O─C bonds.

Figures 2.1(c) and 2.1(d) show the C 1*s* and O 1*s* spectra, respectively, of 248nm PR before and after a 300 s exposure along with corresponding difference spectra. The observed changes in the C 1*s* spectra for both filters are relatively small and for the C─C and C─H regions. However, peak broadening is observed, pointing toward a change in the variability of the chemical environment of the polymeric network. Peak broadening

can be explained by the removal of α-H from the hydroxyl styrene and styrene groups and the subsequent occurrence of cross-linking reactions. This behavior is well known for α-H saturated styrene-type polymers.[2.44]

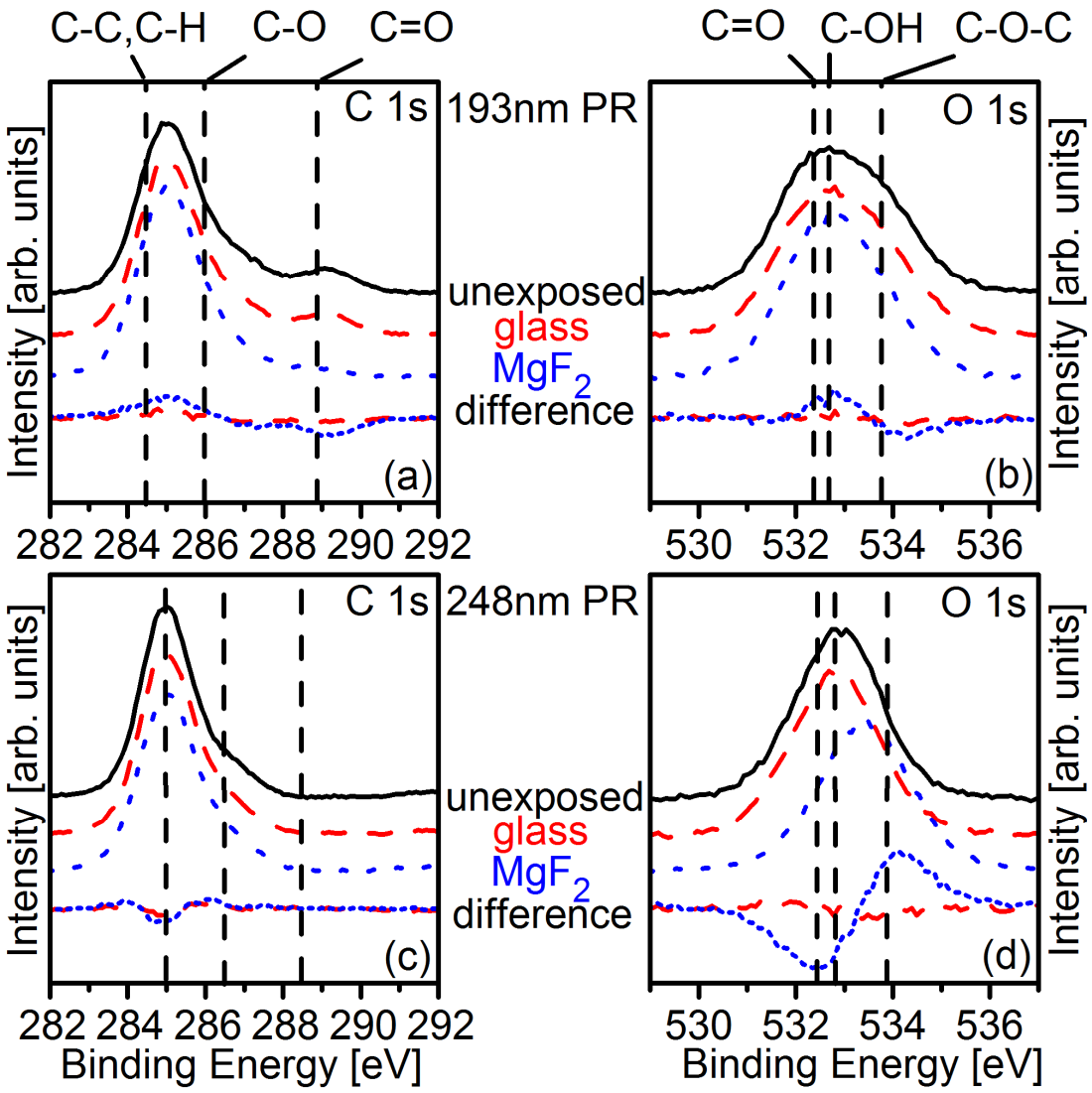

Figure 2.1: *High resolution XPS spectra before and after 300 s plasma exposure to an Ar discharge using the glass and MgF_2 filters together with corresponding difference spectra: (a) C 1s and (b) O 1s spectra of 193nm PR and (c) C 1s and (d) O 1s spectra of 193nm PR and (c) C 1s and (d) O 1s spectra of 248nm PR.*

Unlike the C 1*s* spectra, the O 1*s* spectra show strong differences between glass and MgF_2 filter exposures, even though little oxygen is lost from the material for both exposures. For the glass filter, a small shift toward lower binding energies is observed

and corresponds to a relative increase in C═O bonds. After exposure using the MgF_2 filter, the oxygen peak is shifted toward higher binding energies, corresponding to a strong increase in the relative amount of C─O─C bonds.

Elemental spectra were deconvolved in terms of fundamental bonding contributions to obtain atomic ratios and chemical compositions after various exposure times, as shown in Fig. 2.2. For 193nm PR (Fig. 2.2(a)), the initial atomic O/C ratio of 0.25 continuously decreases at a slow rate to 0.23 when exposed using the glass filter. For exposure using the MgF_2 filter, the O/C ratio drops in the first 120 s to about 0.16, with little evolution afterward. For 248nm PR (Fig. 2.2(b)), no significant changes in the surface atomic O/C ratio can be observed, independent of exposure time and wavelength range used. The O/C ratio stabilizes at around 0.18 (±0.01).

The material compositions based on the spectral decomposition of the O 1*s* spectra for 193nm PR and 248nm PR are shown in Figs. 2.2(c) and 2.2(d), respectively. For the glass filter exposure of 193nm PR, small and comparable amounts of oxygen are lost from all oxygen containing groups. For the MgF_2 filter exposure of 193nm PR, large amounts of oxygen are lost from C═O and C─O─C bonds, leading to an increase in the relative importance of C─OH bonds. For 248nm PR, exposures with either filter leads to a change in the chemical composition of the film surface. One modification observed is the reduction of the relative amount of C─OH groups, even though little oxygen is lost from the PR film surface. The strong O 1*s* spectral changes observed for 248nm PR (Fig. 2.1(d)) are highly dependent on radiation wavelength and can be explained by radiation-induced modification of the hydroxyl group of hydroxyl styrene. But when exposed to higher wavelength photons using the glass filter, the removal of H in the hydroxyl creates

a C═O bond. This moiety further reacts with C radicals, creating C─O─C cross-links when exposed to lower wavelength photons using the MgF_2 filter. These observations are in good agreement with previous reports of increased cross-linking yields for *para*-functionalized styrene polymers as compared to polystyrene polymers.[2.42, 2.43]

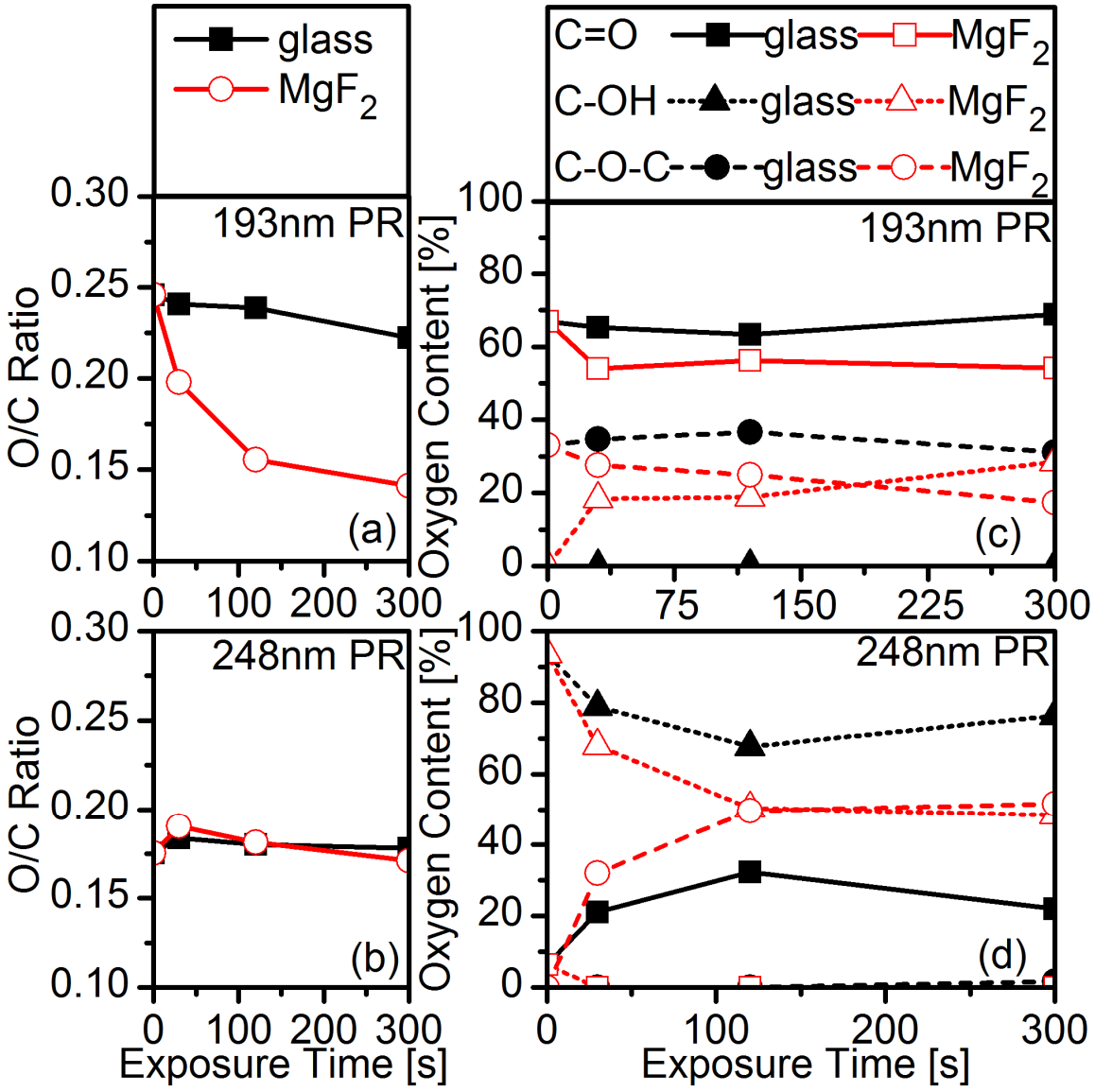

Figure 2.2: *Time evolution of calculated O/C atomic ratios and oxygen content based on XPS surface characterization: ((a) and (b)) 193nm PR and ((c) and (d)) 248nm PR, respectively. The O/C atomic ratios for the PR surface are estimated by integrated area ratios of the O 1s and C 1s spectra applying characteristic sensitivity factors. The oxygen content presented gives the relative composition of the PR surface as estimated by deconvolution of the O 1s spectra for individual bond contributions.*

2.4.1.2 Bulk PR characterization by FTIR

Figure 2.3 shows three characteristic infrared spectral regions for C─O─C bonds, C═O bonds, and ─CH_2─ and ─CH_3 bonds of (a) 193nm PR and (b) 248nm PR before and after 300 s exposure using the glass and MgF_2 filters, respectively. In addition, the corresponding difference spectra between unexposed and exposed materials are shown. 193nm PR shows a substantial decrease in C─O─C and C═O bonds for exposure using the glass filter (Fig. 2.3(a)), which are increasingly lost for the MgF_2 filter exposure, whereas changes in the oxygen-related spectra of 248nm PR even after exposure using the MgF_2 filter are small. The ─CH_3 and ─CH_2─ regions of both materials are almost unaffected by radiation, which indicates that the polymer backbone and the carbon rich pendant groups, i.e., adamantyl and benzene for 193nm PR and 248nm PR, respectively, are not lost from the film.[2.7] Changes in the overall polymer structure of the PR materials by cross-linking or chain-scission reactions cannot be determined by an analysis of the ─CH_2─ and ─CH_3 regions since the formation or destruction of a small amount of carbon bonds can significantly alter the polymer molecular weight without changing the absorbance in the ─CH_3 and ─CH_2─ regions.

In order to quantify the observed changes in the characteristic bond regions, spectra (Fig. 2.3) were integrated and compared with data of the pristine materials. Relative changes with respect to the unexposed material are presented as absorbance loss (Fig. 2.4).

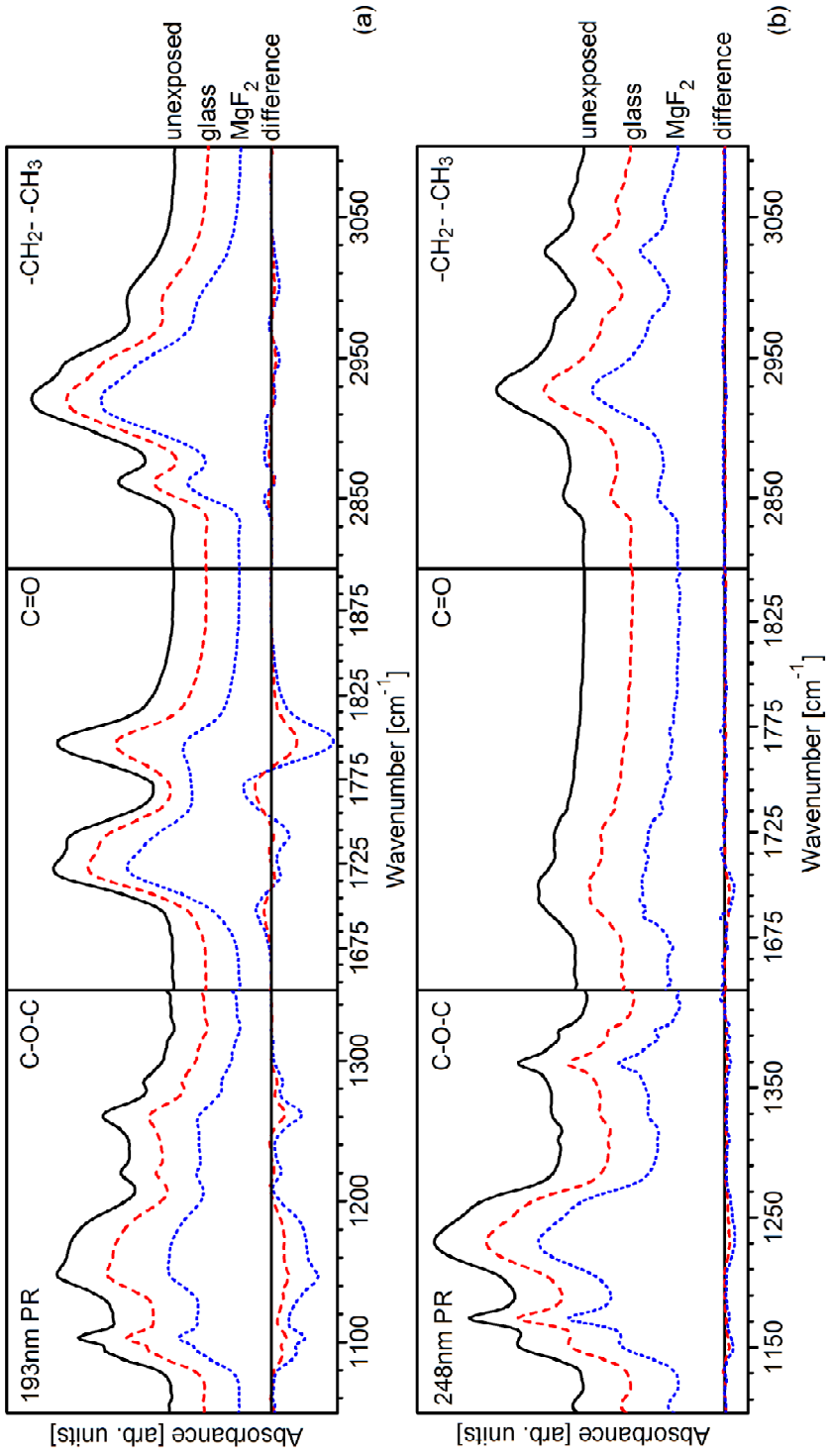

Figure 2.3: *FTIR spectra of C—O—C region (1100-1425 cm^{-1}), C═O region (1650-1850 cm^{-1}), and —CH_3 and —CH_2— region (2800-3100 cm^{-1}) before and after 300 s plasma exposure to an Ar discharge using the glass and MgF_2 filters together with corresponding difference spectra: (a) 193nm PR and (b) 248nm PR.*

We found that 193nm PR (Fig. 2.4(a)) exposed to radiation using the glass filter primarily degrades by losing 10%-15% of its C—O—C bonds, whereas C═O bonds are unaffected. For lower wavelength photon exposures (MgF_2 filter), large losses of C—O—C bonds—up to 32% of the original content—and a loss of up to 13% of initially present C═O can be observed. In contrast to 193nm PR, 248nm PR (Fig. 2.4(b)) only shows small changes in the absorption of oxygen containing bonds. This can be attributed to the low content of acrylate in the terpolymer structure.

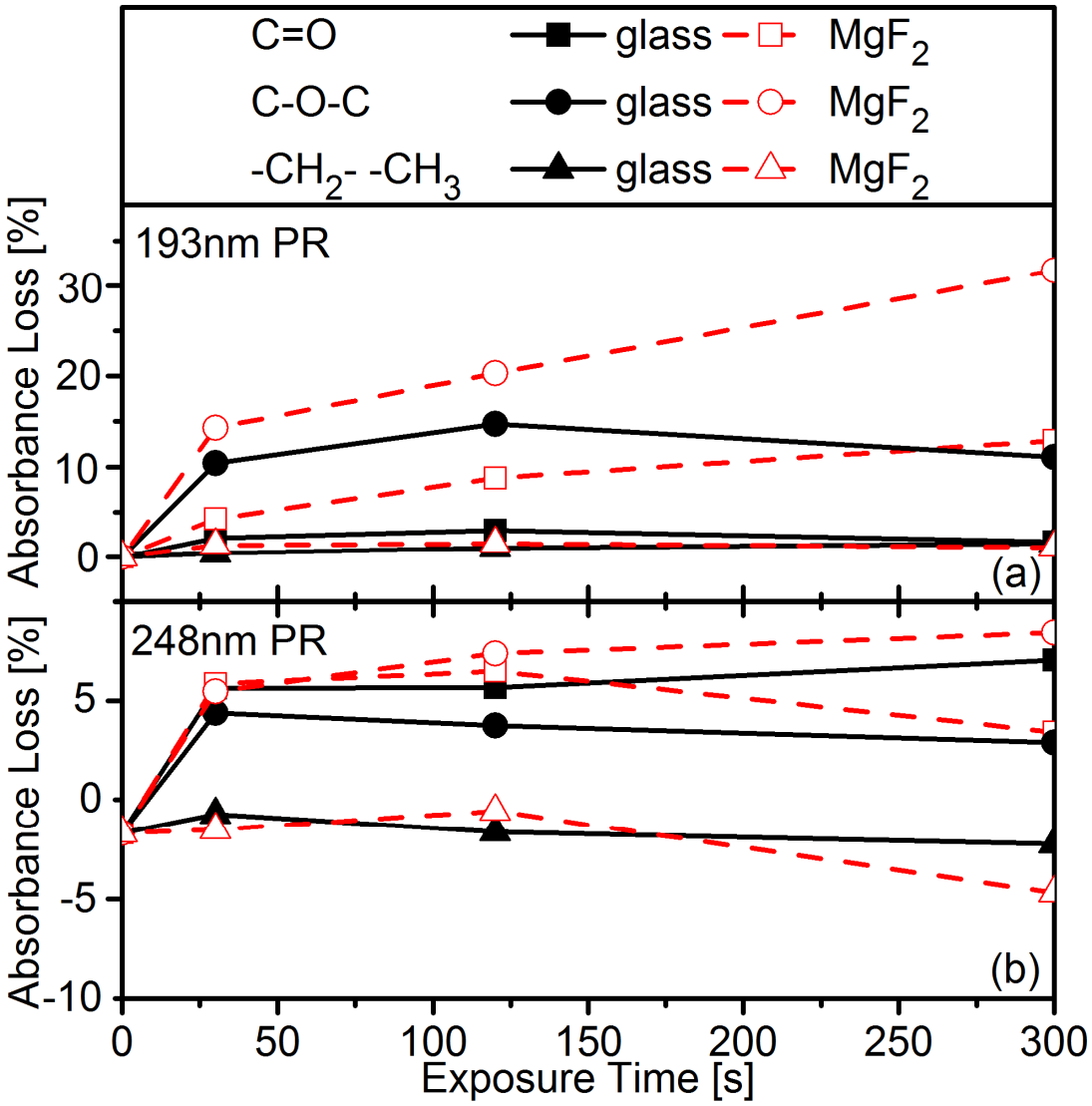

Figure 2.4: *Time evolution of C═O, C—O—C, and —CH_3 and —CH_2— absorbance loss based on integrated area analysis of FTIR spectra of (a) 193nm PR and (b) 248nm PR.*

Of particular interest for 193nm PR is the C=O spectrum, which not only shows a decrease in the lactone and ester peaks at ~1722 and ~1795 cm^{-1}, respectively, but also an increased signal at ~1770 cm^{-1}. This spectral region can be attributed to free lactone following the detachment of the pendant groups by bond-scissioning of the C–O–C bonds (Fig. 2.3).[2.28, 2.41, 2.45-2.47] Figure 2.5 presents the changes in the C=O bond spectra in three characteristic regions. The range for free lactone was selected at the inflection points of the difference spectra next to the free lactone peak.

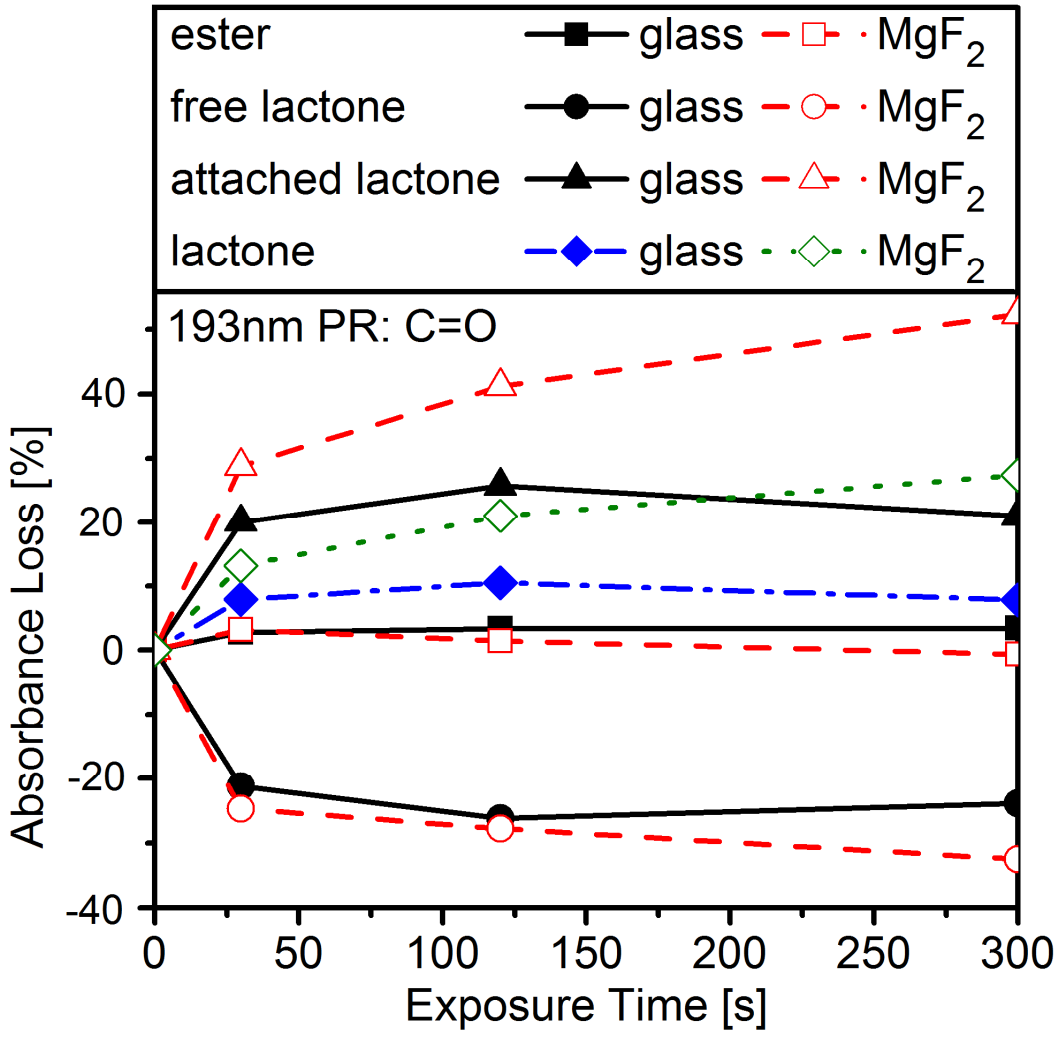

Figure 2.5: *Detailed observation of radiation-induced changes in the C=O bond region of 193nm PR (Fig. 2.4(a)) for three characteristic regions accounting for ester, attached lactone, and free lactone. The detached lactone effectively removed from the film, i.e., the difference of free lactone and attached lactone loss, is presented as lactone.*

Upon radiation exposure, the ester group decreases by less than 5%. Spectral changes show a peak widening toward lower wavenumbers, which indicates a change in the structural environment. This is likely due to the strong reduction of the C─O─C bonds connecting the pendant groups with the polymer backbone. For radiation exposure using the glass filter, the attached lactone signal is reduced by more than 20%, while the signal of free lactone is increased by ~20%. This result indicates that the overall lactone loss is small and a significant amount of the detached lactone is not completely removed and stays within the PR film. With the addition of lower wavelength photons for the MgF_2 filter, we find that ~55% of the attached lactone is lost, whereas the absorbance of free lactone is slightly increased to 30%. This leads to an effective lactone loss of ~25% and indicates that lower wavelength photons transmitted by the MgF_2 filter are energetic enough to decompose the lactonyl structure.[2.41] These observations are in good agreement with the surface modification where a relative increase in C─OH bonds corresponding to detached lactone was observed (Sec. 2.4.1.1).

Furthermore, if more than 50% of the lactone in the 400 nm thick 193nm PR is detached after long exposures using the MgF_2 filter, we can conclude that this modification takes place at a depth of at least 200 nm. Assuming a detachment of every lactone in the modified depth, this estimate is in good agreement with observations made by Kawahira *et al.*[2.41], in which a gradient shaving method and FTIR probed polymer conformational changes. In addition to lactone detachment, the extent of C─O─C bond loss (Fig. 2.4) indicates that the adamantyl pendant groups must be detached. But unlike lactone, the detached adamantyl is radiation stable and remains in the PR film, as indicated by minute changes in the spectra of ─CH_3 and ─CH_2─ bonds (Fig. 2.5(a)). The

detached adamantyl groups that remain in the polymer film can act as a plasticizer softening the PR film.[2.41]

Additionally, changes in the polymer structure can be expected by chain-scission reactions, which are promoted by the observed cleavage of ester side chains.[2.48] Indeed, we have found that whereas unexposed 193nm PR only dissolves in a good solvent (acetone), upon radiation exposure it becomes soluble in a poor solvent (isopropyl-alcohol). Specifically, the change in the solubility is due to the disintegration of the polymer structure into smaller fragments by chain-scission reactions.[2.49] Additionally, we investigated differences in solubility change by replacing the bulkier α-CH_3 group opposing the pendant group with a smaller α-H group. Changing the dominant photo-degradation mechanism from chain-scission (α-CH_3) to cross-linking (α-H) reactions caused a decrease in solubility after photon radiation exposure, further supporting the proposed mechanism of solubility change by chain-scission reactions.

2.4.1.3 Film thickness change

Changes in the film thickness were measured with ellipsometry after radiation exposure. The thickness changes strongly depend on the polymer material and radiation exposure wavelength range. The 400 nm thick 193nm PR film showed a thickness reduction of up to 11 nm after 300 s of radiation exposure using the MgF_2 filter and only 4.5 nm thickness loss for 300 s exposure using the glass filter. In contrast, the 248nm PR films did not show any significant thickness reduction (≤1 nm) when exposed to both wavelength ranges. For all exposures, we found that thickness reductions are rapid for short times and saturated for extended exposure times.

In order to determine the origin of the film thickness reduction and its temporal behavior, we consider the surface and bulk chemical changes caused by radiation. Surface modification as measured by XPS cannot explain the observed large thickness changes of 193nm PR. The amount of oxygen lost and corresponding densification would result in much smaller thickness reductions. Thus, the thickness change can only be explained by bulk material modification. Figure 2.6 shows the relationship of observed chemical modifications of the material bulk and thickness changes for both PR materials. Data are displayed for the two optical filters and radiation exposures between 30 and 300 s.

The results for 193nm PR show a strong correlation of the film thickness reduction to C─O─C bond and lactone loss, as estimated in the C═O spectrum. Thickness loss can be explained by material loss and densification due to the collapse of the polymer structure. This is also consistent with the temporal evolution of thickness reduction, which is limited by the remaining radiation sensitive bonds for long exposure times. The small amount of material loss for irradiated 248nm PR is consistent with the relatively small thickness changes. The radiation stability of 248nm PR is given by styrene based groups with high overall radiation stability and incorporation of only a small amount of ester (t-butylacrylate) in the PR formulation.

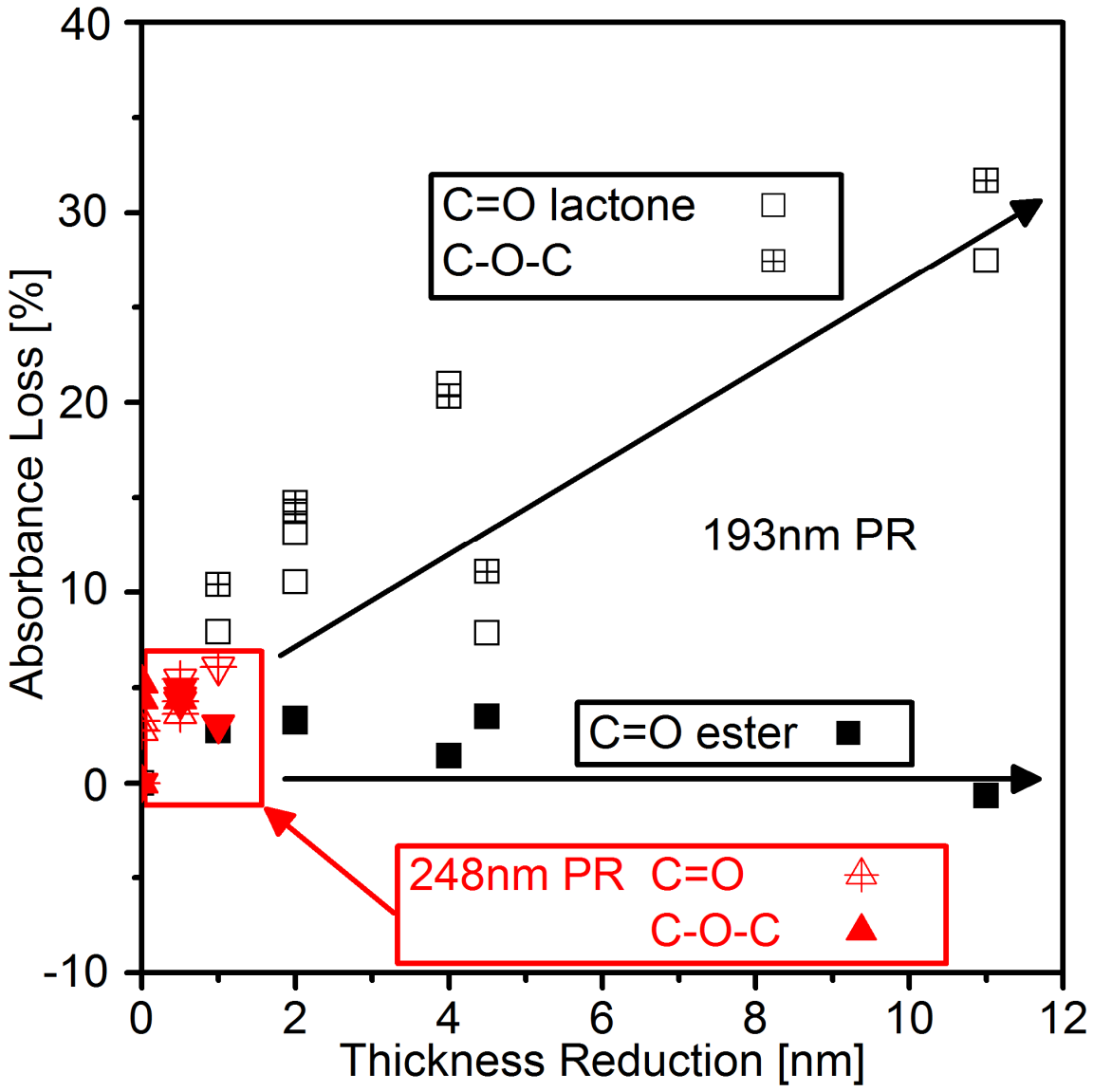

Figure 2.6: *Correlation of film thickness reduction as estimated by ellipsometric measurements and bulk material modifications of 193nm PR and 248nm PR as observed by FTIR. Thickness reduction is directly correlated with absorbance loss in the C—O—C spectra and in the characteristic region for lactone in the C═O spectra for 193nm PR. Changes observed for exposure using the glass filter are significantly smaller than for exposure using the MgF_2 filter. 248nm PR shows high structural stability and only minute thickness changes.*

2.4.1.4 Thermal behavior

In order to further investigate material modifications in the PR bulk, a thermal analysis was performed. The film thickness change of the pristine and radiation exposed PR materials was measured with ellipsometry as a function of sample temperature. PR samples were heated on a hot plate at a constant heating rate of 4.3 °C/min over a temperature range of 80-220 °C. This type of characterization is similar to thermal gravimetric analysis (TGA), which measures temperature dependent weight loss to determine thermal degradation temperatures. Figures 2.7(a) and 2.7(b) show the heating curves of pristine and 300 s radiation exposed 193nm PR and 248nm PR, respectively. The starting temperatures T_0 of thermal decomposition indicate the temperature required to thermally volatilize the protective leaving groups from the polymer matrix.

For 193nm PR, T_0 drops from ~190 °C for the pristine material to ~180 and ~100 °C after radiation exposure using the glass and MgF_2 filters, respectively. The measured T_0 for the unexposed material is in good agreement with our previous TGA measurements.[2.12] Once the sample is heated above T_0, rapid thickness reduction by more than 100 nm takes place. This indicates that pendant groups are not preferentially detached, but rather removed altogether. This thickness reduction of 100 nm after the removal of the adamantyl pendant groups, which account for ~50% of the total weight of the PR material, is in good agreement with expectations based on the previous estimation of an ~200 nm modification depth of 193nm PR after radiation exposure (Sec. 2.4.1.2). Exposure to lower wavelength photons with the MgF_2 filter drastically decreases T_0 by the radiation-induced breakdown of C─O─C ester bonds. The detached pendant groups remain within the PR film, as observed by FTIR (Fig. 2.4), and get easily volatilized at

reduced temperatures. Exposure to higher wavelength photons with the glass filter shows another thermal event at 125 °C. FTIR measurements (Figs. 2.4 and 2.5) suggest that this thickness reduction of only a few nanometers is caused by the removal of free lactone, which remains in larger concentrations in the film after radiation exposure.

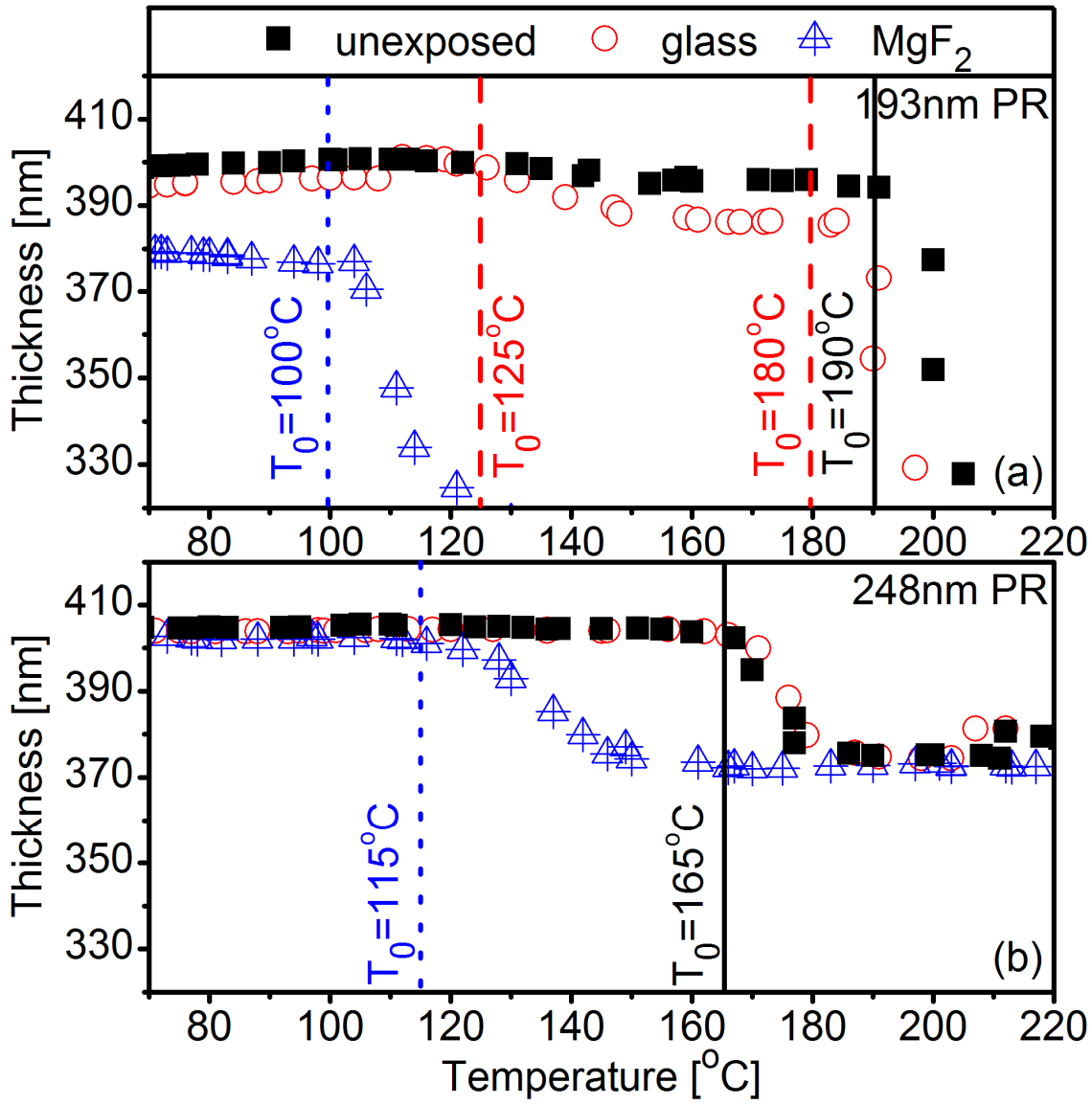

Figure 2.7: *Thermal behavior of (a) 193nm PR and (b) 248nm PR after 300 s radiation exposure using the glass and MgF_2 filter. The temperature plots are labeled with starting temperatures for thermal decomposition (T_0) also indicated with solid, dashed, and dotted lines for the unprocessed material, and radiation exposures using the glass and MgF_2 filter, respectively.*

Further support comes from measurements with the 248nm PR. In this case, changes in thermal behavior only can be detected after radiation exposures using the MgF_2 filter. This reduces T_0 from 165 to 115 °C. The observed thickness reduction is only 40 nm in this case, much less than the thickness reduction measured for 193nm PR. The fact that a similar T_0 is observed as compared to 193nm PR suggests that the material loss may be due to small amounts of t-butylacrylate in the PR formulation. Our results indicate that the styrene based functional groups are not only radiation stable but also temperature stable and that pendant groups remain attached. Even after heating to 250 °C, no significant reduction of film thickness could be observed for styrene polymers.

Therefore, the observed changes in thermal behavior further support the differences of the two PR materials in terms of chain-scissioning and cross-linking materials. Radiation exposure of 193nm PR causes main chain-scission reactions and detachment of pendant groups (Sec. 2.4.1.2). This creates low molecular weight species, which are volatilized at reduced temperatures and decrease the viscosity of the modified film.[2.50] For 248nm PR, the amount of material volatilized at lower temperatures is limited and can be attributed to the t-butylacrylate component in the PR formulation. Radiation-induced cross-linking of 248nm PR (Sec. 2.4.1.1) prevents further volatilization of species.

Ellipsometry alone can, in principle, be used to measure glass transition temperatures (T_g) of thin polymer films.[2.51] However, for the materials used here, T_g and T_0 are similar, and changes in film properties at T_g are obscured by material loss at T_0.[2.12] Results of thermal measurements and FTIR together suggest changes in T_g upon radiation exposure of the PR materials. Changes in T_g can be commonly observed after the removal

of pendant groups, which act as a plasticizing agent in the PR material.[2.52] Methacrylate-based polymers were found to exhibit a linear relationship in T_g and T_0,[2.53] and the change in T_0 for 193nm PR by ~90 °C is in good agreement with previously observed changes in T_g of 193nm PR after plasma exposure.[2.46] Since the glass transition is not a sharp transition, first changes in the material properties can start to occur at temperatures below T_g. This may lower the temperature required for material softening of 193nm PR after photon radiation exposure to a temperature range relevant for plasma processing. For 248nm PR, a higher T_g is expected after radiation exposure since the removal of pendant groups and thickness reduction during the thermal experiments are both small. In addition, cross-linking takes place (Sec. 2.4.1.1), leading to an increased T_g (see report for polystyrene [2.54]).

2.4.1.5 Morphological and topographical characterization

The surface morphologies of 193nm PR and 248nm PR examined by AFM did not show any roughness development after radiation exposures. The surface roughness of 248nm PR was unchanged after radiation exposure of up to 300 s (rms=0.29±0.02 nm) and independent of the radiation wavelength range applied. For radiation exposure of 193nm PR using the glass filter, a similar behavior was observed (rms=0.36±0.02 nm). These minute changes in rms roughness for both materials are smaller than the measurement accuracy. After irradiation with lower wavelength photons of 193nm PR using the MgF_2 filter, a small, continuous rms roughness reduction was observed with increasing radiation exposure time, reducing the rms roughness to 0.32 nm. This is in good agreement with previous observations for our beam exposures.[2.7]

Similar changes in surface morphology upon radiation exposure are seen in the cross-sectional SEM images of 193nm PR trench patterns (Fig. 2.8(a)). The standing wave patterns on the feature sidewalls of the patterned samples are due to the missing bottom antireflection coating and are formed during the lithographic patterning step, resulting in a larger cross-sectional line edge roughness.[2.55] The small scale surface roughness of the pristine material vanishes, and the surface becomes smoother when exposed to lower wavelength photons using the MgF_2 filter.

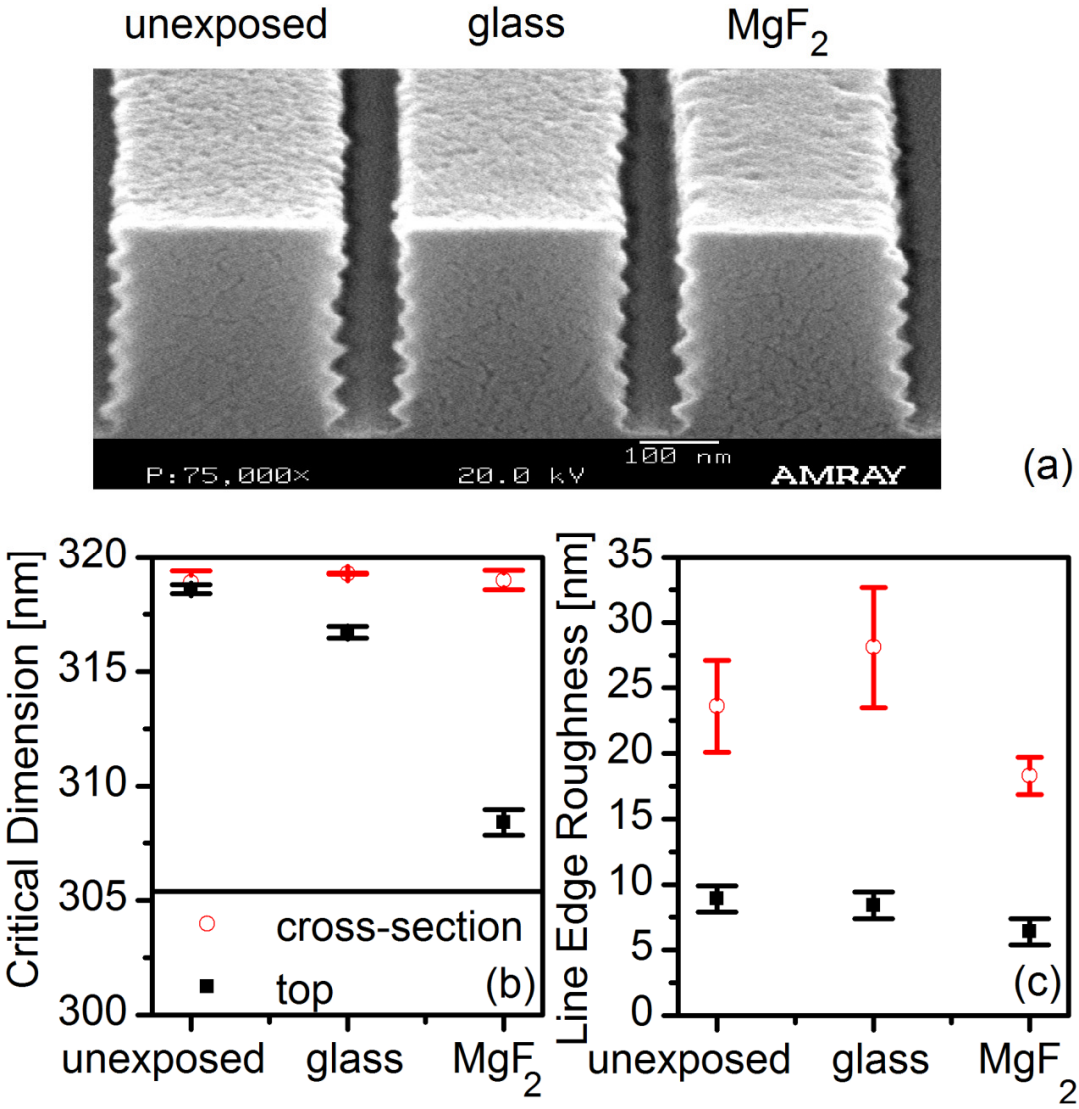

Figure 2.8: *(a) SEM images after 300 s radiation exposure of 193nm PR trench patterns together with changes in (b) CD and (c) LER.*

Furthermore, thickness reduction and changes in CD and LER were investigated. The observed thickness reductions of the PR patterns in the vertical direction after 300 s radiation exposure using the MgF_2 filter and the glass filter are 13 and 6 nm, respectively, in excellent agreement with our ellipsometric measurements. In addition to the vertical thickness reduction, we observed a significant reduction in CD at the feature top (up to 10 nm), whereas the overall CD along feature height (cross-section) remained stable (Fig. 2.8(b)). Although the measurement of changes in the cross-section was challenging due to the existence of the standing wave pattern, a significant reduction in LER was observed for lower wavelength photon exposure using the MgF_2 filter. This trend is especially evident for the LER on the feature top. The initial LER of ~9 nm was reduced after radiation exposures to ~8 nm with the glass filter and to ~6 nm with the MgF_2 filter (Fig. 2.8(c)). The observed changes in CD and LER of PR patterns at the feature top and sidewalls are important for industrial processing where photoresist features can be expected to get modified to a larger degree due to their small size and film thickness (~200 nm).

2.4.2 Plasma chemistry dependent material modification

The dependence of material degradation by plasma photon radiation on discharge chemistry was tested for 193nm PR in Ar and C_4F_8/90% Ar discharges. Adding C_4F_8 to the Ar discharge causes a strong increase in the photon flux in the 150-210 nm wavelength range due to C and FC related emission.[2.20] The photon energy corresponding to this wavelength range is large enough to enable dissociation of most chemical bonds of 193nm PR. In particular, dissociation of oxygen containing moieties, i.e., C═O and C─O─C bonds, is expected (see Sec. 2.3). Furthermore, photons in this wavelength range

are assumed to penetrate deeper into the material bulk as compared to lower wavelength photons in Ar emission. To address the effect of C_4F_8 addition to the Ar discharge, we included a sapphire filter in this part of the work. Use of this filter reduced the VUV wavelength range, and enabled a correlation of observed PR modifications with photon emission characteristic of FC containing discharges. Significant differences between C_4F_8/90% Ar discharges and Ar discharges are discussed below.

2.4.2.1 Surface characterization by XPS

High resolution C 1*s* and O 1*s* XPS spectra of 193nm PR exposed to plasma photon radiation of Ar and C_4F_8/90% Ar discharges were measured to compare the exposures using the glass, sapphire, and MgF_2 filters. Elemental spectra were analyzed, and atomic ratios and chemical compositions were calculated for various exposure wavelength ranges (Fig. 2.9).

The changes observed for the Ar and C_4F_8/90% Ar discharge exposures using the glass filter are similar and show only little modification of the PR film surface. For both, almost no oxygen is lost (~1%), and the chemical composition changes only slightly. This is in good agreement with the expectations that the characteristic Ar and FC emission are being cut out by the glass filter. Lower wavelength photons are transmitted through the sapphire and MgF_2 filters and can dissociate carbon oxygen bonds (see Secs. 2.2.2 and 2.3). We observed strongly increased oxygen loss in this case. The chemical composition of the PR material is significantly altered by loss of C═O and/or C─O─C bonds and the formation of C─OH bonds.

For the C_4F_8/90% Ar discharge, exposures using the sapphire filter led to a much higher total reduction of the atomic O/C ratio (~9%) than the Ar discharge (~4%). This

reduction is comparable to the reduction seen for exposure using the MgF_2 filter in the Ar discharge (~11%). The resulting chemical compositions after photon radiation exposure to the Ar and C_4F_8/90% Ar discharges are almost identical. The oxygen is mainly lost from C═O, while at the same time C─OH bonds are formed. The higher degree of oxygen loss for the C_4F_8/90% Ar discharge can be attributed to the increased photon flux due to C and FC related emission in the wavelength range defined by the sapphire filter. This shows the importance of intermediate wavelength radiation for the material modification of 193nm PR.

For the MgF_2 filter exposures, oxygen loss and changes in chemical composition vary between the Ar and C_4F_8/90% Ar discharge. The Ar discharge leads to an additional reduction in atomic O/C ratio of ~7% compared to the sapphire filter. The oxygen is primarily lost from the C─O─C bonds, while C═O and C─OH bonds remain stable. C_4F_8/90% Ar exposures using the MgF_2 filter lead to lower oxygen loss than exposures using the sapphire filter. This effect is observed by both XPS surface characterization and bulk material characterization by FTIR. We attributed this effect to a reduced transmission of the MgF_2 filter due to material degradation by ion bombardment. Degradation of MgF_2 filters in plasma environments is a well known effect [2.56, 2.57] and is enhanced for the higher ion energy in the FC containing discharge. If the material degradation of the MgF_2 filter could be ignored, we would expect that the PR material modifications for the pristine MgF_2 filter should be at least as high as those for the sapphire filter and should equal or exceed the modifications found for the MgF_2 filter in an Ar discharge. The sapphire filter did not show reduced transmission due to material degradation by energetic ions. In the following subsection, we will focus on the

differences found for the sapphire filter between the two discharge chemistries since the wavelength range defined by the filter is coincident with the difference in characteristic photon emission by FC species.

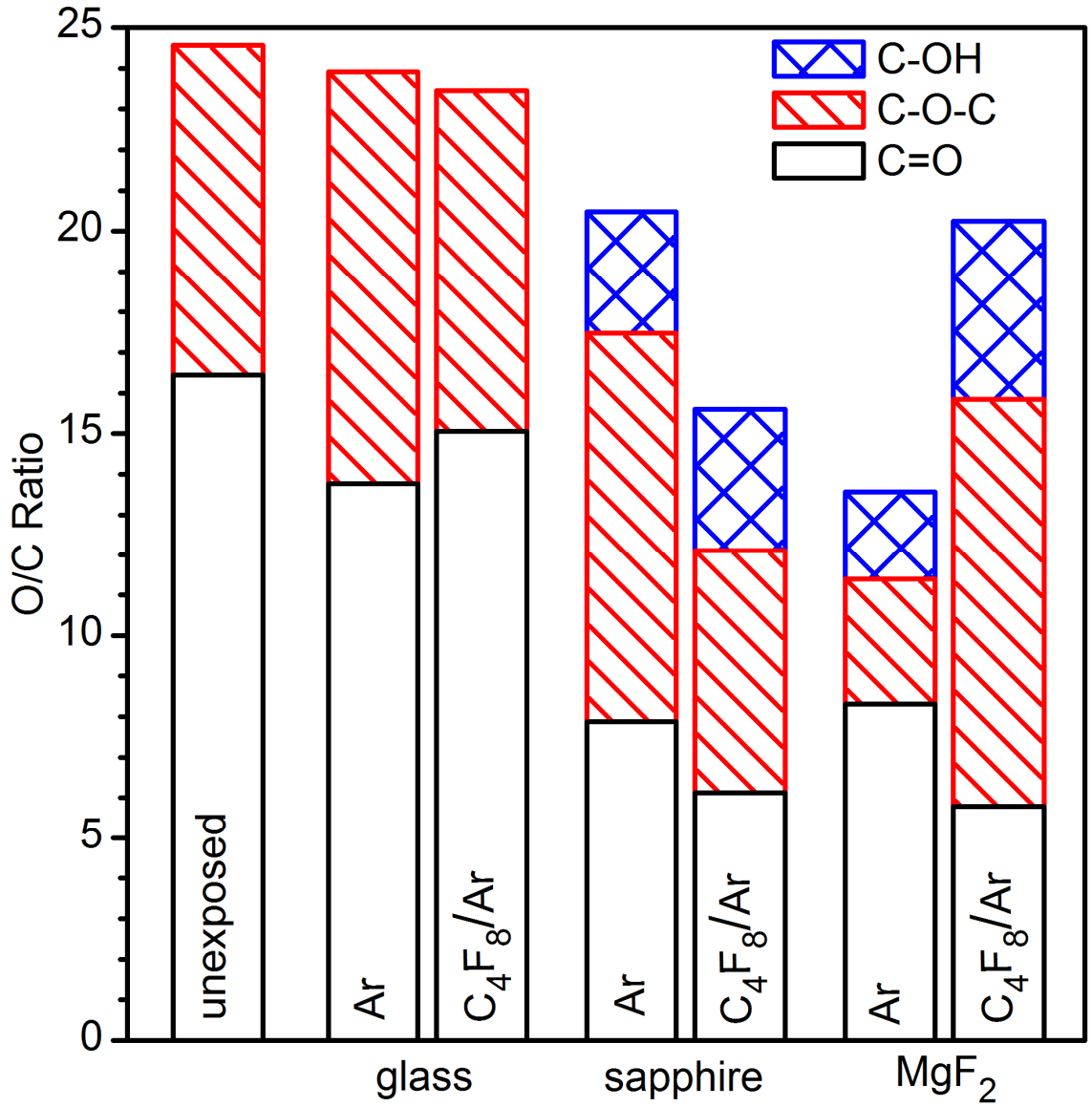

Figure 2.9: *Wavelength range dependence of calculated atomic O/C ratios (bar) and oxygen content (bar inset) based on XPS surface characterization for Ar and C_4F_8/90% Ar. The O/C atomic ratios for the PR surface are estimated by integrated area ratios of the O 1s and C 1s spectra applying characteristic sensitivity factors. The oxygen content presented gives the relative composition of the PR surface as estimated by deconvolution of the O 1s spectra for individual bond contributions.*

2.4.2.2 Bulk PR characterization by FTIR

The bulk material modifications were quantified by integrating characteristic peaks measured with FTIR, as discussed above (Figs. 2.10(a) and 2.10(b)). A more detailed discussion about changes in the C═O bond spectra is shown in Figs. 2.10(c) and 2.10(d).

Upon exposure to both discharge chemistries, C─O─C and C═O bonds are increasingly lost with lower radiation wavelength using the glass, sapphire, and MgF_2 filters, respectively (Fig. 2.10 (a)). The PR material, when exposed to the C_4F_8/90% Ar discharge using the sapphire filter, showed the strongest bulk material modifications (Fig. 2.10 (b)). This is in good agreement with the observations on the surface chemical changes and consistent with the expected importance of increased photon flux at higher wavelengths in the VUV spectral range (λ═143-300 nm).

For exposures to both plasma chemistries using the glass filter, only small changes are observed, mainly by loss of C─O─C bonds. Exposures of the PR using the sapphire filter in the C_4F_8/90% Ar discharge increased losses of C─O─C bonds and C═O bonds by ~14% and ~10%, respectively (Fig. 2.10 (b)). These changes in PR material composition exceed the modifications observed with the MgF_2 filter in the Ar discharge.

The increased loss of C═O bonds for radiation exposure to the C_4F_8/90% Ar discharge using the sapphire filter is due to the increased loss of the attached lactone, whereas changes in the ester group are identical to those observed with the Ar discharge (see Figs. 2.10(c) and 2.10(d)). The strong reduction in the attached lactone region (greater than 40%) is accompanied by increased lactone loss and a conversion to free lactone. The amount of free lactone remaining in the PR bulk appears to be independent

of the discharge chemistry. This implies that in the high wavelength VUV photon range, more lactone is detached from the PR structure, but also more is removed from the polymer matrix. The low degree of bulk material modification in the C_4F_8/90% Ar discharge when using the MgF_2 filter can be explained by reduced photon transmission of the optical filter mentioned above.

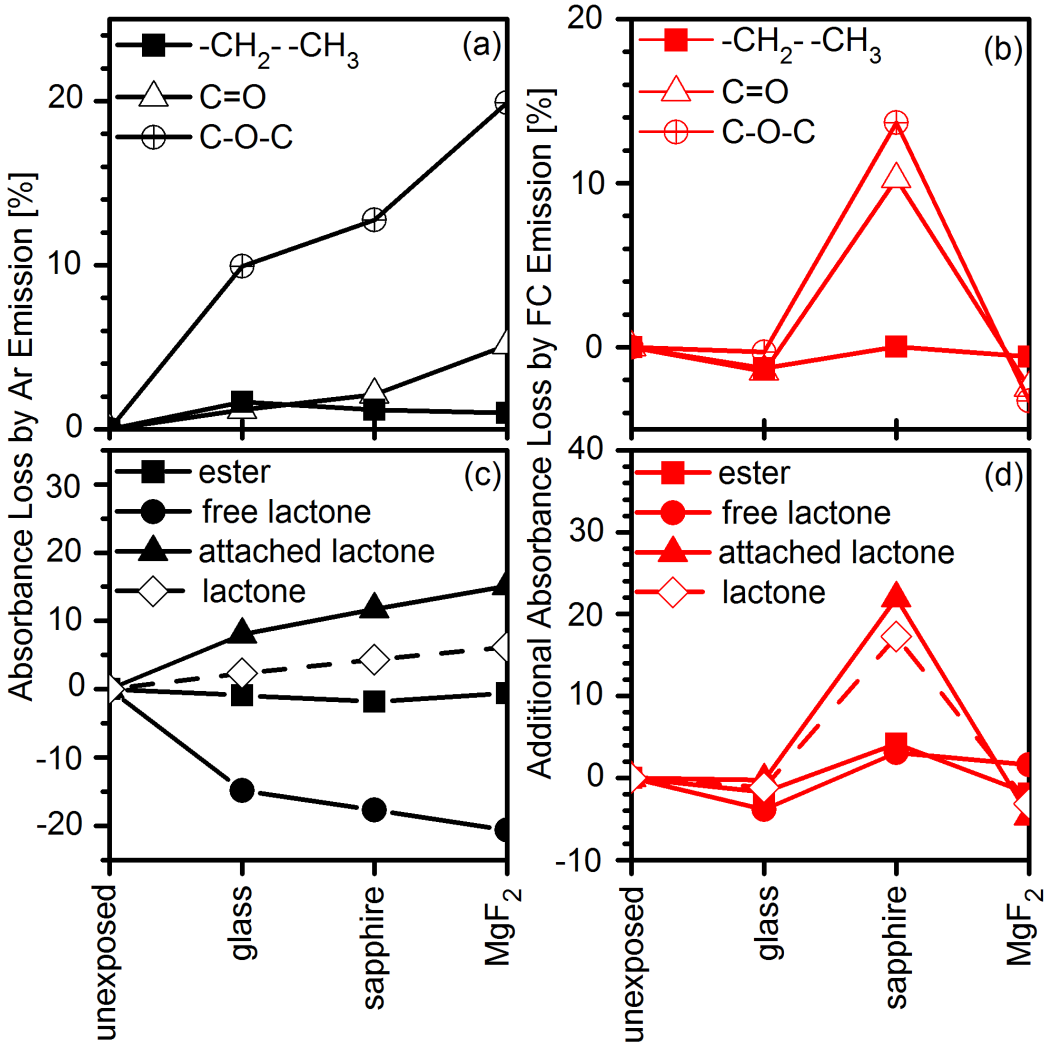

Figure 2.10: *Wavelength range dependence of C═O, C—O—C, and —CH_3 and —CH_2— absorbance loss based on integrated area analysis of FTIR measurements of (a) Ar and (b) C_4F_8/90% Ar. Detailed observation of radiation-induced absorbance loss in the C═O bond region of 193nm PR exposed to (c) Ar and (d) C_4F_8/90% Ar for three characteristic regions accounting for ester, attached lactone, and free lactone. The detached lactone effectively removed from the film, i.e., the difference of free lactone and attached lactone loss, is presented as lactone.*

2.4.2.3 Film thickness measurements by ellipsometry

The film thickness reduction caused by radiation exposure was characterized with ellipsometry and correlated with bulk material modifications (Fig. 2.11). The direct relationship of thickness reduction with loss of C—O—C bonds and removal of detached lactone groups in the material bulk for the Ar exposures in Sec. 2.4.1.3 (Fig. 2.6) is also seen for the C_4F_8/90% Ar discharge.

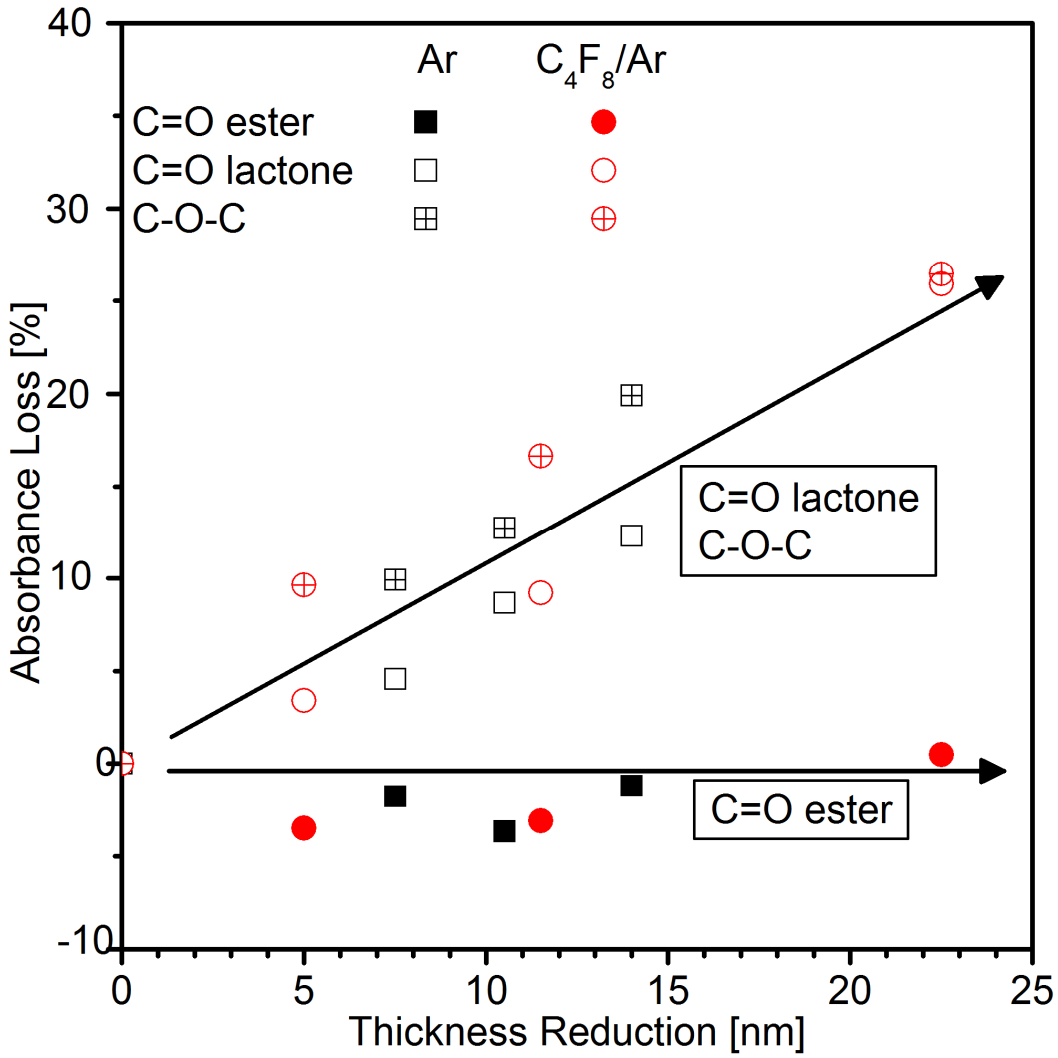

Figure 2.11: *Correlation of film thickness reduction as estimated by ellipsometric measurements and bulk material modifications of 193nm PR after 300 s radiation exposure to various wavelengths ranges in Ar and C_4F_8 /90% Ar discharges observed as absorbance loss by FTIR. Thickness reduction is directly related to absorbance loss in the C—O—C spectra and in the characteristic region for lactone in the C=O spectra.*

The increase in bulk material modifications for the C_4F_8/90% Ar discharge using the sapphire filter causes film thickness reductions exceeding 22 nm after 300 s radiation exposure. This drastic increase is directly correlated with the loss of C─O─C bonds and removal of detached lactone groups (Fig. 2.10). The fact that this behavior of strong material modification can already be observed for the sapphire filter exposures using C_4F_8/90% Ar plasma further emphasizes the importance of increased photon flux in the high wavelength VUV range by FC emission.

2.5 Conclusions

We studied the effects of plasma photon radiation-induced modifications of 193nm PR and 248nm PR to gain insight into material changes on a molecular level and to establish the importance of photon radiation wavelength, polymer structure, and plasma chemistry. The observed material modifications are summarized in Tab. 2.2.

<table>
<tr><td>Material</td><td>248nm PR</td><td colspan="2">193nm PR</td></tr>
<tr><td>Gas</td><td>Ar</td><td>Ar</td><td>C_4F_8/ 90%Ar</td></tr>
<tr><td>Surface modification</td><td>Weak oxygen loss</td><td colspan="2">Strong oxygen loss,
reduction of C=O and C-O-C bonds,
strongly increased for C_4F_8/90%Ar</td></tr>
<tr><td rowspan="2">Bulk material modification</td><td rowspan="2">Small</td><td>Strong, increasing with Photon Energy</td><td>Strongly increased for Sapphire Filter</td></tr>
<tr><td colspan="2">Detachment of pendant groups acting as plasticizer,
partial removal of lactone</td></tr>
<tr><td>Structural changes</td><td>Cross-linking</td><td colspan="2">Chain-scissioning</td></tr>
<tr><td>Depth</td><td>15-40nm</td><td colspan="2">200nm</td></tr>
<tr><td rowspan="2">Thickness reduction</td><td rowspan="2">1nm</td><td>11nm (MgF_2)</td><td>23nm (sapphire)</td></tr>
<tr><td colspan="2">Correlated to C-O-C bond and lactone loss</td></tr>
</table>

Table 2.2: *Summary of photon radiation-induced material modifications.*

In agreement with prior studies, 193nm PR and 248nm PR were found to fundamentally differ in radiation modification at the polymer surface and in the material bulk (Sec. 2.4.1). 248nm PR shows high radiation stability independent of photon wavelength, whereas 193nm PR is progressively modified as photon wavelength decreases. For 193nm PR, radiation modification leads to severe oxygen loss, detachment, and removal of polymer pendant groups, chain-scission reactions, softening of the material bulk, and reduction in film thickness and pattern feature size. The lactone

containing functional group of 193nm PR was found to be the most labile component of the polymer structure.

The radiation modification of 193nm PR strongly depends on plasma chemistry (Sec. 2.4.2). The addition of C_4F_8 to the Ar discharge and the corresponding increase in photon flux in the 150-210 nm wavelength range significantly increased the radiation modification on the film surface and in the PR bulk. This shows that both plasma photon radiation in the low wavelength VUV spectral range as emitted by Ar and radiation in the high wavelength VUV spectral range as emitted by FC lead to severe material modifications. Thus, VUV radiation in FC containing discharges between 150 and 210 nm has to be considered in industrial pattern transfer processes.

Based on these results, it is evident that 193nm PR is significantly less radiation stable than 248nm PR due to the high oxygen content, large amount of ester linkages, inclusion of lactone, and saturation of polymer backbone with α-CH_3, which drastically reduce plasma radiation stability. With the continued relevance of 193nm PR in immersion and extreme ultraviolet lithography, future design of PR materials has to take material modification by plasma radiation into account. Our findings suggest that reduction of ester linkages, lactone, and the overall oxygen content and replacement of α-CH_3 with α-H in the PR structure would significantly improve the performance of novel mask materials. Additionally, characteristic emission of FC containing plasma discharges in the high wavelength VUV spectral range has to be considered in process design. This will enable us to fundamentally understand the complex synergistic effects of various plasma species leading to roughness development of PR in direct plasma environments.

Chapter 3

Real-time measurements of plasma photoresist modifications: The role of plasma vacuum ultraviolet radiation and ions

F. Weilnboeck, N. Kumar, and G.S. Oehrlein

Department of Materials Science and Engineering and Institute for Research in Electronics and Applied Physics, University of Maryland

T.-Y. Chung, and D. Graves

Department of Chemical Engineering, University of California, Berkeley

M. Li

Dow Electronic Materials

E. A. Hudson

Lam Research Corporation

E. C. Benck

National Institute of Standards and Technology

Journal of Vacuum Science and Technology B, in preparation

Abstract

Plasma-induced roughness development of photoresist (PR) can be due to synergistic interactions of surface modifications introduced by ions, bulk material modifications by ultraviolet (UV)/vacuum ultraviolet (VUV) radiation, and increased temperature. While previous work identified the individual contributions of energetic ions and UV/VUV radiation, the dynamics of the concurrent modifications remained unclear.

We studied the interactions of plasma radiation and ions with 193nm PR and 248nm PR in Ar plasma by *in-situ* ellipsometry. Ellipsometry provides valuable information on changes in film thickness and material optical properties in real-time during plasma processing. MgF_2, sapphire, and glass optical filters were used to reduce the plasma-material interactions to the radiation component of a selected wavelength range in the UV/VUV spectral region. Ar plasma radiation and its transmission through different optical filters were characterized by VUV spectroscopy. This characterization allowed for the identification of the relative contribution of specific wavelength ranges to the overall material modification in direct plasmas. Exposure of 193nm PR to plasma UV/VUV radiation led to film thickness reduction and an increase in the refractive index ($\tilde{N}$) which was enhanced for shorter wavelengths. For direct plasma exposure at low maximum ion energy ($E_{ion} \leq 25$ eV), radiation effects dominated and bulk material modifications saturated after ≈30 s. By comparison, for 248nm PR film thickness reduction and increase of $\tilde{N}$ were modest and were only seen for UV/VUV exposure with wavelength lower than 142 nm. Both material surfaces remained relatively smooth during

60 s exposure to plasma radiation (0.3 mm to 0.6 nm RMS roughness) independent of radiation wavelengths used.

For direct Ar plasma exposure involving energetic ion bombardment ($E_{ion} \leq 125$ eV), a graphitic surface layer was established within 3 s to 5 s. During this time period ≈30% of the saturation UV/VUV modification in the material bulk of 193nm PR were reached, which corresponds to a 60 nm thick soft layer underneath the ion crust. For 248nm PR less than 20% of the bulk material modification that were established in 60 s were reached during formation of the ion-crust. This corresponds to a ≈4 nm thick hard layer underneath the ion-modified surface. This shows that for 193nm PR, bulk material modifications by plasma UV/VUV radiation were fast and contributed significantly to the overall material modification in the first seconds of plasma exposure, whereas UV/VUV modifications of 248nm PR were slow and small. This material specific difference in the dynamics of material modification was in good agreement with 193nm PR developing much higher surface roughness (≈6.0 nm) than 248nm PR (≈1.6 nm) during 60 s exposure to plasma exposures involving both UV/VUV radiation and energetic ion bombardment.

3.1 Introduction

Plasma-based transfer of photoresist (PR) patterns into other materials is a key process for production of nano-scale devices used in microelectronic technology. In the semiconductor industry, reduction of feature sizes and increased control over critical dimensions (CD) have closely followed Moore's law in the past decades.[3.1] A significant change was the transition in lithographic wavelength from 248 nm to 193 nm, which required a change from styrene-based 248nm PR materials to methacrylate-based 193nm PR materials.[3.2] This change in the material platform introduced new challenges during plasma processing such as increased roughness development, reduced etch resistance, and pattern distortion.[3.3-3.7] Currently, 193nm lithography and its modified version, 193nm immersion lithography, are successfully used to produce devices with CD of 30 nm and lower. However, improved CD control by reducing roughness development during plasma etching has become increasingly important. For 2016 the International Technology Roadmap for Semiconductors (ITRS) projects CD as small as 15 nm with a tolerance of only ±1.8 nm, which is significantly lower than the roughness of current 193nm PR materials after plasma processing.[3.1]

This article is part of an ongoing investigation on plasma-polymer interactions during pattern transfer processes. In prior work we have systematically studied 193nm PR, 248nm PR, and other model polymers relevant for organic masking materials.[3.6-3.21] Oehrlein et al. have recently reviewed progress on this topic.[3.19] We found in our plasma systems that 193nm PR trench patterns developed significantly more surface and sidewall roughness than 248nm PR trench patterns during plasma processing.[3.20] For 193nm PR surface roughness formation is initially a very rapid process (≈3s to 5 s) and coincides

with strong surface modifications by ions.[3.20, 3.21] Energetic ion bombardment leads to pronounced oxygen and hydrogen depletion, densification, and graphitization within a ≈2 nm thick surface layer referred to as the 'ion-crust'.[3.11, 3.13] After formation of the ion-crust, surface roughness increases linearly with processing time.[3.20] During this time period the amplitude of the initially established surface roughness increases while the lateral spatial orientation of roughness features remains fairly unchanged. This can be explained by a selective etching mechanism.[3.21] In contrast to 193nm PR, 248nm PR develops little surface roughness during formation of the ion-crust and roughness does not increase for longer processing times.[3.20] The differences in roughness development between 193nm PR and 248nm PR can be attributed to material specific energy deposition densities at the PR surface which take material removal rates into account.[3.17, 3.18] The sidewall roughness of PR patterns introduced during plasma processing is based on transfer of the surface roughness at the feature top edge by a micromasking effect and is established at significantly longer timescales (≈30 s) than surface roughness.[3.18, 3.20] Thus it is crucial to understand surface roughness development to improve control over CD.

In a separate vacuum beam system, we found that 193nm PR developed surface roughness when exposed to energetic ions (Ar, 150 eV) and ultraviolet (UV)/vacuum ultraviolet (VUV) radiation (Ar plasma emission), and roughness was amplified at increased temperature (100 ^{o}C).[3.14, 3.16] 248nm PR exposed to the same condition remained relatively smooth.[3.14, 3.16] Furthermore, severe roughness formation of 193nm was found to be a synergistic effect and only occurred when materials were exposed to ions and photons (fundamental plasma components) at the same time.[3.14, 3.16] Since the

surface modification by ions is relatively independent of the PR composition and structure, differences between 193nm and 248nm PR in roughness development are likely due to the plasma UV/VUV radiation component.[3.8, 3.11, 3.22, 3.23]

In prior work we exposed 193nm and 248nm PR to the radiation component of Ar plasma using a filter approach and found that 193nm PR was significantly more sensitive to plasma radiation than 248nm PR.[3.8] UV/VUV-exposed 193nm PR is subjected to detachment and removal of polymer pendant groups and chain-scissioning of the polymer backbone to a depth of up to 200 nm.[3.8] Some of the detached pendant groups and other photolysis products such as adamantane, lactone, CO, CO_2, and H_2 diffuse to the surface and are removed during processing.[3.10] The detached pendant groups remaining in the polymer matrix may act as a plasticizer and are expected to cause, together with the shorter polymer chains, material softening (reduced Young's modulus) and reduced glass transition temperature.[3.8, 3.24-3.27] UV/VUV exposure of 248nm PR mainly leads to cross-linking of a relatively shallow surface layer (≈15 nm to 40 nm) which is often associated with material hardening (increased Young's modulus).[3.8]

We have shown that for Ar plasma-treated polystyrene, a UV/VUV-insensitive material, that surface roughness can be explained by wrinkling of the thin ion-crust on top of a softer polymer bulk.[3.13] We believe that the strong differences in roughness development between 193nm PR and 248nm PR are due to differences in bulk material mechanical properties that are altered by UV/VUV radiation concurrently with the ion-crust formation.

The present article is an effort to improve our understanding of the timescales of concurrent material modifications by ions and UV/VUV radiation in Ar plasma. We

monitored changes in film thickness and material optical properties of 193nm and 248nm PR in real-time using *in-situ* ellipsometry. Contributions of various wavelength ranges to the overall radiation modification were studied using a filter approach. Plasma emission spectra in the UV/VUV spectral range were characterized by UV/VUV spectroscopy. This study aims to gain insight into synergistic material modifications in a real plasma environment leading to roughness development and understand PR material dependencies.

3.2 Experimental

3.2.1 Materials

The materials used in this study were full formulation 193nm PR and 248nm PR. The random terpolymer structure of 193nm PR consists of methyl-2-adamantyl-methacrylate in the leaving group, α-gamma-butyrolactone methacrylate in the lactone group, and R-functionalized–adamantyl-methacrylate in the polar group. 248nm PR is a terpolymer structure and consists of hydroxystyrene, styrene, and t-butylacrylate. Additionally, our PR contained photo-acid-generator (3 wt.% triphenylsulfonium-perfluorobutylsulfonate) and base (0.2 wt.% trioctyl-amine). All PR components were spin coated together on silicon wafers as ≈400 nm thick blanket films. Detailed descriptions of the molecular structure and functional groups can be found elsewhere. [3.6, 3.28]

3.2.2 Plasma processing

The plasma and material studies presented in this work were carried out in an inductively coupled plasma (ICP) system. This ICP reactor has been used in previous studies and is well characterized for a wide range of processes relevant to semiconductor fabrication.[3.11-3.13, 3.29] Briefly, the plasma was induced in the system by supplying a planar, water cooled brass coil on top of a quartz window through an L-type matching network with a 0 W to 2000 W source power supply at 13.56 MHz. The RF current through the coil induced a current in the plasma generation region ≈20 mm to 30 mm below the quartz window, igniting and maintaining the plasma discharge. The plasma was confined with a 195 mm diameter anodized Al confinement ring and a 125 mm diameter Si substrate located at a variable position (85 mm to 145 mm) below the quartz

window. Due to the inductive coupling, a low plasma potential (V_{PP}≈25 V) with reference to the floating wall was created charge buildup on the substrate.[3.13] This built-up charge determines the maximum energy of ions (E_{ion}) impacting the wafer and can be further increased independent of the plasma generation by applying a self-bias potential (V_{SB}) to the substrate with a 0 W to 1000 W RF power supply at 3.7 MHz. The resulting maximum ion energy E_{ion} in eV corresponds to $V_{PP}+V_{SB}$ in V. Liquid backside cooling maintained the bottom electrode temperature during processing at 10 ^{o}C and thermal bonding of PR coated Si samples (25x25 mm^2) to the bottom electrode with thermal grease prevented significant material heating due to ion bombardment. The chamber base pressure before processing was below $7x10^{-4}$ Pa ($5x10^{-6}$ Torr) and the chamber pressure during processing was established at constant gas flow with an exhaust throttle valve.

For our material studies we used pure Ar plasmas which are representative of typical plasma processes such as 90%Ar/C_4F_8 used for transfer of PR patterns into dielectric materials.[3.30-3.32] Removing the fluorocarbon (FC) from the gas mixture allows us to directly correlate observations to ion and plasma radiation effects of the Ar component. For processing we used a total gas flow rate of 40 sccm and 1.3 Pa (10 mTorr) operating pressure. The source power was set to 300 W. The maximum ion energy E_{ion} was selected at either 25 eV or 125 eV and conditions will be referred to as the low and high E_{ion} condition, respectively, in the remainder of this publication. The distance between the bottom electrode and quartz window was fixed at the maximum position (145 mm) to reduce material interactions with energetic plasma species.

For the spectroscopic measurements we used pure Ar plasma operated at 500 W source power, a total gas flow of 100 sccm, and an operating pressure of 4.0 Pa (30 mTorr). The distance between the bottom electrode and quartz window was kept constant at the minimum position (85 mm). Higher source power, elevated pressure and reduced distance between quartz window and bottom electrode provided stronger emission of plasma radiation close to the bottom electrode for spectroscopic measurements.

3.2.3 Characterization

Material modifications in Ar plasma were monitored in real-time by *in-situ* ellipsometry. The ellipsometer is an automated rotating compensator ellipsometer working in the polarizer-compensator-sample-analyzer (PCSA) configuration at a ≈72 ^{o} angle of incidence. Measurements were performed in Ψ-Δ-space, corresponding to changes in phase and relative amplitude of the polarized laser light components (HeNe laser, λ=632.8 nm). The recorded data was interpreted in terms of changes in film thickness and index of refraction (Ñ) based on two ellipsometric multilayer models (see Fig. 3.1). For exposure of PR to plasma radiation and direct plasma with $E_{ion} \leq 25$ eV we simulated changes in thickness and Ñ for the PR layer on top of the Si substrate (Fig. 3.1(a)). For exposure of PR to direct plasma with $E_{ion} \leq 125$ eV we introduced an additional layer at the PR film surface representing shallow ion-induced modifications (Fig. 3.1(b)). Ñ of the Si substrate was fixed to $3.866\text{-}0.028i$ [3.33] and Ñ of pristine 193nm PR and 248nm PR films was estimated to be 1.526 and 1.560, respectively. The uncertainty of the ellipsometric measurements is estimated at ±0.1 ° and small compared to observed changes during processing.

In order to study material modifications by the plasma radiation component in real-time we designed a housing that prevented energetic and reactive plasma species from interacting with the PR. A schematic of the housing is shown in Fig. 3.2(a). The stainless steel housing (≈25 mm high and ≈63 mm in diameter) was placed over the sample, which was mounted on the chamber substrate. An opening in the top of the housing (≈19 mm in diameter, centered with the sample) was covered with optical filters. Using various filter materials (MgF_2, sapphire and borosilicate glass) we were able to select the UV/VUV wavelength range interacting with the PR. For probing the sample surface with our ellipsometer *in-situ* during plasma processing, the housing had two small aperture holes on either sides (≈3 mm diameter).

In addition to the ellipsometric measurements, we characterized plasma emission of an Ar discharge and transmission through optical filter materials used in this and our previous studies with VUV spectroscopy. [3.8, 3.11] A schematic of the spectroscopic setup is shown in Fig. 3.2(b). The spectrometer used in these experiments was a 200 mm focal length modified Seya-Nomioka design (McPherson 234/302M)[*)].

The diffraction grating is a 1200 G/mm type IV aberration corrected concave grating with an f-number of 4.5. The spectrometer viewed a cone of light ≈20 mm above and centered with the substrate. Entrance and exit slits were 5 μm wide and 20 mm tall and adjusted for improved resolution while maintaining good intensity. The spectrometer was separated from the plasma system by an MgF_2 window (25 mm diameter, 3 mm thickness) and differentially pumped below $7x10^{-3}$ Pa ($5x10^{-5}$ Torr) (250 l/s turbo-

**) Certain commercial equipment, instruments, or materials are identified in this document. Such identification does not imply recommendation or endorsement by the National Institute of Standards and Technology, nor does it imply that the products identified are necessarily the best available for the purpose.*

molecular pump) to prevent degradation of the spectrometer optics by reactive and energetic plasma species. The photon detector used was a photomultiplier tube (PMT) with an MgF_2 window and a cesium telluride photocathode with backside cooling using a Pelletier element. The measurement range was between 350 nm (≈3.5 eV) and 114 nm (11.3 eV, cut-off wavelength of the MgF_2 window). An evacuated cell with two MgF_2 windows was installed on the spectrometer exit side to thermally isolate the PMT and to establish a vacuum in the spectrometer. The PMT housing was purged with nitrogen gas. For characterization of the glass (0.2 mm thick) and sapphire (0.9 mm thick) filters, we attached the filter materials onto the MgF_2 window which separated the spectrograph from the plasma. All spectra were recorded with a wavelength resolution of 0.1 nm and averaging 5 measurements per wavelength.

PR surface morphology and roughness were characterized after processing by tapping mode atomic force microscopy (AFM, Veeco Multimode) with a fixed scan size of 1x1 μm^2. The surface roughness values reported were calculated from the root mean square (RMS) of the surface profile after the measurement.

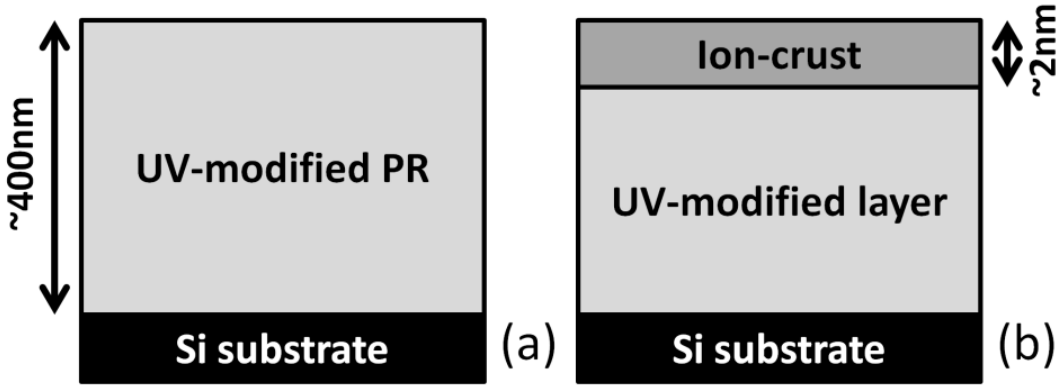

Figure 3.1: *Schematic of ellipsometric multilayer models for PR exposure to (a) direct plasma with the substrate at the plasma potential (V_{PP}≈25 V) and (b) direct plasma with -100 V self-bias voltage applied to the substrate accounting for ion-induced surface modifications. The resulting maximum ion energies are estimated at E_{ion}≤25 eV for the substrate at V_{PP} and E_{ion}≤125 eV for the biased substrate.*

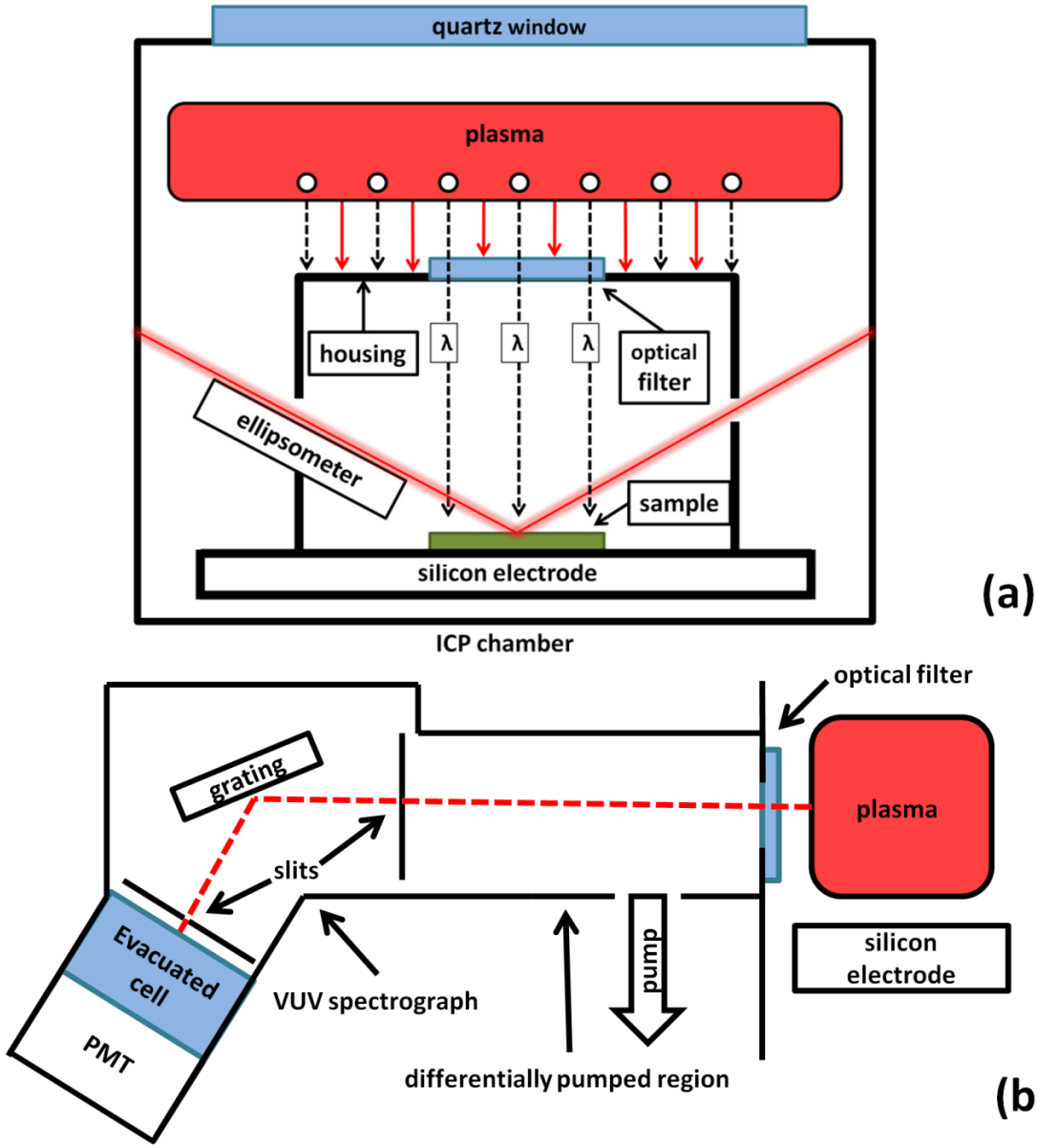

Figure 3.2: *Schematic of the experimental setup (not to scale) for measuring material modifications by plasma radiation in real-time by in-situ ellipsometry (a) and for measuring plasma emission spectra and determining filter cut-off wavelength with VUV spectroscopy (b). For ellipsometric measurements an optical filter (MgF_2, sapphire, or glass) was placed on top of a housing, reducing the plasma-PR interactions to plasma radiation of selected wavelength ranges. The ellipsometer laser probed the sample surface through small aperture holes on either sides of the housing. Direct plasma exposures were performed without the housing. For the spectroscopic measurements plasma emission was measured with a differentially pumped VUV spectrograph viewing a cone of light ≈20 mm above and centered with the substrate. The spectrometer was separated from the plasma system by an MgF_2, sapphire, or glass window to prevent degradation of the spectrometer optics and determine cut-off wavelengths of the filter materials.*

3.3 Results

3.3.1 Plasma radiation

The dependencies of changes in film thickness and Ñ of 193nm PR and 248nm PR on plasma radiation were tested in Ar plasma using the filter approach described in Sec. 3.2.3. Figure 3.3 shows the transmission spectra of Ar plasma through the (a) glass, (b) sapphire and (c) MgF_2 filter. The cut-off wavelengths for high energy photons were determined to be 290 nm, 142 nm, and 114 nm for the glass, sapphire and MgF_2 filters, respectively. At higher wavelengths the most intense emission was atomic C I emission (156 nm, 166 nm, 175 nm, 193 nm, 248 nm) and molecular H_2 emission (150 nm to 250 nm).[3.34, 3.35] The spectrum of an H_2 plasma (same plasma conditions as Ar plasma) is presented in Fig. 3.3(d) for comparison and shows that emission was mainly due to molecular continuum emission (λ>170nm).[3.36] Increasing attenuation of smaller wavelengths by the MgF_2 filter significantly reduced characteristic Werner and Lyman H_2 emission (λ=90 nm to 170 nm) and the most intense emission at 161 nm remained at levels lower than the observed C I emission.[3.37, 3.38] At low wavelengths, radiation was due to attenuated atomic O I emission (λ=130 nm to 131 nm) and H I emission (λ=122 nm).[3.34] Neither characteristic atomic emission of Ar I (λ=105 nm and λ=107 nm) nor continuum emission of Ar molecules (Ar_2^*, λ=100 nm to 140 nm) were observed.[3.34, 3.39, 3.40] Complete attenuation of the low wavelength Ar signal can be explained by the four MgF_2 filters in series between the plasma and PMT during spectroscopic measurements. However, in the case of our material modification experiments, only one MgF_2 filter was used to separate plasma and PR and some reduced transmission may be possible. The

filter characteristic transmission spectra have a direct impact on the rates of material modification by plasma radiation.

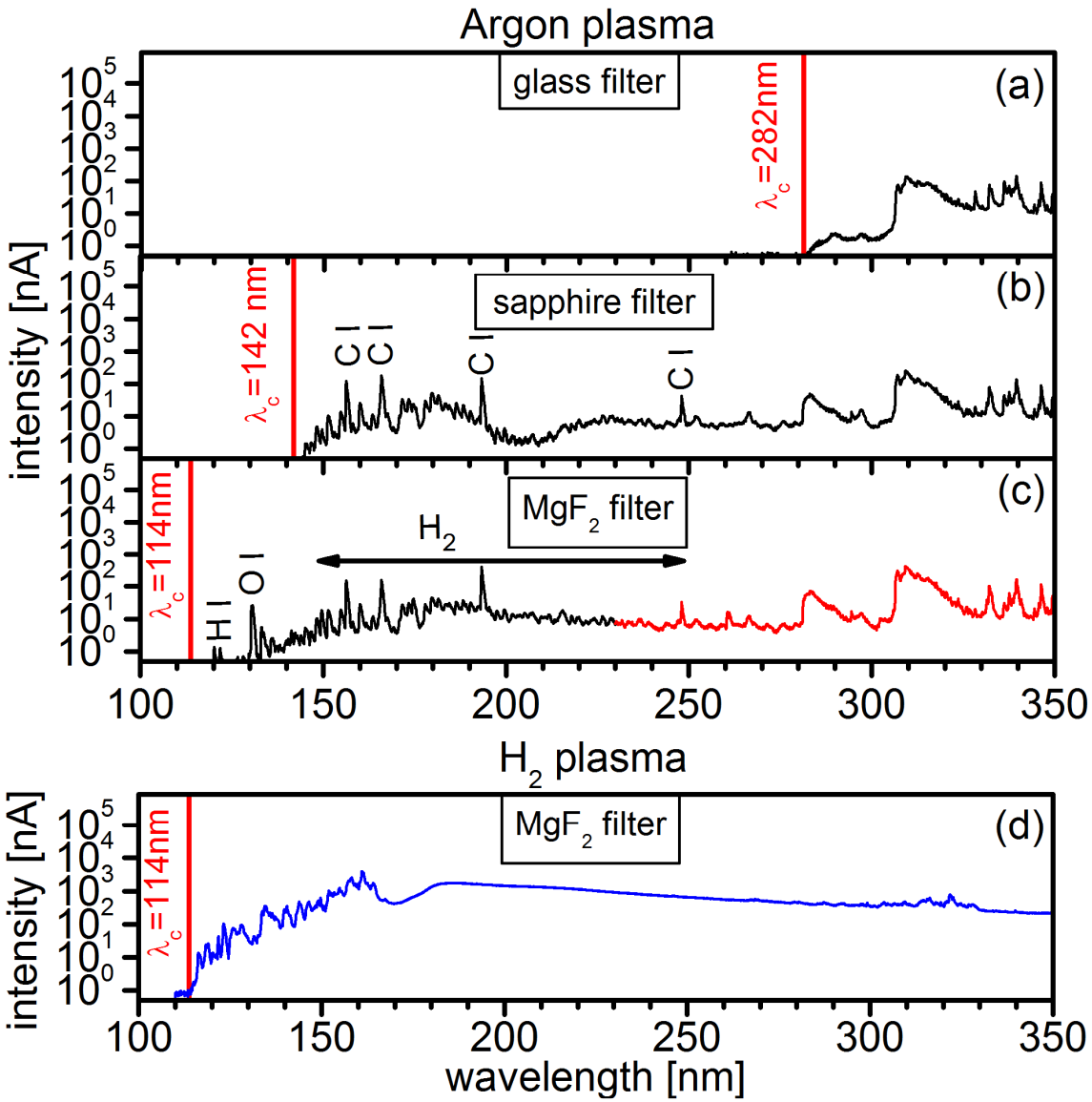

Figure 3.3: *Characteristic Ar plasma emission transmitted through the glass (a), sapphire (b), and MgF_2 filter (c) and H_2 plasma emission transmitted through the MgF_2 filter (d). Cut-off wavelength (λ_c) and assignments of identified emission lines are indicated in the spectra.*

3.3.1.1 193nm PR

Figure 3.4(a) shows the ellipsometric measurements during 4800 s exposure of 193nm PR to Ar plasma radiation through the three filter materials along with an

ellipsometric model. The model accounts for a PR layer with various film thicknesses between 350 nm and 380 nm (solid lines, 10 nm increments) and Ñ between 1.525 and 1.560 (dashed lines, 0.005 increments) on top of the Si substrate ($\Psi \approx 7.0^{o}$ and $\Delta \approx 178.2^{o}$).We observed that during exposure to plasma radiation through the optical filters, 193nm PR undergoes film thickness reduction and an increase in Ñ. For all three filters modifications follow almost identical trends, but modification rates were significantly increased for lower filter cut-off wavelengths. The MgF_2 filter exposure led to the highest degree of modification, the sapphire filter exposure to reduced modification and the glass filter exposure to the lowest degree of modification.

The time resolved changes in film thickness and Ñ extracted from the model are presented in Figs. 3.4(b) and 3.4(c), respectively. It is evident that changes are more rapid at the exposure start and become slower for longer exposure times. The MgF_2 filter exposure led to the highest modification with a film thickness change of ≈19 nm and an increase in Ñ of ≈0.018 during 4800 s exposure. For 4800 s exposure using the sapphire filter, equivalent modifications were observed during ≈2050 s of exposure using the MgF_2 filter (film thickness reduction of ≈12 nm and increase in Ñ of ≈0.012; red dashed lines). For 4800 s exposure using the glass filter, equivalent modifications were observed during 300 s of exposure using the MgF_2 filter (thickness reduction of ≈3 nm and increase in Ñ of ≈0.003; black dotted lines). The resulting modification rates of the PR beneath the sapphire and glass filter compared to those of the PR beneath the MgF_2 filter were reduced by a factor of ≈2.3 and ≈16, respectively. This suggests that material modification occurs for plasma radiation with wavelengths higher than 290 nm and is dependent on the photon flux transmitted through the filters.

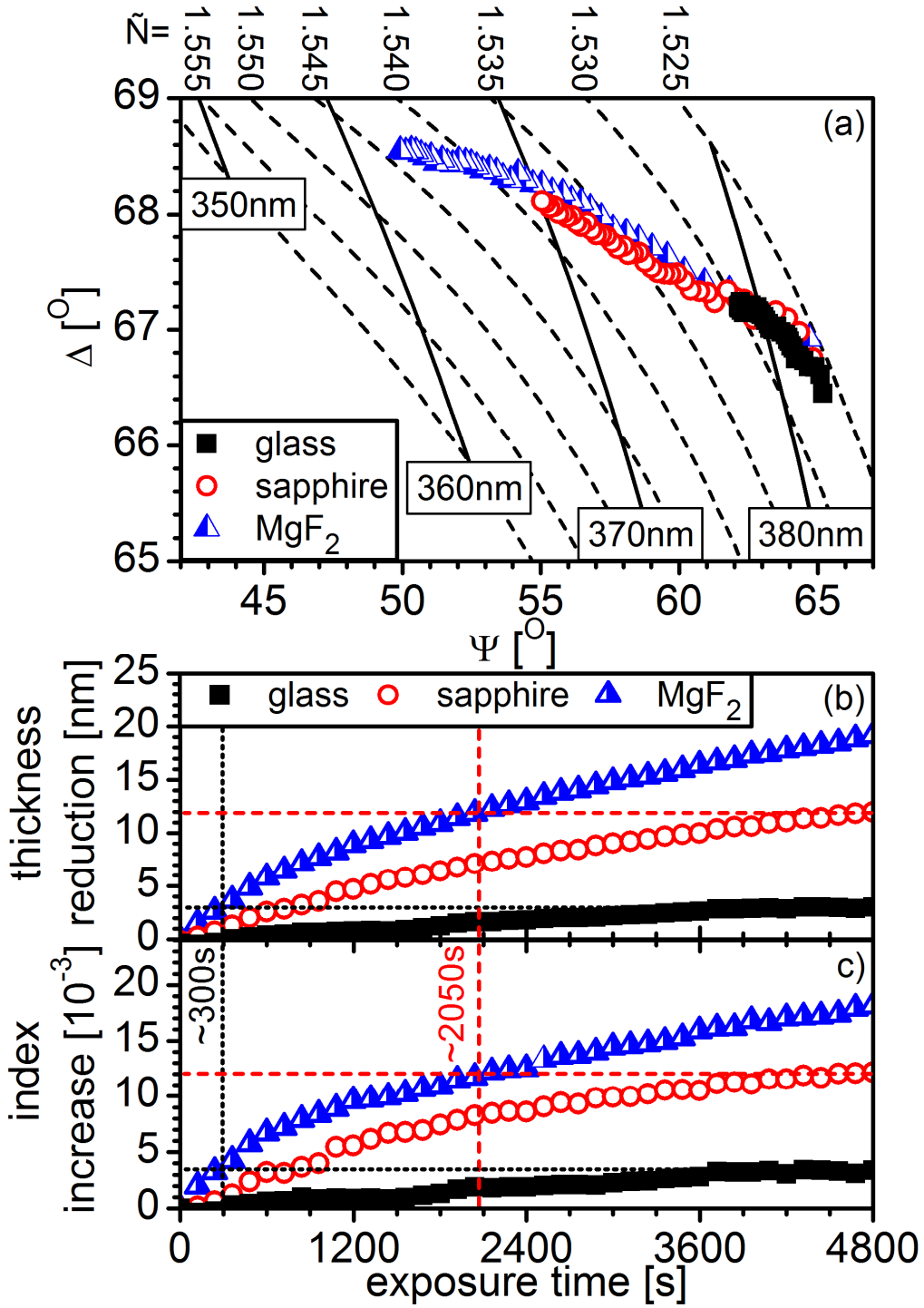

Figure 3.4: *Ellipsometric measurement of (a) 193nm PR exposed to Ar plasma radiation for 4800 s using glass, sapphire, and MgF_2 filters. The ellipsometric model shows trajectories for various film thicknesses (350 nm to 380 nm, solid lines) and $\tilde{N}$ (1.525 to 1.560, dashed lines). Extracted time evolutions of film thickness reduction and increase in $\tilde{N}$ are shown in (b) and (c), respectively. Dashed and dotted lines indicate the MgF_2 exposure times, ≈2050 s and ≈300 s, which led to equivalent thickness reduction and increase in $\tilde{N}$ for 4800 s exposure using the sapphire and glass filter, respectively.*

3.3.1.2 248nm PR

Figure 3.5(a) shows the ellipsometric measurements during 2400 s exposure of 248nm PR to Ar plasma radiation through the three filter materials along with an ellipsometric model. The model accounts for a PR layer with film thicknesses between 392 nm and 400 nm (solid lines, 2 nm increments) and $\tilde{N}$ between 1.560 and 1.566 (dashed lines, 0.002 increments) on top of the Si substrate. We observed that during exposure to plasma radiation through the optical filters, 248nm PR only undergoes film thickness reduction and an increase in $\tilde{N}$ for exposure using the MgF_2 filter (lowest filter cut-off wavelength). 248nm PR exposure to plasma radiation through the glass and sapphire filters led to changes in thickness and $\tilde{N}$ on the order of the measurement precision. Data of the glass filter exposure appears at slightly increased $\tilde{N}$ in this model due to small changes in the experimental ellipsometer angle. The measurements have been analyzed taking the small angular changes into account and observations of minute changes in thickness and $\tilde{N}$ remain unchanged.

The time resolved changes in film thickness and $\tilde{N}$ extracted from the model are presented in Figs. 3.5(b) and 3.5(c), respectively. For exposures using the glass and sapphire filter, $\tilde{N}$ and film thicknesses remain relatively unchanged. Only the MgF_2 filter exposure led to a thickness reduction of $\approx$1 nm and an increase in $\tilde{N}$ of $\approx$0.002. The same extent of bulk material modification was established for 193nm PR after only 120 s exposure using the MgF_2 filter and $\approx$2400 s exposure using the glass filter. This shows that material modification are significantly reduced for 248nm PR and strongly dependent on the photon wavelength. Only plasma radiation with wavelengths lower than 142 nm modifies 248nm PR.

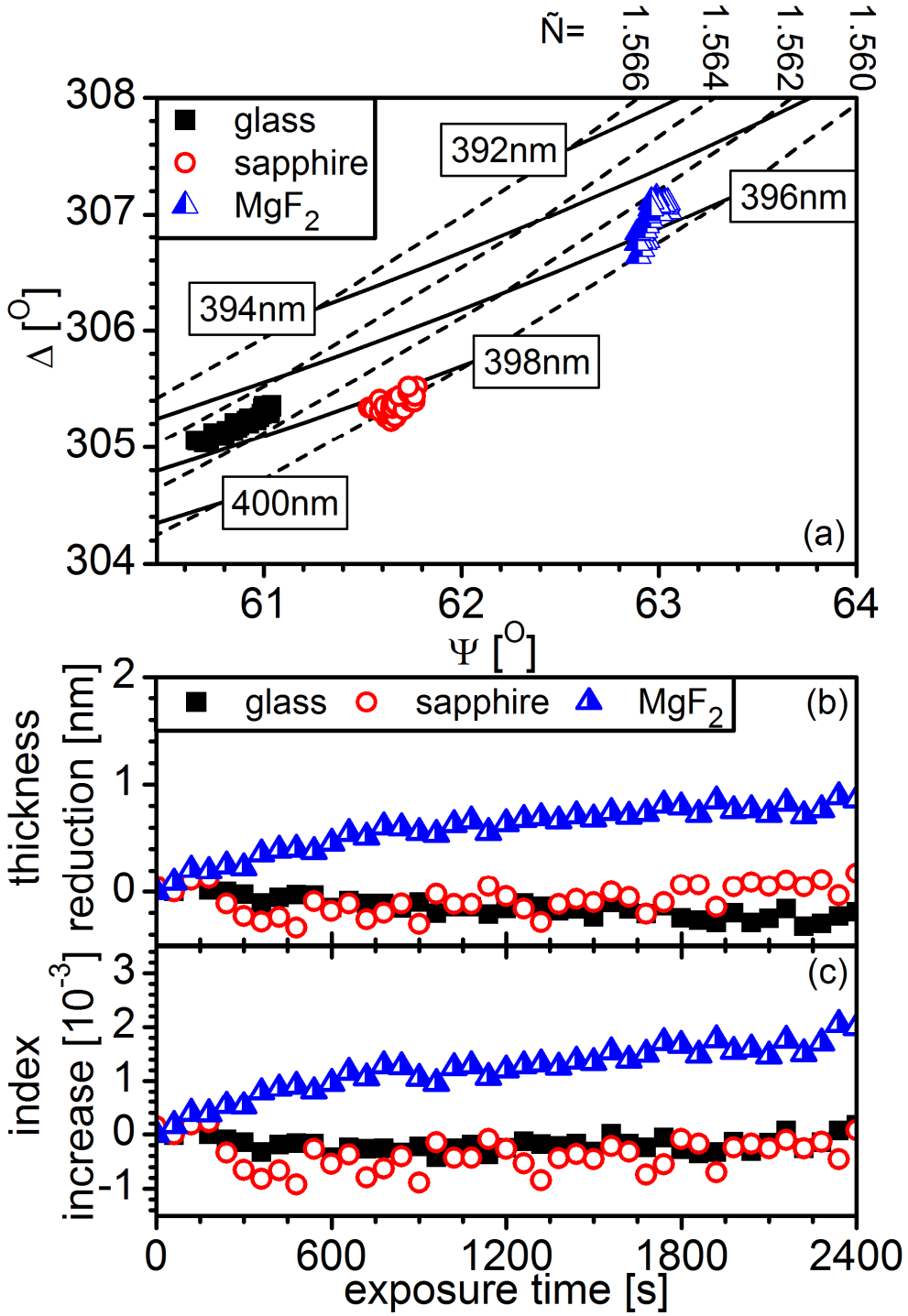

Figure 3.5: *Ellipsometric measurement of (a) 248nm PR exposed to Ar plasma radiation for 2400 s using glass, sapphire, and MgF_2 filters. The ellipsometric model shows trajectories for various film thicknesses (392 nm to 400 nm, solid lines) and Ñ (1.560 to 1.566, dashed lines). Extracted time evolutions of film thickness reduction and increase in Ñ are shown in (b) and (c), respectively.*

3.3.2 Direct plasma

To clarify the individual contributions of ions and plasma radiation to the overall material modification, PR materials were exposed to the low and high E_{ion} condition. For $E_{ion} \leq 25$ eV, E_{ion} is only slightly above the threshold energy for sputtering, and the plasma material interactions were dominated by UV/VUV radiation. This situation is similar to our filter exposures (see Sec. 3.3.1), with the difference that photons with wavelengths smaller than 114 nm (MgF_2 filter cut-off wavelength) can interact with the PR. We have shown previously that plasma radiation can lead to severe bond breakage, pendant group detachment and removal, and chain-scissioning to depths of up to 200 nm for 193nm PR.[3.8] For 248nm PR, material modification by plasma radiation is limited to ≈15 nm to 40 nm depth and dominated by cross-linking reactions.[3.8] Energetic ion bombardment can lead to formation of an ion-crust by removal of large amounts of oxygen and hydrogen, inducing heavy cross-linking, graphitization, and an increase in density from ≈1 g/cm^3 to ≈2.7 g/cm^3.[3.11, 3.13] The maximum thickness of this surface layer depends on the ion penetration depth, which was estimated to be ≈1.8 nm for $E_{ion} \leq 125$ eV and ≈0.1 nm for $E_{ion} \leq 25$ eV.[3.13]

3.3.2.1 193nm PR

Figure 3.6 shows the real-time measurements during plasma processing of 193nm PR for (a) $E_{ion} \leq 25$ eV and (b) $E_{ion} \leq 125$ eV together with ellipsometric models. For the low E_{ion} condition (Fig. 3.6(a)) the model is identical to the model for UV/VUV modification presented in Sec. 3.3.1 ($\tilde{N}$=1.525 to 1.560, increments of 0.005, dashed lines). The thickness of the ion-crust for low E_{ion} is very small (≈0.1 nm) and does not have to be taken into account. For the high E_{ion} condition (Fig. 3.6(b)) our ellipsometric

model introduces an optically dense surface layer ($\tilde{N}$=1.870-0.197*i*) representing the ion-crust on top of the UV/VUV-modified bulk material. The ellipsometric map shows simulations for the pristine material ($\tilde{N}$=1.525) without the ion-crust (dashed lines) and UV/VUV-induced changes of the material bulk (same model as for the low E_{ion} condition) below a 1.8 nm thick ion-crust (dotted lines). In the actual simulations the thickness of the ion-crust remains dynamic. Film thicknesses in both models are simulated between 320 nm and 380 nm (black solid lines).

For the low E_{ion} condition (Fig. 3.6(a)), we observed a rapid reduction in film thickness of ≈20 nm and an increase of $\tilde{N}$ from ≈1.525 to ≈1.545 in the first 30 s. From 30 s to 180 s changes in film thickness were significantly slower (≈40 nm in 150 s) and almost no changes in $\tilde{N}$ were observed. This saturation of $\tilde{N}$ indicates that bulk material modifications by plasma UV/VUV radiation saturated within the first 30 s. For the high E_{ion} condition (Fig. 3.6(b)) we observed distinctly different behavior. For 60 s exposure the final film thickness was comparable to that of the low E_{ion} condition after 180 s exposure. This indicates that thickness reduction was significantly faster for E_{ion}≤125 eV. In the first 3 s of exposure the material experienced very rapid optical densification and thickness reduction (>10 nm) which corresponds to the time regime in which the ion-crust is formed. In the subsequent exposure time the film was subject to similar changes as observed for the low E_{ion} condition. Film thickness was continuously reduced while the increase in $\tilde{N}$ saturated after ≈30 s exposure time.

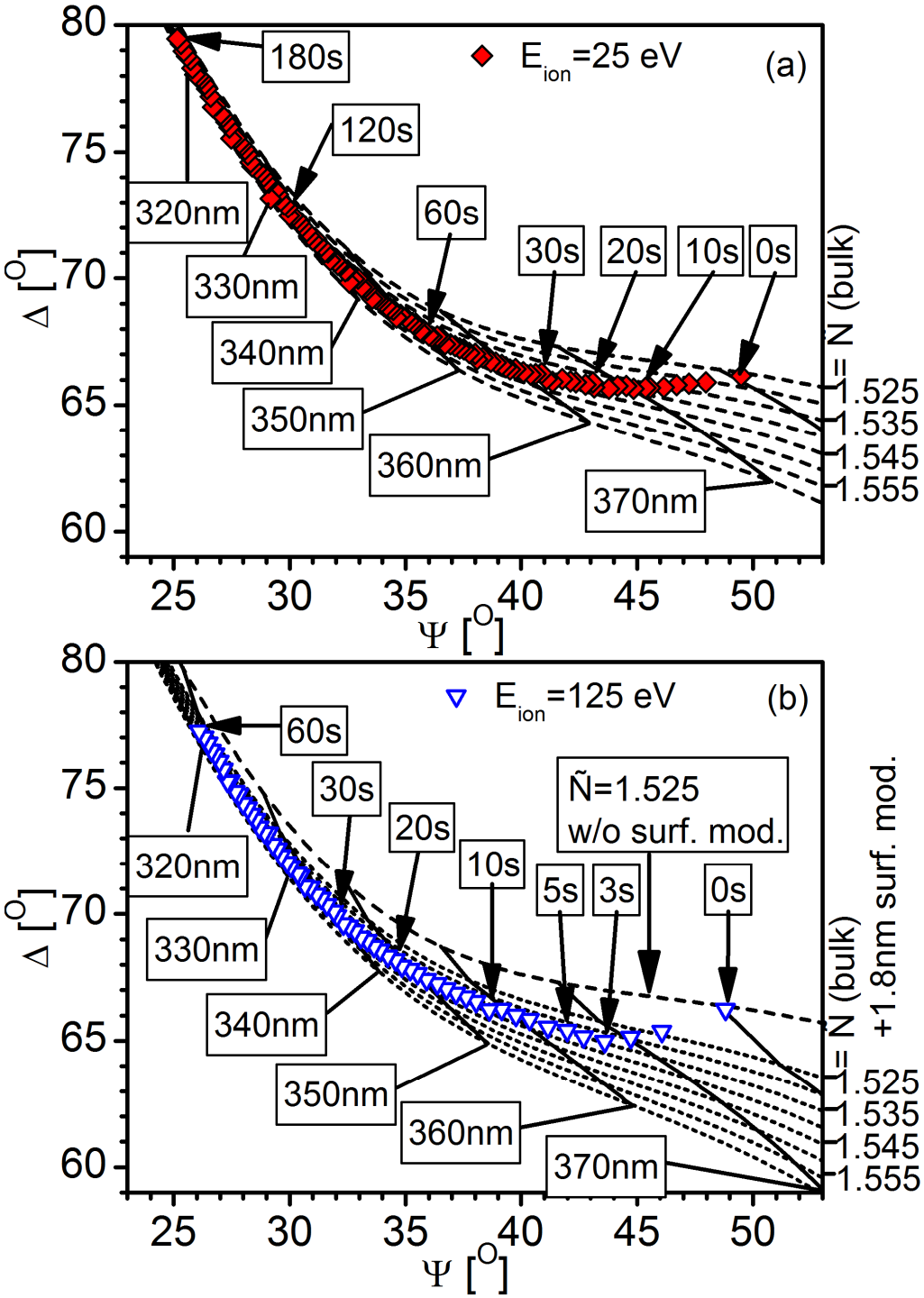

Figure 3.6: *Ellipsometric measurement of 193nm PR exposed to Ar plasma with (a) E_{ion}≤25 eV for 180 s and (b) E_{ion}≤125 eV for 60 s together with ellipsometric models. For E_{ion}≤25 eV the model shows film thicknesses between 370 nm and 320 nm (solid lines) and Ñ (1.525 to 1.560, dashed lines). For E_{ion}≤125 eV a thin (1.8 nm), optically dense (Ñ=1.870-0.197i) ion crust was formed by energetic ion bombardment. Changes in film thicknesses (370 nm to 320 nm, solid lines) and Ñ (1.525 to 1.560, dotted lines) below the modified surface region were modeled in the same fashion as in Fig. 3.4(a).*

Figure 3.7 shows the temporal evolution of ion–crust thickness (a), Ñ increase ((b) and (d)), and film thickness reduction ((c) and (e)) extracted from the ellipsometric models shown in Fig. 3.6. The formation of the ion-crust observed for the $E_{ion} \leq 125$ eV exposure (Fig. 3.7(a)) was a rapid, ion-driven process. Full formation of the surface layer was established within 3 s (dotted line). This is in good agreement with previous insights from plasma exposures.[3.13, 3.21]

Taking the evolution of the surface optical densification into account, we extracted changes in optical density of the bulk material underneath the ion-crust. Figures 3.7(b) and 3.7(d) show the comparison of Ñ increase for both direct exposure cases during the first 5 s and during 180 s exposure time, respectively. We can observe that, independent of E_{ion}, Ñ show the same temporal evolution. This is in good agreement with our expectations that UV/VUV radiation introduces these changes by bulk material modifications which are independent of E_{ion}. Ñ increased rapidly at the exposure start (regime I) and saturated for both conditions after 30 s (see Fig. 3.7(d): regime II, dashed line). At 3 s exposure time (see Fig. 3.7(b): dotted line), when the ion crust was fully established, ≈1/3 of the change in Ñ of the material bulk had taken place. This corresponds to a UV/VUV-modified layer thickness of ≈60 nm assuming a maximum modification depth of 200 nm.[3.8, 3.24, 3.41]

The film thickness reduction (Fig. 3.7(c) and 3.7(e)) shows strong dependence on E_{ion}. Energetic ions ($E_{ion} \leq 125$ eV) removed material from the film surface at much higher rates than low energy ions ($E_{ion} \leq 25$ eV), as can be expected for an E_{ion}-dependent sputter process. We also observed (see Fig. 3.7(e)) that thickness reduction was fast at the exposure start (regime I) and slowed down after 30 s (regime II, dashed line) when steady

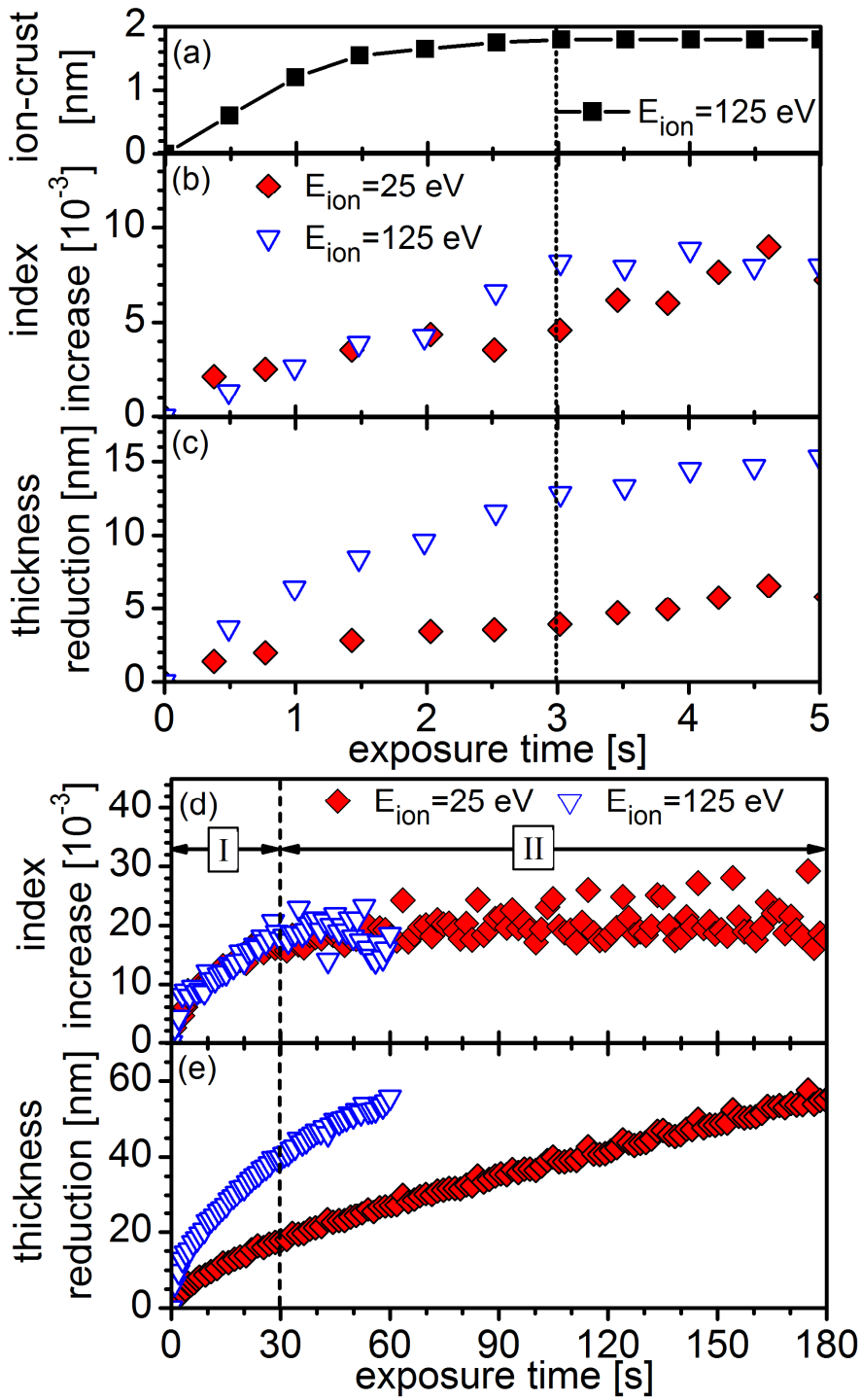

Figure 3.7: *Dependence of (a) ion-crust thickness for E_{ion}≤125 eV, ((b) and (d)) Ñ increase, and ((c) and (e)) film thickness reduction on exposure time of 193nm PR exposed to the low and high E_{ion} condition. Surface modification was a rapid, ion driven process and saturated in 3 s (dotted line). The dashed line indicates two characteristic time regimes: I) material removal and optical densification, and II) further thickness reduction without optical densification.*

state thickness reduction rates began (linear relation of thickness reduction and exposure time). These two time regimes coincide with those identified for Ñ (Fig. 3.7(d)), which points towards a close relation between fast thickness reduction and Ñ increase in the material bulk during the first 30 s of exposure. Comparing the thickness reductions in regime I (Fig. 3.7(e): 30 s, dashed line) shows that ≈50% of the total thickness reduction of the high E_{ion} condition are due to bulk material modifications by UV/VUV radiation (E_{ion}≤25 eV).

3.3.2.2 248nm PR

Figure 3.8 shows the real-time measurements during plasma processing of 248 nm PR for (a) E_{ion}≤25 eV and (b) E_{ion}≤125 eV together with ellipsometric models. Models for UV/VUV-induced bulk material modifications are set up in the same fashion as for plasma radiation exposure of 248nm PR (see Sec. 3.3.1): Ñ=1.560 to 1.570, film thicknesses between 396 nm and 399 nm for the low E_{ion} condition, and film thicknesses between 380 nm and 395 nm for the high E_{ion} condition. Simulations of the ion-crust (Ñ=2.182-0.3188*i*) are set up in the same fashion as for 193nm PR (see Sec. 3.3.2.1).

For the low E_{ion} condition (Fig. 3.8(a)) we observed continuous and slow reduction in film thickness of ≈3 nm and increase of Ñ from ≈1.560 to ≈1.569 during 60 s exposure. These modifications are equivalent to exposing 193nm PR for ≈10 s to the low E_{ion} condition (see Sec. 3.3.2.1).

For the high E_{ion} condition (Fig. 3.8(b)) we observed distinctly different behavior. After 20 s exposure the film thickness was reduced by ≈20 nm, much more than for the low E_{ion} condition after 60 s exposure. In the first 5 s of exposure the material experienced very rapid Ñ increase and thickness reduction (≈10 nm) which corresponds

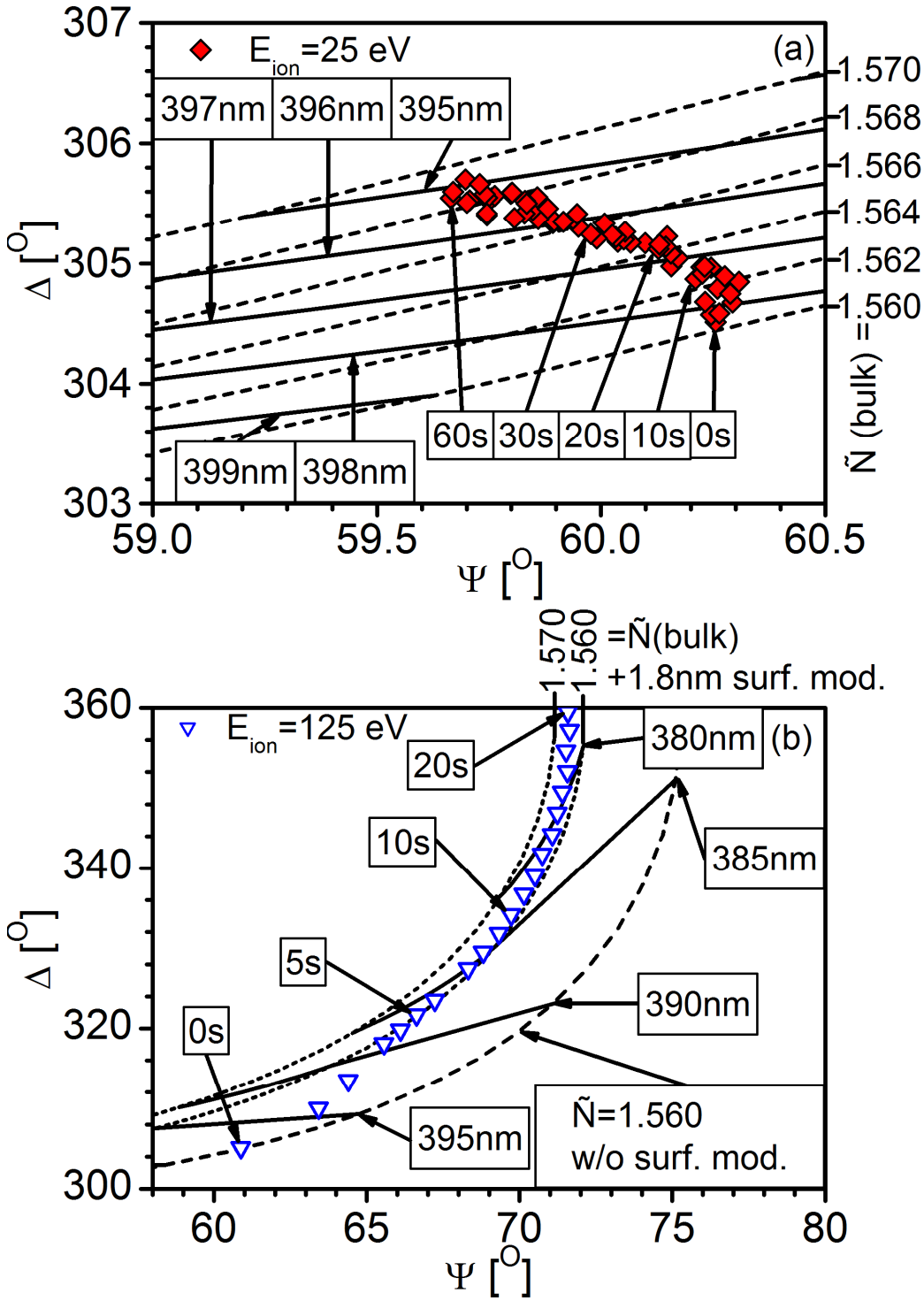

Figure 3.8: *Ellipsometric measurement of 248nm PR exposed to Ar plasma with (a) E_{ion}≤25 eV and (b) E_{ion}≤125 eV for 60 s together with ellipsometric models. For E_{ion}≤25 eV the model shows film thicknesses between 394 nm and 399 nm (solid lines) and Ñ (1.560 to 1.570, dashed lines). For E_{ion}≤125 eV changes in film thicknesses (380 nm to 395 nm, solid lines) and Ñ (1.560 to 1.570, dotted lines) are modeled below the thin (1.8 nm), optically dense (Ñ=2.182-0.319i) ion-crust.*

to the time regime in which the ion-crust is formed. In the subsequent exposure time the increase in Ñ was slow and very small compared to the Ñ increase by ion-crust formation.

Figure 3.9 shows the temporal evolution of ion-crust thickness (a), Ñ increase ((b) and (d)), and film thickness reduction ((c) and (e)) for 248nm PR extracted from the ellipsometric models shown in Fig. 3.8. The formation of the ion-crust observed for the $E_{ion} \leq 125$ eV exposure (Fig. 3.9(a)) was slightly slower than for 193nm PR and full formation of the surface layer was established within 5 s. This difference is in good agreement with previous insights from exposures to FC plasmas.[3.21]

Accounting for the ion-crust we can extract optical densification of both direct exposure cases. Figures 3.9(b) and 3.9(d) illustrate that Ñ has the same temporal evolution independent of E_{ion}. This highlights, that modifications were, as already observed for 193nm PR (see Sec. 3.3.2.1), due to UV/VUV modifications of the material bulk. However, the total increase in Ñ after 60 s was less than half of the increase observed for 193nm PR and fairly linear. This indicates that bulk material modifications were very slow and did not reach saturation during 60 s exposure (regime I). At 5 s exposure time, when the ion-crust was fully established (dotted lines), less than 20% of the change in Ñ in the material bulk had taken place. This corresponds to a UV/VUV-modified layer thickness of at most 4 nm (assuming a maximum modification depth of 20 nm[3.8, 3.41]) - similar to the ion-crust thickness.

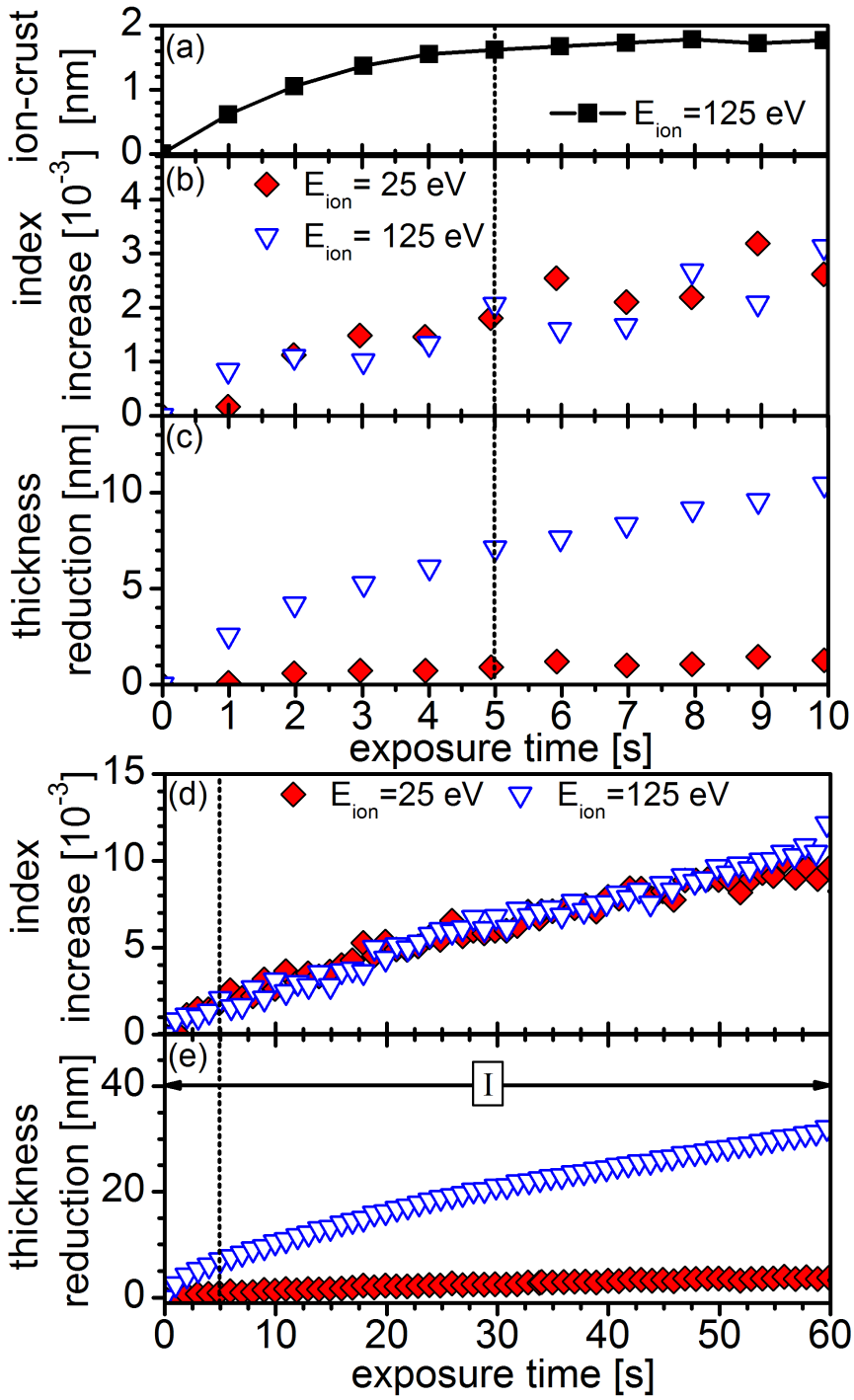

Figure 3.9: *Dependence of (a) ion-crust thickness for $E_{ion} \leq 125$ eV, ((b) and (d)) Ñ increase, and ((c) and (e)) film thickness reduction on exposure time of 248nm PR exposed to the low and high E_{ion} condition. Surface modification was a rapid, ion driven process and saturated in 5 s (dotted line). 248nm PR did not reach saturation of the Ñ increase and both exposures remained in regime I.*

The film thickness reduction (Figs. 3.9(c) and 3.9(e)) shows strong dependence on E_{ion}. In the low E_{ion} condition, thickness reduction by UV/VUV modification of the material was very slow. For energetic ions ($E_{ion} \leq 125$ eV) material removal from the film surface took place at high rates and was hardly increased by bulk material thickness reduction by UV/VUV. This is in strong contrast to 193nm PR where a large amount of the thickness reduction was due to UV/VUV modifications (see Sec. 3.3.2.1). We also observed that thickness reduction was fast at the exposure start and slowed down after 5 s when steady state reduction rates began (linear relation of thickness reduction and exposure time). These two time regimes coincide with those identified in the ion-crust thickness (Fig. 3.9(a)). This behavior indicates that UV/VUV modification of the material bulk does not play a significant role for 248nm PR.

3.4 Discussion

The differences in photon-induced material modifications between 193nm PR and 248nm PR identified in Sec. 3.3.1 are in good agreement with our general understanding of polymer photo-degradation and previous work.[3.8] 248nm PR mainly absorbs radiation for wavelengths below 160 nm due to dipole transitions and electronic excitations of C─H and C─C σ-bonds. [3.42-3.45] This explains why 248nm PR is only modified by photons in the 112 nm to 142 nm wavelength range characteristic for the MgF_2 filter. The expected modification depth (15 nm to 40 nm) is shallow due to high absorption of low wavelength photons.[3.8, 3.41] 193nm PR has, in addition to low wavelength absorption by C─C and C─H bonds, significant absorption by oxygen containing groups in the 160 nm to 360 nm wavelength range.[3.46, 3.47] This is consistent with our observations that even plasma radiation transmitted through the glass filter with $\lambda>290$ nm can modify 193nm PR. Furthermore, high wavelength radiation can penetrate much deeper into the polymer film and we expect modification depth of up to 200 nm.[3.8, 3.24, 3.41]

Comparing the plasma emission spectra (Fig. 3.3) with the filter characteristic modifications of 193nm PR (Fig. 3.4) shows that low photon flux at $\lambda<142$ nm (O I emission, MgF_2 filter) can lead to a higher degree of modification than high photon flux at 142 nm$<\lambda<$290 nm (C I and H_2 emission, sapphire filter). Thus, material modification is also dependent on photon energy. The observed O I and H_2 emissions at $\lambda<250$ nm are of direct relevance for typical pattern transfer plasma processes such as Ar/C_4F_8. These processes are often customized with O_2 and H_2 addition for increased profile control during pattern transfer into low-k materials, and are expected to lead to accelerated modification by UV/VUV radiation.[3.48]

In order to understand the contribution of UV/VUV radiation to the overall material modification in more detail we compared radiation-only exposures (glass, sapphire, and MgF_2 filters) with direct exposures ($E_{ion}\leq25$ eV and $E_{ion}\leq125$ eV). Figures 3.10(a) and 3.10(b) show the correlation of film thickness reduction and Ñ increase for 193nm PR and 248nm PR, respectively. For 193nm PR we can clearly see the two time regimes identified in Sec. 3.3.2. In regime I film thickness decreases linearly with the Ñ increase and in regime II the film thickness further decreases while changes in Ñ are saturated. For 248nm PR, Ñ does not reach saturation and exposures remain in region I.

For the $E_{ion}\leq25$ eV exposure of 193nm PR (Fig. 3.10(a)), we can see that, in regime I, trends follow the same trajectories as the filter exposures (plasma radiation only). This indicates that film thickness reduction and Ñ increase are driven by UV/VUV radiation with little contribution from ions. The saturation of UV/VUV modification was reached at a thickness reduction of ≈20 nm (dotted line) corresponding to ≈30 s direct plasma exposure with $E_{ion}\leq25$ eV. The identical correlation of thickness and Ñ change of the filter exposures with the direct exposure allows us to establish wavelength dependencies of modification rates. The modification rates of the PR beneath the MgF_2, sapphire and glass filter were reduced by a factor of ≈160, ≈370, and ≈2560, respectively, compared to the direct plasma exposure (see Tab. 3.1). For the $E_{ion}\leq25$ eV exposure of 248nm PR (Fig. 3.10(b)), we can see that in regime I trends follow the same trajectories as the MgF_2 filter exposure (glass and sapphire filter did not lead to relevant changes in film thickness and Ñ). Comparing these two conditions show that modification rates of the MgF_2 were reduced by a factor of ≈180 compared to the direct plasma exposure (see Tab. 3.1) – similar to our observations for 193nm PR. The strong reduction of

modification rates for the filter exposure highlights the importance of low wavelength Ar I emission for bulk material modifications.

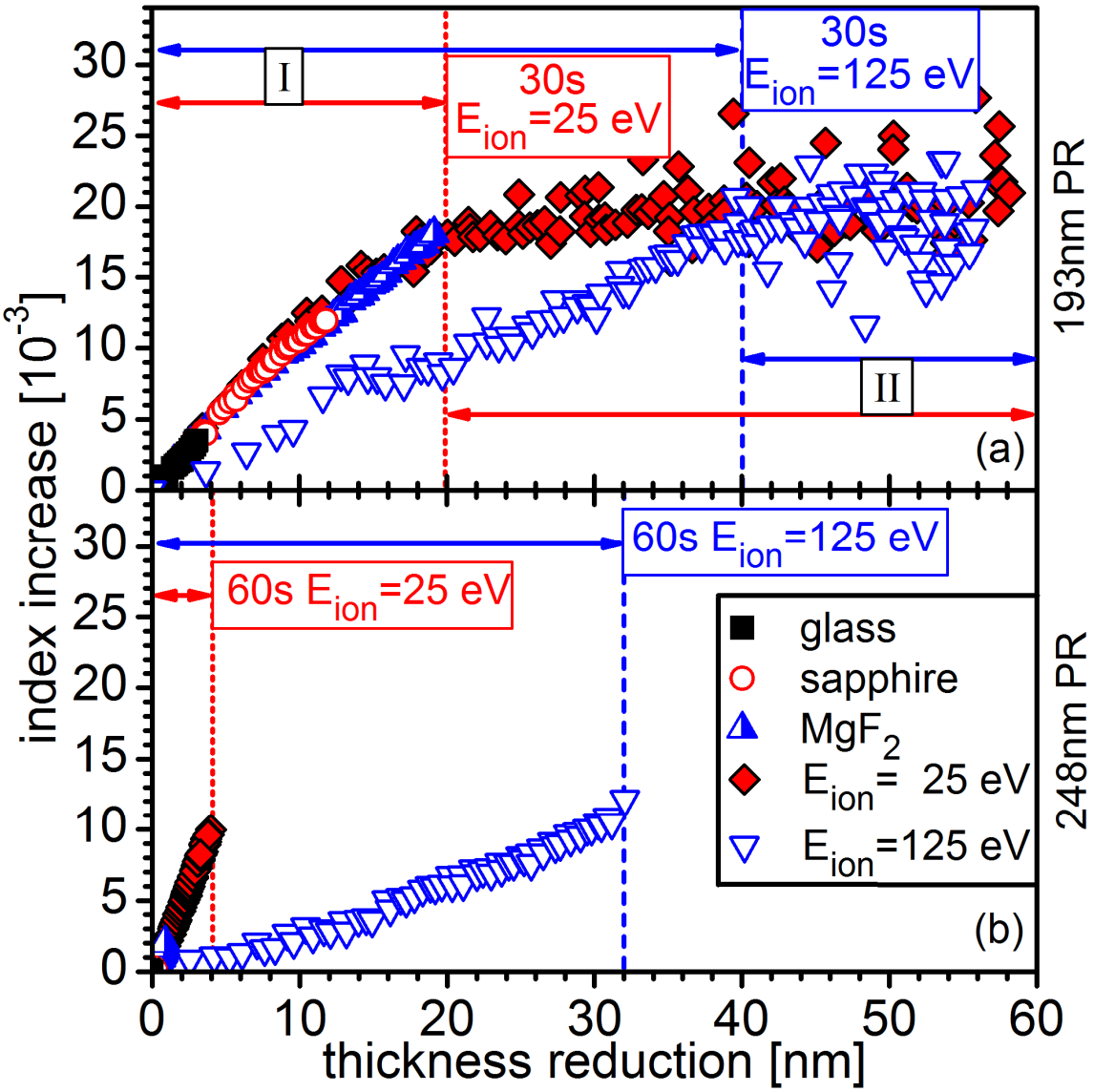

Figure 3.10: *Correlation of film thickness reduction and Ñ increase for exposures to plasma radiation (glass, sapphire, and MgF_2 filters) and direct plasma (E_{ion}≤25 eV and E_{ion}≤125 eV) of (a) 193nm PR and (b) 248nm PR. For plasma radiation and E_{ion}≤25 eV exposures, Ñ and film thickness changed at the same rate and modifications were UV/VUV-dominated. For E_{ion}≤125 eV, film thickness reductions increased due to ion-driven material removal.*

Plasma radiation exposure	Normalized UV modification rate	
	193nm PR	248nm PR
Direct plasma (E_{ion}≤25 eV)	1	1
MgF_2 filter	0.0063	0.0056
Sapphire filter	0.0027	0
Glass filter	0.0004	0

Table 3.1: *UV/VUV modification rates of PR beneath the MgF_2, sapphire and glass filters normalized to the direct exposure (E_{ion}≤25 eV) in an Ar plasma for 193nm PR and 248nm PR.*

Increasing the maximum E_{ion} to 125 eV causes ion-driven material removal from the film surface. For 193nm PR, Ñ saturates at ≈40 nm thickness reduction (dashed line), 20 nm more than for the low E_{ion} condition. This indicates that in regime I about 50% of the total film thickness reduction was due to UV/VUV-induced modifications of the material bulk. For 248nm PR Ñ remains unsaturated and only ≈10% of the total film thickness reduction after 60 s exposure was due to UV/VUV modifications.

In regime I, Ñ can increase through two pathways, 1) an increase in material density ρ or polarizability β (β∝ρ) and 2) a decrease in the molecular weight of the polymer repeat unit M, as expressed by the Lorentz-Lorenz equation (ε_0 is the permittivity of free space and N_A is Avogadro's number):[3.49]

$$\frac{\tilde{N}^2-1}{\tilde{N}^2+2}=\frac{4\pi N_A}{3\varepsilon_0}\frac{\rho\beta}{M} \qquad (3.1)$$

In our previous studies we have shown with Fourier transform spectroscopy measurements that 193nm PR experiences a moderate decrease of CH_x bonds and a large decrease of C=O, and C─O─C bonds (see Fig. 3.11(a)).[3.8-3.10, 3.14-3.16] The loss of C─O─C bonds is characteristic for decomposition of the ester bonds that keep the pendant groups attached to the polymer backbone and is followed by main-chain-scissioning leading to

shorter polymer chains. The C=O bonds decrease primarily in the spectral region characteristic for the lactone group. The decrease of CH_x bonds was attributed to removal of detached pendant groups such as lactone and adamantane.[3.8]

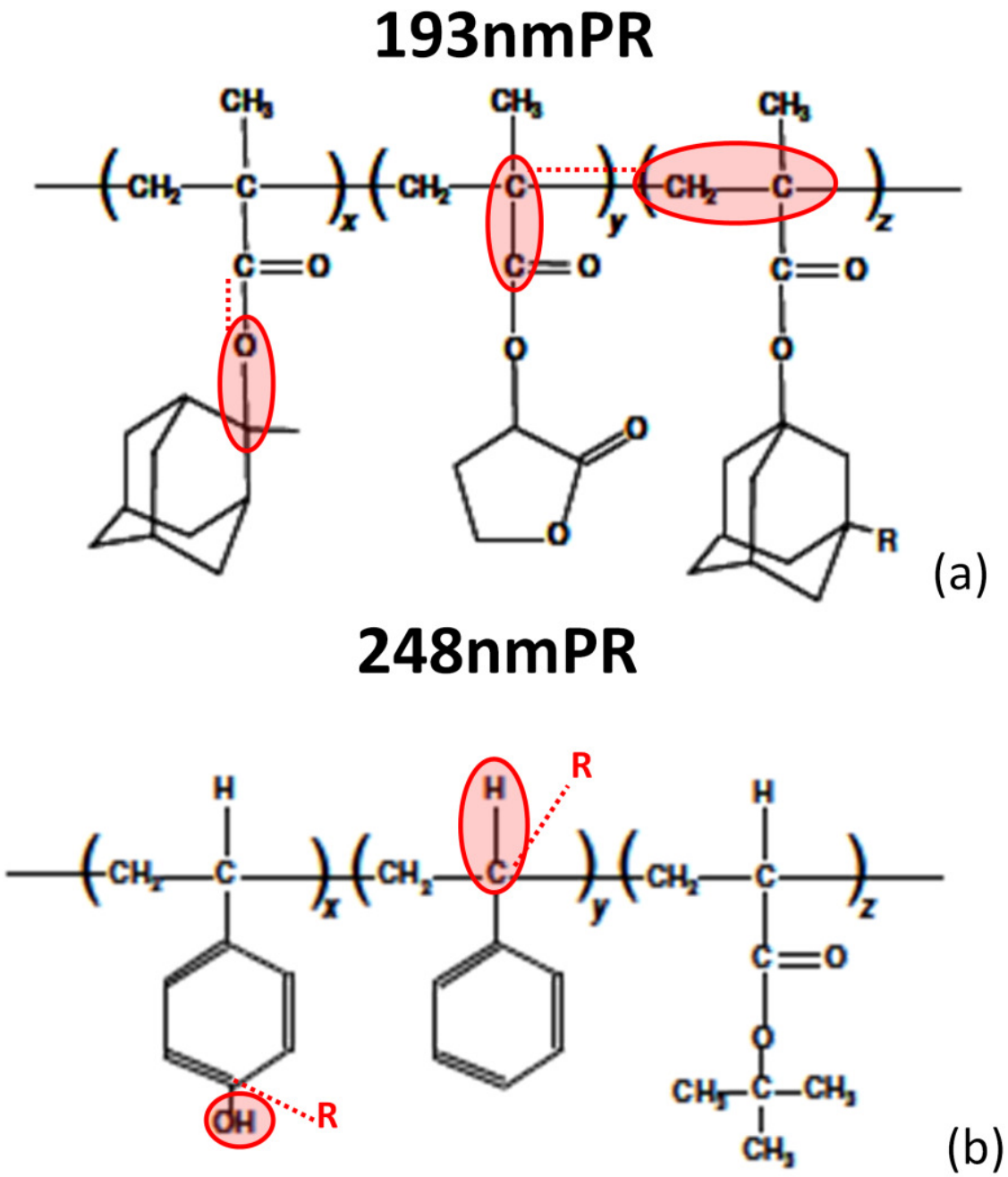

Figure 3.11: *Schematic of bulk material modifications of 193nm PR (a) and 248nm PR (b) by UV/VUV radiation indicating bond scissioning (circled) and re-bonding (dotted lines) in the polymer structure.*

Our recent mass spectroscopy measurements of photolysis products in a beam system showed that VUV exposure (147 nm) led to the release of H_2, CO, CO_2, lactone, and adamantane from the PR film.[3.10] These observations support both mechanisms leading to optical densification. First, ρ is likely to increase after removal of adamantane groups which occupy a relatively large volume per M. Secondly, β increases as a result of bond breakage and out-gassing, forming a more C═C bond-rich composition (C─H, C─O and C═O bonds have lower polarizability). Lastly, M decreases after detachment of polymer pendant groups and main-chain-scissioning.[3.50] This is in good agreement with film thickness changing linearly with optical density, which suggests film thickness reduction by densification and removal of photolysis products. For 248nm PR, bulk material modifications are dominated by cross-linking reactions and the increase in $\tilde{N}$ is mainly due to higher β values for the C-rich composition of the UV/VUV-modified layer (see Fig. 3.11(b)).

In regime II, film thickness reduction of 193nm PR takes place without much further increase in $\tilde{N}$. This can be explained as a steady-state condition where the maximum UV/VUV modification depth has been established (≈200 nm).[3.8] Initially, UV/VUV radiation depletes near surface oxygen bonds, subsequently leading to deeper photon penetration and more bond losses until the remaining near surface C─C bonds absorb the incident radiation.[3.51] Saturation of $\tilde{N}$ at the same level for the low and high E_{ion} condition ($E_{ion}\leq 25$ eV and $E_{ion}\leq 125$ eV) indicates that the bulk material modifications take place at rates exceeding material removal from the surface. This implies that the thickness of the UV/VUV-modified layer remains constant at the maximum modification depth once saturation is reached.

For 248nm PR Ñ saturation was not reached after 60 s exposure, even when material removal rates in the high E_{ion} condition were lower than those of 193nm PR by almost a factor of two. This shows that 248nm PR has significantly lower UV/VUV modification rates and plasma material interactions are dominated by ion effects.

The systematic differences in the type and dynamics of UV/VUV modifications described in this section are closely related to the surface roughness development. Figure 3.12 shows AFM measurement of the surface topography of 193nm PR ((a) and (b)) and 248nm PR ((c) and (d)) after 60 s exposure to the two direct plasma conditions. As expected, in the radiation-dominated low E_{ion} condition surface morphology and roughness of 193nm PR (Fig. 3.12(a)) and 248nm PR (Fig. 3.12(b)) remained relatively unchanged compared to the pristine material.[3.8] For the high E_{ion} condition, exposure to energetic ions and UV/VUV radiation at the same time led to synergistic roughness introduction and morphological changes for 193nm PR (Fig. 3.12(b)) and 248nm PR (Fig. 3.12(d)). Energetic ions led for both materials to formation of an ion-crust, introducing compressive stress in the surface layers by material densification.[3.13] However, 193nm PR undergoes much stronger roughening than 248nm PR which can be explained by material dependent differences in radiation sensitivity and modifications dynamics. We previously reported for a UV/VUV-insensitive polymer (PS) that surface roughness can be explained by wrinkling of the thin stressed ion curst on top of a compliant layer, and that the roughness amplitude increased for a soft underlayer material. The differences in roughness formation between 193nm PR and 248nm PR are in good agreement with this explanation. During formation of the ion crust 193nm PR undergoes rapid softening of the material bulk in a depth of ≈60 nm leading to reduced

stability of the surface and strong roughening. In contrast, 248nm PR is slowly modified to a depth of only ≈4 nm during ion-crust formation. The modified layer is stabilized by material hardening (cross-linking) and roughness formation is limited. This shows that differences in UV/VUV modifications (modification type and dynamics) between 193nm and 248nm PR determine the degree of synergistic roughness formation during plasma processing.

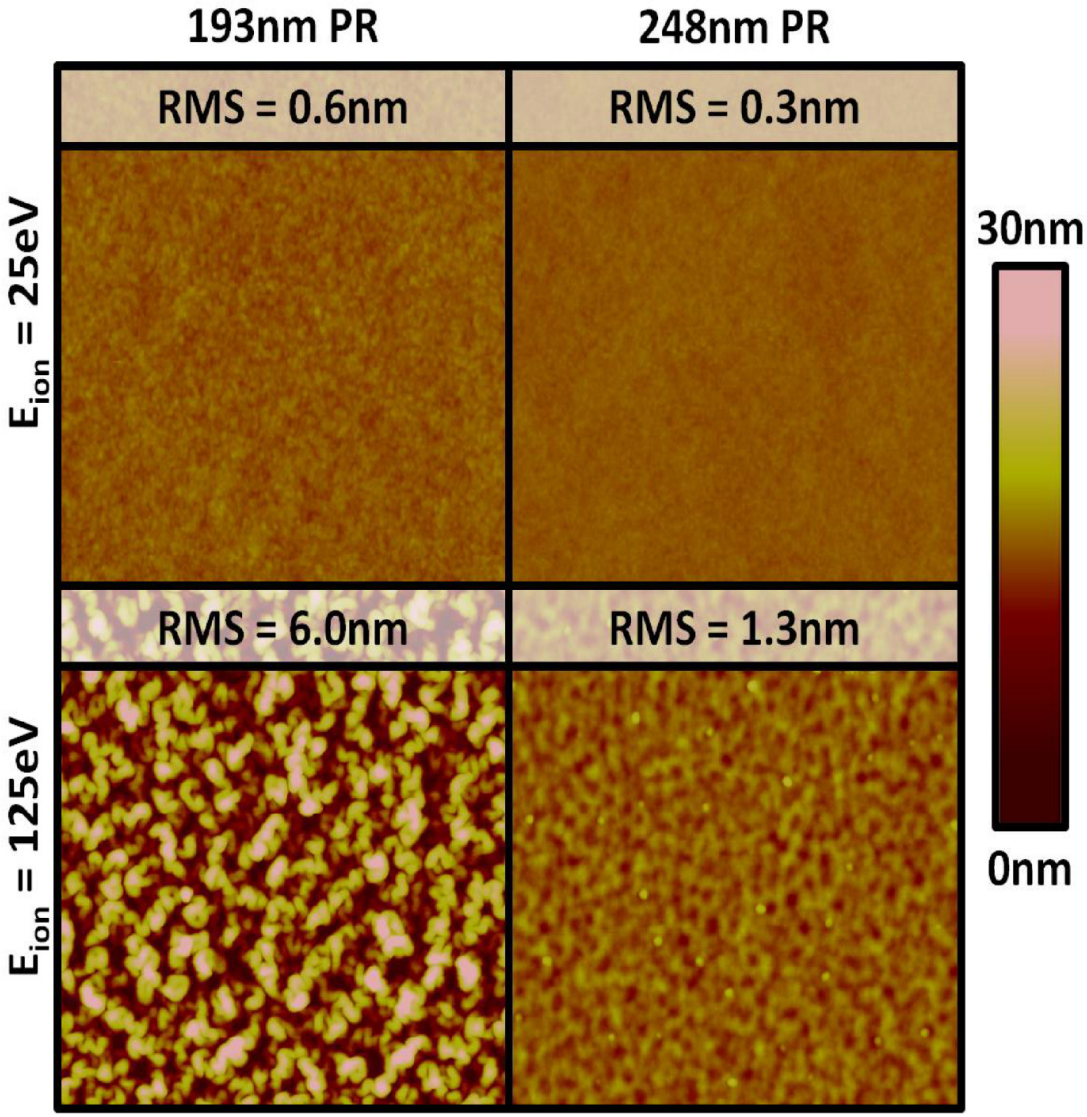

Figure 3.12: *Surface roughness and morphology of 193nm PR ((a) and (b)) and 248nm PR ((c) and (d)) after 60 s exposure to direct Ar plasma with low E_{ion} ((a) and (c)) and high E_{ion} ((b) and (d)).*

3.5 Conclusions

We studied dynamics of material modifications of 193nm PR and 248nm PR by Ar plasma in real-time to gain insight into the relative contribution of ions and UV/VUV radiation to the overall material modification.

In agreement with prior studies we found that 193nm PR and 248nm PR differ significantly in modification by plasma UV/VUV radiation (see Sec. 3.3.1). 248nm PR is highly radiation stable; bulk material modifications by UV/VUV radiation only occur for $\lambda<142$ nm (MgF_2 filter and direct exposures), and no saturation of the optical modification ($\tilde{N}$ increase) was reached within 60 s exposure time. 193nm PR is very sensitive to UV/VUV radiation and is progressively modified as photon wavelengths decrease from $\lambda>290$ nm to $\lambda<112$ nm. For plasma exposures at low E_{ion}, saturation of the $\tilde{N}$ increase was reached after ≈30 s. AFM characterization confirmed that exposure to UV/VUV radiation is not introducing surface roughness (RMS roughness = 0.3 nm to 0.6 nm).

The difference in the dynamics of radiation modification between 193nm PR and 248nm PR also directly impacts the timescales of concurrent material modifications during plasma exposure with energetic ions ($E_{ion}\leq125$ eV) (see Sec. 3.3.2). Bombardment of the PR surfaces within the first 3 s to 5 s plasma exposure leads to formation of an ion-crust, i.e. a ≈1.8 nm thick, C-rich, dense, and graphitic surface layer. Concurrently with the ion-crust formation, the PR material underneath is modified by plasma UV/VUV radiation and modifications are highly material dependent. For 193nm PR, we found that ≈1/3 of the change in $\tilde{N}$ had taken place during ion-crust formation, corresponding to an estimated UV/VUV modification depth of 60 nm. For 248nm PR, we found that, in the

same time period, less than 20% of the Ñ change after 60 s plasma exposure have taken place, corresponding to a UV/VUV modification depth of 4 nm at most.

Our results show that roughness development of PR materials is a synergistic effect of concurrent material modification by ions and UV/VUV radiation. Wrinkling theory describes roughness as a result of compressive stress in the ion modified surface layer on top of a soft layer underneath.[3.13] For the UV/VUV-sensitive 193nm PR, roughness was increased to ≈6 nm, as expected for a rapidly softened material bulk. For the UV/VUV-stable 248nm PR, roughness was limited, to ≈1 nm as can be explained by slow surface close material hardening.[3.13] This highlights the synergistic character of roughness formation by concurrent surface and bulk material modifications and dependencies of these effects on the type and dynamics of UV/VUV modifications. With the extension of 193nm PR materials to 193 nm immersion and possibly even extreme ultraviolet lithography, we believe that the understanding of the timescales of concurrent material modifications by ions and plasma UV/VUV radiation will contribute to improved pattern transfer processes with reduced roughness development. For future technology nodes, there seem to be two promising pathways to accomplish CD control below 2 nm: Improving masking materials by reducing the amount of UV/VUV radiation sensitive components (e.g. ester bonds), and introducing UV/VUV modifications before the pattern transfer process, i.e. curing, thus breaking the synergistic effect of concurrent modifications by ions and UV/VUV radiation.

Chapter 4

Characterization and mechanism of He plasma pretreatment of nanoscale polymer masks for improved pattern transfer fidelity

F. Weilnboeck, D. Metzler, N. Kumar, G. S. Oehrlein

Department of Material Science and Engineering, and Institute for Research in Electronics and Applied Physics, University of Maryland

R.L. Bruce, S. Engelmann, and N. Fuller

IBM T. J. Watson Research Center

Applied Physics Letters, in preparation

Abstract

Roughening of nanoscale polymer masks during plasma etching (PE) limits feature critical dimensions in current and future lithographic technologies. Roughness formation of 193nm photoresist (PR) is mechanistically explained by plasma-induced changes in mechanical properties introduced at the PR surface (~2 nm) by ions and in parallel in the material bulk (~200 nm) by ultraviolet (UV) plasma radiation. Synergistic roughening of polymer masks can be prevented by pretreating PR patterns with a high dose of He plasma UV exposure to saturate bulk material modifications. During subsequent PE, PR patterns are stabilized and exhibit improved etch resistance and reduced surface/line edge roughness.

4.1 Introduction

Photoresist (PR) materials such as methacrylate-based 193nm PR exhibit inherently high surface roughness (SR), line-edge roughness (LER) development and low etch-resistance during plasma-based transfer of patterns into other materials. Resulting limitations in pattern fidelity and etching selectivity (see review by Oehrlein *et al.*[4.1] and references therein) are unresolved problems and future requirements defined in the International Technology Roadmap for Semiconductors are currently not satisfied.[4.1, 4.2]

4.2 Roughening mechanism

Previously, we presented a model for PR roughness development based on wrinkling of a thin, stressed, ion-modified layer on top of a compliant layer and showed that bulk material modifications introduced by plasma UV radiation determine whether a polymer roughens.[4.3, 4.4] SR and LER are synergistically enhanced (or reduced) as radiation-induced softening (or hardening) of the polymer bulk interact with surface

modifications introduced by ion bombardment.[4.3-4.5] Energetic ion bombardment leads to *rapid (~3 s)* removal of H and O, formation of compressive stress (σ) by strong densification (density increase from 1 to ≈2-3 g/cm^3), and a substantially increased plane strain modulus ($\bar{E}_F$) in a thin (h=1.8 nm) ion-crust.[4.3, 4.6] UV radiation introduces, at *longer timescales (~30 s)* polymer-dependent changes in the bulk material plane strain modulus ($\bar{E}_S$) to a depth of up to 200 nm.[4.6, 4.7] The stability of the PR surface depends on the material elasticity of the ion- and UV-modified layer ($\bar{E}_F$ and $\bar{E}_S$) and is described by the critical compressive stress σ_W (Eqn. 4.1).[4.3] If $\sigma > \sigma_W$, the bi-layer system reduces σ by formation of wrinkles with characteristic wavelength (λ) and amplitude (A) (Eqns. 4.2 and 4.3).[4.3]

$$\sigma_W = 0.5\,\bar{E}_F^{\frac{1}{3}}\,\bar{E}_S^{\frac{2}{3}} \tag{4.1}$$

$$\lambda = 4.4\,h\,\bar{E}_F^{\frac{1}{3}}\,\bar{E}_S^{-\frac{1}{3}} \tag{4.2}$$

$$A = h\sqrt{1.9\,\sigma\,\bar{E}_F^{-\frac{1}{3}}\,\bar{E}_S^{-\frac{2}{3}} - 1} \tag{4.3}$$

For instance, SR of 193nm PR (see Fig. 4.1(a)) is enhanced by UV-induced material softening, e.g. resulting from polymer pendant group detachment and chain-scissioning (CS) reactions, and densification (removal of volatile photolysis products) reducing σ_W below σ.[4.6, 4.7] In contrast, SR of other polymers, is reduced (e.g. 248nm PR) or even eliminated (e.g. P4VP) by hardening (cross-linking) of the material bulk, increasing σ_W above σ.[4.4, 4.7]

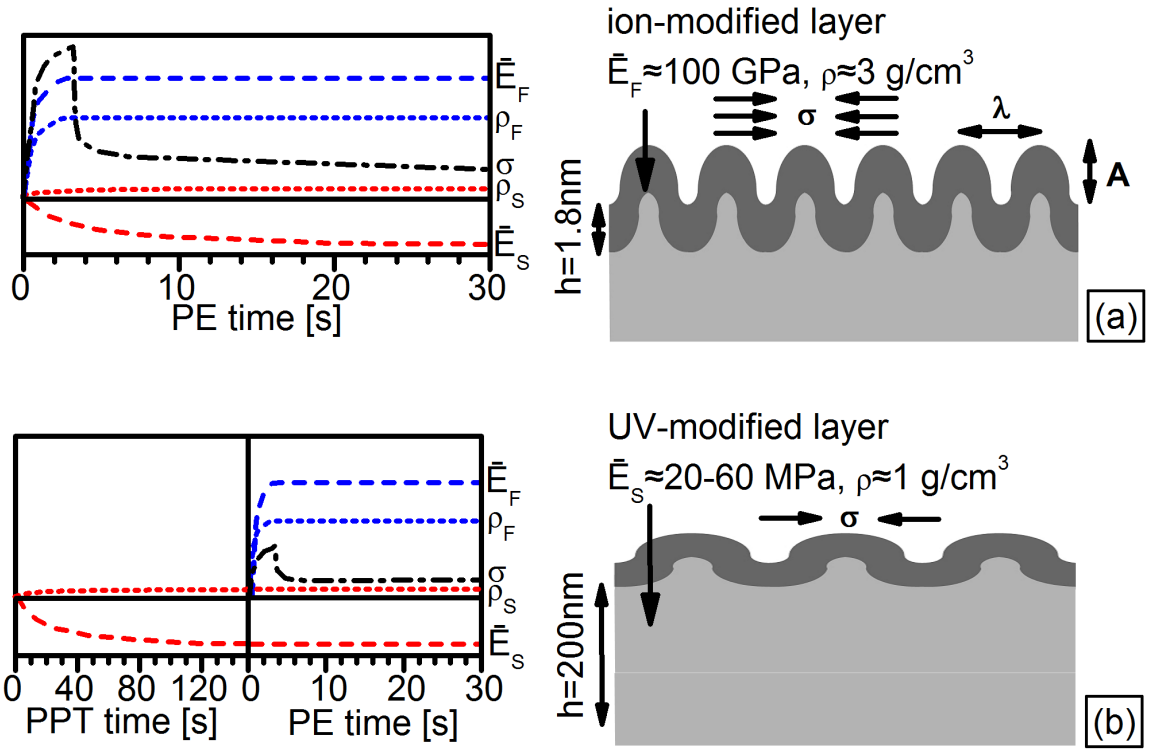

Figure 4.1: *Temporal evolution of material properties and corresponding schematics of rough surface morphologies for stressed bi-layer structures after (a) concurrent and (b) sequential introduction of UV and ion modifications.*

4.3 Plasma pretreatments

In addition to reducing roughness by selecting a cross-linking polymer, it seems possible to reduce or even eliminate SR and LER of materials that generally roughen by sequentially introducing UV and ion modifications (see Fig. 4.1(b)). We expect that UV irradiation at a dose sufficient to achieved bulk modification saturation will soften and densify the material without stress – since not constrained by the ion-crust introduced during conventional plasma etch, allowing to stabilize the material and prevent synergistic roughening during the subsequent plasma etch (PE). Consistent with this expectation, Ar and HBr plasma pretreatments (PPT) have shown promise to reduce roughness after plasma etch (PE), although the underlying mechanism leading to improvements remained unclear.[4.8] Here we demonstrate the proposed approach and

mechanism of stabilizing a PR using a radiation-dominated He PPT. Improvements in roughness formation are quantified by scanning electron microscopy (SEM) and tapping mode atomic force microscopy (AFM), and mechanistically discussed based on Fourier-transform infrared spectroscopic (FTIR), and real-time ellipsometric (632.8 nm) measurements.

4.4 Experimental

To reduce plasma material interactions to the most fundamental plasma components, ions and characteristic UV emission, we used the following approach: For the PPT we exposed PR materials for 0-120 s to a He plasma (800 W source power, $E_{ion} \leq 25$ eV, 100 mTorr pressure, 60 sccm gas flow). These parameters were chosen because high power He plasma has strong photon emission at a low wavelength (58.4 nm [4.9]) and surface modifications by ions are strongly reduced by low mass and ion energy, and enhanced ion-collision processes in the plasma sheath at high pressure. For PE we exposed PR materials for 60 s to Ar plasma (200 W source power, $E_{ion} \leq 125$ eV, 20 mTorr pressure, 55 sccm gas flow). This condition was chosen because Ar introduces changes in roughness similar to typical plasma etching processes without deposition of a FC surface layer that would increase the complexity of mechanistic analysis.[4.1] The work was performed using an inductively coupled plasma (ICP) system and materials that have been described previously.[4.10, 4.11] The base pressure achieved before processing was below 2×10^{-6} Torr and the temperature of PR samples (25x25 mm^2) was stabilized by substrate cooling (10 ^{o}C) during plasma processing. The materials studied were blanket 193nm PR films (~400 nm thick) and 193nm PR trench patterns (120 nm trench, 240 nm

pitch, 140 nm high) with 50 nm bottom antireflection coating. Both materials contained photoacid generator and base and were spin-coated onto Si.

4.5 Pattern morphology

Figure 4.2 shows top-down SEM images of trench pattern array corners (a)-(d) together with extracted changes in critical dimensions (CD), LER, and LWR (e). Compared to the pristine pattern (Fig. 4.2(a)), an increase in CD, along with severe LER and LWR, was introduced as a synergistic effect by exposure to energetic ions and UV radiation during PE at the same time (Figs. 4.2(b) and 4.2(e)). Exposing the pattern to UV radiation by performing a 60 s PPT led to feature shrinkage (decreased CD by ~13 nm) and smoothing (reduced LER and LWR) of PR features (Figs. 4.2(c) and 4.2(e)). During PE following 60 s PPT (Figs. 4.2(d) and 4.2(e)) we observed that CD remained relatively unchanged compared to the PPT. LER and LWR were significantly reduced compared to patterns after PE without PPT.

Comparing the feature surfaces and pattern-free areas after PE (Fig. 4.2(b)) and after PPT followed by PE (Fig. 4.2(d)) clearly shows that PPT did not only improve LER and LWR but also led to strong reduction of SR. The similarities in roughness for surfaces and sidewalls are in good agreement with the general understanding of LER and LWR being introduced by a micro-masking effect where ions transfer SR into the sidewalls.[4.12] This indicates that a mechanistic explanation of roughness reduction by PPT requires an in-depth understanding of SR formation.

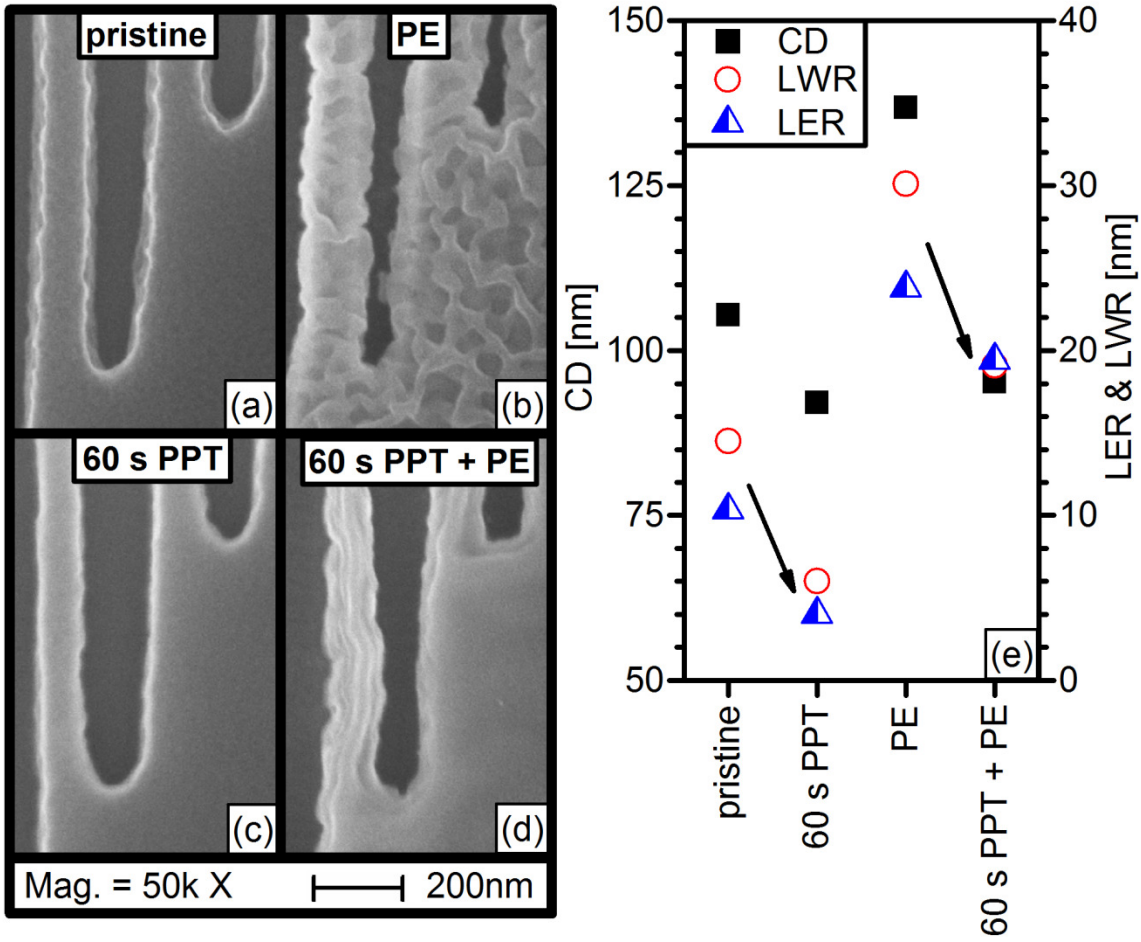

Figure 4.2: *SEM images of PR trench pattern array corners for pristine material (a), 60 s PPT (b), PE (c), and 60 s PPT followed by PE (d). Characteristic changes in CD, LER, and LWR are presented in (e).*

4.6 Surface morphology

Changes in surface morphology and SR of blanket films were characterized by AFM after PPT and 0-120 s PPT followed by PE (see Fig. 4.3). He PPT did not introduce any changes in surface morphology and surfaces remained smooth (Fig. 4.3(a)). Figures 4.3(b)-(d) show that increasing PPT time progressively reduces A (RMS roughness) and increases λ (average wavelength from power spectral density distribution) during PE. The temporal evolution of A and λ for 0-120 s PPT followed by PE (Fig. 4.3(e)) clearly shows that changes in SR and morphology introduced during PPT strongly depend on PPT time. For 90-120 s PPT we observed formation of surface defects (bubbles) during PE, resulting from buckle delamination of the ion-modified surface layer as will be discussed elsewhere.[4.13]

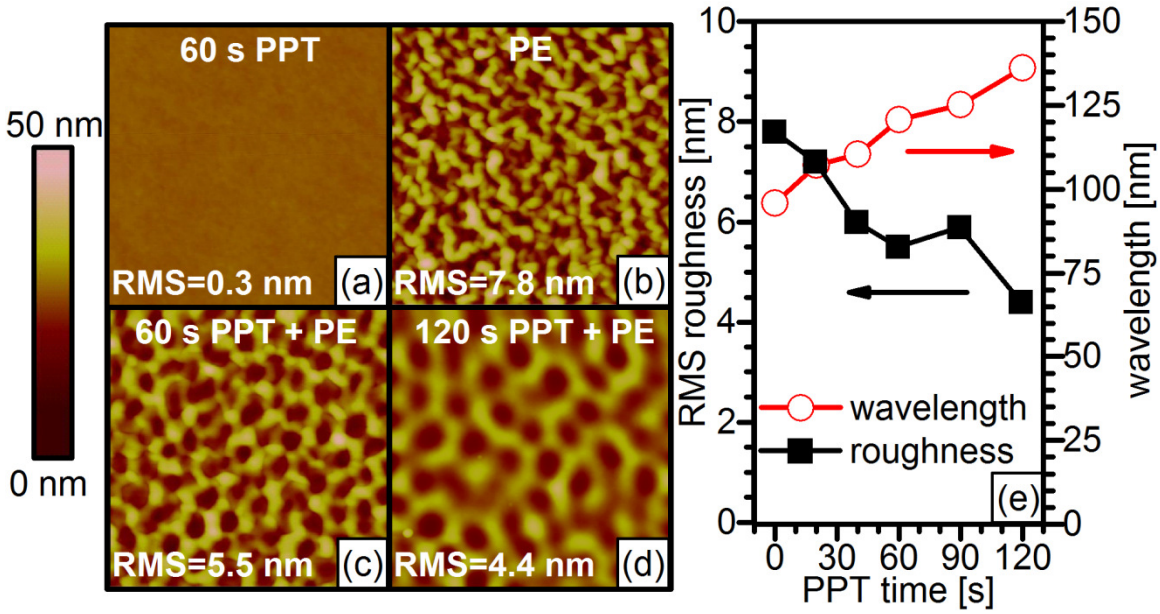

Figure 4.3: *AFM images (1x1 μm^2) of PR topography after 60 s PPT (a), PE (b), 60 s PPT + PE (c), and 120 s PPT + PE (d). RMS roughness and characteristic feature wavelength were extracted for surfaces after 0-120 s PPT followed by PE (e).*

4.7 Mechanical material properties

For quantification of changes in material mechanical properties, we evaluated AFM measurements using Eqns. (4.1)-(4.3) keeping h and $\bar{E}_F$ constant at 1.8 nm and 100 GPa, respectively. Figure 4.4 shows, in agreement with our model (see Fig. 4.1), that the decrease in A is associated with reduced σ (Fig. 4.4(a)) and that the increase in λ with PPT time is based on a reduction of $\bar{E}_S$ (Fig. 4.4(b)). Using the extracted values for $\bar{E}_S$ we estimated σ_W and found that $\sigma > \sigma_W$, independent of PPT time. The changes in $\bar{E}_S$ and σ were substantiated by characterizing bulk material modifications with FTIR and changes in film thickness and optical properties with *in-situ* ellipsometry.

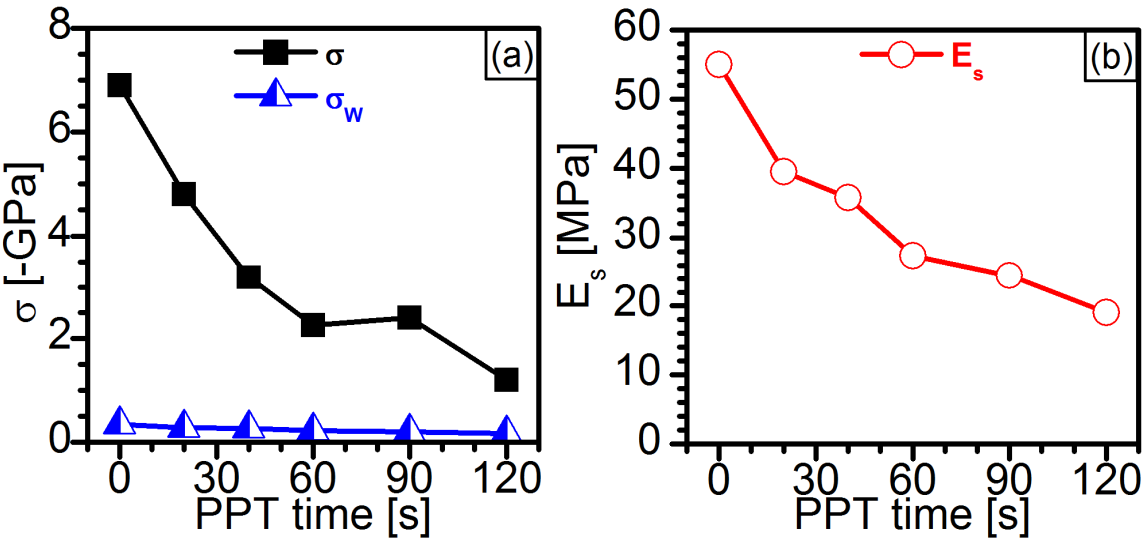

Figure 4.4: *Mechanical material properties after 0-120 s He PPT and PE extracted from AFM measurements: (a) interfacial compressive stress (σ), and critical stress for wrinkling (σ_W), and (b) plane strain modulus of the UV-modified layer ($\bar{E}_s$).*

4.8 Bulk material modifications

FTIR measurements of bulk material modifications after 0-120 s PPT showed rapid absorbance loss of C-O-C, C=O, and CH_x bonds at the exposure start with modifications saturating for long exposure times.[4.7] Bulk material modifications of films

exposed to 0-120 s He PPT followed by the PE were all saturated at levels similar to long PPT. The change in composition (loss of 38% of C-O-C bonds, 31% of C=O bonds, and 15% of CH_x bonds for 120 s PPT) is characteristic for detachment and partial removal of polymer pendant groups.[4.7] These observations are in good agreement with mass spectroscopic measurements during UV-radiation exposures, which show removal of adamantane, lactone, and other photolysis products such as H_2, CO and CO_2.[4.14] In addition to pendant group removal, we believe that CS of the polymer backbone occurred as a secondary reaction following ester bond cleavage and that some of the detached pendant groups remained in the PR film. Lower polymer molecular weight (M_W) and detached pendant groups, acting as a plasticizer, explain the reduced $\bar{E}_S$.[4.5, 4.7, 4.14]

4.9 Film thickness and optical properties

Ellipsometric measurements during PPT showed that film thickness decreased up to 39 nm (≈ 10% of total film thickness) and the index of refraction increased by up to 0.024, following a temporal evolution similar to bulk material modifications characterized with FTIR. The changes in film thickness are explained by removal of photolysis products and stress-free densification of the UV-modified layer (not constrained by the ion-crust).[4.6, 4.14] The increase in $\tilde{N}$ is based on a decrease in M_W (pendant group detachment and CS), higher polarizability (more C-C bonding after C-O-C, C=O, and CH_x bond loss), and by an increase of atomic density (removal of bulky adamantyl groups).[4.6] During PE without PPT, formation of the ion-crust strongly increased $\tilde{N}$ by 0.061. The strong differences in material densification during PE between the ion-modified surface and the pristine PR underneath increased the stress σ above the critical level.

For experiments where the PR materials were exposed to PPT before PE, thickness reduction and Ñ increase during PE were reduced to 26 nm and 0.053, respectively. The reduced increase in Ñ is explained by a lower degree of densification after pre-densification during the PPT leading to reduced σ. The increased etch-resistance of pretreated films during PE is expected because of their reduced oxygen content.[4.15] Comparing the thickness reduction after PE with the total thickness reduction after 20-60 s PPT followed by PE indicates that PPT will not have a negative influence on the total thickness change during transfer of patterns into the underlying material.

4.10 Summary

In summary, we presented data in support of a model for SR development of PR in Ar plasma and showed that He PPT with strong UV-emission can stabilize nanoscale polymer surface features and reduce SR, LER, and LWR during subsequent PE. Roughness formation is based on concurrent UV modification of the polymer bulk and polymer surface modification by ions at different time scales which causes an instability in the bi-layer system. The synergistic surface/feature roughness development can be reduced by introducing UV-induced changes of the polymer bulk at saturation level prior to plasma etch. This pre-densification of the polymer and concomitant changes in mechanical properties serve to stabilize the PR material during PE. Total thickness reduction after 20-60 s PPT and PE was only marginally increased due to increased etch resistance after removal of H- and O-containing photolysis products during PPT. We conclude that an understanding of synergistic effects in plasma processing and rational design of process changes to address these can improve plasma-based pattern transfer processes and enable reduced SR, LER, and LWR of nanoscale features.

Chapter 5

Study of Ti etching and selectivity mechanism in fluorocarbon plasmas for dielectric etch

F. Weilnboeck, E. Bartis, S. Shachar, and G. S. Oehrlein

Department of Materials Science and Engineering and Institute for Research in Electronics and Applied Physics, University of Maryland

D. Farber, T. Lii, and C. Lenox

Texas Instruments

Journal of Vacuum Science and Technology B, submitted

Abstract

For the next generation of integrated circuit fabrication, metallic masking layers are gaining interest for plasma-based pattern transfer into low-k materials driven by expected improvements of etching selectivity (ES) and low-k damage. The present work is aimed at improving our understanding of metallic hardmask erosion in fluorocarbon (FC) plasmas. We studied the behavior of Ti in CF_4/Ar and C_4F_8/Ar discharges using conditions relevant to pattern transfer processes into organosilicate glass (OSG), a reference low-k material investigated in parallel. We examined various material erosion stages and determined the dependencies of etch rates (ER) and ES on the following plasma parameters: self bias voltage (50-150 V), processing pressure (20-60 mTorr) and %CF_4 (10-30%) in CF_4/Ar discharges, and O_2 addition (0-10%) and N_2 addition (0-20%) to C_4F_8/Ar discharges. Erosion behavior and ER were characterized by real-time ellipsometric measurements and multilayer optical modeling. These measurements were complemented by x-ray photoelectron spectroscopy (XPS) to study the surface composition. The impact of plasma parameter changes were investigated by comparing ER and corresponding ES (OSG ER/Ti ER). During the erosion of Ti, the initially oxidized film surface was transformed into a TiF_x layer ($x \approx 3$) covered by a FC film. The FC film thickness strongly depended on the FC feed gas and was significantly thicker for the C_4F_8-based etch (1.5 nm) than for the CF_4-based etch (0.9 nm). Ti erosion was found to be dependent on the energy deposited on the film surface by ion bombardment and to exponentially decrease with increasing FC film thicknesses. For thin FC films (<1 nm), erosion was ion driven, i.e. 'chemical sputtering', and, for thick FC films (>1 nm), erosion was limited by the amount of F that could diffuse through the FC layer to the Ti

interface. In contrast to organic masking materials, Ti hardmasks have lower ES for the more polymerizing C_4F_8-based discharges than for CF_4-based discharges. This can be explained by the consumption of the limited supply of F at the OSG surface by C and H impurities, which form volatile CF_4 and HF etch products. For thin FC films and low ion energy deposition by ion bombardment, ES up to 15 have been achieved.

5.1 Introduction

For the next generations of integrated circuits, new materials and approaches are needed for the fabrication of via and interconnect features. Currently, dual damascene fabrication processes use inorganic masks (SiO_2 and SiC) for transferring patterns into low-k dielectric materials such as organosilicate glass (OSG).[5.1] However, low etching selectivity (ES), severe faceting, and low-k damage are common problems for pattern transfer processes using SiC and SiO_2 masks.[5.1] Novel organic and inorganic masking materials will have to be introduced for future technological generations. The most promising hard mask candidates are metallic masks such as Ti, TiN, Ta and TaN.[5.1] Due to the strong difference in the nature of metallic layers and dielectric materials, i.e. material density and energy required to volatilize etch products, we expect metallic masking materials to be superior in ES to Si-based masks. Few systematic studies have investigated the performance of metallic hardmasks for pattern transfer into dielectric materials; most of the available work has focused on TiN.[5.1-5.3] In this study we investigated basic considerations, etching mechanisms, and erosion properties of Ti metal hardmasks for pattern transfer into low-k materials using fluorocarbon (FC)/Ar plasmas.

We report the results of this study in two parts. The present article describes the temporal evolution of Ti erosion behavior and plasma parametric dependencies using CF_4/Ar and C_4F_8/Ar plasmas. Differences in the Ti and OSG erosion mechanisms are discussed and guidelines are provided for improving ES. The companion article compares Ti and TiN etching mechanisms in FC/Ar plasmas and discusses post-etch surface reactions.

This article is organized as follows: After describing the experimental procedures in Sec. 5.2, we present in Sec. 5.3.1 real-time measurements of Ti erosion behavior using *in-situ* ellipsometry and x-ray photoelectron spectroscopy (XPS). We compare in Sec. 5.3.2 Ti and OSG etch rates (ER) in CF_4- and C_4F_8-based plasmas with varying self-bias voltage (V_{SB}). In Secs. 5.3.3 and 5.3.4 we investigate the impact of changes in chamber pressure and $\%CF_4$ in CF_4/Ar plasmas as well as the impact of O_2 and N_2 addition to C_4F_8/Ar plasmas, respectively. In Sec. 5.4, we discuss the fundamental differences in the erosion behavior between Ti and OSG, and ES.

5.2 Experiment

5.2.1 Description of materials

The materials used in this study were Ti films prepared by physical vapor deposition (PVD) and spin coated OSG. Both materials were deposited on ~38 nm of thermally grown SiO_2 on Si substrates to increase the sensitivity of ellipsometric measurements during erosion. The OSG had a composition of 28 at.% C, 33 at.% H, 14 at.% Si and 25 at.% O, and a density of ~1.2 g/cm^3.

5.2.2 Plasma processing

The two inductively coupled high-density plasma reactors used in this study have been described in previous publications.[5.4,5.5] In the 125 mm substrate diameter reactor, a planar coil placed on top of a quartz window was powered through an L-type matching network at 13.56 MHz with a power supply (0-2000 W).[5.4] The plasma induced by the electromagnetic field was confined to a narrow region 2–3 cm below the quartz window. An additional radio frequency bias power supply (0–1000 W) independently controlled the V_{SB} at 3.7 MHz. The resulting ion energies (E_{ion}) for singly-charged ions corresponded to the sum of the applied V_{SB} and the plasma potential (~25 V) in eV.[5.6] The chamber base pressure before processing each sample was ~5x10^{-6} Torr. This reactor is equipped with an *in-situ* ellipsometer which was used to measure changes in film thickness and optical properties during plasma processing.

The 300 mm substrate diameter reactor is similar to the previously described reactor except the radio frequency bias power supply is operated at 13.56 MHz.[5.5] The base pressure before processing each sample was ~5x10^{-5} Torr due to the larger chamber volume. This reactor has the capability to vacuum transfer samples to a surface analysis

system. For both reactors the processing pressure was controlled using an exhaust throttle valve. The temperature of the bottom electrode was kept at 10 °C by circulating a cooling liquid. During plasma processing, samples were bonded to the bottom electrode using thermal grease between the sample and electrode. These steps were necessary to rule out contributions from temperature effects.

In this study, two FC-based gas chemistries were investigated, CF_4/Ar and C_4F_8/Ar, which are often used for high aspect ratio and contact hole etching of dielectrics.[5.7-5.9] The anchor condition of the CF_4/Ar discharge was: 20%CF_4/80%Ar, 400 W source power, -100 V V_{SB}, 40 mTorr pressure, and 50 sccm total gas flow rate. The anchor condition of the C_4F_8/Ar discharge was: 10%C_4F_8/90%Ar, 300 W source power, -100 V V_{SB}, 10 mTorr pressure, and 50 sccm total gas flow rate. The lower source power in the C_4F_8/Ar anchor condition was selected to achieve similar ion current densities (ICD) as the CF_4/Ar anchor condition.

Specific processing parameters in the CF_4/Ar discharge examined in this work include: %CF_4 (10%, 20%, and 30%), pressure (20 mTorr, 40 mTorr, and 60 mTorr) and V_{SB} (-50 V, -100 V, and -150 V). For the 60 mTorr discharge the total gas flow was increased to 100 sccm. Processing parameters in the C_4F_8/Ar discharge include V_{SB} (-50 V, -100 V, and -150 V), O_2 addition (0%, 5%, and 10% by gas flow rate), and N_2 addition (0%, 10%, and 20% by gas flow rate). Before each experiment, the chamber was cleaned using O_2 plasma followed by a one-minute plasma chamber conditioning step applying the conditions of the discharge being investigated.

5.2.3 Characterization

Material characterization was performed in real-time by *in-situ* ellipsometry and after processing by angle resolved vacuum-transfer XPS. The ellipsometric measurements were performed with a HeNe ellipsometer in the polarizer-rotating compensator-sample-analyzer configuration at a wavelength of 632.8 nm and an angle of incidence of ~72 ^{o}. Multilayer modeling of the metallic masking layer on top of ~38 nm SiO_2 on a Si substrate allowed us to extract individual film thicknesses and ER. The optical material properties used were $\tilde{N}$=3.866-0.028*i* for Si, $\tilde{N}$=1.457-0*i* for SiO_2, $\tilde{N}$=3.23-3.62*i* for Ti, and $\tilde{N}$=2.2-0*i* for TiO_2.[5.10]

XPS analysis provided information on compositional changes of the film surface. The analysis was performed with a Vacuum Generators ESCA Mk II surface analysis chamber at an electron takeoff angle of 90 ° (deep probing depth) and 20 ° (shallow probing depth) relative to the surface. The spectra presented were collected at 90 °. Electrons were excited using a non-monochromatic Mg-Kα source (1253.6 eV). The pass energy of the hemispherical analyzer was set to 20 eV.

High resolution Ti 2*p*, C 1*s*, F 1*s*, N 1*s*, O 1*s* and Si 2*p* spectra were decomposed using a least square fit with 50/50 Gaussian-Lorentzian peaks after Shirley background correction and charge compensation by calibrating the binding energy (BE) position of the C-C peak in the C 1*s* spectrum to 285 eV.[5.11] Charge correction of the Ti 2*p* spectra was performed separately due to differential charging effects[5.12] , so BE are referenced to the metallic Ti peak at 453.8 eV.[5.13] The spectral decomposition of high resolution Ti 2*p* spectra for Ti is challenging due to the complexity of the spectra and inconsistency among reported values in literature (see review by Prieto *et al.*[5.14]).

The fitting procedure presented was established by decomposing Ti 2*p* spectra and is summarized in Tab. 5.1; findings (Sec. 5.3.1.2) are in good agreement with relevant literature.[5.15-5.20] The resulting BE for Ti and its oxides were kept constant. The BE shifts of the oxides with respect to metallic Ti are identical to those established by Wolff et al.[5.15]: 1.2 eV, 3.0 eV, and 4.9 eV for TiO, Ti_2O_3, and TiO_2, respectively. The TiF_x BE shift of 7.25 eV is in good agreement with the work by Robey *et al.*[5.16] and was constrained to a range of ±0.2 eV accounting for effects such as differences in FC layer thickness, differential charging, and differences in the degree of Ti fluorination, i.e. TiF_x with x=1-4.

Ti-bond	BE	SOS
Ti	453.8 eV	6.1
TiO	455 eV	5.7
Ti_2O_3	456.8 eV	5.7
TiO_2	458.7 eV	5.7
TiF_x	461.05±0.2 eV	5.8

Table 5.1: *XPS binding energy (BE) assignments and spin-orbit splitting (SOS) for Ti 2p spectra.*

The spin orbit splitting (SOS) was kept at 6.1 eV for Ti, 5.7 eV for Ti-oxides and 5.8 eV for TiF_x, in agreement with Siemensmeyer *et al.*[5.17]. For fluorinated Ti surfaces, area ratios of the $p_{3/2}$ to $p_{1/2}$ peaks were kept constant at 2.2:1. Deviations from the theoretical $p_{3/2}$ to $p_{1/2}$ peak area ratio of 2:1 originate from errors in the background subtraction, an effect discussed in detail by others.[5.15, 5.17, 5.18] Peak full widths at half maximum (FWHM) of the $p_{1/2}$ peaks were kept higher than the $p_{3/2}$ FWHM by a factor of 1.4 for Ti and all Ti-oxides, and 1.1 for TiF_x. The peak broadening of the $p_{1/2}$ peak with respect to the $p_{3/2}$ is related to the Coster-Kronig process found in 3*d* transition metals.[5.19]

The surface composition was calculated from data obtained at 90 ° using the integrated peak areas of Ti 2*p*, N 1*s*, O 1*s*, C 1*s*, F 1*s* and Si 2*p* elemental spectra after

applying atomic sensitivity factors of 1.80, 0.42, 0.66, 0.25, 1.00 and 0.27, respectively.[5.20] Estimation of FC layer thicknesses was performed by evaluating angle resolved measurements with an attenuation model following Rueger *et al.*[5.21]. The attenuation model takes advantage of the attenuation of signals from the material bulk by the FC layer on the film surface and the increased effective thickness of the FC layer for electrons escaping at a shallow take-off angle (here, 20 ^{o}). The attenuated signal used in this work is from the Ti 2*p* spectrum. The attenuation length of the FC layer was calculated using Cumpson and Seah's CS2 equation[5.22]. For light elements such as F, C, N, and O, calculated attenuation lengths are largely independent of atomic composition but change strongly with material density. For our calculations of the FC film attenuation length, we used a medium density polymer with ρ=1.5 g/cm^3. The resulting attenuation length was 2.5 nm.[5.21]

Additionally, ICD were estimated by monitoring changes in the bias power while keeping the V_{SB} constant. The ICD is calculated by dividing the bias power by the V_{SB} and chamber substrate area. Furthermore, trends in F concentrations in the plasma discharge can be qualitatively monitored by optical emission spectroscopy (OES) by measuring the relative intensities of a characteristic F (685.6 nm) and Ar (706.7 nm) emission line.[5.1]

5.3 Results

5.3.1 Erosion stages of Ti

The temporal evolution of Ti etching in FC plasmas was measured ellipsometrically and was complemented by time-resolved surface characterization by XPS. We identified three characteristic erosion stages (see Fig. 5.1): (a) removal of oxidized Ti surface layers, (b) steady state erosion with a strongly fluorinated Ti surface covered by a FC film, and (c) erosion of the SiO_2 underlayer with some Ti remaining at the surface. We observed these characteristic erosion stages for all plasma conditions investigated here and will exemplify the temporal evolution with the CF_4/Ar anchor condition.

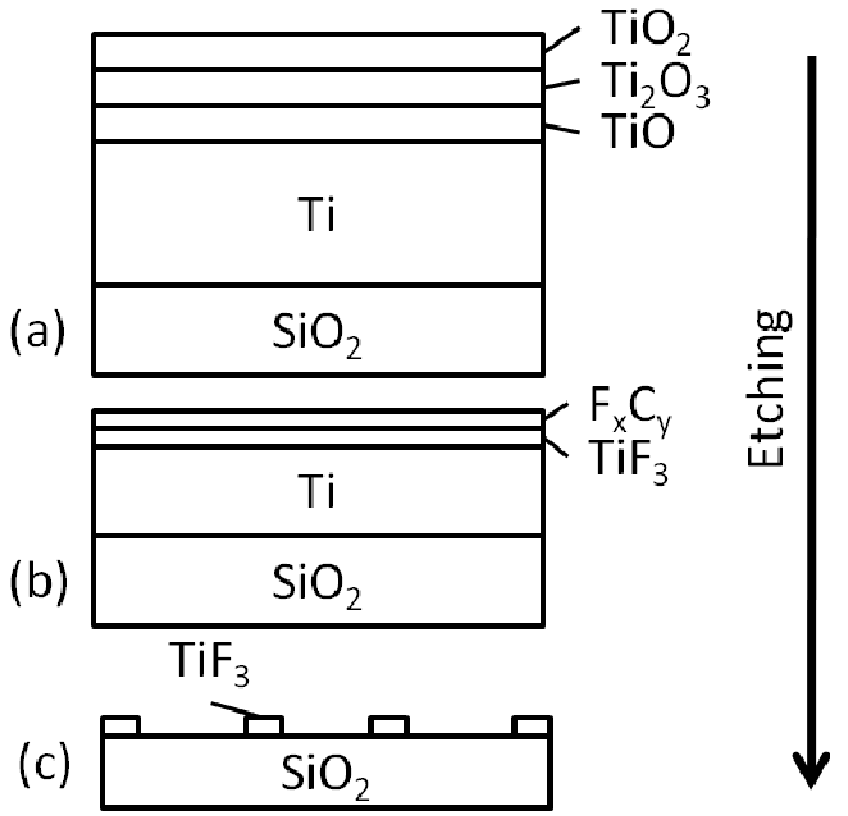

Figure 5.1: *Schematic of Ti hardmask erosion stages: (a) before processing, (b) during steady-state hardmask erosion, and (c) during etching of the SiO_2 layer underneath the Ti film.*

5.3.1.1 Real-time ellipsometric measurements

Figure 5.2 shows the ellipsometric measurements during etching of Ti (black circles) together with two ellipsometric multilayer models. The models account for Ti with a TiO_2 top layer for the erosion start and Ti with a FC surface layer for steady state erosion, as described in Fig. 5.1. Both models simulate those layers on top of the Si substrate with a SiO_2 layer between the substrate and the Ti film. Here, we describe the model starting with the Si substrate and subsequently add the individual layers.

The reference point of the Si substrate is at $\Psi \approx 7.0^{\circ}$ and $\Delta \approx 178.2^{\circ}$. On top of the Si substrate, SiO_2 layers are modeled in 1 nm increments (black open squares, solid black line) shown in Fig. 5.2 between 29 nm and 43 nm. On top of 38 nm SiO_2 we simulate metallic Ti layers in 1 nm increments (red open triangles, solid red line). This simulation provides a near-perfect fit of the experimental measurement for metallic Ti layers up to a thickness of 13 nm. This stage of erosion will be referred to as steady state erosion and is used to extract Ti ER. Ti films thicker than 13 nm correspond to the time frame between erosion start and steady state erosion where a significant deviation from the metallic Ti simulation can be observed. This deviation can be explained by the removal of the native surface oxide before steady state erosion is reached. The presented multilayer model includes simulations for TiO_2 layers up to 2 nm thickness in 0.5 nm increments (dashed blue lines) on top of 10–15 nm thick metallic Ti layers.

Initially, erosion closely follows the simulation for decreasing TiO_2 thickness at constant Ti thickness (solid blue line), which indicates that oxide removal dominates. Subsequent erosion shows simultaneous removal of TiO_2 (change along solid blue line) and metallic Ti (change along dashed blue line) and/or removal of sub-stoichiometric Ti-

oxides. It can be seen that the simulations describe the removal of the oxidized surface well during the initial erosion stage. This is in good agreement with our expectations that TiO_2 is the most common and stable oxidation state of Ti. Other oxidation states such as Ti_2O_3 and TiO have been reported to form at interfaces between Ti and TiO_2.[5.18] These sub-stoichiometric Ti-oxides are not taken into account here due to the lack of available optical properties in literature, but will be discussed in Sec. 5.3.1.2.

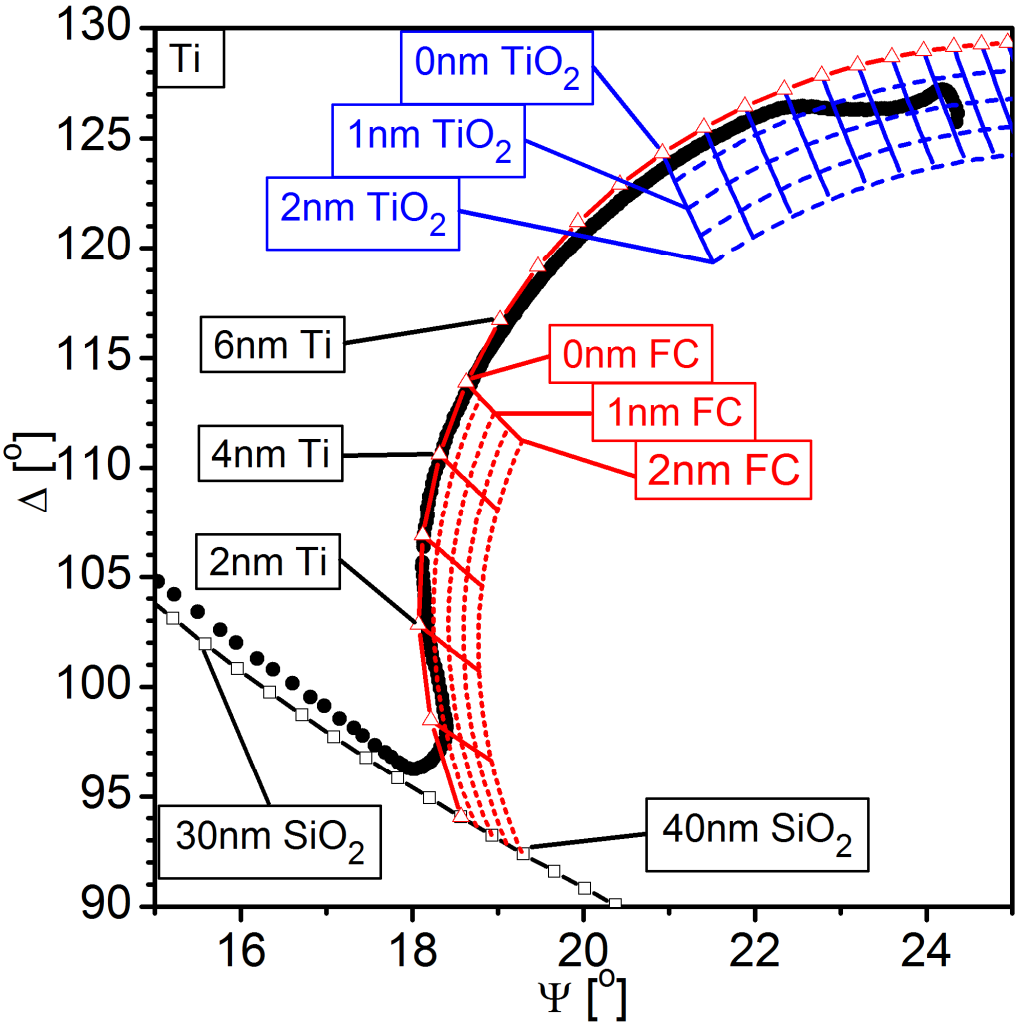

Figure 5.2: *Real-time ellipsometric measurements of Ti erosion in a 20%CF_4/Ar plasma (black circles) superimposed on multilayer optical models. The models describe the initial removal of a TiO_2 layer (dashed blue lines) from the Ti surface, followed by steady state erosion of Ti (solid red line, open triangles), and the erosion of the SiO_2 film (solid black line, open squares). Also shown is the influence of FC films on top of the Ti surface during steady state erosion (dotted red lines).*

After steady-state erosion of Ti, Fig. 5.2 shows the etching of the Ti/SiO_2 interface. The blunt transition of the measurement, in comparison to the sharp transition of the simulation, suggests that SiO_2 is being eroded while there is still Ti remaining on the surface (~1 nm). Even after etching through the Ti/SiO_2 interface, measurements deviate from the SiO_2 simulations. This observation is consistent with some Ti material (<1 nm) remaining on the SiO_2 surface (see Sec. 5.3.1.2).

Additionally, we present a multilayer model for FC covering the Ti surface during steady state erosion. This model is set up in a similar fashion as the previously described model, but it simulates a FC film on top of the Si/SiO_2/Ti stack instead of TiO_2. FC films with a thickness of up to 2 nm are simulated in 0.5 nm increments (dotted red lines) for 0–5 nm thick Ti. Using this kind of simulation in principle allows us to determine the FC layer thickness during erosion, assuming precise knowledge of SiO_2 layer thickness underneath the Ti layer.

However, cross section transmission electron microscopy (TEM) characterization of samples from several locations on one wafer showed significant non-uniformity with SiO_2 thickness variations of ±1.5 nm (not shown here). Therefore modeling of the FC layer thickness resulted only in moderate reproducibility, so angle-resolved XPS characterization is used to determine FC layer thicknesses. ER are extracted using a two layer ellipsometric model of Ti on top of SiO_2 without taking the FC film into account. Leaving out the FC layer leads only to an overestimation of the SiO_2 thickness, which does not affect the extracted ER during steady state erosion since the optical properties of the FC layer ($\tilde{N}$=1.420-0i)[5,23] and SiO_2 ($\tilde{N}$=1.457-0i) are almost identical.

5.3.1.2 XPS surface characterization

Complementary post-plasma characterization was performed by XPS. Figure 5.3 shows Ti 2*p* spectra for the identified erosion stages of Ti: (a) pristine material, (b) steady-state erosion of the hardmask and (c) steady-state erosion of SiO_2. Individual peaks and peak assignments after spectral decomposition are shown as well.

The pristine Ti film is composed of 24 at.% Ti, 53 at.% O and 23 at.% C. The C 1*s* spectrum (not shown here) indicates that C is mainly in the C-C bonding state, with small contributions from the C-O and C=O bonding states. Angle resolved measurements show that C is located at the film surface. The origin of the C can be explained by surface contamination introduced after film deposition. The Ti 2*p* spectrum (Fig. 5.3(a)) reveals that most of the Ti is oxidized (89%) with small amounts of metallic Ti (11%). The oxidized Ti is mainly in the TiO_2 (67%) and Ti_2O_3 (14%) oxidation state. Angle-resolved characterization (not shown here) shows that the amount of TiO (8%) and metallic Ti are strongly reduced for shallow probing depths. This suggests a layered structure of $Ti/TiO/Ti_2O_3/TiO_2$ from the bottom of the film to the top as reported by others.[5.18] This is consistent with the fact that our ellipsometric measurements closely follow TiO_2 simulations at the erosion start (see Sec. 5.3.1.1).

During steady state erosion of Ti in a FC-containing plasma the Ti surface is saturated with F and covered with a FC film. The Ti surface is composed of 21 at.% Ti, 63 at.% F, 13 at.% C, and 3 at.% O. The Ti 2*p* spectrum (Fig. 5.3(b)) reveals that 73% of Ti is in its fluorinated state (TiF_x), 17% in its metallic state, and 10% in its oxidized state. At a shallow probing depth almost 90% of the Ti is fluorinated. This enables us to compare relative amounts of TiF_x in the Ti 2*p* and F 1*s* spectra and reveals that TiF_x has a

bonding state of x≈3.1. Furthermore, by performing angle resolved analysis of the C 1*s* spectrum (not shown here) we find that C in the FC film is mainly in its C-C bonding state (64%). Most of the C-C bonds are located at the very top of the 0.9 nm thick FC film while the CF_x bonds are located in between the C-C and TiF_x layer. During steady state erosion of the SiO_2 layer (Fig. 5.3(c)) there are still small amounts of fluorinated Ti remaining at the film surface (~2 at.%). This occurs because Ti is removed much more slowly than SiO_2.

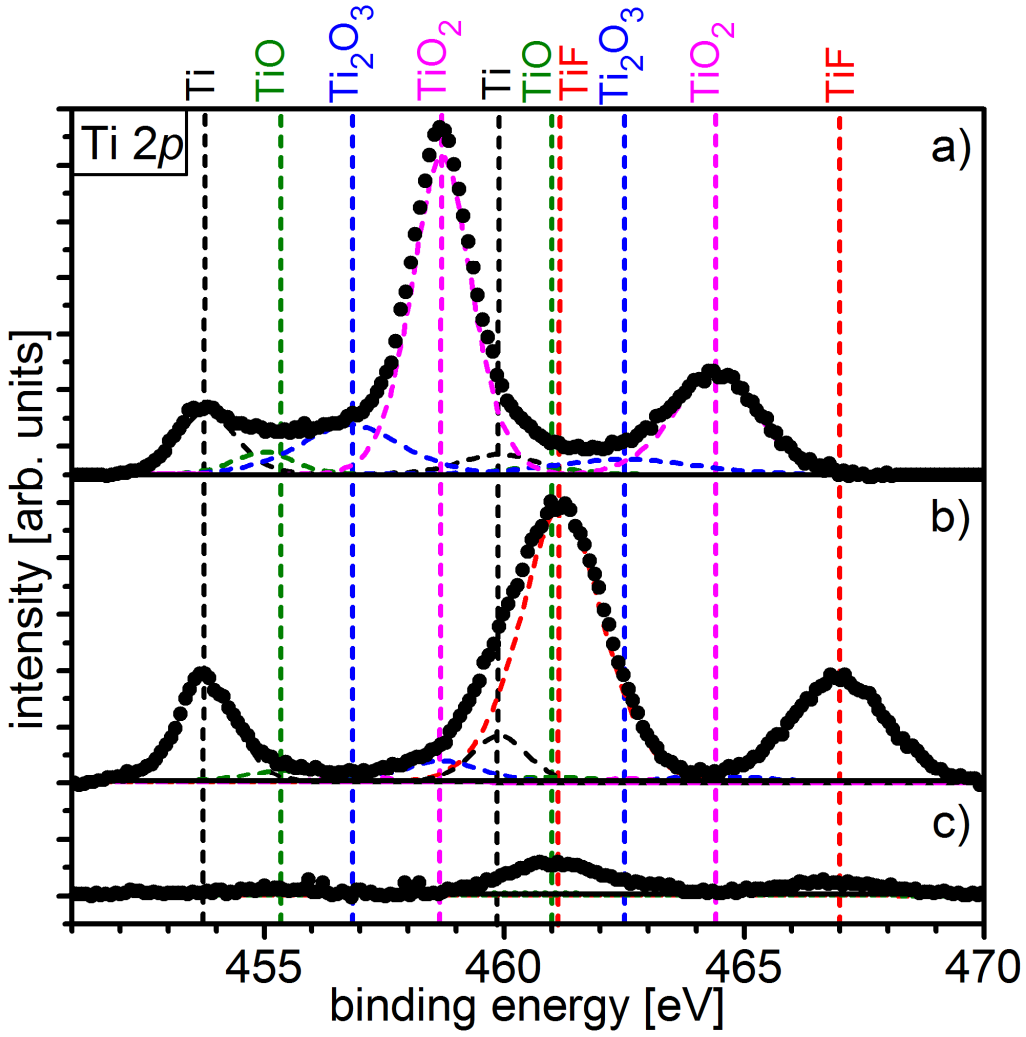

Figure 5.3: *High resolution Ti 2p XPS spectra of Ti (a) before processing, (b) during steady state hardmask erosion and (c) during erosion of the SiO_2 layer in a 20%CF_4/Ar plasma. Peak assignments for Ti, Ti-oxides and Ti-fluorides are indicated at the top of the spectra.*

5.3.2 Steady state erosion in CF_4/Ar and C_4F_8/Ar

5.3.2.1 Surface composition and FC layer thickness

Mixtures of CF_4 or C_4F_8 with Ar are commonly used plasma chemistries for pattern transfer into low-k materials. These plasma conditions, when operated at sufficiently high E_{ion}, remove the exposed Si-containing low-k material faster than the mask, which causes selective etching. However, even if selective low-k etching can be achieved for both plasma chemistries, the discharges are fundamentally different: C_4F_8-based discharges are known to deposit thicker FC films than CF_4-based discharges since in the C_4F_8-based discharges F_xC_y radicals[5.8, 5.24, 5.25] are generated, whereas F is most commonly produced in CF_4 discharges.[5.26, 5.27]

We compared the Ti film surface during steady state erosion in the C_4F_8 anchor condition with the CF_4 anchor condition presented in Sec. 5.3.1.2. The surface compositions are summarized in Tab. 5.2. We find that the surface states are different for the two conditions and correspond well with our expectations described in the previous paragraph. The film surface after processing in the less polymerizing, CF_4-based discharge contains large amounts of F, most of which is bonded to Ti. This fluorinated Ti surface is covered by a thin (0.9 nm) FC layer. For the more polymerizing C_4F_8-based discharge, the Ti signal is strongly attenuated by a significantly thicker (1.5 nm) FC layer. This is in agreement with the C 1s spectrum, which shows that C is mainly bonded to F as CF_x (x=1-3).

Total composition [at.%]	CF_4	C_4F_8	C 1*s* spectral composition [%]	CF_4	C_4F_8
Ti	21	11	C–C,C–H	64	35
F	63	54	$C–F_x$	36	65
C	13	33	F 1*s* spectral composition [%]	CF_4	C_4F_8
O	3	2	F–C	15	52
N	0	0	F–Ti	85	48

Table 5.2: *Ti surface composition for the CF_4 and C_4F_8 anchor condition together with composition of the C 1s and F 1s elemental spectra.*

5.3.2.2 Ti and OSG etch rates

For organic masks, ES strongly depends on the FC film thickness and thus on the plasma chemistry used. For highly volatile products formed from organic masks, a thicker FC film can reduce mask ER and increase ES.[5.28, 5.29] In contrast to the situation with organic masks, metal hardmasks are difficult to etch in FC plasmas and are intrinsically etch resistant. In order to understand if the thicker FC films lead to reduced ER for Ti hardmasks, we compared the erosion of CF_4/Ar plasmas with C_4F_8/Ar plasmas for V_{SB} between -50 V and -150 V. V_{SB} directly determines the energy that ions deposit at the surface, which, if high enough, can break chemical bonds to release volatile etch products. To achieve net erosion, a sufficiently high V_{SB} has to be applied, especially for very polymerizing plasma discharges.[5.30] Reducing E_{ion} causes ions to penetrate less deeply and reduces power deposition on the film surface without affecting the amount of Ar^+, F^+ and $C_xF_y^+$ ions, and the ICD.

Ti ER were measured ellipsometrically and extracted for steady state erosion (see Sec. 5.3.1.1). In addition, we also processed a reference low-k material (OSG) in the same plasma environment to determine ES (ER_{OSG} / ER_{Ti}). ES determines the feature depth that can be achieved during pattern transfer. We will assume that the differences

between the two discharges discussed in Sec. 5.3.2.1 generally hold for the OSG material. Results of ER measurements and corresponding ES are presented in Fig. 5.4.

When comparing the OSG ER of the two plasma conditions, it is clear that the FC layer thickness has a direct impact on the ER. CF_4-based discharges enable ER that are three times higher than those measured for C_4F_8-based discharges. In contrast to the OSG mask, Ti shows only marginally higher ER in CF_4-based plasmas at 26 nm/min compared to 24 nm/min for C_4F_8-based plasmas. This indicates that Ti ER are much less sensitive to changes in the FC film thickness and a thick FC layer is much more inhibiting for OSG. As a result, ES in CF_4-based discharges are superior to those in C_4F_8 discharges. This mechanism is in strong contrast to our expectations from organic masking materials where thick FC layers inhibit mask erosion more than low-k material erosion and lead to increased ES.[5.31]

Increasing V_{SB} from -50 V to -150 V leads to a nearly linear increase in ER for the CF_4-based discharges. This indicates that Ti and OSG ER are directly proportional to the energy deposited on the surface by each ion. This trend does not hold for the low self bias condition in the C_4F_8-based discharge where ER of Ti and OSG decrease by more than a factor of four. At such low V_{SB} conditions, the ions are not energetic enough to penetrate the thick FC layer and maintain enough energy to volatilize etch products.

The resulting ES is strongly dominated by the FC film thickness which is determined by the discharge chemistry. Furthermore, for all conditions except the low V_{SB} C_4F_8 discharge, the ES show increasing trends with decreasing Ti and OSG ER. This indicates that the OSG ER is not only more sensitive to the FC film thickness but also to

ion energy E_{ion} determined by V_{SB}. Results indicate that the highest ES can be achieved in CF_4 plasma discharges at low V_{SB} that are slightly above the net erosion threshold.

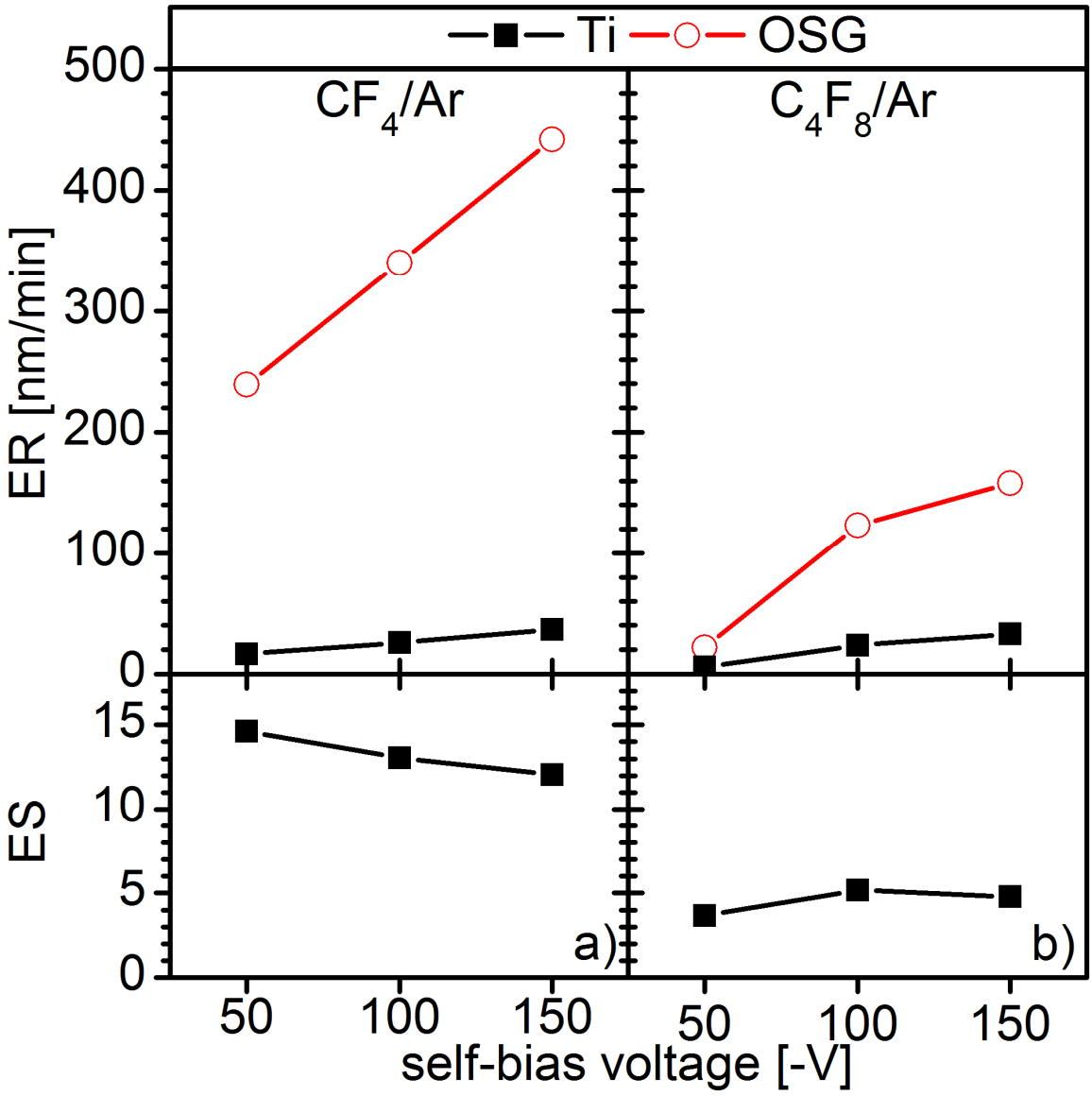

Figure 5.4: *Plasma parameter dependence of Ti and OSG etch rates (ER) on V_{SB} together with corresponding etch selectivities (ES) for (a) CF_4-based and (b) C_4F_8-based plasma discharges.*

5.3.3 Changes in chamber pressure and $\%CF_4$ in CF_4/Ar

In addition to the FC film thickness and V_{SB} investigated in Sec. 5.3.2.2, ICD and F concentration can influence ER and increase ES. Increasing the pressure of the discharge causes the electron mean free path in the plasma to decrease, leading to a lower degree of ionization for Ar and a higher degree of dissociation for the FC feed gas.[5.32] This results in reduced ICD and higher F concentration in the plasma discharge.[5.21, 5.23] We anticipate that increasing the relative amount of the FC feed gas in the discharge will cause similar effects as increasing the pressure. More of the power coupled into the plasma is used to dissociate the FC feed gas so less power remains to ionize Ar, which leads to increased F concentration and reduced ICD.[5.33, 5.34] In our experiments, parameters were individually changed while keeping other parameters constant at our anchor condition: 20%CF_4/Ar, 40 mTorr, and -100 V V_{SB}.

We observe for both materials that the highest ER are measured at 20 mTorr and the lowest ER at 40 mTorr as shown in Fig. 5.5(a). The high pressure condition (60 mTorr) has a slightly increased ER when compared to 40 mTorr. ICD and OES measurements show that increasing the pressure decreases the ICD and increases the F concentration. These observations indicate that ER in the medium and high pressure conditions are limited by the number of ions bombarding the sample surface due to the low ICD. The resulting changes in the ES shown in Fig. 5.5(a) are similar to those observed for the change in E_{ion}. ES are highest for low ER conditions (here 40 mTorr) due to OSG ER decreasing relatively less than the Ti ER.

Figure 5.5(b) shows the changes in the $\%CF_4$ in CF_4/Ar mixtures where we observe the highest ER for 20% CF_4 addition. We can conclude that ER are ion current-

limited and F concentration-limited for high and low $\%CF_4$ discharges, respectively. The resulting changes in ES are relatively small; the highest ES are achieved at high $\%CF_4$ where the F-rich, ion current-limited etching regime dominates.

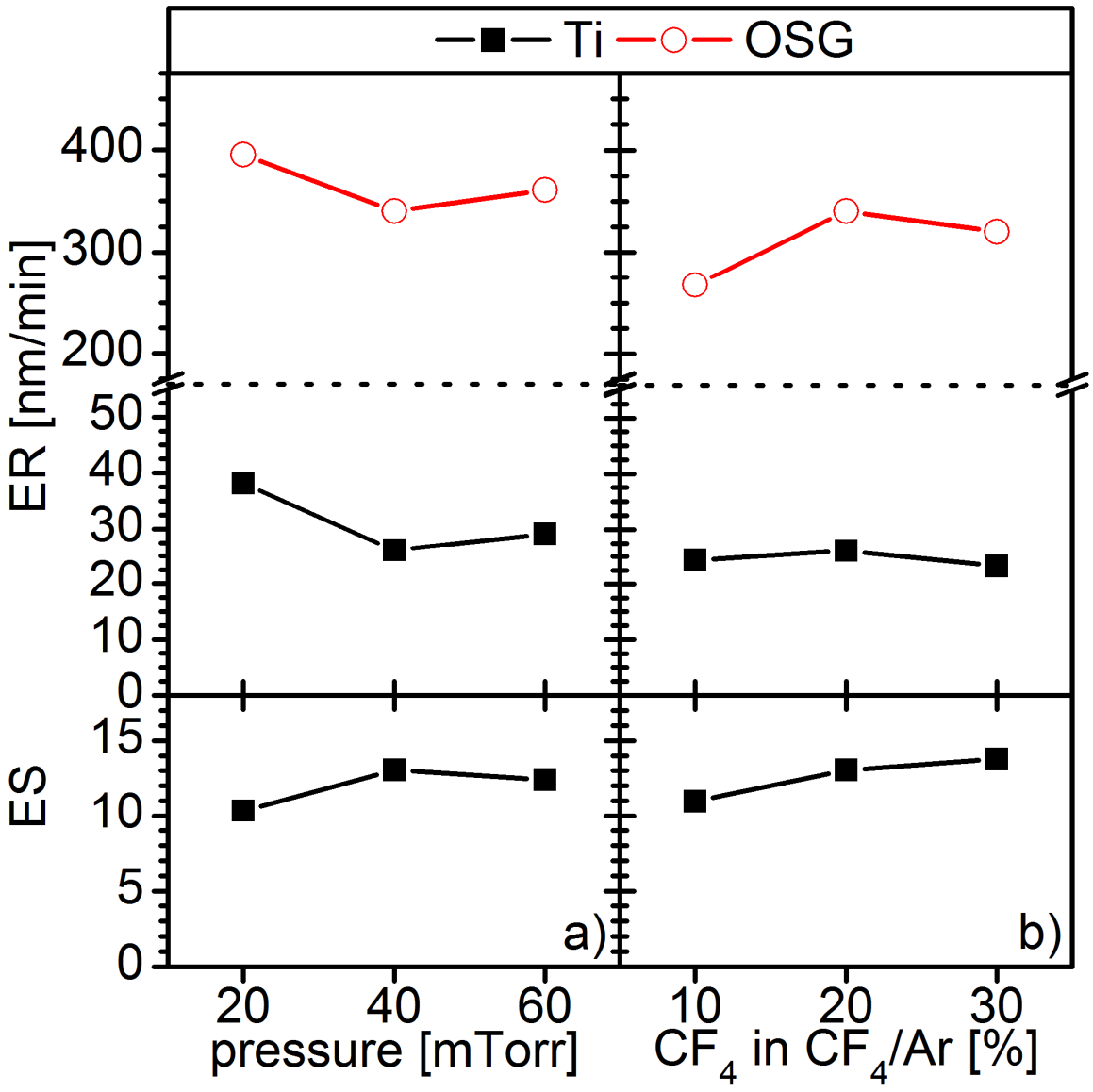

Figure 5.5: *Plasma parameter dependence of Ti and OSG etch rates (ER) on (a) pressure and (b) $\%CF_4$ in the CF_4/Ar discharge together with corresponding etch selectivities (ES).*

5.3.4 O_2 and N_2 addition to C_4F_8/Ar

An alternative pathway to potentially increase ES in polymerizing plasma conditions, i.e. C_4F_8-based discharges, is to add reactive gases such as O_2 or N_2 to the discharge. After dissociation in the gas phase, O and N react with the FC film surface and form volatile products such as NF_3, CNF_x, and CO, CO_2 and COF_2.[5.35] The formation of these volatile products can reduce steady state FC film thickness, increase material removal rates, and significantly alter film surface compositions.[5.5] However, the addition of O_2 or N_2 to the discharge consumes some of the power available for dissociation of C_4F_8 and ionization of Ar. The result is a decrease in ICD and the amount of reactive species available for material erosion.[5.36] Additionally, reactive species can be further reduced in the gas phase by, for example, the recombination of F or CF_x and N_2 leading to the formation of NF_3 or CNF_x.[5.35]

5.3.4.1 Surface composition and FC layer thickness

High resolution XPS Ti 2*p*, N 1*s*, F 1*s*, C 1*s* and O 1*s* spectra of Ti films after plasma processing under the C_4F_8-anchor condition and for various amounts of O_2 and N_2 addition are presented in Fig. 5.6. The corresponding surface compositions and FC layer thicknesses are summarized in Tab. 5.3. Relevant findings will be described starting with the anchor condition, followed by O_2 and N_2 addition, respectively.

For the anchor condition shown in Fig. 5.6(a), the Ti surface is highly fluorinated, slightly oxidized and covered with a thick FC layer. The F 1*s* spectrum clearly shows two distinct peaks for F-Ti and F-C bonds with 48% of the F bonded to Ti. C 1*s* spectra show that the FC layer is F-rich (CF_x with x=1-3). The minute amounts of oxygen (see O 1*s*

spectra) are primarily bonded to C in the FC layer as O-C and O=C bonds and can be attributed to post plasma reactions during vacuum transfer to the analysis chamber.

	Ti [at.%]	N [at.%]	F [at.%]	C [at.%]	O [at.%]	FC thickness [nm]
C_4F_8/Ar	11	0	54	33	2	1.5
+5% O_2	20	0	59	17	4	0.8
+10% O_2	20	0	59	16	5	0.6
+10% N_2	10	6	59	23	2	1.4
+20% N_2	12	7	56	22	2	1.3

Table 5.3: *Surface composition and FC layer thickness of Ti films for 20%C_4F_8/Ar, 5% and 10% O_2 addition, and 10% and 20% N_2 addition.*

Figures 5.6(b) and 5.6(c) show elemental spectra for O_2 addition to the discharge. We find that the shape of the Ti 2*p* spectra remains relatively unchanged and only the intensity of the signal is increased due to less attenuation by a thinner FC layer. F-C bonds in the F 1s spectra and the C-F_x bonds (x=1-3) in the C 1s spectra are strongly decreased compared to the anchor condition. O 1*s* spectra also show that film surfaces are being oxidized and that oxygen is mainly bonded to the surface as O-C and O=C bonds. Angle resolved measurements reveal that the FC layer thickness is reduced by ~0.7-0.9 nm resulting in a FC film thickness of ~0.6-0.8 nm. The resulting Ti surfaces after addition of O_2 to the anchor condition remain highly fluorinated and are covered with a partially oxidized C-rich surface layer.

Figures 5.6(d) and 5.6(e) show elemental spectra for N_2 addition to the discharge. We find that the shape and intensity of the Ti 2*p* spectra remain relatively unchanged. This suggests that, in contrast to O_2 addition, N_2 addition does not significantly reduce the FC layer thickness. F 1*s* spectra show that the amount of F-C bonds remains relatively stable.

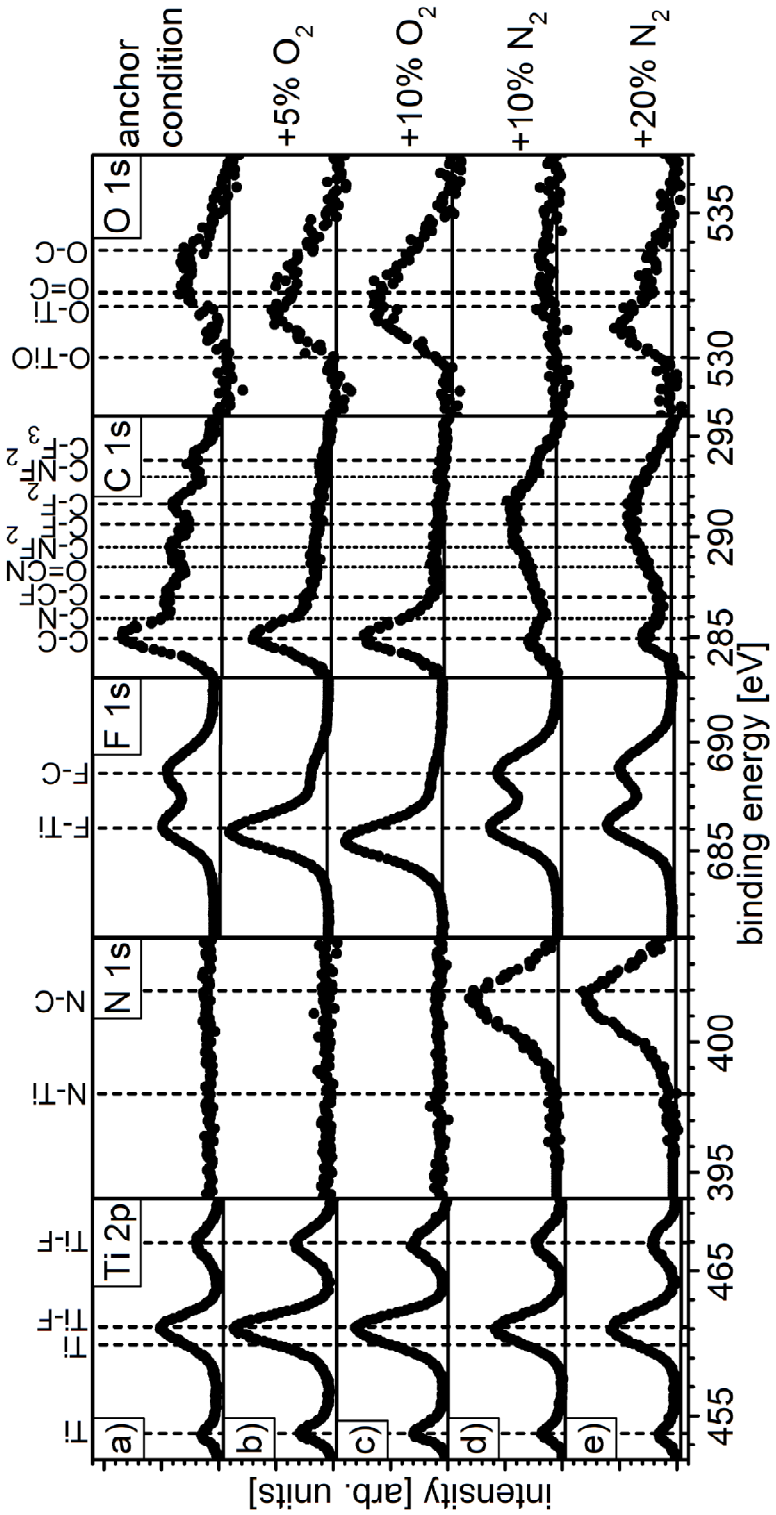

Figure 5.6: *High resolution Ti 2p, N 1s, F 1s, C 1s, and O 1s XPS spectra (from left to right) of Ti surfaces (a) after processing in the C_4F_8 anchor condition, after processing in the anchor condition with (b) 5% and (c) 10% O_2, and (d) 10% and (e) 20% N_2 addition. Peak assignments are indicated at the top of the spectra.*[5.11 ,5.18, 5.43-5.47]

In agreement with the F 1*s* spectra, C 1*s* spectra show that the distinct structure of CF_x bonds (x=1-3) vanishes and is replaced by a broad indistinct peak, which can be attributed to a mixture of CF_x (x=1-3) and CN bonds. This is consistent with the N 1*s* spectra showing the formation of N-C bonds while no N-Ti bonds are formed. There are no changes in the O 1*s* spectra compared to the anchor condition, which indicates that changes in oxidation of the surface do not occur. Slight variations can be attributed to post plasma oxidation of the N-containing FC layer. Angle resolved measurements reveal that the FC layer thickness remains fairly constant with small thickness reductions of ~0.1-0.2 nm. The resulting film surfaces after addition of N_2 to the anchor condition remain highly fluorinated and are covered with a partially nitrided FC surface layer.

5.3.4.2 Ti and OSG etch rates

Figure 5.7 shows that adding O_2 to the C_4F_8 anchor condition significantly increases the OSG ER but has little effect on the Ti ER. The strong increase of the OSG ER can be attributed to a reduction of the FC film thickness and increased material removal rates by formation of volatile etch products such as CO, CO_2, COF_2.[5.5] The slight increase in Ti ER for 5% O_2 addition can be explained by the significantly reduced FC layer thickness (see Sec. 5.3.4.1). However, after increasing the O_2 addition to 10%, ER decrease to values similar to the anchor condition with the thick FC layer. This behavior indicates that the ER must be limited by the ICD which decreases for 10% O_2 addition by more than a factor of two. An alternative explanation is a limitation based on the amount of F available for formation of volatile TiF_4. F deficiency can arise either from the reaction of O_2 and C_4F_8 in the gas phase or from the deficiency of F in the FC layer (see Sec. 5.3.4.1). This deficiency can limit the formation of TiF_4.[5.35, 5.37] The surface

composition and the Ti 2*p* spectra of the Ti surfaces remain relatively unchanged, indicating that the observed changes in ER are dominated by the FC layer thickness and ICD reductions. The corresponding ES for Ti can be increased by 40% by the addition of 10% O_2 to the C_4F_8 discharge as a result of the increased OSG ER and decreased hardmask ER.

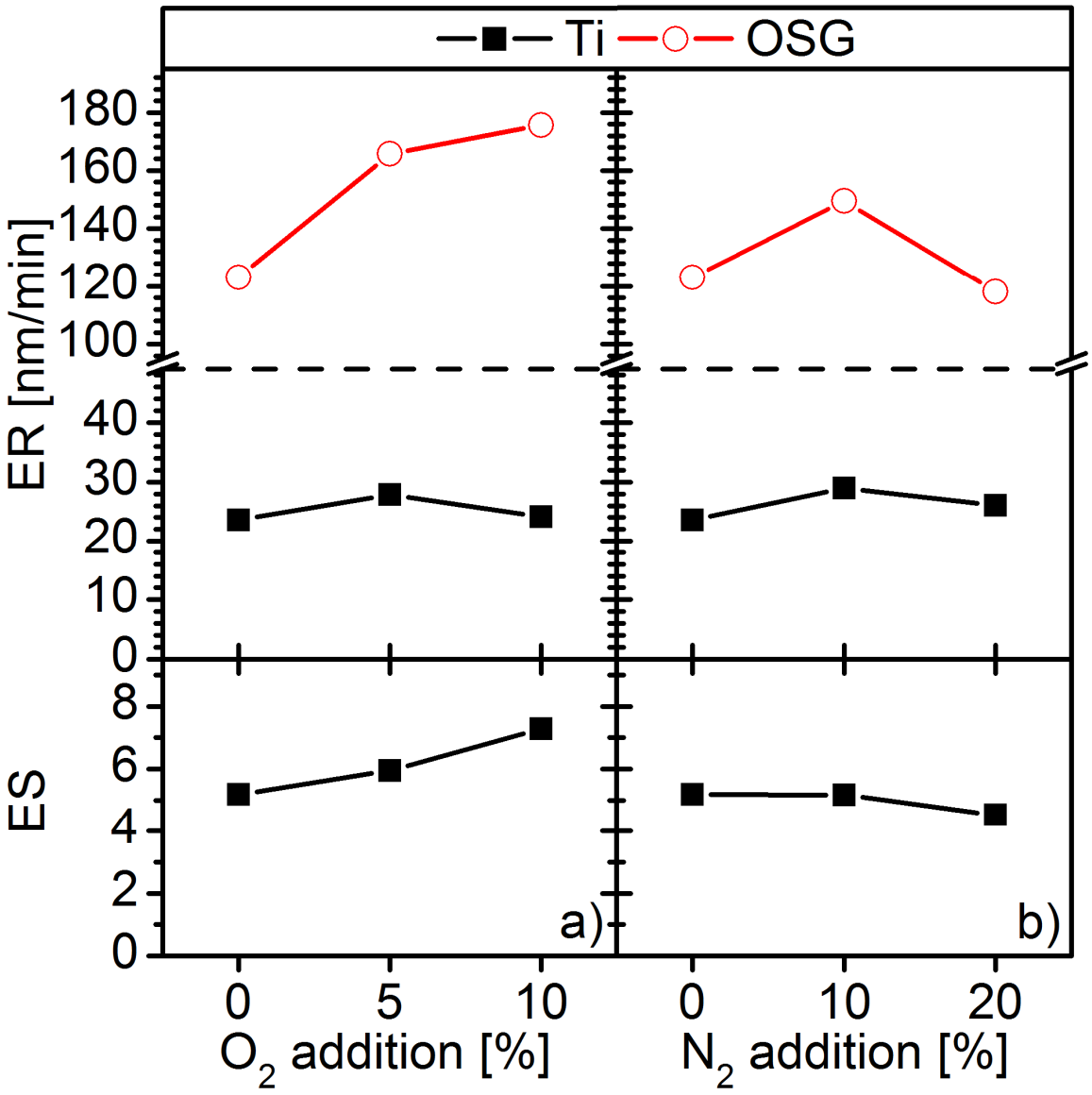

Figure 5.7: *Plasma parameter dependencies of Ti and OSG etch rates (ER) on (a) O_2 and (b) N_2 addition in the C_4F_8/Ar discharge together with corresponding etch selectivities (ES).*

When N_2 is added to the C_4F_8 discharge, ER remain relatively constant and show similar trends as the O_2 addition. However, the FC layer thickness only changes by less than 0.2 nm. This indicates that the FC layer thickness is not the determining factor leading to the observed ER changes. For Ti we observe small increases in ER (~20% for 10% N_2 addition and ~10% for 20% N_2 addition). The most significant difference in the surface composition is a strongly reduced C content from ~33 at.% to ~22 at.%; the formation of small amounts of C-N bonds and a slight increase of the F content also occur. For 10% N_2 addition, ER increase due to the higher availability of F, so the formation of volatile Ti etch products dominates. For 20% N_2 addition, decreased ICD lead to a slight reduction of ER. In contrast to the hardmask materials, OSG ER are strongly dependent on N_2 addition. For 10% N_2 addition, ER increase by ~20% while for 20% N_2 addition ER decrease by ~5% as compared to the anchor condition. We speculate that the ER increase at 10% N_2 addition is based on the reaction of N_2 with the OSG surface and the formation of volatile etch products such as HCN.[5.38] This is similar to our observations for O_2 addition where formation of CO, CO_2 and COF_2 is believed to increase ER.[5.35] However, if the N_2 addition to the discharge is further increased to 20%, ER become limited by the ICD and possibly by an OSG surface with increased etch resistance by formation of CN and SiN bonds. The corresponding ES are highest without N_2 addition.

5.4 Discussion

The experimental results presented in Sec. 5.3 suggest that there is a general mechanism that can explain how Ti and OSG ER depend on processing parameters. We will show that the formation of the FC layer and energy deposition at the surface by ion impact determine Ti etch rates. Furthermore we will discuss how ES depend on the OSG material composition and why conditions that provide high ES for patterning OSG with an organic mask show low ES for Ti masks.

5.4.1 Mechanism of Ti etching

Figure 5.8(a) shows the measured Ti etch rates as a function of the FC film thickness for V_{SB} between -50 V and -150 V in the CF_4-based discharge as well as O_2 addition (0-10%) and N_2 addition (0-20%) to the C_4F_8-based discharge. Neither of these parameter spaces shows a clear correlation of ER with FC layer thickness. When increasing V_{SB}, ER increase even if there is no change in FC layer thickness. When adding N_2 or O_2 to the C_4F_8 discharge, FC layer thicknesses decrease and ER increase for 5% gas addition and decrease for 10% gas addition.

We discussed in Sec. 5.3.4.2 that the addition of N_2 or O_2 reduces FC film thickness as well as ICD due to the source power being consumed by dissociation of the molecular N_2 and O_2 gas molecules. In order to account for changes in the ICD, it is more useful to correlate etch yields (EY) with the FC layer thickness: $EY = ER * \rho * j^{-1}$. EY describe the removal of atoms per incident ion, employing film density (ρ) and ICD (j), and are identical to sputter yields for plasma conditions in which no volatile products are formed (reactive etch). The Ti ρ used in the calculations is 4.51 g/cm^3.[5.39]

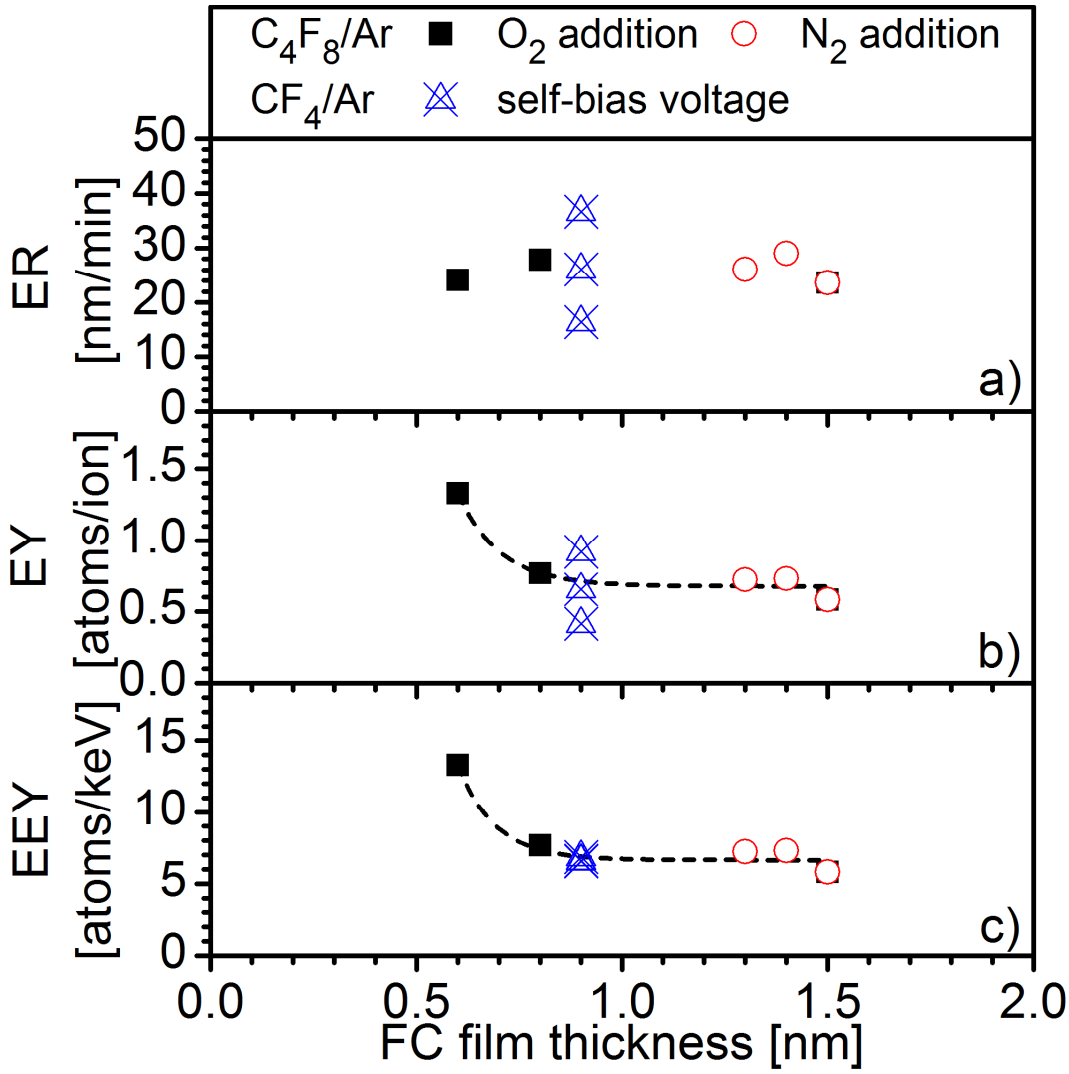

Figure 5.8: *Correlation of FC film thickness with (a) etch rate (ER), (b) etch yield (EY), and (c) energy etch yield (EEY) for O_2 and N_2 addition to the C_4F_8/Ar discharge and various V_{SB} in the CF_4/Ar discharge.*

Figure 5.8(b) shows that EY for all conditions at -100 V V_{SB} (including the CF_4 condition) exponentially decreases with FC layer thickness. This behavior is in excellent agreement with the findings by Schaepkens *et al.*[5.30] who established the same exponential dependence of Si ER on FC layer thickness. The fact that the FC film thickness controls EY rather than ER indicates that each individual ion contributes directly to material removal by providing energy at the surface for volatilizing etch products.

This mechanism is further supported by the EY dependence on FC film thickness of the CF_4 discharge for various V_{SB}. Figure 5.8(b) shows that EY increase strongly when increasing the V_{SB} while the FC layer thickness remains unchanged. In order to account for the differences in E_{ion} we introduce here the energy etch yield (EEY): EEY = EY / E_{ion}. Figure 5.8(c) shows the universal behavior observed between EEY and FC film thickness. This effect is consistent with previous observations made by Standaert *et al.*[5.37] who investigated ER dependencies of SiO_2 and other materials in CF_4- and C_4F_8-containing discharges on the FC layer thickness. They found that ER for thin FC films are independent of FC film thickness and are directly related to the E_{ion}. This etching regime is referred to as 'chemical sputtering' where most of the ions penetrate the FC film and can reach the substrate material.[5.37, 5.40] In contrast, under conditions with thick FC films, ion interactions with the substrate strongly decrease, so the transport of F to the substrate/FC film interface may become the determining factor that limits ER. This etching regime is referred to as the 'diffusion controlled' etching regime.[5.37, 5.40] We can conclude that the three factors that determine Ti ER are: ICD, E_{ion} and FC film thickness.

5.4.2 Differences in Ti and OSG erosion and selectivity

The mechanism described above explains how Ti ER can be influenced, but it does not explain how ES depends on the plasma parameters investigated here. The correlation of Ti ER with the ES for all plasma conditions are presented in Fig. 5.9. The correlation plot shows two distinct universal behaviors which will be discussed in detail in this section: First, ES are consistently higher for the less polymerizing CF_4-based plasmas than for the C_4F_8-base plasmas. Secondly, the highest ES is achieved at low Ti and OSG ER.

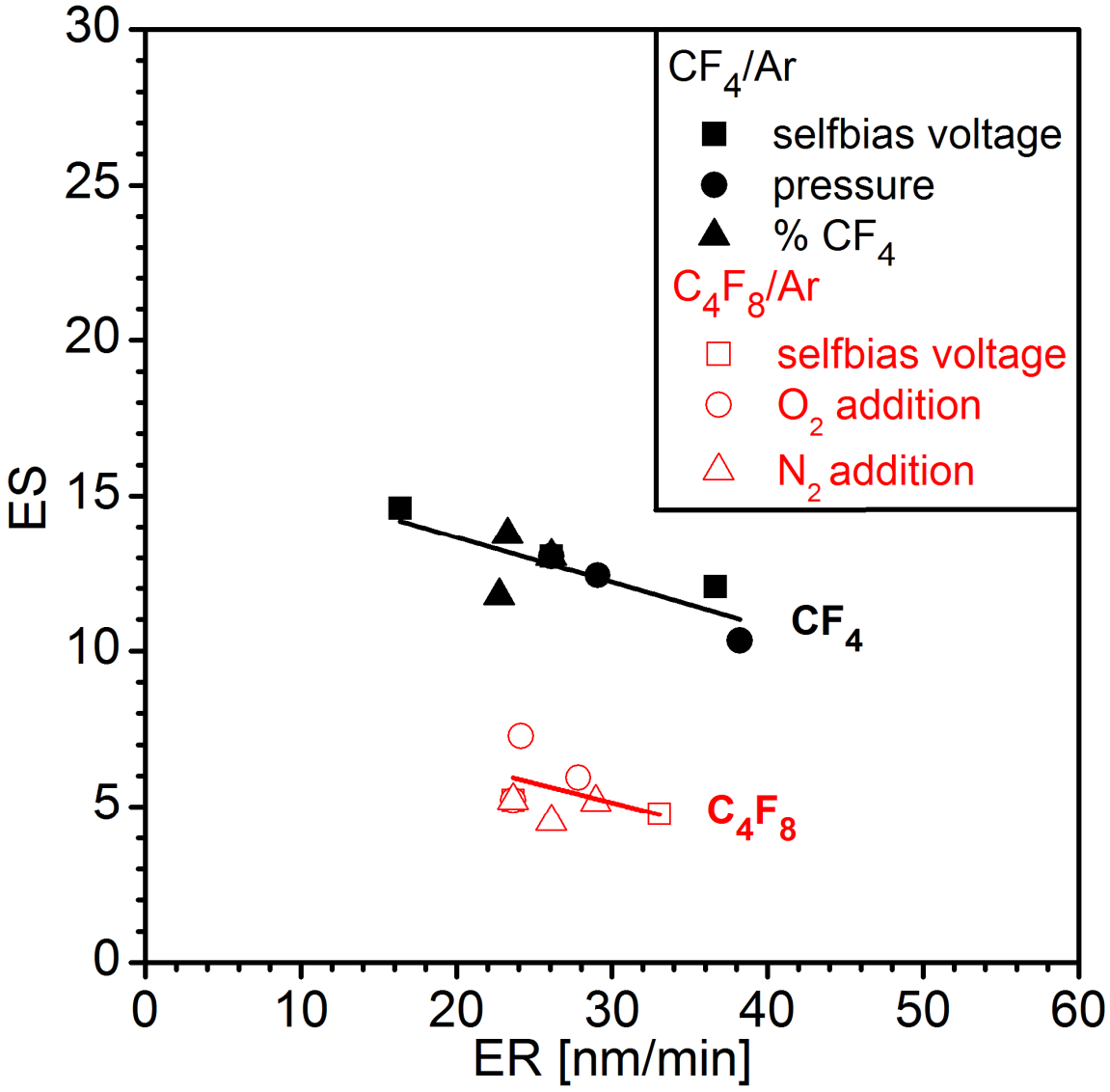

Figure 5.9: *Correlation of etch rate (ER) and etch selectivity (ES) for Ti erosion for plasma parameters investigated in the CF_4/Ar and C_4F_8/Ar discharges.*

The difference in ES between Ti and OSG are based on systematic differences in the material erosion. Ti is eroded by the stepwise increase in the number of F-atoms associated with Ti. Once Ti is fully fluorinated (TiF_4) it can be volatilized upon ion impact.[5.41] The required energy can be expressed in terms of the boiling point (BP) of TiF_4 (BP=284 °C).[5.41] OSG is eroded through the formation of a variety of volatile species such as SiF_4, CO, CO_2, COF_2 and others.[5.5] However, all these products require

significantly less energy to be volatilized compared to TiF_4: BP(SiF_4)=-86 °C, BP(CO)=-192 °C, BP(CO_2)=-79 °C.[5.42] This explains why, for particular plasma operating conditions, the same amount of energy deposited at the film surface can remove significantly more OSG than Ti.

In order to understand from where the systematic differences in ES between the CF_4 and C_4F_8-based discharges originate, interactions of the FC film and the substrate material must be considered. Previously, Standaert *et al.*[5.37, 5.40] investigated ER dependencies of SiO_2 and other low-k materials in CF_4- and C_4F_8-containing discharges on the FC layer thickness and found that material impurities such as C and H (both contained in OSG) become important in the 'diffusion controlled' etching regime. The erosion pathway of these impurities is the formation of CF_4 and HF and the removal rates strongly rely on the F available at the OSG/FC film interface. In contrast to OSG, Ti ER are not that strongly reduced in the 'diffusion controlled' etching regime since all available F is used for the formation of volatile TiF_4.

The mechanism that explains why CF_4-based plasmas provide higher ES for Ti hardmasks can also explain why C_4F_8-based plasmas provide higher ES for organic masking materials. For organic masking materials, the masking layer contains more impurities (C and H), than the low-k material. In some cases, the masking layer may contain only impurities. To achieve high ES in these situations, plasma discharges have to be operated in the 'diffusion controlled' regime where thick FC layers limit erosion of the organic mask layer more than the erosion of the low-k material.

5.5 Conclusions

We have studied the erosion of Ti and OSG in CF_4/Ar and C_4F_8/Ar plasma discharges to gain insight into material- and plasma-dependent erosion behavior. We have identified three characteristic hardmask erosion stages by ellipsometric real-time measurements and complementary surface characterization by XPS. In the first stage, the highly oxidized film surface is removed. During steady state erosion, the Ti surface is strongly fluorinated and covered by a FC layer. The thickness of the FC film is significantly higher for the more polymerizing C_4F_8-based plasmas (1.5 nm) than for the less polymerizing CF_4-based plasmas (0.9 nm). After erosion of the hardmask, SiO_2 erosion begins with small amounts of fluorinated Ti remaining on the SiO_2 surface (~2 at.%).

The plasma parametric studies show that Ti ER depend on E_{ion} and ICD, both of which determine the total energy deposited at the material surface as well as the FC layer thickness. These parameters can be adjusted by changing V_{SB}, pressure, %FC feed gas in the FC/Ar gas mixture, and by adding O_2 or N_2 to the FC/Ar gas mixture. ES between OSG and Ti are generally based on differences in the energy required for volatilizing etch products and increase for low OSG and Ti ER because OSG has a lower sensitivity to changes in energy deposition.

However, ES are significantly higher for the less polymerizing CF_4-based plasma conditions than for the more polymerizing C_4F_8-based plasma conditions. This is in strong contrast to organic masking materials where more polymerizing plasma conditions typically lead to increased ES over low-k materials. For the less polymerizing conditions with thin FC films, erosion is ion driven whereas, for the more polymerizing conditions

with thick FC films, erosion is limited by diffusion of F through the FC layer. For the erosion of Ti, ER do not change significantly between the two regimes since Ti is the only species consuming F when forming volatile TiF_4. In contrast to Ti, OSG ER strongly decrease in the diffusion-limited regime due to the consumption of the already limited F by C and H impurities for the formation of volatile CF_4 and HF etch products. This is in good agreement with more polymerizing plasma discharges providing higher ES for organic masks since in this system the mask is the more impurity-rich material.

The ES achieved in this study are as high as 15 and we expect that ES can be further increased by limiting the amount of energy provided to the surface by reducing ICD and/or E_{ion} and minimizing the FC layer thickness. Changes in the ICD, E_{ion}, and FC layer thickness can be achieved by using weakly polymerizing plasma conditions such as CF_4, increasing the pressure, decreasing the %FC feed gas in the gas mixture and adding gases such as O_2 or N_2 to the discharge.

Chapter 6

Differences in erosion mechanism and selectivity between Ti and TiN in Fluorocarbon (FC) plasmas for dielectric etch

F. Weilnboeck, E. Bartis, S. Shachar, and G.S. Oehrlein

Department of Materials Science and Engineering, and Institute for Research in Electronics and Applied Physics, University of Maryland

D. Farber, T. Lii, and C. Lenox

Texas Instruments

Journal of Vacuum Science and Technology B, submitted

Abstract:

Metallic masking materials are promising candidates for plasma-based pattern transfer into low-k materials for fabricating integrated circuits. Improving etching selectivity (ES) between the low-k and hardmask material requires a fundamental understanding of material erosion in fluorocarbon (FC) plasmas. The authors have previously reported on the erosion mechanism and plasma parametric dependencies of Ti etch in FC discharges. The present work focuses on elucidating differences in the erosion behavior between Ti and TiN hardmasks. We studied erosion of Ti, TiN, and organosilicate glass (OSG), a reference low-k material, in CF_4/Ar and C_4F_8/Ar plasmas. Changes in surface composition, FC surface reaction layer thicknesses, erosion rates and corresponding ES were established by x-ray photoelectron spectroscopy (XPS) and *in-situ* ellipsometry. We found that the erosion stages and plasma parameter dependent surface compositions were similar for Ti and TiN. The previously established dependence of Ti erosion rates on FC layer thickness and energy deposition on the hardmask surface by ions generally holds for TiN as well. However, TiN etch rates (volumetric removal rates) and etch yields (atomic removal rates) were increased by a factor of 1-1.4 compared to Ti. This difference can be explained by the rapid removal of N from the TiN surface, increasing the Ti atom number density at the surface above values of the Ti hardmask. The resulting increase in surface reactivity is in good agreement with the enhanced erosion rates compared to Ti. Differences in erosion rates have a direct impact on the ES and the highest ES relative to OSG (up to 15) were achieved for Ti hardmasks in CF_4/Ar plasmas with low ion energy.

6.1 Introduction

Ti and TiN are well-known materials in semiconductor fabrication due to their superior performance as adhesion and barrier layers between other metals and Si.[6.1, 6.2] More recently, Ti and TiN have attracted attention as masking layers in the dual damascene etching process for patterning of low-k materials by possibly increasing etching selectivities (ES) and reducing severe faceting and low-k damage.[6.3] So far, research has mainly focused on TiN due to high optical transparency for layers thinner than 20 nm leading to good photolithographic performance in multilayer masking schemes.[6.3-6.5]

Previously, we have studied the erosion of Ti and organosilicate glass (OSG) in CF_4/Ar and C_4F_8/Ar plasma discharges to gain insight into material- and plasma-dependent erosion behavior.[6.6] For Ti, we have identified three characteristic erosion stages by real-time ellipsometry and post-process x-ray photoelectron spectroscopy (XPS) characterization: 1) removal of a highly oxidized surface, 2) steady state erosion of highly fluorinated Ti covered with a fluorocarbon (FC) layer (~0.9 nm for CF_4/Ar and ~1.5 nm for C_4F_8/Ar plasmas), and 3) erosion of SiO_2 after hardmask erosion with some fluorinated Ti remaining on the surface (~2 at.%).[6.6] During steady state erosion, Ti etch rates (ER) are directly related to the FC layer thickness and the total amount of energy deposited by ions on the surface, determined by both maximum ion energy (E_{ion}) and ion current density (ICD).[6.6]

We compared plasma parameter-dependent changes of Ti and OSG ER and found that ES are mainly determined by OSG ER. The highest ES (~15) are achieved for the less polymerizing CF_4-based plasma conditions where material erosion is an ion-driven

process and hardly affected by the thin FC-layer. For more polymerizing C_4F_8-based plasmas, material surfaces are covered with a thicker FC film and OSG erosion is limited by both diffusion of F through the FC layer, reduced ion bombardment and consumption of F by C and H in the OSG (formation of volatile CF_4 and HF etch products), leading to reduced ES.[6.6] This is in strong contrast to organic masking materials which provide the highest ES in more polymerizing plasma chemistries, e.g. C_4F_8/Ar discharges, since organic masks have a higher C and H content and ER are more strongly reduced by a limited supply of F than OSG.[6.6]

Our results indicate that integration of Ti in addition to or as a replacement of TiN hardmasks in the wafer flow has to be considered. However, before integration, a systematic investigation must determine differences between Ti and TiN in hardmask performance and underlying etching mechanisms.

This article is organized as follows: After describing the experimental procedures in Sec. 6.2, we present real-time measurements of TiN erosion by ellipsometry and post plasma surface characterization by XPS in Sec. 6.3.1. In Sec. 6.3.2, we compare surface composition and ER of Ti and TiN in CF_4/Ar and C_4F_8/Ar plasma discharges for various plasma processing parameters, i.e. self bias voltage (V_{SB}), pressure, %CF_4 in CF_4/Ar, and N_2 and O_2 addition to C_4F_8/Ar discharges. In Sec. 6.4, we discuss the fundamental differences in the erosion behavior between Ti and TiN and corresponding ES.

6.2 Experiment

Experimental setup, characterization and analysis techniques were discussed in detail in our complementary study and only the most relevant details will be presented here.[6.6]

6.2.1 Description of materials

The materials used in this study were Ti and TiN films prepared by physical vapor deposition (PVD) and spin coated OSG. All materials were deposited on ~38 nm of thermally grown SiO_2 on Si substrates to increase the sensitivity of ellipsometric measurements during erosion. The OSG had a composition of 28 at.% C, 33 at.% H, 14 at.% Si and 25 at.% O, and a density of ~1.2 g/cm^3. For Ti and TiN we assumed a density of 4.56 g/cm^3 and 5.40 g/cm^3, respectively.[6.7, 6.8]

6.2.2 Plasma processing

Plasma processing was performed in two inductively coupled plasma (ICP) reactors (125 mm and 300 mm substrate electrode diameters).[6.9, 6.10] In both reactors, a planar coil placed on top of a quartz window was powered through an L-type matching network, which ignites and maintains the plasma. An additional radio frequency bias power supply independently controlled the self-bias voltage (V_{SB}) at the substrate electrode. The resulting maximum ion energy (E_{ion}) for singly-charged ions corresponded to the sum of the applied V_{SB} and the plasma potential (~25 V) in eV.[6.11] The temperature of the bottom electrode was kept at 10 °C by circulating a cooling liquid. During plasma processing, samples were bonded to the bottom electrode using thermal grease between

the sample and electrode. These steps were necessary to rule out contributions from temperature effects.

We investigated two FC-based gas chemistries, CF_4/Ar and C_4F_8/Ar, which are often used for high aspect ratio and contact hole etching of dielectrics.[6.12-6.14] The anchor condition of the CF_4/Ar discharge was: 20%CF_4/80%Ar, 400 W source power, -100 V V_{SB}, 40 mTorr pressure, and 50 sccm total gas flow rate. The anchor condition of the C_4F_8/Ar discharge was: 10%C_4F_8/90%Ar, 300 W source power, -100 V V_{SB}, 10 mTorr pressure, and 50 sccm total gas flow rate. The lower source power in the C_4F_8/Ar anchor condition was selected to achieve similar ICD as for the CF_4/Ar anchor condition. Specific processing conditions examined in this work are summarized in Tab. 6.1. Before each experiment, the chamber was cleaned using O_2 plasma followed by a one-minute plasma chamber conditioning step applying the conditions of the discharge being investigated.

	Gas composition			Source power	V_{SB}	Pressure
CF_4/Ar plasmas	20% CF_4	80% Ar		400 W	-50 V -100 V -150 V	40 mTorr
	20% CF_4	80% Ar		400 W	-100 V	20 mTorr 40 mTorr 60 mTorr
	10% CF_4 20% CF_4 30% CF_4	90% Ar 80% Ar 70% Ar		400 W	-100 V	40 mTorr
C_4F_8/Ar plasmas	10% C_4F_8	90% Ar		300 W	-50 V -100 V -150 V	10 mTorr
	10.0% C_4F_8 9.5% C_4F_8 9.0% C_4F_8	90.0%Ar 85.5%Ar 81.0%Ar	0% O_2 5% O_2 10% O_2	300 W	-100 V	10 mTorr
	10.0% C_4F_8 9.0% C_4F_8 8.0% C_4F_8	90.0%Ar 81.0%Ar 72.0%Ar	0% N_2 10% N_2 20% N_2	300 W	-100 V	10 mTorr

Table 6.1: *Processing conditions used in this work.*

6.2.3 Characterization

Material characterization was performed in real-time during processing in the 125 mm ICP by *in-situ* ellipsometry or after processing in the 300 mm ICP by angle-resolved vacuum-transfer XPS. The ellipsometric measurements were performed with a HeNe ellipsometer (632.8 nm) at an angle of incidence of ~72 ^{o}. Multilayer modeling of the metallic masking layer on top of ~38 nm SiO_2 on a Si substrate allowed us to extract individual film thicknesses and ER. The optical material properties used were $\tilde{N}$=3.866-0.028*i* for Si, $\tilde{N}$=1.457-0*i* for SiO_2, $\tilde{N}$=1.39-1.76*i* for TiN, $\tilde{N}$=3.23-3.62*i* for Ti, and $\tilde{N}$=2.2-0*i* for TiO_2.[6.15]

XPS analysis provided information on compositional changes of the film surface. The analysis was performed with a Vacuum Generators ESCA Mk II surface analysis chamber (Mg-Kα source (1253.6 eV); pass energy = 20 eV) at an electron takeoff angle of 90 ° (deep probing depth) and 20 ° (shallow probing depth) relative to the surface. The spectra presented were collected at 90 °.

High resolution Ti 2*p*, C 1*s*, F 1*s*, N 1*s*, O 1*s* and Si 2*p* spectra were decomposed using a least square fit with 50/50 Gaussian-Lorentzian peaks after Shirley background correction and charge compensation by calibrating the binding energy (BE) position of the C─C/C─H peak in the C 1*s* spectrum to 285 eV.[6.16] Charge correction of the TiN Ti 2*p* spectra was performed separately due to differential charging effects[6.17], so BE are referenced to the TiN peak at 454.7 eV.[6.18]

The fitting procedure presented was established by decomposing Ti 2*p* spectra following the work of Bertoti *et al.*[6.18], who combined oxide peaks with TiN loss peaks (L_1 and L_2) as introduced by Strydom *et al.*[6.19]. The TiN loss peaks originate from energy

losses due to intraband transitions between molecular orbitals derived from N 2*p* and Ti 3*d* energy levels and losses due to transitions between surface states formed by oxidation.[6.19] The three resulting peaks in addition to TiN are TiN_xO_y & L_1, Ti_2O_3 & L_2, and TiO_2 with BE shifts of 1.6 eV, 3.0 eV and 4.1 eV, respectively.[6.18] The $TiNF_x$ BE shift of 4.9 eV is in agreement with the work by Robey *et al.*[6.20] and was constrained to a range of ±0.2 eV accounting for effects such as differences in FC layer thickness, differential charging, and differences in the degree of fluorination of $TiNF_x$ (x=1-3).

The spin-orbit splitting (SOS) was kept constant at 5.7 eV for TiN, TiN_xO_y & L_1, Ti_2O_3 & L_2, and TiO_2 and at 5.8 eV for $TiNF_x$, in agreement with Siemensmeyer *et al.*[6.21]. Area ratios of the $p_{3/2}$ to $p_{1/2}$ peaks were kept between 1.8:1 and 2.5:1. Deviations of the $p_{3/2}$ to $p_{1/3}$ peak area ratio from the theoretical value of 2:1 originate from uncertainty in the background subtraction as discussed by others.[6.21-6.23] Peak full widths at half maximum (FWHM) of the $p_{1/2}$ peaks were kept higher than the $p_{3/2}$ FWHM by a factor of 1.1 for fluorinated TiN, and 1.4 for all TiN-oxides and $TiNF_x$. The peak broadening of the $p_{1/2}$ peak with respect to the $p_{3/2}$ is related to Coster-Kronig processes found in 3*d* transition metals.[6.24] The established fitting procedure is summarized in Tab. 6.2 and findings (Secs. 6.3.1.2 and 6.3.2.1) are in good agreement with relevant literature.[6.17-6.24]

Ti-bond	BE (Ti $2p_{3/2}$)	SOS
TiN	454.7 eV	5.7 eV
TiN_xO_y+L_1	456.3 eV	5.7 eV
Ti_2O_3+L_2	457.7 eV	5.7 eV
TiO_2	458.8 eV	5.7 eV
$TiNF_x$	459.6eV±0.2 eV	5.8 eV

Table 6.2: *XPS binding energy (BE) assignments of Ti $2p_{3/2}$ peaks and spin orbit splitting (SOS) for TiN.*

The surface composition was calculated from data obtained at 90 ° using the integrated peak areas of Ti 2*p*, N 1*s*, O 1*s*, C 1*s*, F 1*s*, and Si 2*p* elemental spectra after applying atomic sensitivity factors of 1.80, 0.42, 0.66, 0.25, 1.00, and 0.27, respectively.[6.25] Estimation of FC layer thicknesses was performed by evaluating angle-resolved measurements of the Ti 2*p* spectrum with an attenuation model[6.26] using an attenuation length of 2.5 nm as estimated by Cumpson and Seah's CS2 equation[6.27] for a medium density FC layer (ρ = 1.5 g/cm^3).

Additionally, ICD were estimated by monitoring changes in the bias power while keeping the V_{SB} constant. The ICD is calculated by dividing the bias power by the V_{SB} and chamber substrate area.

6.3 Results

6.3.1 Erosion stages of TiN

The temporal evolution of TiN etching in FC plasmas was measured ellipsometrically and complemented by time-resolved surface characterization by XPS. We identified three characteristic erosion stages (see Fig. 6.1) similar to those identified for Ti in our complementary study[6.6]: (a) removal of oxidized TiN surface layers, (b) steady state erosion with a strongly fluorinated TiN surface covered by a FC film, and (c) erosion of the SiO_2 underlayer with small amounts of fluorinated Ti remaining on the surface. We observed these characteristic erosion stages for all plasma conditions investigated here and will exemplify the temporal evolution with the CF_4/Ar anchor condition.

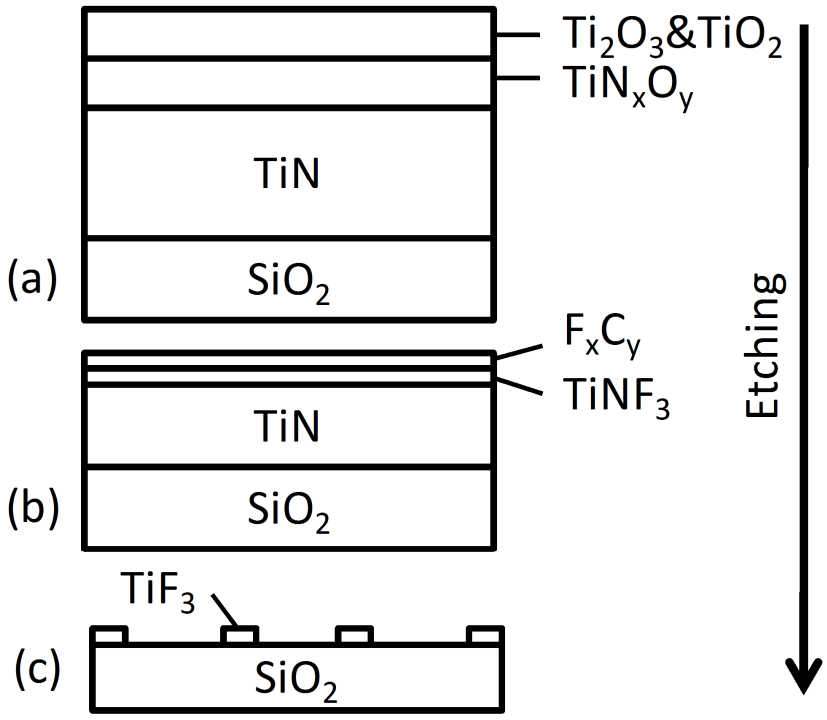

Figure 6.1: *Schematic of TiN hardmask erosion stages: (a) before processing, (b) during steady-state hardmask erosion, and (c) during etching of the SiO_2 layer underneath the TiN film.*

6.3.1.1 Real-time ellipsometric measurements

Figure 6.2 shows the real-time ellipsometric measurements during etching of TiN (black circles) together with two ellipsometric multilayer models. The models for TiN erosion were set up in a similar fashion as for the Ti erosion[6.6] and accounted for TiN with a TiN_xO_y top layer for the erosion start and TiN with a FC surface layer for steady state erosion as described in Fig. 6.1. Both models simulated those layers on top of the Si substrate ($\Psi \approx 7.0^{\circ}$ and $\Delta \approx 178.2^{\circ}$) with a SiO_2 layer between substrate and the TiN film.

The SiO_2 layers were modeled in 1 nm increments and are shown in Fig. 6.2 between 30 nm and 50 nm (black open squares, solid black line). On top of 38 nm SiO_2, we simulated TiN layers in 1 nm increments (red open triangles, solid red line), which provided a near-perfect fit of the experimental measurement for layers up to a thickness of 4 nm. This stage of erosion will be referred to as steady state erosion and was used to extract TiN ER. Between erosion start and steady state erosion, measurements deviated significantly from the TiN simulations. This deviation can be explained by the removal of oxidized surface layers before steady state erosion is reached. Optical properties of TiN_xO_y reported in literature span a wide range ($\tilde{N}$=2.0–2.6) and strongly depend on individual film composition and microstructure.[6.28] We simulated here TiN_xO_y layers for thickness of up to 3 nm in 1 nm increments (solid blue lines) and optical properties between $\tilde{N}$=2.0 and $\tilde{N}$=2.6 in increments of 0.3 (dashed blue lines) on top of 38 nm SiO_2 and 4 nm TiN. Initially, erosion closely followed the simulation for $\tilde{N}$=2.0 until it transitions after ~0.5 nm thickness reduction to simulations of $\tilde{N}$ = 2.6 where it remained until the interface between TiN and TiN_xO_y was reached. We believe that this change in optical properties corresponded to the transition from oxygen-rich TiN_xO_y or Ti-oxides to

more nitrogen-rich TiN_xO_y, as will be discussed in Sec. 6.3.1.2. After steady-state erosion of TiN, Fig. 6.2 shows that measurements deviated from the SiO_2 simulations indicating that there are still small amounts of Ti remaining on the surface (<1 nm) (see Sec. 6.3.1.2).

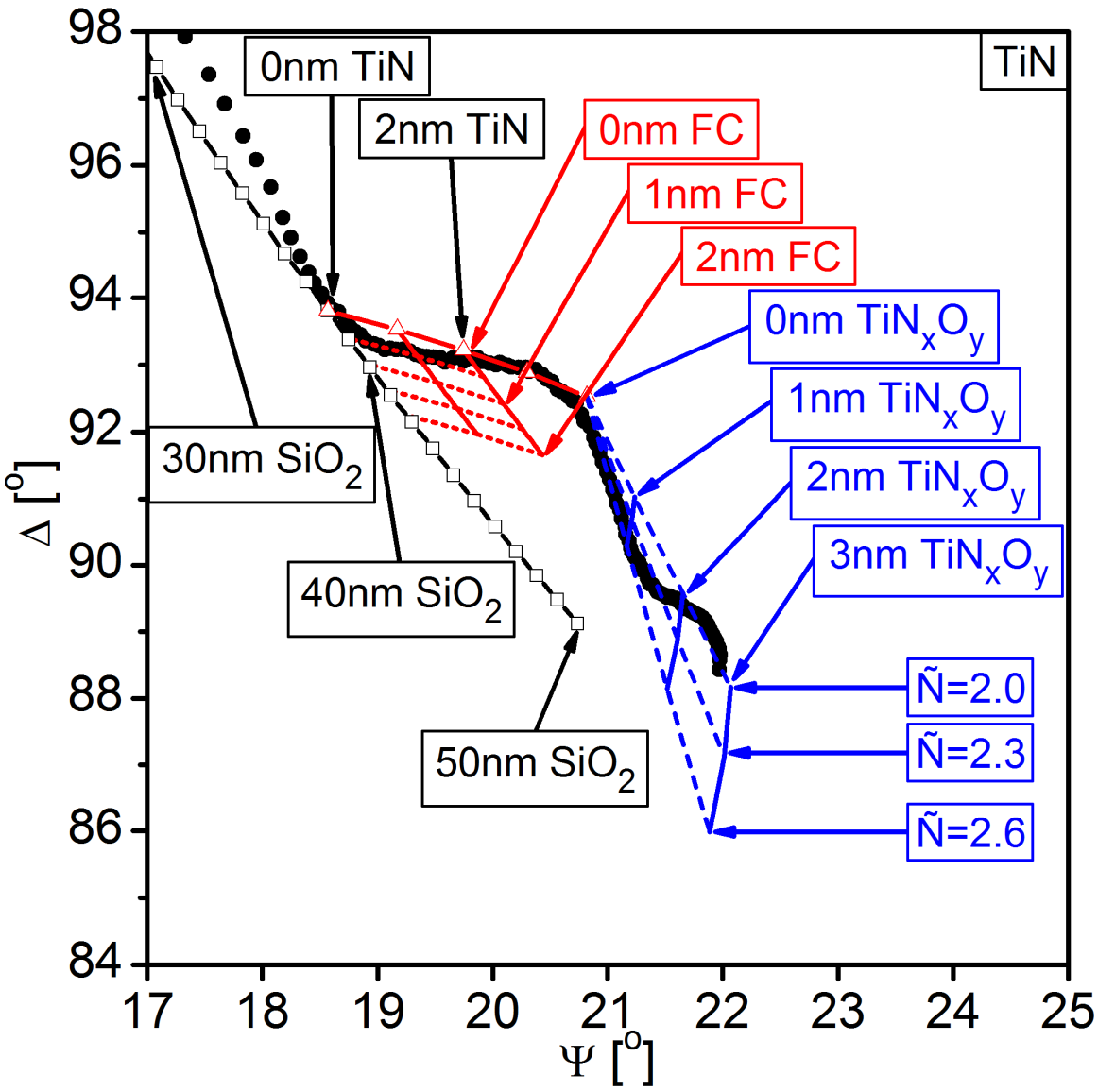

Figure 6.2: *Real-time ellipsometric measurements of TiN erosion in a 20%CF_4/Ar plasma (black circles) superimposed on multilayer optical models. The models describe the initial removal of oxidized layers (dashed blue lines) from the TiN surface, followed by steady state erosion of TiN (solid red line, open triangles), and the erosion of the SiO_2 film (solid black line, open squares). Also shown is the influence of FC films on top of the TiN surface during steady state erosion (dotted red lines).*

Additionally, we present here multilayer simulations for FC films in 0.5 nm increments (dotted red lines) covering the TiN surface during steady state erosion (TiN layer thickness: 0-2 nm). As discussed previously, extraction of the FC thickness from this model was not possible due to significant thickness fluctuations of the SiO_2 layer underneath the TiN film (±1.5 nm) as determined with transmission electron microscopy (TEM).[6.6] However, due to the similarity in optical properties of the FC layer ($\tilde{N}$=1.420-0*i*)[6.29] and SiO_2 ($\tilde{N}$=1.457-0*i*), extracted ER during steady-state erosion of TiN remained unaffected.[6.6]

6.3.1.2 XPS surface characterization

Post-plasma characterization was performed by vacuum-transfer XPS and complemented our ellipsometric measurements. Figure 6.3 shows Ti 2*p* spectra for the identified erosion stages of TiN: (a) pristine material, (b) steady state erosion of the hardmask, and (c) steady state erosion of SiO_2. Individual peaks and peak assignments after spectral decomposition are shown as well.

The pristine TiN film was composed of 26 at.% Ti, 21 at.% N, 26 at.% O, and 27 at.% C. Angle-resolved C 1*s* spectra (not shown here) indicated that C (mainly in the C-C bonding state) was located at the film surface and was likely due to surface contamination introduced after film deposition. The Ti 2*p* spectrum (Fig. 6.3(a)) reveals that most of the TiN was oxidized (91%) with small amounts of TiN (9%). The amount of oxidized TiN includes contributions from the loss peaks (L_1 and L_2) since the relative contribution of the loss peaks could not be distinguished unambiguously. Typically, loss peaks are significantly lower in intensity than the TiN signal ($I(L_1)\approx 50\%\ I(TiN)$ and $I(L_2)\approx 15\%\ I(TiN)$)[6.18] and are not expected to reduce the oxide intensities significantly. The

dominant oxidation state of TiN was TiN_xO_y (65%).[6.30] Angle resolved characterization (not shown here) indicated that higher oxidation states such as Ti_2O_3 (18%) and TiO_2 (7%) were strongly increased for shallow probing depths. This suggested a layered structure of $TiN/TiN_xO_y/Ti_2O_3+TiO_2$ from the bottom of the film to the top. This layered behavior is consistent with our ellipsometric observations (see Sec. 6.3.1.1).

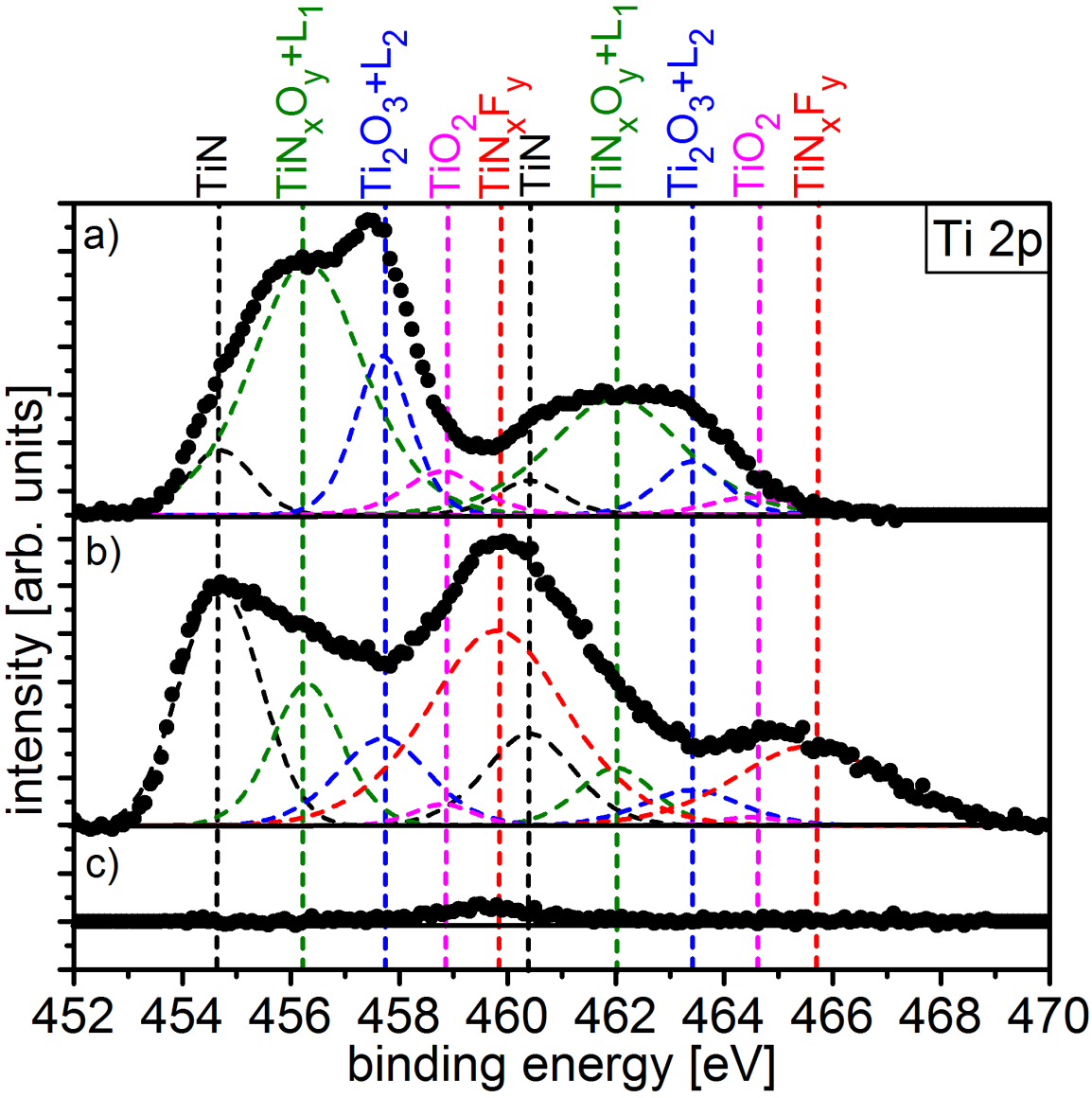

Figure 6.3: *High resolution Ti 2p XPS spectra of TiN (a) before processing, (b) during steady state hardmask erosion and (c) during erosion of the SiO_2 layer in a 20%CF_4/Ar plasma. Peak assignments for TiN, oxides, loss peaks, and fluorides are indicated at the top of the spectra.*

During steady state erosion of TiN in a FC-containing plasma, the TiN surface was saturated with F and covered with a ~0.8 nm thick FC film. The TiN surface was composed of 21 at.% Ti, 20 at.% N, 5 at.% O, 14 at.% C, and 40 at.% F. The Ti 2*p* spectrum (Fig. 6.3(b)) consisted of 47% $TiNF_x$, and 28% of unmodified TiN (not accounting for loss peaks). Comparison of the relative amounts of $TiNF_x$ in the Ti 2*p* and F 1*s* spectra revealed that $TiNF_x$ had a bonding state of $x \approx 2.9$. Furthermore, by performing angle resolved analysis of the C 1*s* spectrum (not shown here) we found that most of the C-C bonds were located at the very top of the FC film while the CF_x bonds were located in between the C-C and $TiNF_x$ layer. During steady state erosion of the SiO_2 layer below the TiN film (Fig. 6.3(c)), minute amounts of fluorinated TiN remained on the surface (~0.2 at.%).

6.3.2 Differences between Ti and TiN erosion

For organic masks, ES over low-k materials strongly depend on the composition and structure of the mask. Low mask ER and correspondingly high ES are found for organic masks with low oxygen content as expressed by the Ohnishi parameter and high content of aromatic structures as described by the ring-parameter.[6.31, 6.32] In contrast to organic masks, metallic masks such as Ti and TiN are difficult to etch in FC plasmas and intrinsically etch-resistant. In order to understand how differences in material composition and density between Ti and TiN impact ER, we compared the erosion of the two materials in CF_4/Ar and C_4F_8/Ar plasmas.

6.3.2.1 Surface composition and FC layer thickness

Surface composition and FC layer thickness after plasma processing under the C_4F_8/Ar anchor condition for various amounts of O_2 and N_2 addition were characterized

by XPS. The corresponding surface compositions and FC layer thicknesses of Ti (see our complementary study[6.6]) and TiN are summarized in Tab. 6.3. Figure 6.4 shows high resolution Ti 2*p*, N 1*s*, F 1*s*, C 1*s*, and O 1*s* spectra of TiN films processed in C_4F_8/Ar plasmas. Relevant findings will be described starting with the anchor condition, followed by O_2 and N_2 addition, respectively, and compared to our previous findings for Ti surfaces.[6.6]

	Plasma condition	Ti [at.%]	N [at.%]	F [at.%]	C [at.%]	O [at.%]	FC thickness [nm]
Ti	C_4F_8/Ar	11	0	54	33	2	1.5
	+5% O_2	20	0	59	17	4	0.8
	+10% O_2	20	0	59	16	5	0.6
	+10% N_2	10	6	59	23	2	1.4
	+20% N_2	12	7	56	22	2	1.3
TiN	C_4F_8/Ar	14	13	46	24	3	1.4
	+5% O_2	17	16	43	17	8	1.0
	+10% O_2	20	17	35	16	12	0.7
	+10% N_2	15	20	41	21	2	1.1
	+20% N_2	15	21	41	21	3	1.4

Table 6.3: *Surface composition and FC layer thickness of Ti and TiN films for the C_4F_8/Ar anchor condition, 5% and 10% O_2 addition, and 10% and 20% N_2 addition.*

For the anchor condition, Ti and TiN surface layers were highly fluorinated, slightly oxidized and covered with a 1.4-1.5 nm thick FC layer (see Tab. 6.3 and Fig. 6.4(a)). The F 1*s* and C 1*s* spectra of TiN show that ~39% of the F were bonded to Ti and ~ 61% of the F were bonded to C in a very F-rich FC layer (CF_x with x=1-3). The minute amounts of oxygen (see O 1*s* spectrum) were primarily bonded to C in the FC layer as O-C and O=C bonds and can be attributed to post plasma reactions during vacuum-transfer to the analysis chamber. Compared to the Ti surface, ~9% of the TiN surface bonding sites were occupied by N, which reduced the amount of F bonded to Ti.

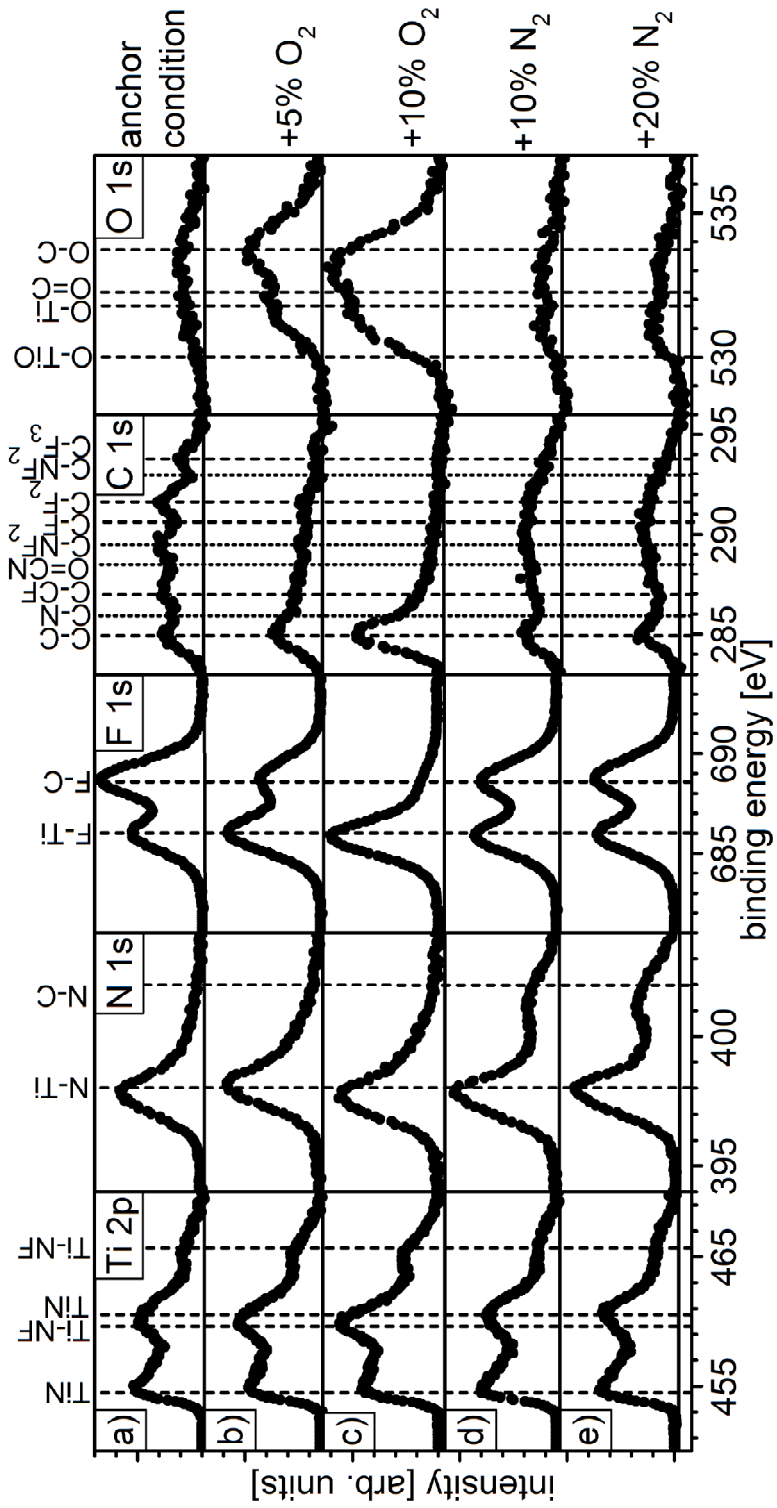

Figure 6.4: *High resolution Ti 2p, N 1s, F 1s, C 1s, and O 1s XPS spectra (from left to right) of TiN surfaces (a) after processing in the C_4F_8/Ar anchor condition and after processing in the anchor condition with (b) 5% and (c) 10% O_2 and (d) 10% and (e) 20% N_2 addition. Peak assignments are indicated at the top of the spectra.*[6.23, 6.25, 6.40-6.44]

For the addition of O_2 to the discharge, FC layers covering Ti and TiN were thinner (0.6 - 1.0 nm), oxidized, and contained less C (see Tab. 6.3 and Figs. 6.4(b) and 6.4(c)). We found that the shape of the Ti 2*p* spectra remains fairly unchanged. The generally higher intensity of the Ti 2*p* spectra can be explained by reduced attenuation of the Ti signal by a thinner FC layer. Comparing F 1*s* and C 1*s* spectra for O_2 addition with the anchor condition reveals that the F-C bonds in the F 1*s* spectra and the C-F_x bonds (x=1-3) in the C 1*s* spectra were strongly decreased. O 1*s* spectra also showed that film surfaces were being oxidized and that oxygen was mainly bonded to the surface as O-C and O=C bonds. The change in the FC layer thickness and composition can be explained by O reacting with the FC film forming volatile products such as CO, CO_2, and COF_2.[6.9] Compared to Ti surfaces, TiN etching with O_2 addition led to strong reduction of F in the FC layer.

For the addition of N_2 to the discharge, FC layers remained constant in thickness (1.1-1.4 nm), were nitrided, and contained less C (see Tab. 6.3 and Figs. 6.4(d) and 6.4(e)). In contrast to O_2 addition, N_2 addition does not reduce the FC layer thickness significantly. We found that the shape and intensity of the Ti 2*p* spectra remained unchanged compared to the anchor condition. F 1*s* spectra show that the amount of F-C bonds slightly decreased compared to the anchor condition. In agreement with the F 1*s* spectra, C 1*s* spectra showed that the distinct structure of CF_x bonds (x = 1 - 3) vanished and was replaced by a broad undefined peak. This change can be attributed to the formation of C-N bonds and is consistent with the N 1*s* spectra showing an additional peak at high BE. TiN peaks at lower BE in the N 1*s* spectra remained unchanged. There were no changes in the O 1*s* spectra compared to the anchor condition, which indicates

that changes in oxidation of the surface did not occur. N_2 addition led to stronger reduction of C-C and C-CF in FC layers for Ti surfaces than TiN surfaces. Overall, changes in surface composition and structure with addition of O_2 or N_2 to the C_4F_8/Ar discharges were very similar for Ti and TiN.

6.3.2.2 Ti and TiN etch rates

Ti and TiN ER were measured ellipsometrically during steady state erosion (see Sec. 6.3.1.1 and Ref. 6) and results are presented in Fig. 6.5. We can observe that for all conditions in both discharge chemistries, i.e. CF_4/Ar (Figs. 6.5(a)-(c)) and C_4F_8/Ar plasmas (Figs. 6.5(d)-(f)), TiN ER were higher than Ti ER by a factor of ~1.0-1.4 and that parameter dependent changes in ER followed similar trends for the two materials. We have previously discussed parameter dependencies for Ti in detail and only present here the most relevant insights.[6.6]

Increasing V_{SB} from -50 V to -150 V in CF_4/Ar and C_4F_8/Ar plasmas (Figs. 6.5(a) and 6.5(d)) increased E_{ion}, leading to higher energy deposition on the surface and thus higher ER. For the low V_{SB} condition in the C_4F_8/Ar discharge, a thick FC film was deposited on the hardmask surface and E_{ion} were not sufficiently high enough to penetrate through the thick FC layer and provide enough energy to volatilize etch products.

Increasing the pressure in the CF_4/Ar condition (Fig. 6.5(b)) led to reduced ICD and higher F concentration in the plasma. These changes can be explained by a higher degree of collision processes in the plasma at high pressures leading to a lower degree of ionization of Ar and a higher degree of dissociation of CF_4.[6.26, 6.29, 6.33] Similar trends were observed when the relative amount of FC feed gas in the CF_4/Ar discharge (Fig. 6.5(c)) was increased.[6.34, 6.35] Dissociation of the O_2 or N_2 added to the discharge (Figs. 6.5(e)

and 6.5(f)) consumed some of the power coupled into the plasma and reduced Ar ionization and C_4F_8 dissociation. This resulted in an ICD decrease and a lower amount of reactive FC species (F and CF_x), which were additionally decreased by recombination with O or N in the gas phase leading to formation of NF_3, CNF_x, COF_2, and other products.[6.9, 6.35] In all cases - change in pressure, change in $\%CF_4$, and O_2/N_2 addition - ER were either limited by the energy input by ions on the surface (reduced ICD) or by the amount of F available for the formation of volatile etch products.

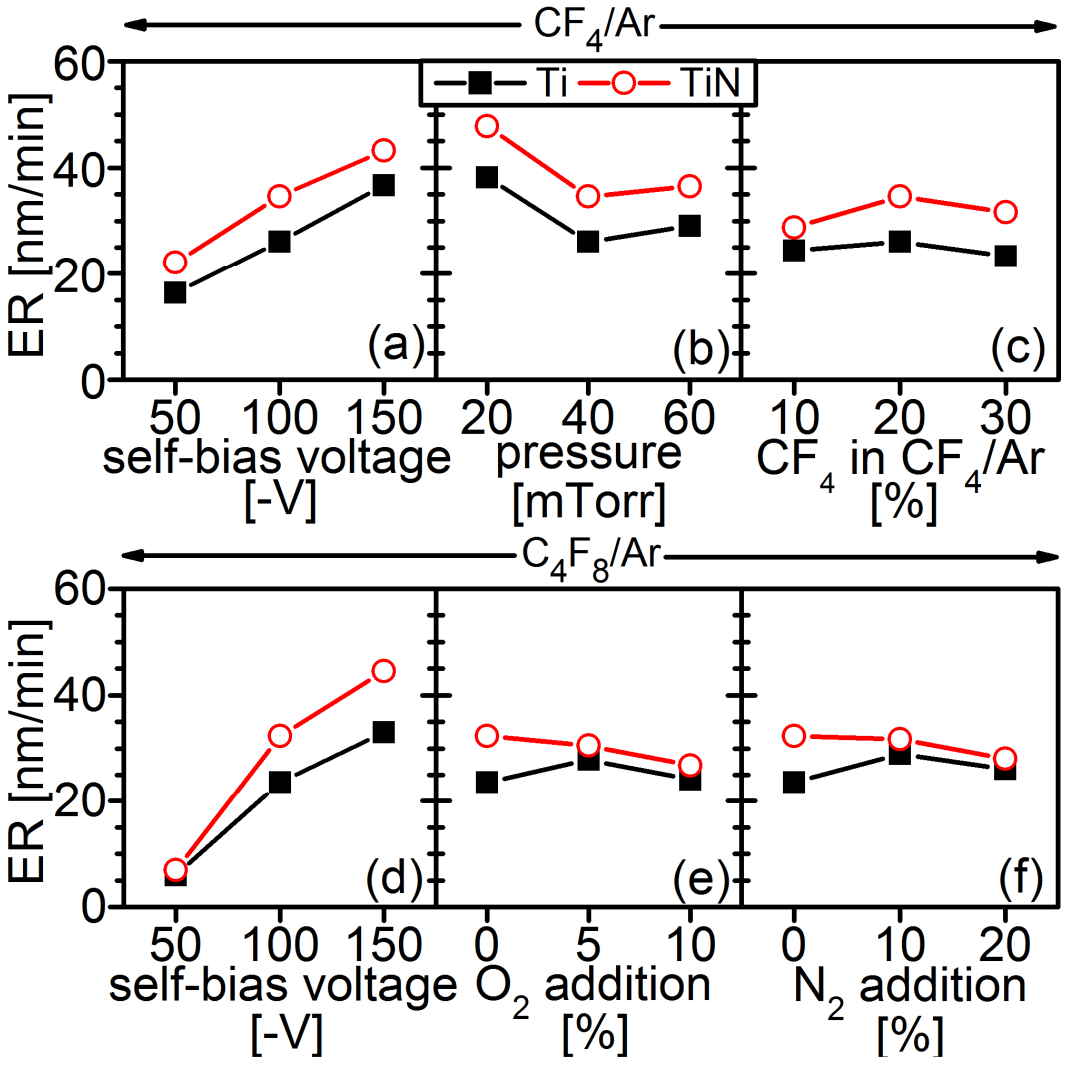

Figure 6.5: *Plasma parameter dependence of Ti and TiN etch rates (ER) on (a) V_{SB}, (b) pressure, and (c) $\%CF_4$ in CF_4/Ar plasmas and (d) V_{SB}, (e) O_2, and (f) N_2 addition in C_4F_8/Ar plasmas.*

6.4 Discussion

6.4.1 Ti and TiN etch mechanism

We discussed in the previous section that ER of Ti and TiN strongly depended on the energy deposition at the surface by ions. Additionally, we have shown previously that erosion of Ti took place in two regimes that were determined by the FC layer thickness. For thin FC layers, etching occurred through chemical sputtering. Thick FC layers limited the ER by reducing ion interactions with the film below the FC layer as well as diffusion of F through the FC layer.[6.6]

In order to account for plasma parameter-dependent differences in ICD and changes in V_{SB}, we calculated etch yields (EY) and energy etch yields (EEY) in addition to TiN ER. EY describe the removal of Ti atoms per incident ion and take material density (ρ) and ICD (j) into account: $EY = ER * \rho * j^{-1}$. The composition and removal during steady state erosion of TiN was assumed to be stoichiometric. EEY consider differences in V_{SB}: $EEY = EY / E_{ion}$.

Figure 6.6 shows the correlation of the three erosion parameters (ER, EY, and EEY) for TiN with the FC layer thickness for varying V_{SB} in CF_4/Ar plasmas as well as for O_2 and N_2 addition to C_4F_8/Ar plasmas. While the ER (Fig. 6.6(a)) did not show any correlation with the FC layer thickness, we found that the EY correlates well with the FC layer thickness for conditions with V_{SB} = -100 V (Fig. 6.6(b), solid black line) and that the EEY followed a universal behavior for all conditions (Fig. 6.6(c), black solid line). These observations are similar to those made for Ti erosion under the same plasma conditions (see dashed lines in Figs. 6.6(b) and 6.6(c)).[6.6] However, when comparing the universal behavior of TiN and Ti, we observed that, in addition to the volumetric material

removal rates (ER), the atomic material removal rates (EY and EEY) increased for TiN as well (see Sec. 6.3.2.2, Figs. 6.6(b) and 6.6(c)). This indicates that there is a fundamental difference in the erosion mechanism between the two materials independent of material density.

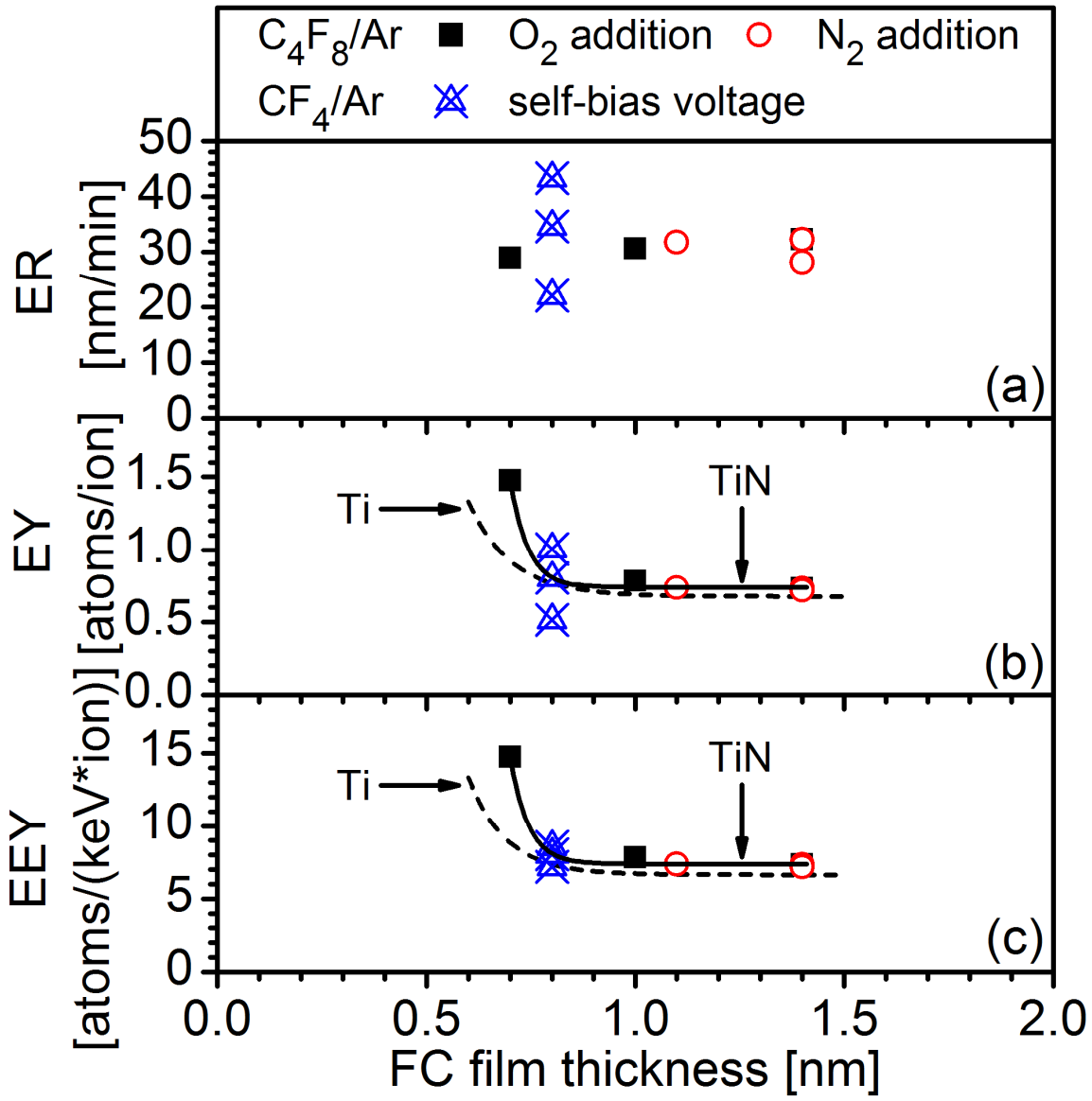

Figure 6.6: *Dependence of (a) TiN etch rate (ER), (b) etch yield (EY), and (c) energy etch yield (EEY) on FC layer thickness for O_2 and N_2 addition to the C_4F_8/Ar discharge and various V_{SB} in the CF_4/Ar discharge. Correlations of Ti EY and EEY with the FC layer thickness are shown as well (dashed lines).*[6.6]

The proposed mechanism of TiN erosion in SF_6 plasmas by Choi *et al.*[6.36] is a four-step process described by increasing the number of F associated with Ti by one in each step, which finally results in volatile TiF_3 or TiF_4. This mechanism is in agreement with our expectations for Ti etching in FC plasmas. However, the removal of N when etching TiN is not considered. We believe that taking the fate of N into account is essential to understand the differences between Ti and TiN erosion rates.

In order to understand material specific differences, we present in Fig. 6.7 the correlation of Ti EY with TiN EY for all CF_4/Ar (a) and C_4F_8/Ar (b) plasma processes. In addition we show in Fig. 6.7(a) data for a pure Ar discharge (same plasma conditions as the CF_4/Ar anchor condition). In pure Ar discharges material erosion is taking place by physical sputtering. During Ar sputtering of TiN, N removal rates are substantially higher than Ti removal rates as estimated by SRIM simulations (Stopping and Range of Ions in Matter).[6.37] This difference in sputter rates leads to strong depletion of N in the surface layer, so TiN ER are mainly determined by the Ti number density. Our expectations are that the corresponding EY of Ti and TiN, which take the individual Ti number densities into account, are very similar. In good agreement with our expectations, we found (Fig. 6.7(a)) that $EY_{TiN} = 1.01 \times EY_{Ti}$, which shows that the densities used for EY calculations are representative for our materials and that N sputtering was fast for TiN and did not slow the removal of Ti atoms.

For addition of FC gas, i.e. CF_4 or C_4F_8, to the Ar discharge, erosion is taking place by chemical sputtering where removal rates of Ti atoms are increased due to reduced threshold energies of TiF_4 evaporation. Tonotani *et al.*[6.38] discuss plasma etching of TiN in terms of the boiling point (BP) of volatile species and conclude that in FC

plasmas the main etch products are TiF_4 (BP = 284 °C) and NF_3 (BP = -128.8 °C), which have significantly lower BP than TiF_3 (BP = 1400 °C). By comparing the BP of TiF_4 and NF_3 it is obvious that the evaporation probability of NF_3 during plasma processing will be significantly higher than for TiF_4 and Ti removal will be the erosion limiting factor.

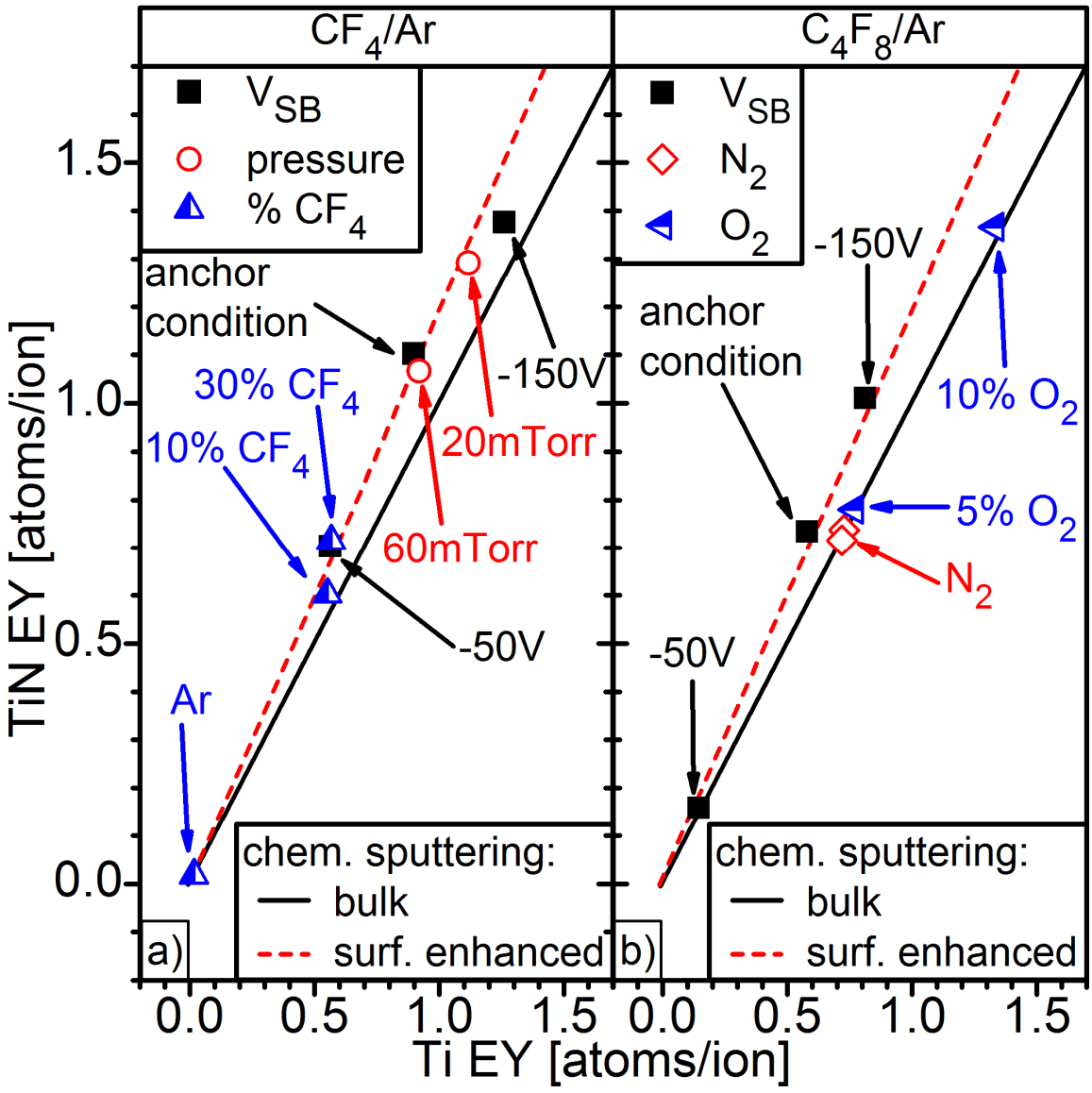

Figure 6.7: *Correlation of Ti and TiN EY for (a) CF_4/Ar and (b) C_4F_8/Ar plasmas for various plasma parameters.*

Under the assumption that Ti number densities determine the erosion behavior, we would expect that TiN ER are higher than Ti ER ($\rho_{\#}$(Ti) = 5.7x10^{22} cm^{-3} and $\rho_{\#}$(Ti) = 5.3x10^{22} cm^{-3}) and EY are identical for both materials under a particular plasma condition (see solid lines in Fig. 6.7).

However, Fig. 6.7 shows that most of the TiN EY in the CF_4/Ar discharges (a) and the TiN EY in the C_4F_8/Ar discharges without addition of O_2 or N_2 (b) were increased by a factor of ~1.2 compared to those of Ti (see dashed lines). The fact that changes in most plasma parameters resulted in the same characteristic EY increase for TiN shows that there must be a systematic difference between Ti and TiN erosion in FC plasmas.

The importance of F for accelerated removal of Ti atoms from TiN is evident for the two CF_4/Ar plasma conditions (Fig. 6.7(a)) that showed only slightly increased EY for TiN: 10% CF_4 addition and -150V V_{SB}. In both conditions the amount of F available for formation of volatile etch products was limited due to the reduced addition of FC gas addition to the plasma (10% CF_4 addition) or rapid consumption of F by fast material removal. This limitation in F supply led to surface sites that remained unsaturated with F and erosion was partially taking place by physical sputtering.

For the C_4F_8/Ar based conditions (Fig. 6.7(b)) we found that for the anchor condition and changes in V_{SB}, the EY of TiN were enhanced and even the most rapid erosion condition (V_{SB}=-150 V) was not F deficient. However, for addition of N_2 and O_2 to the discharge, EY were not material dependent, indicating that TiN EY were F limited as can be explained by recombination of F and N or O in the gas phase (see Sec.

6.2.2.2).[6.9, 6.35] This is in good agreement with our observations of changes in the surface composition (see Sec. 6.3.2.1).

Overall, we found that TiN EY were enhanced in the chemical sputtering and diffusion limited etching regime if the F concentration in the plasma was sufficiently high. One possible explanation for the observed differences in EY between Ti and TiN is based on the rapid removal of N from the TiN surfaces by the formation of highly volatile NF_3. Upon removal of N, additional Ti surface sites are exposed and expected to become rapidly resaturated with F. The introduction of these additional surface sites also leads to a higher areal density of Ti atoms at the film surface (ρ_A). We calculated ρ_A for Ti, TiN with an intact TiN surface (face centered cubic crystal structure), and TiN with all N removed from the topmost monolayer of the TiN surface. For Ti, ρ_A is estimated at ~0.15 Ti atoms/Å^2. For TiN, we found that removing N from the surface and exposing Ti atoms from the crystal plane below results in an increase in ρ_A from ~0.14 Ti atoms/Å^2 to ~0.20 Ti atoms/Å^2. Comparing ρ_A of Ti with TiN after removal of all N shows that ρ_A (TiN) is higher than ρ_A (Ti) by a factor of ~1.3. However, we have established in Sec. 6.3.1.2 that TiN surfaces are slightly less F-saturated than Ti surfaces (TiF_x with x=3.1 and $TiNF_x$ with x=2.9). If we take the reduced fluorination of TiN into account and reduce the increase in ρ_A of TiN by the amount of Ti bonding sites occupied by N (~9%, see Sec. 6.3.2.1) we find that ρ_A of TiN is higher than ρ_A of Ti by a factor of ~1.2. This result is in excellent agreement with the established EY differences between Ti and TiN and indicates that erosion rates of hardmasks are rather determined by the surface area than volume number density of Ti atoms.

This mechanism is in good agreement with the well-established surface kinetics of Si and SiO_2 etching in F-based plasmas.[6.39] Erosion of Si takes place by formation of volatile SiF_4 and erosion rates depend on the availability of F and Si surface sites for chemisorption of F. For SiO_2, surface sites are terminated by O and are not taking part in chemical erosion until the O is removed by an ion sputter process. Thus, EY of SiO_2 (EY only refers to Si atoms) are limited by the amount of surface sites occupied by O and lower compared to Si. For TiN, N exhibits exactly the opposite behavior compared to O in SiO_2. N gets rapidly removed, creating additional Ti surface sites and increases TiN EY.

6.4.2 Selectivity

The differences in the erosion mechanism between Ti and TiN also have a direct impact on the ES over low-k materials that can be achieved with the two hardmask materials. We have previously discussed ES of Ti hardmask over OSG in FC containing plasmas, which were found to be in strong contrast to our expectations from organic masking materials. ES were highest for the less polymerizing CF_4/Ar plasma chemistries and lowest for the more polymerizing C_4F_8/Ar plasma chemistries that typically provide superior ES for photoresists. Since ER of Ti did not change significantly between the two plasma chemistries, it was the OSG ER that determined ES. OSG ER were high in the chemical sputtering regime (thin FC films, CF_4/Ar plasmas) and were strongly reduced in the diffusion limited regime (thick FC layers, C_4F_8/Ar plasmas).

The underlying mechanism of the strong ER reduction in the diffusion limited regime is the limited supply of F which is required in large amounts for low-k material erosion. Furthermore, we found that ES are higher for low Ti ER where low energy input

by ions (low ICD or V_{SB}) reduces Ti ER more strongly than OSG ER since OSG etch products require less energy to get volatilized.[6.6] Figure 6.8 shows ES as a function of hardmask ER for Ti and TiN for all plasma conditions. We observe that less polymerizing plasmas and lower hardmask ER lead to higher ES for Ti and TiN. However, the increased ER of TiN led to a systematic reduction in ES, so Ti remained superior to TiN in terms of ES.

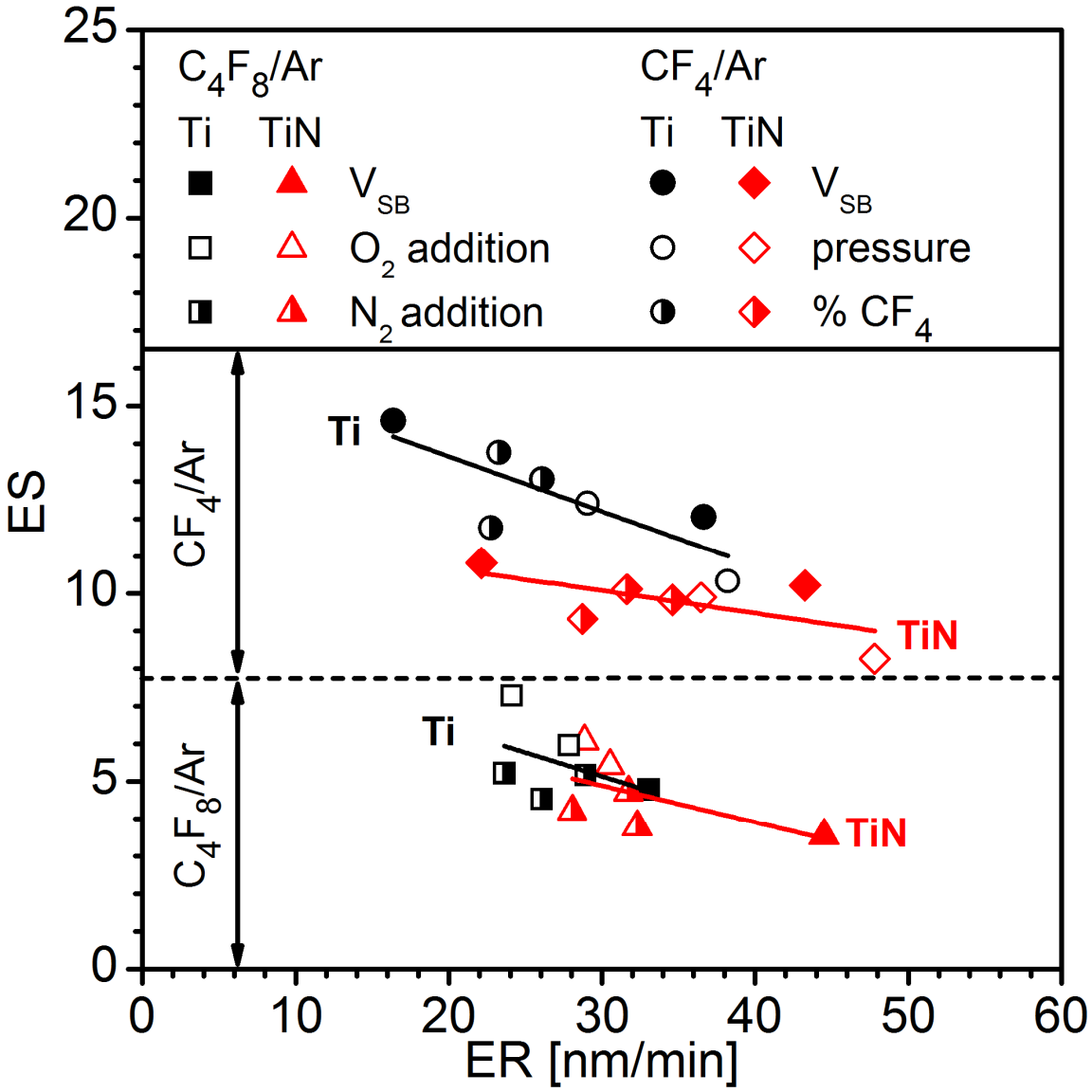

Figure 6.8: *Correlation of etch rates (ER) and etch selectivities (ES) for Ti and TiN erosion in CF_4/Ar and C_4F_8/Ar discharges.*

6.5 Conclusions

We have studied the erosion of Ti and TiN hardmask materials in CF_4/Ar and C_4F_8/Ar plasma discharges to gain insight into material-dependent differences in erosion behavior. For TiN, we have identified using ellipsometric real-time measurements and post-plasma XPS characterization three characteristic erosion stages that were in general agreement with those previously established for Ti: At the start of erosion, oxidized surface layers were removed; during steady-state erosion the TiN surface was strongly fluorinated and covered by a FC layer; during SiO_2 erosion (after removal of the hardmask) some fluorinated Ti remained on the surface.

Plasma parametric studies showed that changes in the surface composition, FC layer thickness, and ER follow the same trends for Ti and TiN. However, TiN ER were found to be higher by a factor of ~1-1.4 than Ti ER. In addition to the volumetric material removal rates (ER) we also compared atomic removal rates (EY and EEY) of the two materials. We found that Ti and TiN atomic removal rates depend on the FC layer thickness and energy deposition by ions. Even EY and EEY of TiN, which take material density into account, were increased by a factor of ~1.2 compared to Ti.

The only plasma conditions that led to reduced differences in EY were F-deficient conditions, indicating that the systematic difference between Ti and TiN was a chemical etching effect and related to fast removal of N from the TiN surface. We believe that removal of N led to the formation of unoccupied surface sites which rapidly became resaturated with F. We estimated the Ti atom number density per surface area after removal of most N in the topmost monolayer and found that it was higher than that of Ti

by a factor of ~1.2. This increase in reactive surface area compared to Ti is in good agreement with the systematically higher TiN ER, EY and EEY that we observed.

The fundamental differences in erosion rates also had a direct impact on the ES over low-k materials. CF_4/Ar plasma provided higher ES than C_4F_8/Ar plasmas mainly due to differences in the OSG ER and ES of Ti were superior to those of TiN. Based on the insights presented here, the introduction of Ti in addition to or as a replacement of TiN has to be carefully considered, weighing the benefits of increased ES and reduced material transparency for optical alignment of the mask.

Chapter 7

General conclusions and future directions

The studies presented in this dissertation are relevant to current and future technologies in nano-manufacturing and make a contribution to the fundamental understanding of plasma-material interactions on the atomic level by: 1) Identifying the contribution of individual plasma components to the modifications of masking materials during plasma-based pattern transfer, 2) determining the influence of material structure and composition on the plasma-induced material modifications, and 3) establishing criteria for plasma conditions, material structure and composition to improve pattern transfer processes.

In Chapter 2, we presented on photoresist (PR) modifications by plasma ultraviolet (UV) and vacuum ultraviolet (VUV) radiation (λ>114 nm) and established modification dependencies on radiation wavelength, polymer structure, and plasma chemistry. Plasma-material interactions were reduced to plasma radiation by a filter approach. This approach prevented PR modifications by ions and other energetic plasma species, and allowed for selection of the exposure wavelength range by using filter materials (borosilicate glass, sapphire and MgF_2) with different cut-off wavelengths in the UV/VUV spectral region.

We found that modifications at the polymer surface and in the polymer bulk by Ar plasma radiation differed fundamentally for 193nm PR and 248nm PR. Styrene-based 248nm PR was highly radiation stable independent of radiation wavelength and was cross-linking in a 15-40 nm deep surface layer. Methacrylate-based 193nm PR was increasingly modified in the material bulk (~200 nm) for reduced radiation wavelength. Radiation exposure led to material shrinkage, oxygen loss, polymer pendant-group detachment, chain-scissioning reactions, and likely softening of the modified layer.

Addition of C_4F_8 to the Ar discharge, typically used for high selectivity pattern transfer into low-k materials, increased radiation in the 150-210 nm wavelength range and led to amplified material modification.

In Chapter 3, we described *in-situ* ellipsometric measurements of PR modifications in Ar plasmas. A custom housing, in combination with the previously introduced filter approach, enabled measurements of changes in PR thickness and optical properties by UV/VUV radiation in real-time and allowed for estimation of modification rates by plasma radiation in different wavelength ranges. For direct plasma exposures, energetic ions (~125 eV) led to rapid (~3-5 s) formation of an ion-crust, i.e. a ~1.8 nm thick, C-rich, dense, and graphitic surface layer. This surface modification was observed for 193nm PR and 248nm PR. However, simultaneous exposure to energetic ions and UV/VUV radiation resulted in significantly higher roughness development for 193nm PR (~6 nm RMS roughness) than for 248nm PR (~1 nm RMS roughness), while both materials remained smooth during UV/VUV radiation exposure. Roughness formation is a synergistic effect of surface modifications by ions and bulk-material modifications by UV/VUV radiation. We found, that during formation of the ion-crust, 193nm PR was modified to a depth of ~60 nm by UV/VUV radiation, while the radiation modification depth of 248nm PR was with ~4 nm on the order of the ion-crust thickness. These material-dependent differences in the modification dynamics and consideration of the changes in mechanical properties can explain the significantly higher roughness formation of 193nm PR by wrinkling of the thin, stressed, ion-modified layer on top of a compliant layer.

In Chapter 4, we showed that He plasma pretreatments (PPT) with strong VUV emission ($\lambda \approx 58.4$ nm) reduced surface and sidewall roughness formation of 193nm PR trench patterns during a subsequent plasma etch (PE). Roughness formation was explained by wrinkling of a thin stiff ion-crust on top of a compliant VUV-modified layer which form simultaneously during PE. The characteristic roughness wavelength is determined by the plane strain moduli of the two layers and the characteristic roughness amplitude depends on the compressive stress at the layer interface that is introduced during surface densification by ions.

During PPT, the PR experienced bulk material softening and stress-free pre-densification (not constrained by the ion crust), thus reducing synergistic effects during the subsequent PE. Furthermore, PPT increased etch resistance during PE by removal of H- and O-containing photolysis products, resulting in only marginally increased total thickness reduction after PPT and PE.

In Chapter 5, we presented erosion stages and plasma parametric erosion dependencies of Ti, a potential future hardmask material, together with organosilicate glass (OSG), a reference low-k material. In the first erosion stage, the highly oxidized surface layers were removed. During steady state erosion, the Ti surface was highly fluorinated (TiF_x with $x \approx 3.1$) and covered with a FC layer. During erosion of the SiO_2 layer underneath, some fluorinated Ti remained on the SiO_2 surface.

During steady state etching, Ti erosion rates were determined by the FC layer thickness and the total energy deposition by ions on the film surface as expressed by the energy etch yield (EEY) that takes ion energy, ion current density, and material density into account. For thin FC layers (CF_4/Ar discharges) erosion was dominated by chemical

sputtering and for thick FC layers (C_4F_8/Ar discharges) erosion was limited by diffusion of F through the surface layer. However, for Ti, etch rates (ER) did not change significantly for the two regimes.

In contrast to Ti, OSG ER were more sensitive to changes in plasma conditions. Etch selectivities (ES) were low in the polymerizing C_4F_8/Ar plasmas due to the limited supply of F for formation of volatile etch products such as CF_4 and HF. ES were high (~15) in the less polymerizing CF_4/Ar discharges at low ion energies where erosion is ion-driven and reduced energy deposition limits removal of etch products from the surface more for Ti than OSG. These observations are in strong contrast to patterning of low-k materials with PR where highest ES are achieved in the diffusion limited regime. This systematic difference can be explained by the stronger ER reduction of PR, which require more F for formation of volatile etch products than low-k materials.

In Chapter 6, we compared material erosion differences between Ti and TiN in FC plasmas. We found that during steady state etching erosion stages, FC layer thicknesses, ER trends, and dependencies of EEY on FC layer thickness and energy deposition by ions were similar for both materials. However, TiN ER and EEY were increased ($EEY_{TiN} \approx 1.2 x EEY_{Ti}$) for conditions without limited F supply. One possible explanation for the difference in EEY is the rapid removal of N from the TiN surface exposing additional Ti atoms from the layer below. Calculations of the Ti atom surface coverage showed that the differences in EEY are in good agreement with the increased surface reactivity of TiN after N removal.

The presented work shows several possible pathways to improve pattern transfer processes for polymeric and metallic masking material to meet demanding manufacturing tolerances of future semiconductor devices.

For PR materials, we have shown that roughness development is a synergistic effect of simultaneous material modifications by energetic ions and plasma UV/VUV radiation. For UV/VUV-sensitive materials such as methacrylate-based 193nm PR, roughness formation during PE was almost one order of magnitude higher than for styrene-based 248nm PR. This strong difference in roughness formation is based on the individual polymer structures. For 193nm PR, the high oxygen content, large amount of ester-bonds and saturation of the polymer backbone with α-CH_3 make the polymer very sensitive to UV/VUV modifications such as pendant group detachment and chain-scissioning reactions that lead to material softening. The low oxygen content, low ester bond concentration and saturation of the polymer backbone with α-H make 248nm PR significantly more radiation stable and prone to cross-linking reactions. Our findings suggest that lower oxygen content, a reduced amount of ester-bonds and saturation of the polymer backbone with α-H in the PR structure would significantly improve the performance of 193nm PR and other novel polymer masks.

Furthermore, we have shown that UV/VUV modifications of 193nm PR are strongly depending on the plasma emission spectrum. Addition of FC to Ar plasmas (typical plasma chemistry for pattern transfer into low-k materials) increased material modification by higher radiation emission of C and FC in the 150-210 nm wavelength range. This shows that future design of reactive plasma processes has to take changes in the emission spectrum into account to minimize roughness formation.

In addition to improving PR materials and optimizing plasma processes, we developed an understanding of the dependence of surface morphology on mechanical material properties. The synergistic effect of roughness formation for blanket and patterned 193nm PR films was reduced by sequentially introducing VUV modifications during He PPT and surface modifications by energetic ions during the PE. Additionally, PPT provided higher etch resistance during PE and PPT are not expected to reduce the feature depth that can be achieved during pattern transfer into low-k materials. Future studies will investigate PPT based on Ar, He, and H_2 plasmas that have strong emission at different wavelength in the UV/VUV spectral region and test PPT on a wide range of polymers relevant to immersion, electron-beam, and extreme ultraviolet lithography.

For metallic hardmask, we have identified differences in the erosion behavior between Ti and TiN and explained the underlying mechanism of selective transfer of patterns into low-k materials. Highest ES were achieved for the less polymerizing plasmas (CF_4/Ar) at low ion energies. Under these conditions OSG ER are not limited by the F available for formation of volatile etch products and metal hardmask experience stronger reduction in ER than OSG since the removal of Ti etch products requires more energy. This is in strong contrast to pattern transfer processes with PR where highly polymerizing plasma discharges provide high ES and shows that for metallic hardmask future etch processes need to be redesigned. The differences in ER and EY between Ti and TiN are based on surface enhanced chemical sputtering for TiN after rapid removal of N creating a more reactive surface. This difference is leading to a systematically lower ES of TiN which is currently the material of choice for metal hardmask in industry. Material selection for the future integration of hardmask in semiconductor manufacturing

will rely on a careful evaluation of the tradeoff between the superior ES of Ti and high transparency of TiN which allows for thicker masks during optical alignment. Additionally, the performance and erosion mechanism of other promising metallic hardmask materials, such as Ta and TaN, need to be carefully tested for pattern transfer processes.

Overall, the ideas identified here, i.e. understanding of the root-cause of PR morphology changes during plasma processing and the fundamentally different etching selectivity mechanisms of metallic hardmask compared to PR when transferring a pattern into a low-k material are a very useful foundation for rational innovations in future design of materials and plasma processes.

References

Chapter 1

1.1 International Technology Roadmap for Semiconductors, www.itrs.net (2009).

1.2 A. Reiser, *Photoreactive Polymers: The Science and Technology of Resists*. (Wiley, New York, 1989).

1.3 G. S. Oehrlein, M. F. Doemling, B. E. E. Kastenmeier, P. J. Matsuo, N. R. Rueger, M. Schaepkens and T. E. F. M. Standaert, IBM J. Res. Dev. **43** (1-2), 181-197 (1999).

1.4 S. Wolf and R. N. Tauber, *Silicon processing for the VLSI era*, 2nd ed. (Lattice Press, 2000).

1.5 E. A. Hudson, Z. Dai, Z. Li, S. Kang, S. Lee, W.-L. Chen and R. Sadjadi, Proc. Int. Symp. Dry. Process. **3**, 253-258 (2003).

1.6 G. S. Oehrlein, R. J. Phaneuf and D. B. Graves, J. Vac. Sci. Technol. B **29** (1), 010801 (2011).

1.7 X. Hua, S. Engelmann, G. S. Oehrlein, P. Jiang, P. Lazzeri, E. Iacob and M. Anderle, J. Vac. Sci. Technol. B **24** (4), 1850-1858 (2006).

1.8 L. Ling, X. Hua, X. Li, G. S. Oehrlein, E. A. Hudson, P. Lazzeri and M. Anderle, J. Vac. Sci. Technol. B **22** (6), 2594-2603 (2004).

1.9 S. Engelmann, R. L. Bruce, F. Weilnboeck, G. S. Oehrlein, D. Nest, D. B. Graves, C. Andes and E. A. Hudson, Plasma Processes and Polymers **6** (8), 484-489 (2009).

1.10 S. Engelmann, R. L. Bruce, T. Kwon, R. Phaneuf, G. S. Oehrlein, Y. C. Bae, C. Andes, D. Graves, D. Nest, E. A. Hudson, P. Lazzeri, E. Lacob and M. Anderle, J. Vac. Sci. Technol. B **25** (4), 1353-1364 (2007).

1.11 X. F. Hua, M. S. Kuo, G. S. Oehrlein, P. Lazzeri, E. Iacob, M. Anderle, C. K. Inoki, T. S. Kuan, P. Jiang and W. L. Wu, J. Vac. Sci. Technol. B **24** (3), 1238-1247 (2006).

1.12 E. Soda, S. Kondo, S. Saito, K. Koyama, B. Jinnai and S. Samukawa, J. Vac. Sci. Technol. B **27** (5), 2117-2123 (2009).

1.13 D. T. Clark and A. Dilks, Journal of Polymer Science Part A-Polymer Chemistry **15** (10), 2321-2345 (1977).

1.14 S.-J. Choi, J. Vac. Sci. Technol. B **25** (3), 868-872 (2007).

1.15 A. Bazin, E. Pargon, X. Mellhaoui, D. Perret, B. Mortini and O. Joubert, Proceedings of SPIE **6923**, 692337 (2008).

1.16 H. Kawahira, N. N. Matsuzawa, E. Matsui, A. Ando, K. M. A. Salam, M. Yoshida, Y. Yamaguchi, K. Kugimiya, T. Tatsumi, H. Nakano, T. Iwai and M. Irie, Proceedings of SPIE **6153**, 615319 (2006).

1.17 A. P. Mahorowala, Proceedings of SPIE **5753**, 575380 (2005).

1.18 E. Pargon, M. Martin, K. Menguelti, L. Azarnouche, J. Foucher and O. Joubert, Appl. Phys. Lett. **94** (10), 103111 (2009).

1.19 E. Pargon, K. Menguelti, M. Martin, A. Bazin, O. Chaix-Pluchery, C. Sourd, S. Derrough, T. Lill and O. Joubert, J. Appl. Phys. **105** (9), 094902 (2009).

1.20 D. P. Kim, X. Yang, J. C. Woo, D. S. Um and C. I. Kim, J. Vac. Sci. Technol. A **27** (6), 1320-1325 (2009).

1.21 M. Darnon, T. Chevolleau, D. Eon, R. Bouyssou, B. Pelissier, L. Vallier, O. Joubert, N. Posseme, T. David, F. Bailly and J. Torres, Microelectronic Engineering **85** (11), 2226-2235 (2008).

1.22 M. Darnon, T. Chevolleau, D. Eon, L. Vallier, J. Torres and O. Joubert, J. Vac. Sci. Technol. B **24** (5), 2262-2270 (2006).

1.23 X. Li, L. Ling, X. F. Hua, M. Fukasawa, G. S. Oehrlein, M. Barela and H. M. Anderson, J. Vac. Sci. Technol. A **21** (1), 284-293 (2003).

1.24 X. F. Hua, X. Wang, D. Fuentevilla, G. S. Oehrlein, F. G. Celii and K. H. R. Kirmse, J. Vac. Sci. Technol. A **21** (5), 1708-1716 (2003).

1.25 T. E. F. M. Standaert, P. J. Matsuo, S. D. Allen, G. S. Oehrlein and T. J. Dalton, J. Vac. Sci. Technol. A **17** (3), 741-748 (1999).

1.26 R. J. Shul and S. J. Pearton, *Handbook of advanced plasma processing techniques*. (Springer, Berlin, New York, 2000).

1.27 J. F. Rabek, *Photodegradation of Polymers: Physical Characteristics and Applications*. (Springer, Berlin, New York, 1996).

1.28 W. Chen and H. Ahmed, Appl. Phys. Lett. **62** (13), 1499-1501 (1993).

1.29 H. H. Solak, D. He, W. Li, S. Singh-Gasson, F. Cerrina, B. H. Sohn, X. M. Yang and P. Nealey, Appl. Phys. Lett. **75** (15), 2328-2330 (1999).

1.30 H. Oizumi, T. Kumise and T. Itani, J. Vac. Sci. Technol. B **26** (6), 2252-2256 (2008).

1.31 H. G. Tompkins and W. A. McGahan, *Spectroscopic Ellipsometry and Reflectometry: A User's Guide*. (Wiley, New York, 1999).

1.32 H. G. Tompkins, *A user's guide to ellipsometry*. (Academic Press, Boston, 1993).

1.33 D. Briggs, *Surface analysis of polymers by XPS and static SIMS*. (Cambridge University Press, Cambridge, U.K., New York, 1998).

Chapter 2

2.1 L. Ling, X. Hua, X. Li, G. S. Oehrlein, E. A. Hudson, P. Lazzeri, and M. Anderle, J. Vac. Sci. Technol. B 22, 2594 (2004).

2.2 E. A. Hudson, Z. Dai, Z. Li, S. Kang, S. Lee, W.─L. Chen, and R. Sadjadi, Proc. Int. Symp. Dry Process 3, 253 (2003).

2.3 X. F. Hua *et al.*, J. Vac. Sci. Technol. B 24, 1238 (2006).

2.4 S. Engelmann *et al.*, J. Vac. Sci. Technol. B 25, 1353 (2007).

2.5 S. Engelmann, R. L. Bruce, F. Weilnboeck, G. S. Oehrlein, D. Nest, D. B. Graves, C. Andes, and E. A. Hudson, Plasma Processes Polym. 6, 484 (2009).

2.6 D. Nest, D. B. Graves, S. Engelmann, R. L. Bruce, F. Weilnboeck, G. S. Oehrlein, C. Andes, and E. A. Hudson, Appl. Phys. Lett. 92, 153113 (2008).

2.7 D. Nest *et al.*, Plasma Processes Polym. 6, 649 (2009).

2.8 C. M. Stafford, B. D. Vogt, C. Harrison, D. Julthongpiput, and R. Huang, Macromolecules 39, 5095 (2006).

2.9 S. K. Basu, A. M. Bergstreser, L. F. Francis, L. E. Scriven, and A. V. McCormick, J. Appl. Phys. 98, 063507 (2005).

2.10 P. C. Lin and S. Yang, Appl. Phys. Lett. 90, 3 (2007).

2.11 R. L. Bruce *et al.*, J. Appl. Phys. 107, 084310 (2010).

2.12 Y. C. Bae and C. Andes (unpublished).

2.13 E. Reichmanis, O. Nalamasu, and F. M. Houlihan, Acc. Chem. Res. 32, 659 (1999).

2.14 X. Hua, X. Wang, D. Fuentevilla, G. S. Oehrlein, F. G. Celii, and K. H. R. Kirmse, J. Vac. Sci. Technol. A 21, 1708 (2003).

2.15 F. E. Truica-Marasescu and M. R. Wertheimer, Macromol. Chem. Phys. 206, 744 (2005).

2.16 S. Tajima and K. Komvopoulos, Appl. Phys. Lett. 89, 124102 (2006).

2.17 N. Negishi, H. Takesue, M. Sumiya, T. Yoshida, Y. Momonoi, and M. Izawa, J. Vac. Sci. Technol. B 23, 217 (2005).

2.18 V. Krastev, I. Reid, C. Galassi, G. Hughes, and E. McGlynn, J. Mater. Sci. Mater. Electron. 16, 541 (2005).

2.19 D. Humbird and D. B. Graves, J. Appl. Phys. 96, 65 (2004).

2.20 J. R. Woodworth, M. E. Riley, V. A. Arnatucci, T. W. Hamilton, and B. P. Aragon, J. Vac. Sci. Technol. A 19, 45 (2001).

2.21 D. T. Clark and A. Dilks, J. Polym. Sci., Part A-Polym. Chem. Ed. 18, 1233 (1980).

2.22 D. T. Clark and A. Dilks, J. Polym. Sci., Part A-Polym. Chem. Ed. 15, 2321 (1977).

2.23 R. L. Bruce *et al.*, J. Vac. Sci. Technol. B 27, 1142 (2009).

2.24 H. G. Tompkins and W. A. McGahan, *Spectroscopic Ellipsometry and Reflectometry: A User's Guide* (Wiley, New York, 1999).

2.25 D. Briggs, *Surface Analysis of Polymers by XPS and Static SIMS* (Cambridge University Press, Cambridge, UK, 1998).

2.26 S. Ben Amor, G. Baud, M. Jacquet, G. Nansé, P. Fioux, and M. Nardin, Appl. Surf. Sci. 153, 172 (2000).

2.27 T. E. F. M. Standaert, M. Schaepkens, N. R. Rueger, P. G. M. Sebel, G. S. Oehrlein, and J. M. Cook, J. Vac. Sci. Technol. A 16, 239 (1998).

2.28 G. Socrates, *Infrared Characteristic Group Frequencies* _Wiley, Chichester, 1980_.

2.29 R. H. Partridge, J. Chem. Phys. 45, 1685 (1966).

2.30 S. Onari, J. Phys. Soc. Jpn. 26, 500 (1969).

2.31 R. H. Partridge, J. Chem. Phys. 47, 4223 (1967).

2.32 R. H. Partridge, J. Chem. Phys. 49, 3656 (1968).

2.33 J. F. Rabek, *Mechanisms of Photophysical Processes and Photochemical Reactions in Polymers: Theory and Applications* (Wiley, Chichester, West Sussex, 1987).

2.34 J. F. Rabek, *Photodegradation of Polymers: Physical Characteristics and Applications* (Springer, Berlin, 1996).

2.35 V. E. Skurat and Y. I. Dorofeev, Angew. Makromol. Chem. 216, 205 (1994).

2.36 S. H. Wheale, C. P. Barker, and J. P. S. Badyal, Langmuir 14, 6699 (1998).

2.37 M. Hudis and L. E. Prescott, J. Polym. Sci., Part B: Polym. Lett. 10, 179 (1972).

2.38 M. Kuzuya, T. Yamashiro, S. Kondo, M. Sugito, and M. Mouri, Macromolecules 31, 3225 (1998).

2.39 R. Wilken, A. Holländer, and J. Behnisch, Surf. Coat. Technol. 116─119, 991 (1999).

2.40 A. Holländer, R. Wilken, and J. Behnisch, Surf. Coat. Technol. 116─119, 788 (1999).

2.41 H. Kawahira *et al.*, Proc. SPIE: Adv. Resist Tech. Process. XXIII 6153, 615319 (2006).

2.42 J. E. Mark, *Physical Properties of Polymers Handbook* (AIP, Woodbury, NY, 1996).

2.43 A. Reiser, *Photoreactive Polymers: The Science and Technology of Resists* (Wiley, New York, 1989).

2.44 L. A. Wall and D. W. Brown, J. Phys. Chem. 61, 129 (1957).

2.45 H. K. Hall and R. Zbinden, J. Am. Chem. Soc. 80, 6428 (1958).

2.46 E. Pargon, K. Menguelti, M. Martin, A. Bazin, O. Chaix-Pluchery, C. Sourd, S. Derrough, T. Lill, and O. Joubert, J. Appl. Phys. 105, 094902 (2009).

2.47 J. Y. Lee, P. C. Painter, and M. M. Coleman, Macromolecules 21, 346 (1988).

2.48 H. Hiraoka, IBM J. Res. Dev. 21, 121 (1977).

2.49 Y. Koval, J. Vac. Sci. Technol. B 22, 843 (2004).

2.50 A. Kamińska and M. Świątek, J. Therm. Anal. 46, 1383 (1996).

2.51 M. Y. Efremov, S. S. Soofi, A. V. Kiyanova, C. J. Munoz, P. Burgardt, F. Cerrina, and P. F. Nealey, Rev. Sci. Instrum. 79, 043903 (2008).

2.52 M. J. May, B. Mortini, M. Heitzmann, P. Gautier, C. Sourd, C. Brochon, and G. Hadziioannou, Microelectron. Eng. 83, 1098 (2006).

2.53 K. Hatada, T. Kitayama, N. Fujimoto, and T. Nishiura, J. Macromol. Sci., Pure Appl. Chem. A30, 645 (1993).

2.54 T. Sasaki, S. Kawagoe, H. Mitsuya, S. Irie, and K. Sakurai, J. Polym. Sci., Part B: Polym. Phys. 44, 2475 (2006).

2.55 S. Engelmann *et al.*, J. Vac. Sci. Technol. B 27, 92 (2009).

2.56 R. C. Preston, C. Brookes, and F. W. J. Clutterbuck, J. Phys. E 13, 1206 (1980).

2.57 P. J. Key and R. C. Preston, J. Phys. E 13, 866 (1980).

Chapter 3

3.1 International Technology Roadmap for Semiconductors, www.itrs.net (2009).

3.2 T. Kajita, Y. Nishimura, M. Yamamoto, H. Ishii, A. Soyano, A. Kataoka, M. Slezak, M. Shimizu, P. R. Varanasi, G. Jordahamo, M. C. Lawson, R. Chen, W. R. Brunsvold, W. Li, R. D. Allen, H. Ito, H. D. Truong and T. I. Wallow, Proceedings of SPIE: Advances in Resist Technology and Processing XVIII **4345**, 712-724 (2001).

3.3 L. Ling, X. Hua, X. Li, G. S. Oehrlein, E. A. Hudson, P. Lazzeri and M. Anderle, J. Vac. Sci. Technol. B **22** (6), 2594-2603 (2004).

3.4 E. A. Hudson, Z. Dai, Z. Li, S. Kang, S. Lee, W.-L. Chen and R. Sadjadi, Proc. Int. Symp. Dry. Process. **3**, 253-258 (2003).

3.5 X. F. Hua, M. S. Kuo, G. S. Oehrlein, P. Lazzeri, E. Iacob, M. Anderle, C. K. Inoki, T. S. Kuan, P. Jiang and W. L. Wu, J. Vac. Sci. Technol. B **24** (3), 1238-1247 (2006).

3.6 S. Engelmann, R. L. Bruce, T. Kwon, R. Phaneuf, G. S. Oehrlein, Y. C. Bae, C. Andes, D. Graves, D. Nest, E. A. Hudson, P. Lazzeri, E. Lacob and M. Anderle, J. Vac. Sci. Technol. B **25** (4), 1353-1364 (2007).

3.7 S. Engelmann, R. L. Bruce, F. Weilnboeck, G. S. Oehrlein, D. Nest, D. B. Graves, C. Andes and E. A. Hudson, Plasma Processes and Polymers **6** (8), 484-489 (2009).

3.8 F. Weilnboeck, R. L. Bruce, S. Engelmann, G. S. Oehrlein, D. Nest, T.-Y. Chung, D. Graves, M. Li, D. Wang, C. Andes and E. A. Hudson, J. Vac. Sci. Technol. B **28** (5), 993-1004 (2010).

3.9 T. Y. Chung, D. Nest, D. B. Graves, F. Weilnboeck, R. L. Bruce, G. S. Oehrlein, D. Wang, M. Li and E. A. Hudson, J. Phys. D-Appl. Phys. **43** (27), 272001 (2010).

3.10 T.-Y. Chung, D. B. Graves, F. Weilnboeck, R. L. Bruce, G. S. Oehrlein, M. Li and E. A. Hudson, Plasma Processes and Polymers (2011).

3.11 R. L. Bruce, S. Engelmann, T. Lin, T. Kwon, R. J. Phaneuf, G. S. Oehrlein, B. K. Long, C. G. Willson, J. J. Vegh, D. Nest, D. B. Graves and A. Alizadeh, J. Vac. Sci. Technol. B **27** (3), 1142-1155 (2009).

3.12 R. L. Bruce, F. Weilnboeck, T. Lin, R. J. Phaneuf, G. S. Oehrlein, B. K. Long, C. G. Willson and A. Alizadeh, J. Vac. Sci. Technol. B **29** (4), 041604 (2011).

3.13 R. L. Bruce, F. Weilnboeck, T. Lin, R. J. Phaneuf, G. S. Oehrlein, B. K. Long, C. G. Willson, J. J. Vegh, D. Nest and D. B. Graves, J. Appl. Phys. **107** (8), 084310 (2010).

3.14 D. Nest, T. Y. Chung, D. B. Graves, S. Engelmann, R. L. Bruce, F. Weilnboeck, G. S. Oehrlein, D. Y. Wang, C. Andes and E. A. Hudson, Plasma Processes and Polymers **6** (10), 649-657 (2009).

3.15 D. Nest, T. Y. Chung, J. J. Vegh, D. B. Graves, R. L. Bruce, T. Lin, R. J. Phaneuf, G. S. Oehrlein, B. K. Long and C. G. Willson, J. Phys. D-Appl. Phys. **43** (8), 085204 (2010).

3.16 D. Nest, D. B. Graves, S. Engelmann, R. L. Bruce, F. Weilnboeck, G. S. Oehrlein, C. Andes and E. A. Hudson, Appl. Phys. Lett. **92** (15), 153113 (2008).

3.17 S. Engelmann, R. L. Bruce, M. Sumiya, T. Kwon, R. Phaneuf, G. S. Oehrlein, C. Andes, D. Graves, D. Nest and E. A. Hudson, J. Vac. Sci. Technol. B **27** (1), 92-106 (2009).

3.18 S. Engelmann, R. L. Bruce, F. Weilnboeck, M. Sumiya, T. Kwon, R. Phaneuf, G. S. Oehrlein, C. Andes, D. Graves, D. Nest and E. A. Hudson, J. Vac. Sci. Technol. B **27** (3), 1165-1179 (2009).

3.19 G. S. Oehrlein, R. J. Phaneuf and D. B. Graves, J. Vac. Sci. Technol. B **29** (1), 010801 (2011).

3.20. X. Hua, S. Engelmann, G. S. Oehrlein, P. Jiang, P. Lazzeri, E. Iacob and M. Anderle, J. Vac. Sci. Technol. B **24** (4), 1850-1858 (2006).

3.21 M. Sumiya, R. Bruce, S. Engelmann, F. Weilnboeck and G. S. Oehrlein, J. Vac. Sci. Technol. B **26** (5), 1637-1646 (2008).

3.22 J. J. Vegh, D. Nest, D. B. Graves, R. Bruce, S. Engelmann, T. Kwon, R. J. Phaneuf, G. S. Oehrlein, B. K. Long and C. G. Willson, Appl. Phys. Lett. **91** (23), 233113 (2007).

3.23 J. J. Vegh, D. Nest, D. B. Graves, R. Bruce, S. Engelmann, T. Kwon, R. J. Phaneuf, G. S. Oehrlein, B. K. Long and C. G. Willson, J. Appl. Phys. **104** (3), 034308 (2008).

3.24 H. Kawahira, N. N. Matsuzawa, E. Matsui, A. Ando, K. M. A. Salam, M. Yoshida, Y. Yamaguchi, K. Kugimiya, T. Tatsumi, H. Nakano, T. Iwai and M. Irie, Proceedings of SPIE **6153**, 615319 (2006).

3.25 H. Hiraoka, IBM J. Res. Dev. **21** (2), 121-130 (1977).

3.26 E. Pargon, K. Menguelti, M. Martin, A. Bazin, O. Chaix-Pluchery, C. Sourd, S. Derrough, T. Lill and O. Joubert, J. Appl. Phys. **105** (9), 094902 (2009).

3.27 M. J. May, B. Mortini, M. Heitzmann, P. Gautier, C. Sourd, C. Brochon and G. Hadziioannou, Microelectronic Engineering **83** (4-9), 1098-1102 (2006).

3.28 E. Reichmanis, O. Nalamasu and F. M. Houlihan, Accounts Chem. Res. **32** (8), 659-667 (1999).

3.29 X. Hua, X. Wang, D. Fuentevilla, G. S. Oehrlein, F. G. Celii and K. H. R. Kirmse, J. Vac. Sci. Technol. A **21** (5), 1708-1716 (2003).

3.30 N. Negishi, H. Takesue, M. Sumiya, T. Yoshida, Y. Momonoi and M. Izawa, J. Vac. Sci. Technol. B **23** (1), 217-223 (2005).

3.31 V. Krastev, I. Reid, C. Galassi, G. Hughes and E. McGlynn, J. Mater. Sci.-Mater. Electron. **16** (8), 541-547 (2005).

3.32 D. Humbird and D. B. Graves, J. Appl. Phys. **96** (1), 65-70 (2004).

3.33 H. G. Tompkins and W. A. McGahan, *Spectroscopic Ellipsometry and Reflectometry: A User's Guide*. (Wiley, New York, 1999).

3.34 Yu. Ralchenko, A.E. Kramida, J. Reader and NIST ASD Team, NIST Atomic Spectra Database (ver. 4.1.0) (2011).

3.35 B. P. Lavrov, A. S. Melnikov, M. Käning and J. Röpcke, Physical Review E **59** (3), 3526 (1999).

3.36 A. C. Fozza, M. Moisan and M. R. Wertheimer, J. Appl. Phys. **88** (1), 20-33 (2000).

3.37 B. R. LaFreniere, D. R. Wiederin, V. A. Fassel and R. S. Houk, Spectrochimica Acta Part B: Atomic Spectroscopy **51** (1), 3-12 (1996).

3.38 K. Myneni and J. Kielkopf, Journal of Physics B: Atomic, Molecular and Optical Physics **21** (16), 2871 (1988).

3.39 D. T. Clark and A. Dilks, Journal of Polymer Science Part A-Polymer Chemistry **18** (4), 1233-1246 (1980).

3.40 D. T. Clark and A. Dilks, Journal of Polymer Science Part A-Polymer Chemistry **15** (10), 2321-2345 (1977).

3.41 F. E. Truica-Marasescu and M. R. Wertheimer, Macromolecular Chemistry and Physics **206** (7), 744-757 (2005).

3.42 Partridg.Rh, Journal of Chemical Physics **45** (5), 1685 (1966).

3.43 Partridg.Rh, Journal of Chemical Physics **47** (10), 4223 (1967).

3.44 Partridg.Rh, Journal of Chemical Physics **49** (8), 3656 (1968).

3.45 S. Onari, Journal of the Physical Society of Japan. **26**, 500 (1969).

3.46 J. F. Rabek, *Mechanisms of Photophysical Processes and Photochemical Reactions in Polymers: Theory and Applications*. (Wiley, Chichester [West Sussex], New York, 1987).

3.47 J. F. Rabek, *Photodegradation of Polymers: Physical Characteristics and Applications*. (Springer, Berlin, New York, 1996).

3.48 J. R. Woodworth, M. E. Riley, V. A. Arnatucci, T. W. Hamilton and B. P. Aragon, J. Vac. Sci. Technol. A **19** (1), 45-55 (2001).

3.49 B. H. Ong, X. Yuan and S. C. Tjin, Appl. Opt. **45** (31), 8036-8039 (2006).

3.50 K. J. Miller, Journal of the American Chemical Society **112** (23), 8533-8542 (1990).

3.51 M. J. Titus, D. G. Nest and D. B. Graves, J. Phys. D-Appl. Phys. **42** (15), 4 (2009).

Chapter 4

4.1 G. S. Oehrlein, R. J. Phaneuf and D. B. Graves, J. Vac. Sci. Technol. B 29 (1), 010801 (2011).

4.2 International Technology Roadmap for Semiconductors, www.itrs.net (2009).

4.3 R. L. Bruce, F. Weilnboeck, T. Lin, R. J. Phaneuf, G. S. Oehrlein, B. K. Long, C. G. Willson, J. J. Vegh, D. Nest and D. B. Graves, J. Appl. Phys. 107 (8), 084310 (2010).

4.4 R. L. Bruce, F. Weilnboeck, T. Lin, R. J. Phaneuf, G. S. Oehrlein, B. K. Long, C. G. Willson and A. Alizadeh, J. Vac. Sci. Technol. B 29 (4), 041604 (2011).

4.5 D. Nest, D. B. Graves, S. Engelmann, R. L. Bruce, F. Weilnboeck, G. S. Oehrlein, C. Andes and E. A. Hudson, Appl. Phys. Lett. 92 (15), 153113 (2008).

4.6 F. Weilnboeck, N. Kumar, G. S. Oehrlein, T.-Y. Chung, D. B. Graves, M. Li and E. A. Hudson, J. Vac. Sci. Technol. B (to be submitted).

4.7 F. Weilnboeck, R. L. Bruce, S. Engelmann, G. S. Oehrlein, D. Nest, T.-Y. Chung, D. Graves, M. Li, D. Wang, C. Andes and E. A. Hudson, J. Vac. Sci. Technol. B 28 (5), 993-1004 (2010).

4.8 E. Pargon, M. Martin, K. Menguelti, L. Azarnouche, J. Foucher and O. Joubert, Appl. Phys. Lett. 94 (10), 103111 (2009).

4.9 Yu. Ralchenko, A.E. Kramida, J. Reader and NIST ASD Team, NIST Atomic Spectra Database (ver. 4.1.0) (2011).

4.10 T. E. F. M. Standaert, P. J. Matsuo, S. D. Allen, G. S. Oehrlein and T. J. Dalton, J. Vac. Sci. Technol. A 17 (3), 741-748 (1999).

4.11 S. Engelmann, R. L. Bruce, T. Kwon, R. Phaneuf, G. S. Oehrlein, Y. C. Bae, C. Andes, D. Graves, D. Nest, E. A. Hudson, P. Lazzeri, E. Lacob and M. Anderle, J. Vac. Sci. Technol. B **25** (4), 1353-1364 (2007).

4.12 X. Hua, S. Engelmann, G. S. Oehrlein, P. Jiang, P. Lazzeri, E. Iacob and M. Anderle, J. Vac. Sci. Technol. B 24 (4), 1850-1858 (2006).

4.13 D. Metzler, F. Weilnboeck, G. S. Oehrlein, R. L. Bruce, S. Engelmann and N. Fuller, J. Vac. Sci. Technol. B in preparation (2011).

4.14 T.-Y. Chung, D. B. Graves, F. Weilnboeck, R. L. Bruce, G. S. Oehrlein, M. Li and E. A. Hudson, Plasma Processes and Polymers (2011).

4.15 H. Gokan, S. Esho and Y. Ohnishi, J. Electrochem. Soc. 130 (1), 143-146 (1983).

Chapter 5

5.1 M. Darnon, T. Chevolleau, D. Eon, L. Vallier, J. Torres and O. Joubert, J. Vac. Sci. Technol. B 24 (5), 2262-2270 (2006).

5.2 M. Darnon, T. Chevolleau, D. Eon, R. Bouyssou, B. Pelissier, L. Vallier, O. Joubert, N. Posseme, T. David, F. Bailly and J. Torres, Microelectronic Engineering 85 (11), 2226-2235 (2008).

5.3 M. Darnon, T. Chevolleau, T. David, J. Ducote, N. Posseme, R. Bouyssou, F. Bailly, D. Perret and O. Joubert, J. Vac. Sci. Technol. B 28 (1), 149-156 (2010).

5.4 T. E. F. M. Standaert, M. Schaepkens, N. R. Rueger, P. G. M. Sebel, G. S. Oehrlein and J. M. Cook, J. Vac. Sci. Technol. A 16 (1), 239-249 (1998).

5.5 X. F. Hua, X. Wang, D. Fuentevilla, G. S. Oehrlein, F. G. Celii and K. H. R. Kirmse, J. Vac. Sci. Technol. A 21 (5), 1708-1716 (2003).

5.6 R. L. Bruce, F. Weilnboeck, T. Lin, R. J. Phaneuf, G. S. Oehrlein, B. K. Long, C. G. Willson and A. Alizadeh, J. Vac. Sci. Technol. B 29 (2011).

5.7 N. Negishi, H. Takesue, M. Sumiya, T. Yoshida, Y. Momonoi and M. Izawa, J. Vac. Sci. Technol. B 23 (1), 217-223 (2005).

5.8 V. Krastev, I. Reid, C. Galassi, G. Hughes and E. McGlynn, J. Mater. Sci.-Mater. Electron. 16 (8), 541-547 (2005).

5.9 D. Humbird and D. B. Graves, J. Appl. Phys. 96 (1), 65-70 (2004).

5.10 H. G. Tompkins and W. A. McGahan, *Spectroscopic Ellipsometry and Reflectometry : A User's Guide*. (Wiley, New York, 1999).

5.11 D. Briggs, *Surface analysis of polymers by XPS and static SIMS*. (Cambridge University Press, Cambridge, U.K., New York, 1998).

5.12 R. d'Agostino, F. Fracassi, C. Pacifico and P. Capezzuto, J. Appl. Phys. 71 (1), 462-471 (1992).

5.13 C. D. Wagner, Riggs, W.M., Davis, L.E., and Moulder, J.F. , *Handbook of X-ray Photoelectron Spectroscopy*. (Perkin Elmer, 1979).

5.14 P. Prieto and R. E. Kirby, J. Vac. Sci. Technol. A 13 (6), 2819-2826 (1995).

5.15 M. Wolff, J. W. Schultze and H. H. Strehblow, Surface and Interface Analysis 17 (10), 726-736 (1991).

5.16 S. W. Robey, M. A. Jaso and G. S. Oehrlein, J. Appl. Phys. 65 (8), 2951-2956 (1989).

5.17 B. Siemensmeyer and J. W. Schultze, Surface and Interface Analysis 16 (1-12), 309-314 (1990).

5.18 E. McCafferty and J. P. Wightman, Applied Surface Science 143 (1-4), 92-100 (1999).

5.19 R. Nyholm and et al., Journal of Physics F: Metal Physics 11 (8), 1727 (1981).

5.20 D. Briggs and M. P. Seah, *Practical surface analysis : by auger and x-ray photoelectron spectroscopy*. (Wiley, Chichester ; New York, 1983).

5.21 N. R. Rueger, J. J. Beulens, M. Schaepkens, M. F. Doemling, J. M. Mirza, T. E. F. M. Standaert and G. S. Oehrlein, J. Vac. Sci. Technol. A 15 (4), 1881-1889 (1997).

5.22 P. J. Cumpson and M. P. Seah, Surface and Interface Analysis 25 (6), 430-446 (1997).

5.23 N. R. Rueger, M. F. Doemling, M. Schaepkens, J. J. Beulens, T. E. F. M. Standaert and G. S. Oehrlein, J. Vac. Sci. Technol. A 17 (5), 2492-2502 (1999).

5.24 M. Schaepkens, I. Martini, E. A. Sanjuan, X. Li, G. S. Oehrlein, W. L. Perry and H. M. Anderson, J. Vac. Sci. Technol. A 19 (6), 2946-2957 (2001).

5.25 J.-H. Min, G.-R. Lee, J.-K. Lee and S. H. Moon, J. Vac. Sci. Technol. B 22 (6), 2580-2588 (2004).

5.26 S. Engelmann, R. L. Bruce, F. Weilnboeck, M. Sumiya, T. Kwon, R. Phaneuf, G. S. Oehrlein, C. Andes, D. Graves, D. Nest and E. A. Hudson, J. Vac. Sci. Technol. B 27 (3), 1165-1179 (2009).

5.27 H.-H. Doh, J.-H. Kim, S.-H. Lee and K.-W. Whang, J. Vac. Sci. Technol. A 14 (5), 2827-2834 (1996).

5.28 S. Engelmann, R. L. Bruce, F. Weilnboeck, G. S. Oehrlein, D. Nest, D. B. Graves, C. Andes and E. A. Hudson, Plasma Processes and Polymers 6 (8), 484-489 (2009).

5.29 C. H. Lee, D. H. Kim, N. E. Lee and G. C. Kwon, J. Vac. Sci. Technol. A 24 (4), 1386-1394 (2006).

5.30 M. Schaepkens, T. E. F. M. Standaert, N. R. Rueger, P. G. M. Sebel, G. S. Oehrlein and J. M. Cook, J. Vac. Sci. Technol. A 17 (1), 26-37 (1999).

5.31 C. W. Lee and Y. T. Kim, J. Vac. Sci. Technol. B 24 (4), 1956-1956 (2006).

5.32 S. Engelmann, R. L. Bruce, M. Sumiya, T. Kwon, R. Phaneuf, G. S. Oehrlein, C. Andes, D. Graves, D. Nest and E. A. Hudson, J. Vac. Sci. Technol. B 27 (1), 92-106 (2009).

5.33 X. Li, L. Ling, X. F. Hua, G. S. Oehrlein, Y. C. Wang and H. M. Anderson, J. Vac. Sci. Technol. A 21 (6), 1955-1963 (2003).

5.34 X. Li, X. F. Hua, L. Ling, G. S. Oehrlein, M. Barela and H. M. Anderson, J. Vac. Sci. Technol. A-Vac. Surf. Films 20 (6), 2052-2061 (2002).

5.35 X. Hua, X. Wang, D. Fuentevilla, G. S. Oehrlein, F. G. Celii and K. H. R. Kirmse, J. Vac. Sci. Technol. A 21 (5), 1708-1716 (2003).

5.36 X. Li, L. Ling, X. F. Hua, M. Fukasawa, G. S. Oehrlein, M. Barela and H. M. Anderson, J. Vac. Sci. Technol. A 21 (1), 284-293 (2003).

5.37 T. Standaert, C. Hedlund, E. A. Joseph, G. S. Oehrlein and T. J. Dalton, J. Vac. Sci. Technol. A 22 (1), 53-60 (2004).

5.38 J. Hong and G. Turban, Diamond and Related Materials 8 (2-5), 572-576 (1999).

5.39 W. W. Martienssen, H.;, *Springer Handbook of Condensed Matter and Materials Data*. (Springer, Berlin, 2005).

5.40 T. E. F. M. Standaert, P. J. Matsuo, S. D. Allen, G. S. Oehrlein and T. J. Dalton, J. Vac. Sci. Technol. A 17 (3), 741-748 (1999).

5.41 J. Tonotani, T. Iwamoto, F. Sato, K. Hattori, S. Ohmi and H. Iwai, J. Vac. Sci. Technol. B 21 (5), 2163-2168 (2003).

5.42 P. Leerungnawarat, K. Lee, S. Pearton, F. Ren and S. Chu, Journal of Electronic Materials 30 (3), 202-206 (2001).

5.43 M. Koh, H. Yumoto, H. Higashi and T. Nakajima, Journal of Fluorine Chemistry 97 (1-2), 239-246 (1999).

5.44 P. J. Matsuo, T. E. F. M. Standaert, S. D. Allen, G. S. Oehrlein and T. J. Dalton, J. Vac. Sci. Technol. B 17 (4), 1435-1447 (1999).

5.45 N. Ohtsu, K. Kodama, K. Kitagawa and K. Wagatsuma, Applied Surface Science 255 (16), 7351-7356 (2009).

5.46 P. Gonon, The European Physical Journal - Applied Physics 32 (01), 15-21 (2005).

5.47 S. Ben Amor, G. Baud, M. Jacquet, G. Nanse, P. Fioux and M. Nardin, Applied Surface Science 153 (2-3), 172-183 (2000).

Chaper 6

6.1 M. Y. Kwak, D. H. Shin, T. W. Kang and K. N. Kim, Thin Solid Films 339 (1-2), 290-293 (1999).

6.2 Y. Zeng, S. W. Russell, A. J. McKerrow, P. Chen and T. L. Alford, Thin Solid Films 360 (1-2), 283-292 (2000).

6.3 M. Darnon, T. Chevolleau, D. Eon, L. Vallier, J. Torres and O. Joubert, J. Vac. Sci. Technol. B 24 (5), 2262-2270 (2006).

6.4 M. Darnon, T. Chevolleau, T. David, J. Ducote, N. Posseme, R. Bouyssou, F. Bailly, D. Perret and O. Joubert, J. Vac. Sci. Technol. B 28 (1), 149-156 (2010).

6.5 M. Darnon, T. Chevolleau, D. Eon, R. Bouyssou, B. Pelissier, L. Vallier, O. Joubert, N. Posseme, T. David, F. Bailly and J. Torres, Microelectronic Engineering 85 (11), 2226-2235 (2008).

6.6 F. Weilnboeck, E. Bartis, S. Shachar, G. S. Oehrlein, D. Farber, T. Lii and C. Lenox, J. Vac. Sci. Technol. B submitted to (2011).

6.7 W. W. Martienssen, H.;, *Springer Handbook of Condensed Matter and Materials Data*. (Springer, Berlin, 2005).

6.8 A. Alberti, S. Molinaro, F. La Via, C. Bongiorno, G. Ceriola and S. Ravesi, Microelectronic Engineering 60 (1-2), 81-87 (2002).

6.9 X. Hua, X. Wang, D. Fuentevilla, G. S. Oehrlein, F. G. Celii and K. H. R. Kirmse, J. Vac. Sci. Technol. A 21 (5), 1708-1716 (2003).

6.10 T. E. F. M. Standaert, M. Schaepkens, N. R. Rueger, P. G. M. Sebel, G. S. Oehrlein and J. M. Cook, J. Vac. Sci. Technol. A 16 (1), 239-249 (1998).

6.11 R. L. Bruce, F. Weilnboeck, T. Lin, R. J. Phaneuf, G. S. Oehrlein, B. K. Long, C. G. Willson and A. Alizadeh, J. Vac. Sci. Technol. B 29 (4), 041604 (2011).

6.12 N. Negishi, H. Takesue, M. Sumiya, T. Yoshida, Y. Momonoi and M. Izawa, J. Vac. Sci. Technol. B 23 (1), 217-223 (2005).

6.13 V. Krastev, I. Reid, C. Galassi, G. Hughes and E. McGlynn, J. Mater. Sci.-Mater. Electron. 16 (8), 541-547 (2005).

6.14 D. Humbird and D. B. Graves, J. Appl. Phys. 96 (1), 65-70 (2004).

6.15 H. G. Tompkins and W. A. McGahan, *Spectroscopic Ellipsometry and Reflectometry: A User's Guide*. (Wiley, New York, 1999).

6.16 D. Briggs, *Surface analysis of polymers by XPS and static SIMS*. (Cambridge University Press, Cambridge, U.K., New York, 1998).

6.17 R. d'Agostino, F. Fracassi, C. Pacifico and P. Capezzuto, J. Appl. Phys. 71 (1), 462-471 (1992).

6.18 I. Bertóti, M. Mohai, J. L. Sullivan and S. O. Saied, Applied Surface Science 84 (4), 357-371 (1995).

6.19 I. R. Strydom and S. Hofmann, Journal of Electron Spectroscopy and Related Phenomena 56 (19), 85-103 (1991).

6.20 S. W. Robey, M. A. Jaso and G. S. Oehrlein, J. Appl. Phys. 65 (8), 2951-2956 (1989).

6.21 B. Siemensmeyer and J. W. Schultze, Surface and Interface Analysis 16 (1-12), 309-314 (1990).

6.22 M. Wolff, J. W. Schultze and H. H. Strehblow, Surface and Interface Analysis 17 (10), 726-736 (1991).

6.23 E. McCafferty and J. P. Wightman, Applied Surface Science 143 (1-4), 92-100 (1999).

6.24 R. Nyholm and et al., Journal of Physics F: Metal Physics 11 (8), 1727 (1981).

6.25 D. Briggs and M. P. Seah, *Practical surface analysis : by auger and x-ray photoelectron spectroscopy*. (Wiley, Chichester ; New York, 1983).

6.26 N. R. Rueger, J. J. Beulens, M. Schaepkens, M. F. Doemling, J. M. Mirza, T. E. F. M. Standaert and G. S. Oehrlein, J. Vac. Sci. Technol. A 15 (4), 1881-1889 (1997).

6.27 P. J. Cumpson and M. P. Seah, Surface and Interface Analysis 25 (6), 430-446 (1997).

6.28 H. G. Tompkins, J. Appl. Phys. 70 (7), 3876-3880 (1991).

6.29 N. R. Rueger, M. F. Doemling, M. Schaepkens, J. J. Beulens, T. E. F. M. Standaert and G. S. Oehrlein, J. Vac. Sci. Technol. A 17 (5), 2492-2502 (1999).

6.30 P. Prieto and R. E. Kirby, J. Vac. Sci. Technol. A 13 (6), 2819-2826 (1995).

6.31 H. Gokan, S. Esho and Y. Ohnishi, J. Electrochem. Soc. 130 (1), 143-146 (1983).

6.32 R. R. Kunz, S. Palmateer, A. Forte, R. D. Allen, G. M. Wallraff, R. DiPietro and D. Hofer, Proc. SPIE 2724 (null), 365 (1996).

6.33 S. Engelmann, R. L. Bruce, F. Weilnboeck, G. S. Oehrlein, D. Nest, D. B. Graves, C. Andes and E. A. Hudson, Plasma Processes and Polymers 6 (8), 484-489 (2009).

6.34 X. Li, L. Ling, X. F. Hua, G. S. Oehrlein, Y. C. Wang and H. M. Anderson, J. Vac. Sci. Technol. A 21 (6), 1955-1963 (2003).

6.35 X. Li, X. F. Hua, L. Ling, G. S. Oehrlein, M. Barela and H. M. Anderson, J. Vac. Sci. Technol. A-Vac. Surf. Films 20 (6), 2052-2061 (2002).

6.36 C. J. Choi, Y. S. Seol and K. H. Baik, Japanese Journal of Applied Physics Part 1-Regular Papers Short Notes & Review Papers 37 (3A), 801-806 (1998).

6.37 James F. Ziegler, Jochen P. Biersack and M. D. Ziegler, in *PARTICLE INTERACTIONS WITH MATTER: SRIM 2011* (http://www.srim.org/, 2011).

6.38 J. Tonotani, T. Iwamoto, F. Sato, K. Hattori, S. Ohmi and H. Iwai, J. Vac. Sci. Technol. B 21 (5), 2163-2168 (2003).

6.39 D. C. Gray, I. Tepermeister and H. H. Sawin, J. Vac. Sci. Technol. B 11 (4), 1243-1257 (1993).

6.40 M. Koh, H. Yumoto, H. Higashi and T. Nakajima, Journal of Fluorine Chemistry 97 (1-2), 239-246 (1999).

6.41 P. J. Matsuo, T. E. F. M. Standaert, S. D. Allen, G. S. Oehrlein and T. J. Dalton, J. Vac. Sci. Technol. B 17 (4), 1435-1447 (1999).

6.42 N. Ohtsu, K. Kodama, K. Kitagawa and K. Wagatsuma, Applied Surface Science 255 (16), 7351-7356 (2009).

6.43 P. Gonon, The European Physical Journal - Applied Physics 32 (01), 15-21 (2005).

6.44 S. Ben Amor, G. Baud, M. Jacquet, G. Nanse, P. Fioux and M. Nardin, Applied Surface Science 153 (2-3), 172-183 (2000).